THE UNIVERSITY OF MANITOBA

WEAR BEHAVIOUR AND MICROSTRUCTURAL CHARACTERIZATION OF WORN SURFACES AND WEAR DEBRIS OF A HIGH PURITY Al AND AN Al-Si ALLOY AND AN Al-Si/SiCp COMPOSITE SLIDING AGAINST AN M2 STEEL

XIANYAO LI

A Dissertation Submitted to the Faculty of Graduate Studies in Partial Fulfillment of the Requirements of the Degree of

DOCTOR OF PHILOSOPHY

Metallurgical Science Laboratory
Department of Mechanical and Industrial Engineering
Winnipeg, Manitoba

© MAY, 1999

National Library of Canada
Acquisitions and Bibliographic Services
395 Wellington Street
Ottawa ON K1A 0N4
Canada

Bibliothèque nationale du Canada
Acquisitions et services bibliographiques
395, rue Wellington
Ottawa ON K1A 0N4
Canada

Your file Votre référence

Our file Notre référence

The author has granted a non-exclusive licence allowing the National Library of Canada to reproduce, loan, distribute or sell copies of this thesis in microform, paper or electronic formats.

The author retains ownership of the copyright in this thesis. Neither the thesis nor substantial extracts from it may be printed or otherwise reproduced without the author's permission.

L'auteur a accordé une licence non exclusive permettant à la Bibliothèque nationale du Canada de reproduire, prêter, distribuer ou vendre des copies de cette thèse sous la forme de microfiche/film, de reproduction sur papier ou sur format électronique.

L'auteur conserve la propriété du droit d'auteur qui protège cette thèse. Ni la thèse ni des extraits substantiels de celle-ci ne doivent être imprimés ou autrement reproduits sans son autorisation.

0-612-45008-2

Canada

THE UNIVERSITY OF MANITOBA

FACULTY OF GRADUATE STUDIES

*****

COPYRIGHT PERMISSION PAGE

Wear Behaviour and Microstructural Characterization of Worn Surfaces and Wear Debris of a High Purity Al and an Al-Si Alloy and an Al-Si/SiCp Composite Sliding Against an M2 Steel

BY

Xianyao Li

A Thesis/Practicum submitted to the Faculty of Graduate Studies of The University of Manitoba in partial fulfillment of the requirements of the degree

of

Doctor of Philosophy

XIANYAO LI©1999

Permission has been granted to the Library of The University of Manitoba to lend or sell copies of this thesis/practicum, to the National Library of Canada to microfilm this thesis and to lend or sell copies of the film, and to Dissertations Abstracts International to publish an abstract of this thesis/practicum.

The author reserves other publication rights, and neither this thesis/practicum nor extensive extracts from it may be printed or otherwise reproduced without the author's written permission.

TO

MY PARENTS

ACKNOWLEDGEMENTS

I would like to thank my advisor, Dr. K. N. Tandon for providing me with the opportunity to work on this project under his supervision. I am grateful to him for his encouragement, valuable help and guidance as well as complete freedom that he has provided me to carry out the research during the course of the project.

I would like to acknowledge the advisory committee members, Dr. M. C. Chaturvedi, Dr. J. R. Cahoon of the Department of Mechanical and Industrial Engineering, and Dr. M. S. Mathur of the Department of Physics, for their helpful suggestions and discussions. My deep appreciation also goes to the external examiner, Dr. A. T. Alpas of the University of Windsor for many useful suggestions and constructive comments.

Thanks are also due to Mr. John Van Dorp and Mr. Don Mardis for their dedicated technical assistance which made the experimental work a success. I am particularly indebted to my friends for their help and encouragement which I bear in mind wherever I go.

This project was financially supported by a grant from Natural Sciences and Engineering Research Council of Canada. The University of Manitoba is also acknowledged for a graduate fellowship.

Last but not the least, I would like to express my heartfelt thanks to my wife, Ying, and my son, Jianing, as well as my parents for their patience and encouragement. Not only have they given me inspiration and their love, but also have brought me with happiness and a joy of life. The present thesis would be impossible without all of these invaluable supports.

ABSTRACT

The present dissertation discusses wear behavior and microstructural characterization of the wear surface and wear debris of an Al-Si alloy (A356) and an Al-Si (A356) based composite reinforced with 20 vol.% SiC particulate as well as a high purity (99.99%) Al sliding against an M2 steel under unlubricated conditions using a block-on-ring sliding wear tester. The sliding wear tests were carried out at a constant sliding speed (0.2 m/s) and sliding distance (1000 m) under various sliding loads in a range of 0.5 to 15 kg. It was observed that the wear resistance of the Al-Si/SiCp composite material was superior to that of the Al-Si alloy by one order of magnitude at a low sliding load. With an increase in the sliding load, the wear resistance was almost the same for the composite and the base alloy. The improvement in the wear resistance at low loads was mainly due to the incorporation of the reinforcing SiC particles that acted as load-bearing components during the sliding wear. At high loads, the wear behavior was mainly governed by the formation, fragmentation and delamination of the mechanically mixed layers in which the majority of the SiC particles were fragmented and no longer acted as major load-bearing components. It was also observed that the wear resistance of the Al-Si/SiC composite could slightly be increased by approximately 10 % due to the T6 heat treatment of the composite. The increase in the wear resistance, however, was not significant when compared to the increase in the hardness of the matrix due to the heat treatment. This can be partially attributed to the fact that *in-situ* precipitation occurred in the subsurface during the sliding wear of the as-cast Al composites.

Microstructural characterization of the worn surfaces and wear debris was carried out by using Scanning Electron Microscopy (SEM), Transmission Electron Microscopy (TEM) equipped with Energy Dispersive Spectroscopy (EDS), X-ray mapping and X-ray Diffraction (XRD). In particular, longitudinal cross-section TEM analyses of the worn surfaces and wear debris were successfully conducted in the present work. The results showed that the deformed structures in the worn surfaces of the Al-Si alloy and the composite contained a large number of cells and elongated subgrains with an aspect ratio of 5 to 10. The microstructural evolution along the depth was consistent with the shear strain distribution in the subsurface that could be best described by an exponential law, i.e, $\varepsilon(z) = \varepsilon_s \exp(-kz)$, where ε is shear strain and z depth below the worn surface. It was also observed that mechanically mixed layers (MMLs) were formed during the sliding wear of the Al-Si/SiC composite and Al-Si alloy as well as the high purity (HP) Al against the steel. The MMLs were found to be comprised of elements from both sliding surfaces, which were mainly Al and Fe. The microstructures and chemical conditions of the transferred elements were mainly determined by the sliding loads and were studied in a great detail using SEM and TEM.

Characterization of the wear debris by means of the above mentioned techniques and Mössbauer spectroscopy revealed that the wear debris had features similar to those of the MMLs in the worn surfaces of the Al based materials from which the debris were detached. For all three materials, the debris aggregates generated at low loads consisted mainly of a mechanical mixture of α-Al and α-Fe. With an increase in the sliding load, the agglomerated debris of nanocrystalline structures were incorporated with Fe-Al(Si)

intermetallic compounds, and aluminum- and iron oxides as a result of mechanical alloying and oxidation caused by a large amount of plastic deformation during the sliding process in association with frictional heating. The present work has provided evidence of the formation of the intermetallic compound FeAl as a result of material transfer and mechanical mixing, as revealed by using XRD, TEM and Mössbauer spectroscopy.

Amorphization was observed in the wear debris and worn surfaces of both the Al-Si alloy and the Al-Si/SiC composite sliding against the tool steel under the unidirectional dry sliding wear and a reciprocating dry sliding wear. The amorphous phases were found to coexist with the ultrafine grained aggregates (a few nm to dozens nm depending on the loads) in the wear debris. The mixture of the amorphous phases and the ultrafine grained particles were mainly comprised of Al, Fe and oxygen, suggesting that an extensive mechanical mixing of elements from both the sliding contacts occurred during the sliding wear. In the reciprocating dry wear, the amorphous phase was observed to coexist with precipitates containing Al and Ti, crystallographic structure of which was also characterized using TEM in the present work. The correlation of the microstructural characteristics of the worn surface and wear debris to the wear behavior and mechanisms of the Al-Si alloy and the Al based composite was discussed in detail.

TABLE OF CONTENTS

LIST OF FIGURES

Chapter Two

Chapter Four

Chapter Five

Chapter Six

Chapter Seven

LIST OF TABLES

CHAPTER ONE INTRODUCTION

Friction and wear of materials are subjects with a long history accompanying the civilization of human beings and of practical significance in modern industries. These subjects can be dated back to ancient times when man learned to use frictional heating to start cooking fire, and learned to machine tools from stones. There are evidences that early man used stones as wear resistant materials in the Neolithic period. In modern society, friction and wear of materials are still very important engineering issues that can be found in many industrial applications as well as ordinary life. For example, pistons and liners in engines, shafts, bearings and brakes in automobiles and aircraft are subject to friction and wear. Research on these subjects has been conducted not only from mechanical and chemical viwpoints, but also from a materials science and engineering point of view. Especially, in the last decade, many new materials have been developed for tribological applications[1], which has only been possible due to the research on wear of materials using modern analysis methods and techniques.

Wear is a complex surface/interface process in which several physical and chemical events take place depending on materials, tribological conditions such as different testing geometry, sliding load and speed sliding as well as the environment etc. The conditions of sliding wear, especially in dry (unlubricated) states, produce large plastic strain near the worn surface. Not only does the material removal may occur on both the wear surface and the counterface, but large subsurface strains and plastic deformation gradients can also be generated in the subsurface below the worn surfaces[1, 2, 4]. The high shear and compressive stress in association with frictional heating during wear processes, could induce several events in the worn surface and subsurface, such as work hardening[2], recrystallization(static or dynamic)[3, 4], mechanical twinning[5],

deformation texture[6], strain-induced phase transformation[7]. Since two or three sliding components are involved in a sliding system, a mutual transfer and mechanical mixing of materials from the counterparts are often observed in the worn surface[8]. Once the transfer occurs and mechanically mixed layer is formed, wear behavior of the material is altered due to the distinct features of the mixed layer as compared to the original material. Therefore, problems associated with friction and wear are complicated, and many of them are still open to investigations with respect to a deep understanding of wear mechanisms of materials, especially from a metallurgical point of view.

Recently, more attention has been paid to wear of multiphase materials. Especially, wear of particulate reinforced aluminum metal matrix composites (MMCs) has been studied by numerous researchers[9-30] since MMCs are considered for several tribological applications in the aerospace, aircraft[9, 31] and, in particular the automotive industries[32]. The high strength-to-weight-ratio of aluminum based MMCs makes it an attractive replacement for steels in various engine components; this, in turn, can result in an improved engine efficiency and a reduction of noise and friction. It has been an opportunity and a challenge that metal matrix composites will be gradually introduced into high volume automobile production[32]. Potential automotive applications mainly include engine blocks and cylinder liners, connecting rod and piston, brake rotors, gears and valves, and even drive shaft. In these applications, wear resistance of the components is a major requirement.

Wear phenomenon and wear mechanisms involved in the wear process could be further complicated for multiphase materials owing to the addition of secondary particles. Under certain conditions (load, sliding velocity etc.), wear of a metal matrix composite can be treated as three-body abrasive system (the MMC, sliding counterface and the fragmented particles) as the hard particles are forced away from the matrix and get settled

in the wear track during wear. There have been a number of investigations and reviews[9-12] concerning the wear behavior of MMCs in which an improved wear resistance has been reported. However, wear mechanisms of these multiphase materials are still being investigated due to complications resulting from the addition of the reinforcing phases, especially on microstructural features of the top worn surfaces and microstructural evolutions along the depth below the worn surfaces. In Al alloys and Al based metal matrix composites, for example, formation of a mechanically mixed layer (MML) is generally found, which is reported to be comprised of materials from the sliding surface and the counterpart[13, 22, 23]. However, microstructural characteristics and formation mechanisms still remain open to investigation and discussion. Depending on different experimental conditions under which wear tests were conducted, there are differences of the formation mechanism of the MML between different observations. Some researchers reported that the mixed layer was mainly comprised of oxides[13], and others found little or no oxide in the mixed layer[34]. Clearly, there are a number of important issues that need to be addressed in a greater detail.

The present investigation was carried out with a primary objective of a deeper understanding of wear of multiphase Al alloys in terms of their microstructural characteristics. In particular, wear of an Al based MMC and its base alloy, in which second phases and ceramic reinforcements are present, was targeted for an extensive investigation. In order to understand wear mechanisms of these materials and the influence of reinforcements and second phases on their wear behavior, a high purity Al was also chosen in the present study. In conjunction with the study on the wear behavior of these materials under dry sliding wear conditions, microstructural characterization of the worn surfaces and wear debris were mainly investigated by using Scanning Electron Microscopy(SEM), Transmission Electron Microscopy(TEM), and X-ray Diffraction(XRD) and other physical and metallurgical methods.

The dissertation is divided into eight chapters. In Chapter Two, the relevant literature is reviewed which is followed by a description of the scope of present research in Chapter Three. The materials and experimental procedures and techniques involved in this study are provided in Chapter Four. The wear behavior and microstructural characterization of the worn surfaces are presented and discussed in Chapter Five. Since an amorphous structure coexisting with certain precipitates was found in the worn surface in a reciprocating sliding wear system, a separate chapter (Chapter Six) is dedicated to discuss the amorphization and crystallographic characteristics of the precipitates. Chapter Seven focuses on the microstructural characterization of the wear debris with results from SEM, XRD and TEM as well as Mössbauer spectroscopy. Finally, a comprehensive summary of the dissertation is given in Chapter Eight followed by recommended future work in Chapter Nine.

CHAPTER TWO LITERATURE REVIEW

2.1 WEAR

2.1.1 Definition and Mechanisms of Wear

A general definition of wear is damage to a solid surface when the surface moves relative to a contacting counterface. Wear process generally involves progressive loss of materials from at least one of the contacting components and loose wear debris may be generated. Wear process can also take place without removal of materials, and only material displacement and plastic deformation occur in the surface and subsurface during the wear process accompanying some changes in shape and/or properties[1]. The latter could also induce damage to solid surfaces. However, the definition of wear in terms of loss of material has been emphasized in most of the wear studies[33].

Engineering surfaces are far from being perfectly smooth when observed under a microscope. They actually consist of peaks and valleys, as shown in Fig. 2.1. When two solid surfaces are brought into contact under a load, the true contact area is initially at three or more peaks, which are referred to as individual asperities. Subjected to a load, the contacting asperities deform plastically, and this results in more contact spots to appear. Brought to relative motion, surface damage resulting from the friction and wear events will start from the contacting asperities.

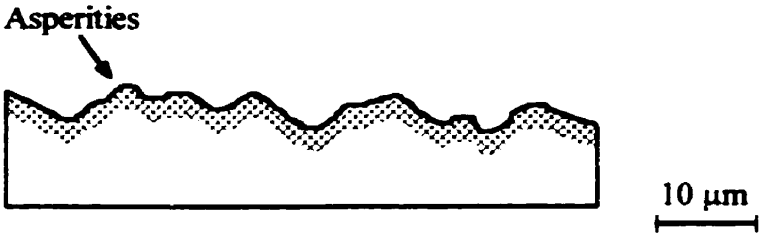

Fig. 2. 1 Schematic illustration of engineering surface of metallic materials on a microscopic scale.

It is common to classify types of wear in terms of different relative motions, such as sliding wear, rolling wear, impact wear and lubricated/unlubricated(dry) wear and so forth. These processes could act on the surfaces in the relative motion either independently or cooperatively; for example, abrasion in a corrosive medium. Therefore, wear mechanisms, which are responsible for material removals, i.e., wear processes, could be different under different conditions. To date, many wear mechanisms have been proposed to address the wear phenomenon, and it seems almost impossible that a single wear mechanism can be expected to be responsible for wear of materials.

The most common wear mechanisms are listed in Fig. 2.2. It can be seen that a wear mechanism is generally built on phenomenological observations. These observations include measurement of wear rate, topographical information and subsurface behavior as well as wear debris generation. Halling[34] introduced the simplest classification of wear into mild wear and severe wear based on numerical analysis of wear rate. Mild wear is generally associated with low loads where the wear debris consists of fine particles. At higher loads, severe wear occurs and the wear debris is of a much larger size, the worn surfaces are much rougher and the wear rate changes by several orders of magnitude. This classification of mild and severe wear was proposed by

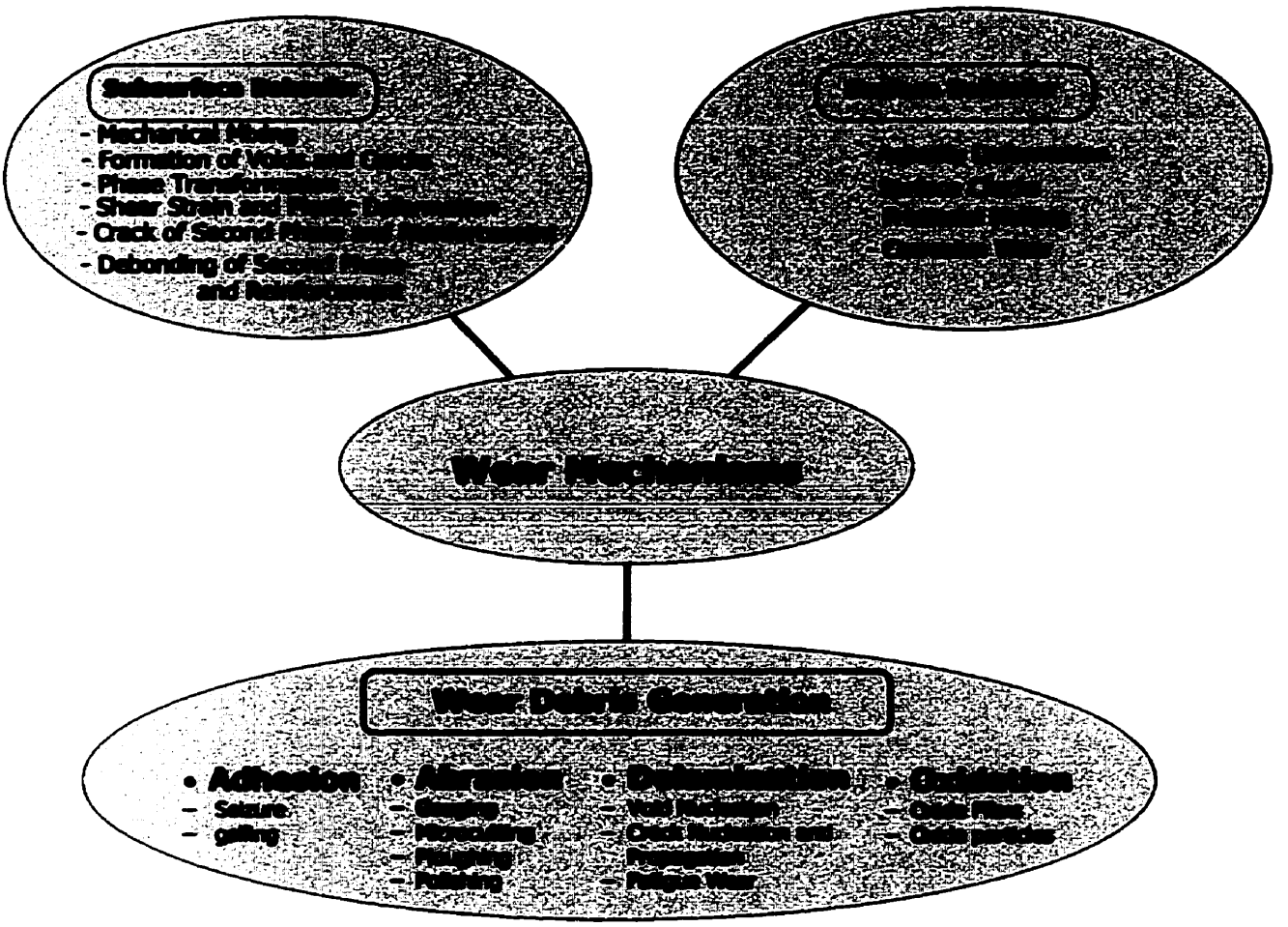

Fig. 2.2 Common Classification of Wear Mechanisms.

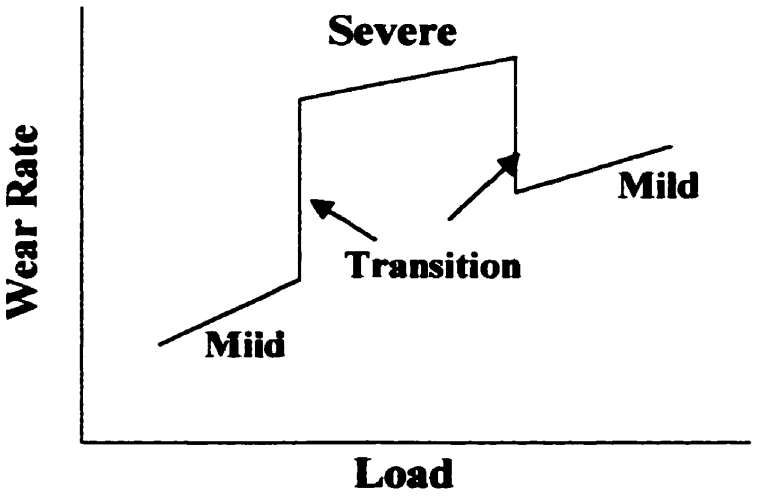

Fig. 2.3 Schematic illustration of transition of wear regimes in metallic materials. After[36].

Archard and Hirst [35] on the basis of wear debris size. In metallic materials the two types of wear regimes can rapidly transit from one to another as the load is increased, as shown in Fig. 2.3.

Samuels et al [37] summarized sliding wear mechanisms based on insights obtained from the morphologic observation of wear debris recovered from a sliding wear system. The adhesion theory of wear, initially proposed by Archard[38, 39], has been widely accepted as a basis for understanding sliding wear phenomena. The approach is based on the concept of the above mentioned small contact asperities, i.e., actual removal of materials can occur only at a very small fraction of the asperity contact as plastically deformed asperities adhere to each other, as shown in Fig. 2.4 (a). Subjected to a high pressure resulting from the load, the contacting asperities are plastically deformed until the areas of contact are large enough to support the load. Large shear forces accumulate at the localized area, so that fracture in one of the materials occurs and a fragment is removed and transferred to the other.

The abrasive wear is usually involved with a third body such as an embedded abrasive particle between the contacting surface or hard protubrances that are forced against and move along the sliding surface. Several mechanisms can be responsible for the surface damage, including plowing, cutting, microcracking, microfatigue and wedge formation[37] during abrasive wear. Fig. 2.4 (b) shows two possible modes of the damage caused by abrasive wear.

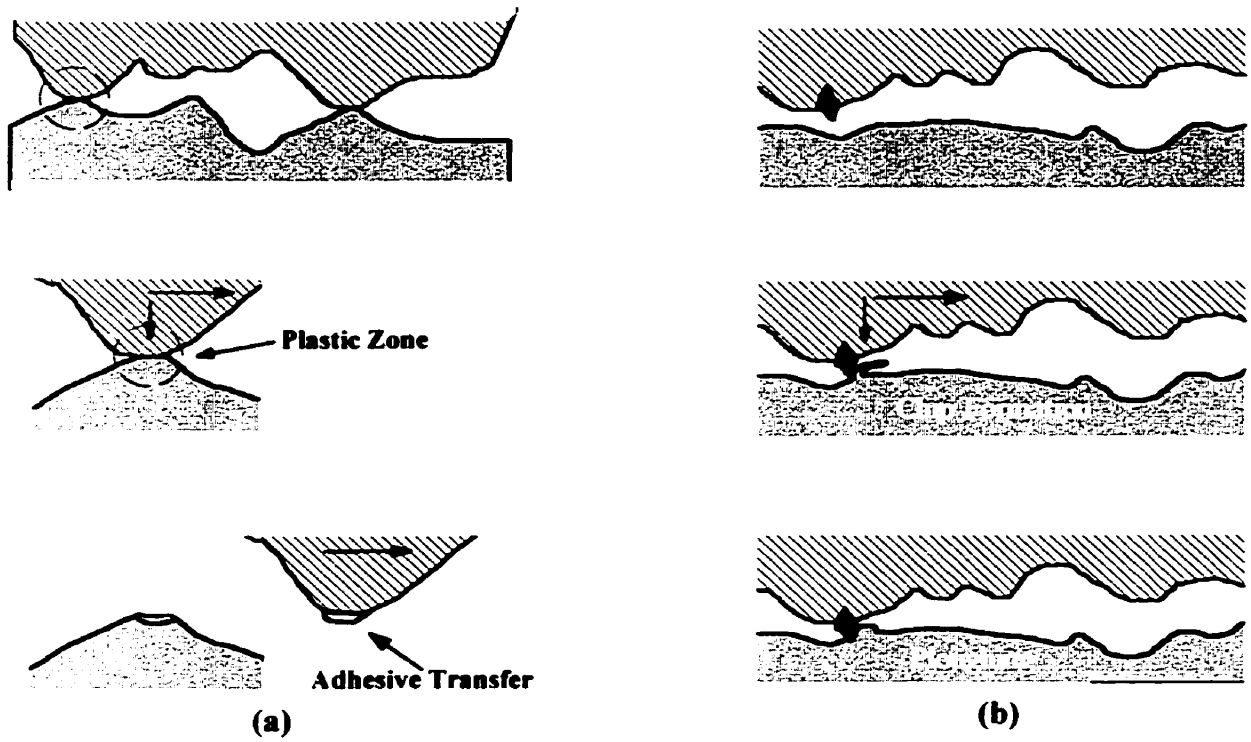

Fig. 2. 4 (a) Schematic illustration of the classical adhesion mechanism of sliding wear.
(b) Schematic illustration of adhesive mechanism of sliding wear, showing two possible modes of interaction between a hard asperity (an embedded abrasive particle) and a second surface.

In a sliding motion, most of the work done against friction is turned into heat resulting in a temperature rise on the surface. Oxidation may be observed in the sliding surface, and a possible mechanism of oxidation wear may result from the repeated formation and removal of a surface oxide film, as demonstrated in Fig. 2.5 (a). Quinn [40] has developed an oxidation theory of mild wear for dry sliding of steels, in which a film of oxide is formed on a sliding asperity and the oxide will be removed when it reaches to a critical thickness and becomes mechanically unstable. It is believed that in many cases tribological oxidation could reduce the wear rate compared to the running in wear stage [40]. This theory is valid only for the case where oxidation is the dominant mechanism, such as at a very high load and a high sliding speed.

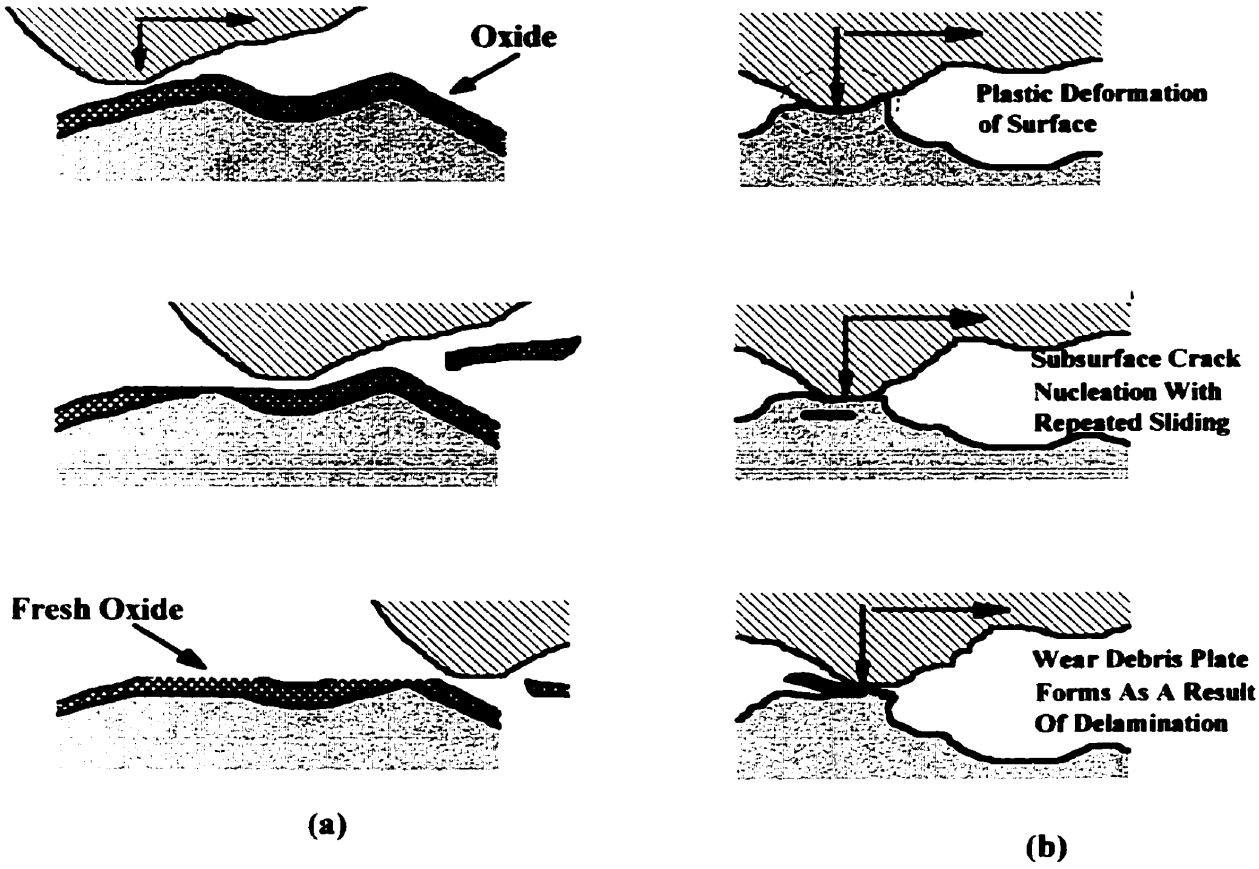

Fig. 2. 5 (a) Schematic illustration of a possible oxidation wear in which a surface oxide film is formed and detached under the sliding conditions.
(b) Schematic illustration of delamination wear showing various stages involved, such as plastic deformation, subsurface crack nucleation and the eventual delamination.

It is also quite common that plate like wear debris is observed in a sliding wear system. This type of wear particle or debris has been the basis for the delamination theory of wear developed by Suh[41] and coworkers[42]. According to the delamination theory, normal and tangential forces are first transmitted through the contacting asperities, and a large plastic shear strain accumulates in the subsurface. Cracks are then nucleated which grow and propagate nearly parallel to the sliding surface, as shown in Fig. 2.5 (b). As a result, loose plate-like particles are generated. The theory has described one of the important aspects of wear debris formation and wear mechanisms involved, but it is still

limited since this model neglects the existence of transfer of materials between the two contacting surfaces and microstructural changes occurring in the worn surface. Actually, other mechanisms have demonstrated that plate-like wear debris may be generated by entirely different mechanisms. Kayaba and Kato[43] suggested that a plastic deformation zone develops early in the interaction between two asperities and that shear displacement occurs in subsurface generating a shear tongue. When a crack eventually develops at the root of the tongue, a fragment consisting of a series of plates detaches from the surface, and individual debris subsequently is generated.

Lim and Ashby[44] proposed wear mechanism maps which show the wear rate and the dominant wear regimes including delamination, mild and severe oxidation, melting and seizure wear, in dry sliding wear system of steels. The diagram can be constructed empirically (i.e., from experimental data alone) and by modeling(by theoretical analysis calibrated to experiments). They obtained the wear rate mechanism map for a steel by using the oxidation wear theory together with thermal analysis of sliding contact, as shown in Fig. 2.6.

In this map, contours of constant normalized wear rates are superimposed on fields showing the regimes of dominances of different wear mechanisms. There are discontinuities in the contours where they cross the field boundaries into the regimes of severe oxidation wear and melting wear. The wear rates given in parentheses are the values when mild wear takes place and the shaded area indicates a transition between mild and severe wear.

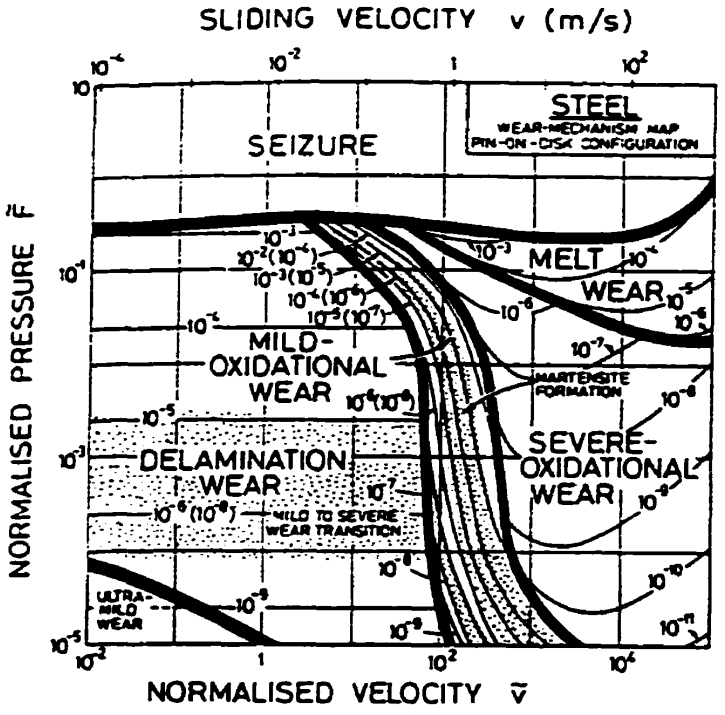

Fig. 2.6 The wear mechanisms map for a steel sliding pair using a pin-on-disk configuration. After [44].

2.1.2 Stress distribution and frictional heating

As mentioned above, many variables are involved in the wear system. These variables include: 1) extrinsic factors, such as test geometry(configuration), normal load, sliding speed and sliding distance, 2) intrinsic factors such as material properties, microstructures and composition. These factors lead to two main phenomena, namely, a complex stress conditions and friction-induced temperature rise in the near surface and subsurface. Since they influence crack nucleation and propagation and are critical to microstructural evolution during the wear process, these factors play vital roles in determining wear behavior and mechanisms.

2.1.2.1 Temperature at the sliding contact

It is well known that most of work done against friction is converted into heat during the sliding motion between two solid surfaces, thus resulting in rise of temperature at the contact. Generally speaking, the higher the sliding speed the higher the surface temperature. The resulting rise in temperature may influence microstructure of the sliding surfaces and modify their mechanical properties, and at a higher speed it may cause them to oxidize or even melt[44]. As a result, the wear rate and wear mechanisms would be significantly influenced by the temperature rise.

Many attempts have been made to estimate the surface temperature created by frictional heating[44-47]. Basically, the frictional heat is generated at tiny contact area, i.e., asperities, which make up the true area of contact at the sliding surface[44]. The instantaneous temperature of those contact spots, i.e., flash temperature is obviously higher than the average bulk temperature of the surface based on the consideration that the contact spots are plane source of heat and the frictional heat is conducted into bulk surface[48]. However, it is difficult to estimate the number and size of the contact asperities during the dynamical wear process, especially for plastically deformed contact spots, and the flash temperature cannot be given accurately [47], and sometimes the estimated temperatures are considerably higher than the measured values.

Many investigations have discussed the influence of the frictional heating on the wear rates and wear mechanisms[39, 44, 49]. Hirst and Lancaster[49] studied wear rates

of brass as a function of sliding speed in a pin and ring apparatus in which the mean temperature of the pin was deliberately altered, i.e., it was increased by insulating it thermally from its holder and decreased by water cooling. As shown in Fig. 2.7, when the pin was cooled (curve B) the wear rate continuously decreased with speed. This was different from that with the metal holder (curve A) which showed an increase in wear rate at high loads (> 100 cm/s). On the other hand, thermal insulation on the pin caused the wear rate to increase earlier (curve C). It appears that the tendency of the wear rate to decrease with speed is limited by the attainment of a critical temperature, rather than a critical speed. By analyzing the mean temperature of the surface of the brass pin and the flash temperature attained at the region of true contact, they concluded that the flash temperature had no discernible influence on the wear rate. The increase in the wear rate at high speeds was attributed to softening of the brass surface as a whole.

Quinn and coworkers [45, 48, 50] have extensively studied frictional heating and its influence on sliding wear and developed an oxidation theory of wear. They proposed that the frictional heat flux generated at the real areas of contact are divided so that part of the heat flows into one specimen while the remainder flows into the second specimen. This raises the temperature of the contacting surface and, if the heat flux and the temperature is sufficiently great, the metal of the contacting asperities undergoes oxidation, so that an oxide film occurs on the contacting surface. The oxide film thickens until, at a critical thickness, it spalls off, attributing to the formation of wear debris. Based on this assumption and with convincing evidence of wear of steels, Quinn has proposed the theoretical wear rate in terms of his oxidation theory:

$$w = \left(\frac{L}{P V f^2 \zeta^2 \rho_o^2}\right) A_p \exp[-Q_p / RT_o]$$

where

w: Wear rate

L: Load

V: Sliding speed

f: Mass fraction of oxygen in the oxide

ζ: Oxide film thickness

ρ_o: Density of the oxide

A_p: Arrhenius constant of the oxidation

Q_p: Activation energy of the oxidation

T_0: Temperature at the contact.

P: Hardness of metal

Lim and Ashby[44] later developed revised equations for bulk and flash temperatures with a consideration of correction of the number of the contact asperities. They calculated the heat flow and temperatures based on an assumption that the unit area of the asperity was constant and the real area of contact changed by changing the number of contacting points dependent upon the load. The calculated values were calibrated against the experimental data, and a temperature map was developed giving a reasonable

picture of the temperatures that appear in a steel pin sliding on a steel disk during dry wear test, as shown in Fig. 2.8.

In terms of an increase in temperature in a wear surface, Lim and Ashby[44] discussed various wear mechanisms, especially oxidation dominated wear mechanisms of steels. When steel surfaces slide at speeds below about 1.0 m/s, the wear debris is largely metallic and surface heating is negligible. The wear failure is mainly caused by plastic deformation. Above 1.0 m/s, the debris consists mainly of iron oxides. A velocity of 1.0 m/s is just sufficient to give flash temperature which will cause oxidation. At speeds in the range of 1.0 m/s < V< 10 m/s, flash temperatures are enough to cause local oxidation, and the oxide film is thin and brittle. In this wear regime, it was reported that martensite transformation occurred when a hot asperity lost contact with the counterface and was quenched by conduction of heat into the underlying bulk. At higher speed(> 10 m/s), surface oxidation becomes more severe, and the oxide film becomes thicker and continuous, covering the entire surface.

Ashby et al [51] later modified their previous model of surface temperature generated during sliding wear. Considering a sliding wear system at a normal load F, sliding speed v, the coefficient of friction μ at a sliding time t. The heat Q, generated at the sliding contact per unit sliding time can be written as

$$Q = \mu F v$$

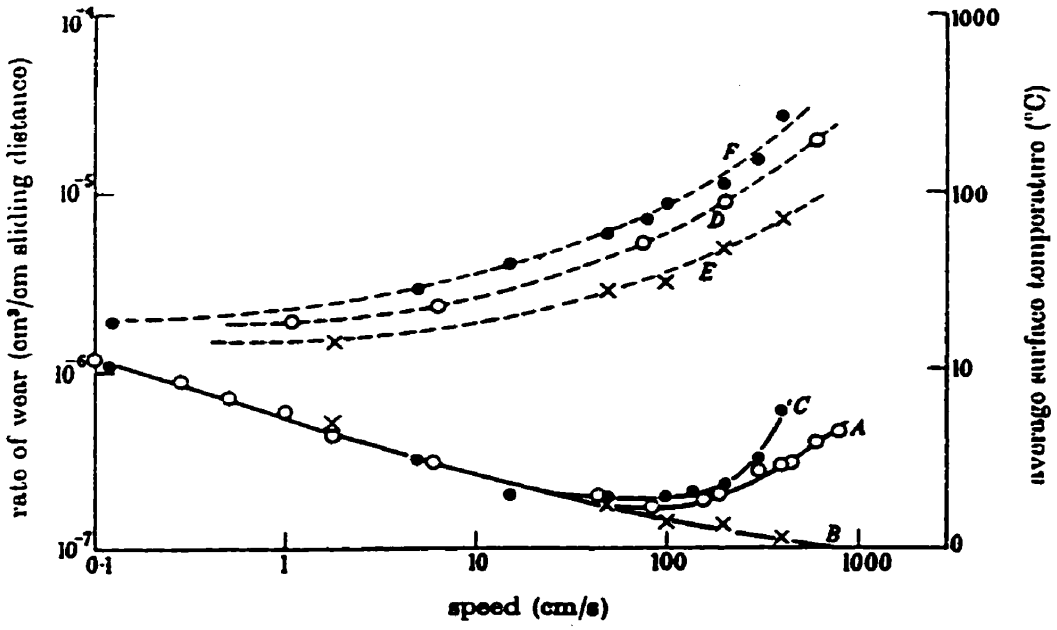

Fig. 2.7 Variation of wear rate and surface temperature with speed for thermally insulated and cooled pins. The solid line, wear rate; the dash line, surface temperature. Line A and line D, metal pin-holder; line B and line E, water-cooled pin-holder; line C and line F, thermally insulated pin-holder. After[49].

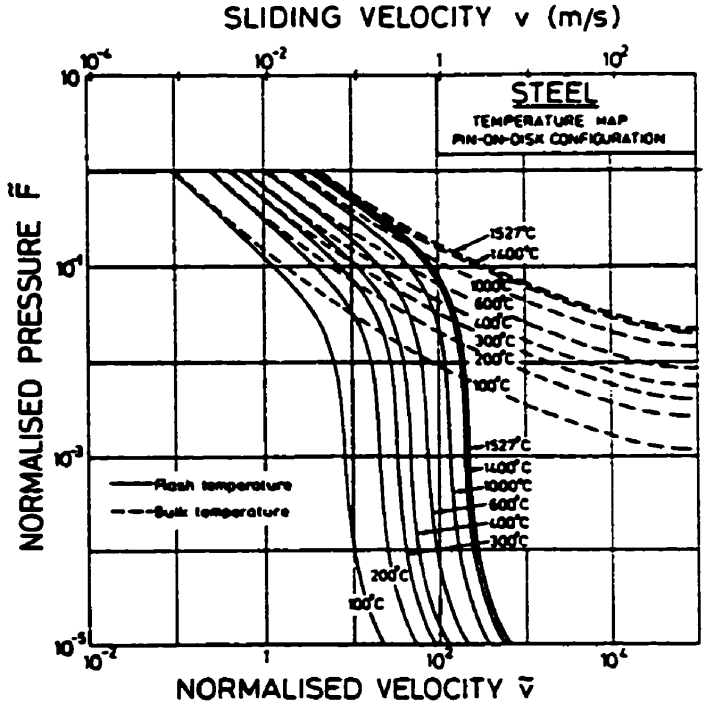

Fig. 2.8 The temperature map for a steel in a pin-on-disk configuration. After [44].

Assuming that the frictional heat is injected uniformly through a normal contact area A_n, the average surface temperature T_b can be written as

$$T_b - T_0 = \frac{\mu F v}{A_n}\left[\frac{k_s}{l_{sb}} + \frac{k_c}{l_{cb}}\right]^{-1}$$

where T_0 is the temperature of a point away from the contact surface to which heat flows, i.e., a heat sink; k_s and k_c are the thermal conductivities of the sample and the counterpart material respectively; l_{sb} and l_{cb} are the equivalent heat diffusion distances mainly dependent on the thermal properties of the sliding contact materials as defined in [51]. The local flash temperature of contact asperities T_f, can be estimated, assuming that the frictional heat is injected only at the asperity contact area A_n,

$$T_f - T_b^{\cdot} = \frac{\mu F v}{A_f}\left[\frac{k_s}{l_{sf}} + \frac{k_c}{l_{cf}}\right]^{-1}$$

where $T_b^{\cdot}$ is the sink temperature, l_{sf} and l_{cf} are the equivalent diffusion distances considering "real" contact asperities for flash temperature estimation. Zhang and Alpas [52] have successfully applied this method to their sliding system of 6061 Al alloy against SAE 52100 steel. They found that the measured values were in good agreement with the calculated ones using the above estimation method of bulk temperature.

2.1.2.2 Strain distribution and deformation structures in the worn surface

The conditions of sliding wear, especially in dry(unlubricated) state, produce large plastic strains at and near the wear surface. Not only does the material removal occur on both the wear surface and the counterface, but large subsurface strains and plastic deformations can also be generated near the worn surfaces[1, 2, 53-56]. Several researchers have emphasized the contribution of surface strains and plastic deformation to wear, either developing and modifying[53] or challenging[57] the adhesive theory. Moore and Douthwaite[53] studied the worn surface focusing on large plastic strains observed at considerable distances from the wear surface, and they suggested that because of strain hardening, an extensive region below the worn surface was also deformed plastically and a large part of the energy expended in the sliding wear might be expected to be absorbed by the plastic deformation. Many investigations [2, 3, 13, 17, 53, 55] have discussed plastic shear strain as a function of depth in the worn surface in a number of ways, such as measurement of deviation of plastic flow from being normal to the worn surface by using a marker technique[53, 55], and microhardness depth profile obtained on the cross section of the worn surface.

With respect to the plastic deformation, the worn surface can be generally considered to be composed of different regions as shown in Fig. 2.9. In addition to a mechanically mixed layer that is located on very top worn surface, plastic deformation regions in the near surface can be described as two subregions, namely 1) a very highly deformed structure which has a strong shear gradient and very fine microstructure, and 2)

plastic deformed region wherein bulk plastic deformation occurs. The depth of deformation can be determined experimentally from the longitudinal cross section. For example, Moore and Douthwaite[53] observed bending of alternative layers of two different metals subjected to unidirectional sliding and measured the high strain and microhardness at points below the worn surface, as shown in Fig. 2.10.

Based on measurements of the displacement of subsurface, the strain distribution below the worn surface could be measured as proposed in [53]. Their method is summarized as follows. As shown in Fig. 2.11, the flow lines are initially normal to the worn surface and progressively bend towards the sliding direction as a result of shear

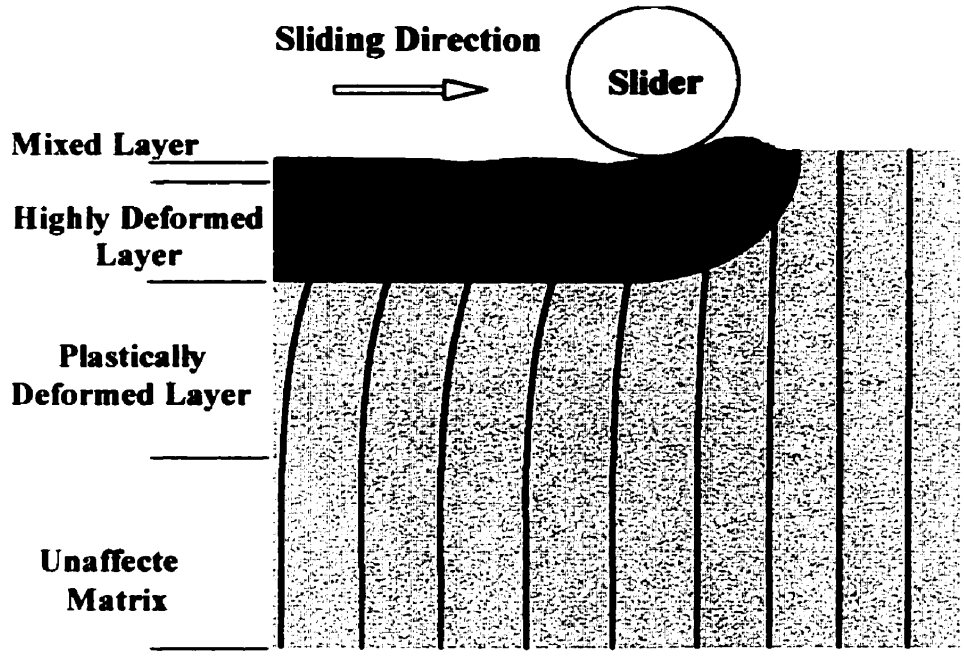

Fig. 2.9 Schematic illustration of a longitudinal cross section of a worn surface. The subsurface are divided into different zones or layers. The curved lines indicate strains below the surface.

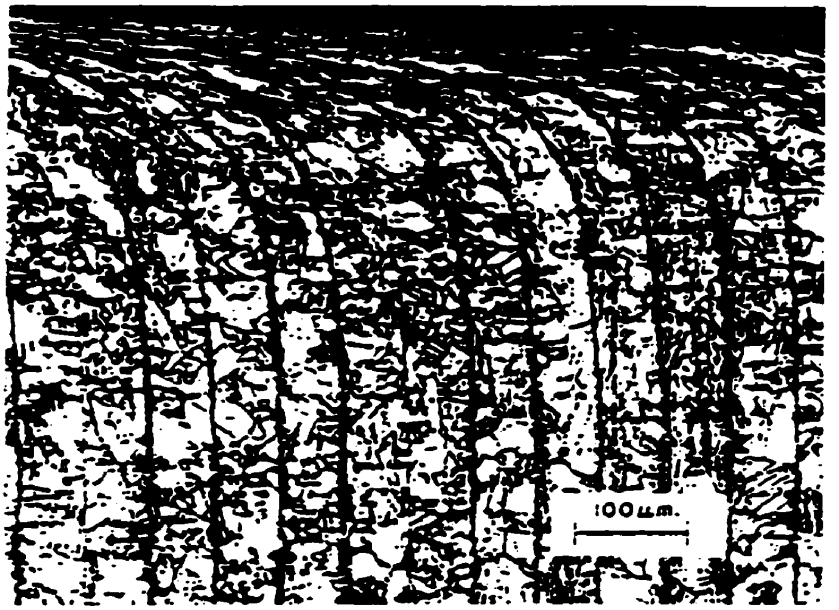

(a)

(b)

Fig. 2.10 Typical sections normal to the worn surface using laminate structure as a marker. (a) After trepanning, showing a high natural strain as compared with (b); (b) after abrasion. After[53].

deformation. The flow lines approach almost parallel to the worn surface in the near surface. The equivalent plastic strain, ε, at any given depth Z, can be estimated by measuring the shear angle of the flow line to the normal and using the following equation:

$$\varepsilon = \frac{\sqrt{3}}{3}\tan(\theta)$$

This method has been used in different sliding wear systems by different researchers, for example, copper sliding against a steel by Alpas et al[58] and aluminum alloys against steels by Venkataraman and Sundararajan[13]. A strain distribution in the subsurface could be described using the above method, and the accuracy of measurement in the very near surface can be reduced due to the presence of mechanical transfer and mixing or oxidation in the near worn surface.

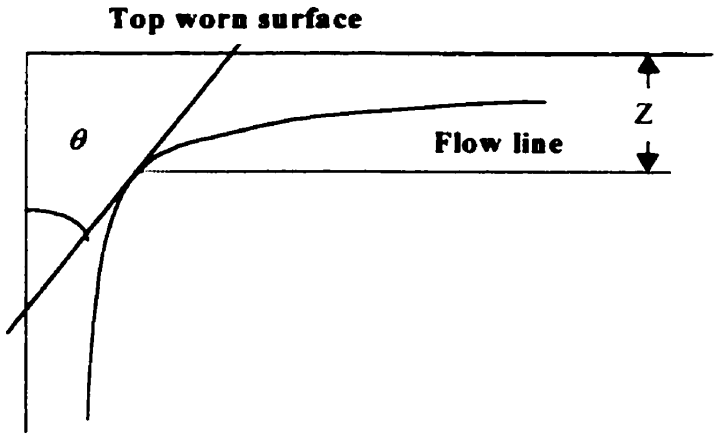

Fig. 2. 11 Illustration of calculation of shear strain below the worn surface using flow lines.

Rigney and Hirth[55] proposed a simple model to consider plastic deformation in a steady state sliding wear. They used a typical stress-strain curve together with a series of successive strain profiles to rationalize their model, as shown in Fig. 2.11. Region A would be associated with Stage I of the stress-strain curve, and region B with Stage II in which work hardening is dominant. Region C would correspond to stage III, in which dynamic recovery is important, and work hardening is then balanced by recovery and cell structure formation.

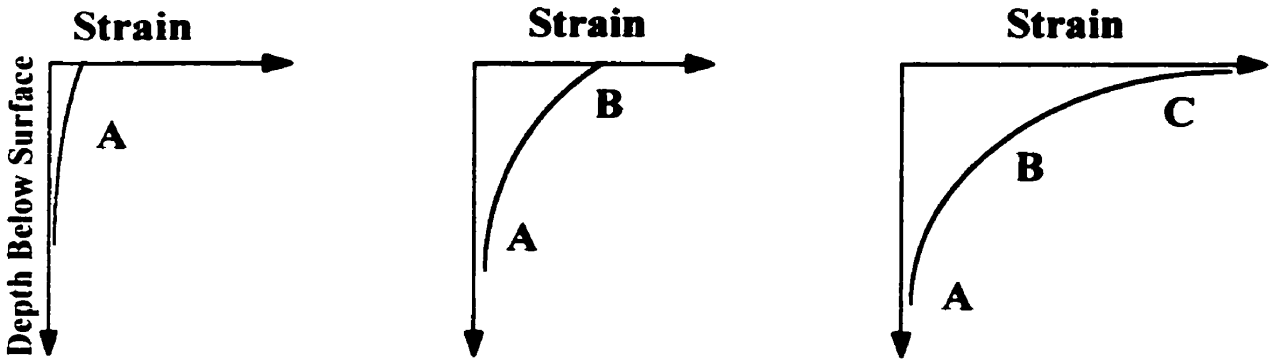

Fig. 2.12 Strain profiles in a longitudinal cross section below a wear surface at successive times during siding. Regions A, B, and C correspond to Stage I, Stage II and Stage III in a stress-strain curve according to the work hardening theory. After[55].

In recent years, some important developments in the understanding of deformation structures and work hardening effects in the worn surface have been possible through the utilization of transmission electron microscopy and other sophisticated techniques[59]. Ohmae et al[60] studied deformation structures of the wear surface in a single crystal of copper subjected to a single pass sliding. By choosing different sliding surfaces and sliding directions which corresponded to primary crystallographic planes

and directions in the FCC structure, they found that the deformation cell structures were similar to that of copper subjected to a tensile deformation at Stage II or Stage III. The dislocation density below the wear surface was extremely high and the formation of the cell structure was predominant, and as the depth from the surface increased, the cell size and the misorientation between the cells became large. Similar deformation structures were also observed by Rigney *et al*[56] and Heilmann *et al* [61]. They characterized the deformation and dislocation substructures formed at large strains during wear of copper. They subdivided the plastically deformed material into different layers. The first layer was the furthest away from the top worn surface, and the structure in the first layer consisted mainly of equiaxed cells bounded by relatively wide cell walls. The cells themselves contained dislocation networks and the cell structure at this depth was less well defined. Closer to the surface, the cell walls were sharper and the cells were elongated parallel to the sidling direction. Near the top surface, the walls were quite sharp and elongated subgrains were formed. The cells and subgrains decreased in size as the strain increased. These observations are very similar to those found in cold-rolled materials[62], and drawn wires [63].

In terms of the stacking fault energy(SFE), Samuels et al [37]summarized two general characteristics of the deformation structure in the wear surface of copper and brass, as schematically shown in Fig. 2.12 . In a metal with medium or high SFE, for example Cu[60, 61], relaxation to form cell structure occurs, and cells and microbands or shearbands are the dominant features in the worn surface, while in materials with low SFE, for examples 70-30 brass[64] and stainless steel[6], dislocations, stacking faults and

deformation twins are typical characteristics of the worn surface.

Several researchers have dealt with recovery and recrystalization in the deformed layer in wear surface[3, 4, 6,]. Dautzenberg[3] provided a good evidence for the presence of recystalized grains in the sliding surface of polycrystalline copper and single crystal copper. He observed fine equiaxed and highly elongated grains in longitudinal cross section by using TEM, and suggested that the equiaxed grains and possibly the elongated grains were recrystalized as difference in dislocations and texture were obvious in the deformation structure. They thought the process was not static recrystallization but dynamic recrystallization which occurred many times during the deformation process, even though the process temperature was relatively low, and the large amount of deformation lowered the dynamic recrytallization temperature.

Kou and Rigney[4] also observed recrystallization phenomenon in sliding wear of Al and Al alloys, in addition to the observation of shear bands similar to microbands. However, it was controversial to determine whether it was static or dynamic process. They observed well developed subgrains and dislocation structures within the subgrains as well as high angle boundaries which might be the evidence of dynamical recrystallization. On the other hand, they doubted that the static recrystallization would occur very quickly if an aluminum specimen was kept at the hot-working temperature after hot working had stopped. Consequently, they concluded that it was difficult to determine whether the recrystallization occurred during dynamic (sliding) or static process(soon after or after the sliding). Recently, Singh and Alpas[65] and Zhang and

Alpas[52] provided metallographic evidence for dynamic recrystallization occurring along subsurface strain gradients during the severe wear of Al alloys at an elevated test temperature (350° C). They observed that the subgrains were elongated in the direction of a strain gradient and had an aspect ration of 2 to 4.

2.1.3. Transfer and mechanical mixing of materials

Transfer of materials from one sliding surface to another occurs in a sliding system either in lubricated or unlubricated conditions. A number of investigations have dealt with the mechanically mixed or alloyed layer generated by sliding wear in the extreme wear surface [66-69]. Since the mixed layer is located on the top surface and may directly contribute to the formation of wear debris, it is important to understand the formation mechanisms and characteristics of mixing layers.

Kerridge and Lancaster[69] systematically studied the transfer of materials in a wear system of brass/hard metal(Stellite, grade 20) using pin on ring experiment at a sliding speed of 4.5 cm/s with a varied of sliding loads. They concluded that wear of the brass pin on the stellite ring is a multi-stage process beginning with transfer of brass to the surface of the ring. Further transfer then occurs preferentially to the ring and a film of brass is formed on the ring, and portions of this film are finally detached as discrete particles. An equilibrium is established in which transfer rate is equal to pin wear rate, and all wear debris are generated from the transfer layer instead of directly from the pin.

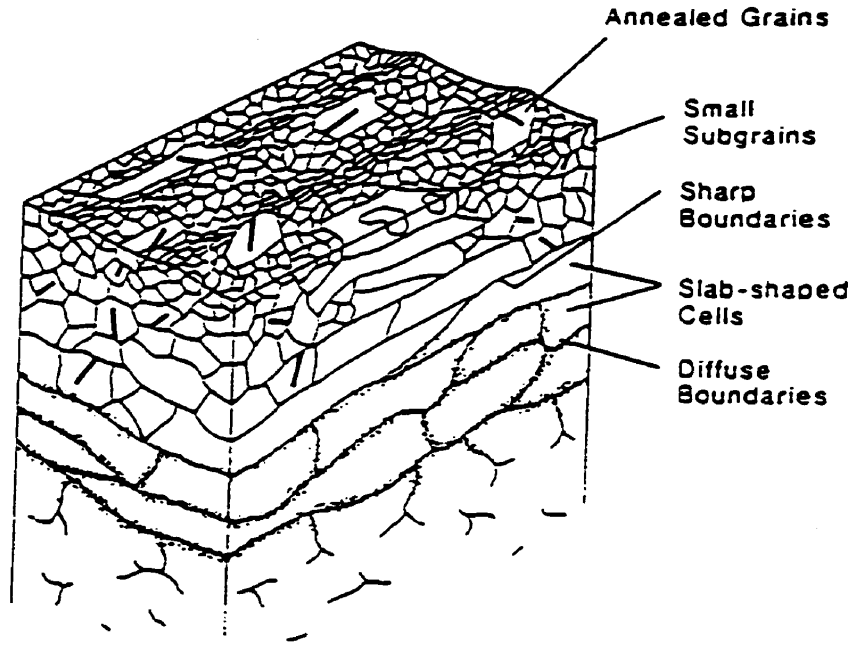

(a)

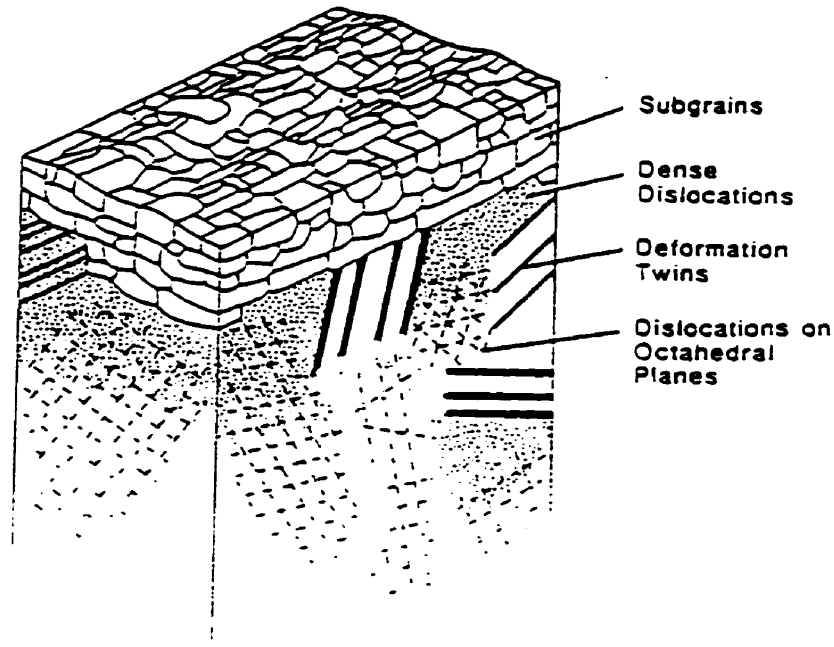

(b)

Fig. 2.13 Schematic illustrations of the structures of worn surfaces of metals with different stacking fault energies(SFE). (a) High SFE; (b) Low SFE. After [37].

The transfer and mechanical mixing of materials from the sliding bodies have been further observed and studied by Sasada[66] and Rigney et al[67] and coworkers[70, 71]for a variety of sliding systems using SEM and EDS techniques. The transfer patches surface layers were developed through accumulation and mixing of small "transfer elements" as defined by Sasada [66] and loose debris particles were generated from the transfer material as observed in dry sliding wear systems of Cu-Ni, Cu-Zn using a pin-on-disk geometry. They noted that the wear debris and the mixed surface layers had the same ultrafine structure, the same average composition, and the same mixture of phases in a pin-on-disk sliding test of different testing materials such as copper, commercial iron, nickel etc., at a constant load of 0.78N, different sliding speeds of 6.9 mm/s and 13.8 mm/s. Heilmann et al [70] studied wear systems of Ni-40wt.%Cu block sliding against a 440C stainless steel ring using a block-on-ring geometry at a load of 200 N, sliding speed 5 cm/s. They found that transfer layers begin to develop at a very early stage, even before loose wear debris can be detected. Their observation is consistent with the early findings by Kerridge and Lancaster[69] which suggest that, when a transfer takes place, only a few contacting points are involved and the early asperities give rise to the small "transfer elements". They also studied microstructural characteristic of the transfer layer using TEM. It was observed that a very fine structure formed in the transfer layer in a system of copper sliding against steel. Both iron and chromium were detected in the fine structure region. They also noted that the amount of transfer material varied considerably with depth below the surface. Moreover, their results showed negligible interdiffusion, either between the very small grains in the transfer layer or between the transfer layer and the base materials. It is interesting to note that the transfer layer consists of an intimate

mechanical mixture of ultrafine crystallites from both sliding partners when unlike materials slide each other, such as in a Cu/steel system. In a self-mated test, such as Cu/Cu, the crystallite sizes are a little larger and the transfer layer is much thicker than for tests with unlike materials.

Rigney [67, 72] has suggested that the mixing process is much similar to the commercial process of mechanical alloying first proposed by Benjamin[73]. In mechanical alloying, metallic powder are trapped between high energy milling balls and undergo a repeated process of heavy deformation, fracture, and intimately mixing. As a result, non-equilibrium phases could be produced during the solid state powder process. Rigney et al [67] compared the microstructural features of the transfer layer in copper against an M2 steel at a load of 133 N, sliding speed 100 mm/s using a block on ring sliding geometry, with those of mechanically alloyed materials. In both cases, a fine substructure developed, including dislocation tangles, twins, dislocation cells or subgrains, both elongated and equiaxed, with structure sizes varying from about 60 to 300 nm.

Antoniou and Borland[34] and Subramanian[74] have discussed the characteristics of mechanical mixing in sliding wear system of Al-Si binary alloys. Based on their experiment conducted in a pin-on-disk dry sliding condition at a sliding speed 0.1 m/s, applied pressure range of 0.1-5 Mpa, they found that there were two processes which were important in mechanical mixing or alloying: (i) debris removal from the wearing interface and (ii) debris particles reprocessing at the wearing surface. The wear

surfaces were protected by the formation of the mixed layer and thus resulted in a lower wear rate. They also found that the formation of the mixed layer was a product of a certain combination of the normal loads and sliding speeds, i.e., high load and low speed. There was no mechanical mixing either at high loads or at high speeds.

Interestingly, amorphization phenomenon has also been found in a variety of dry sliding wear systems[75-77]. Wang et al[75] first gave evidence of amorphous phases being formed in the worn surface of a bearing steel 52100 against a hard metal WC-8%Co using a pin-on-ring dry sliding test at a load of 140 N, sliding speed 2 m/s for 600 m sliding distance. Ganapathi and Rigney[76] reported that nanocrystalline copper formed as wear debris during sliding wear of OFHC Cu against a stainless steel using ring-on-block at a load of 34 kg, sliding speed 5 cm/s. Recently, Bednar and D. Kuhlmann-Wilsdorf[77] have reported that an amorphous and alloy film was formed in sliding wear of silver on copper in a special test geometry of Bridgman anvil apparatus at a low rotation speed 1.0 rpm at a shear stress of 0.5GPa. They have proposed that the formation of the amorphous alloy is mainly due to the severe plastic deformation rather than rapid quenching [76] resulting from the frictional heating[44]. As discussed in [78], the potential applications of the amorphous tribofilms are most likely to be achieved as they could reduce friction and increase wear resistance. However, formation mechanisms of the wear-induced amorphous phases and related phenomena are still not fully understood, especially not only for the pure metal tribo-system, but for multiphase materials as well.

2.1.4. Wear debris

As discussed in the previous section, the conditions existing in the surface layer are, to some extent, an indication of what is going on during a sliding process, and the surface layer directly leads to the formation of loose wear debris in the sliding system subjected to further deformation. The two resultants of the wear system, namely, the worn surface and wear debris, are critical to the understanding of the wear mechanisms thoroughly. The worn surface studied, is a cumulative resultant, and it is likely that the worn surface have been obscured by subsequent events[37]. However, the particles of wear debris that normally fall out of the wear system instantly in a dry sliding wear system, are less likely to have been damaged by the subsequent events but recording previous events before being detached. Thus they are more likely to be representative of single material removal events, although their origin must always be correlated to the worn surface from which the debris are generated.

In their excellent review[37], Samules et al discussed typical types of particles present in the wear debris recovered from a variety of sliding wear systems, mostly from oil-lubricated systems. Their discussion can be summarized in Table 2. 1. Most of the classification and related wear mechanisms are emphasized according to the shape and the size, which are useful, but much more information can be obtained when structural and chemical details are investigated using modern techniques such as X-ray, SEM, TEM and EDS etc.

Table 2.1 Classification of wear debris and related wear mechanisms.

Debris Shape	Features	Wear Mechanisms
Laminar Particles	Thin, plate-shaped, size of ten to tenths of a micrometer	Delamination
Wedge-shaped particles	Plate-like, a little thicker	Low cycle high stress fatigue wear
Ribbon shaped particles	Large aspect ratio, usually curved or curly, serrated on one surface	Abrasive
Irregular particles	Small fragments,	Adhesion, Delamination
Spherical particles	Virtually perfect spheres 1-5 μm in Dia.	Rolling contact fatigue

In recent years, utilization of these modern techniques to investigate the nature of wear debris has made it possible to get more insight and understanding on wear mechanisms. It is generally observed that fine equiaxed particles are generated at a low sliding load, and plate like debris with a relative larger size are present at a higher load. By using TEM, Helimann et al[70] examined wear debris particles of Cu alloys sliding against an M2 steel in a dry sliding wear using a pin-on-disk geometry at a load of 67 and 133 N, sliding speed 5 cm/s. They found that the microstructure of the debris is similar to the transfer layer, i. e. a fine-grained structure without evidence of interdiffusion between the very small grains. The nature of wear debris and transfer layer of worn surface of Al alloys have received particular attention, due to the engineering importance of these materials in terms of tribological applications. It is generally found that in a system of Al alloy sliding against a steel, iron from the counterpart is present in wear debris mainly because of transfer of materials. Regarding the phases present in the wear debris and worn surface, other phases such as oxides have been reported in addition to the original phases (iron, aluminum) [78, 79] on a pin-on-disc sliding against a steel(1%C, 1.5%Cr) at

a sliding speed of 100 cm/s. In contrast, little or no oxide in the wear debris produced in the sliding wear of Al alloys has also been reported [34, 80] in a sliding speed 0.5 m/s over a pressure range of 0.6 to 3 Mpa in a dry sliding wear. The arguments remaining in sliding wear of Al alloys against steels will be reviewed in detail in section 2. 3.

2.2. METAL MATRIX COMPOSITES

Modern composite materials are referred to as advanced materials in which two or more components are combined on a macroscopic and/or microscopic scale. These materials can be tailored to take advantage of the desirable properties and minimize the undesirable properties of their constituents. Consequently, composite materials often exhibit some qualities that their constituent do not possess individually. Metal Matrix Composites (MMCs) are comprised of a metal matrix and reinforcements such as fiber, whisker and particulate ceramics which are incorporated in the matrix in order to provide enhancement in properties such as strength, stiffness, and temperature-dependent strength, wear resistance, as well as modifications of the thermal expansion and electrical conductivity. The development of the MMCs has been one of the major innovations in materials science in the last two decades. These innovations include new materials, manufacturing methods, properties and microstructures of the MMCs. While there are still many areas about MMCs which are not well understood, the work of the last few years has led to a commercial production and utilization of the MMCs in many industries[81].

2.2.1 Modulus of elasticity and strength of MMCs

The modulus of the MMCs is found to be always significantly increased by addition of reinforcement. McDanels[82] investigated composites that had three different SiC morphologies, i.e., whiskers, nodules, and particulate in platelet form. It was observed that the modulus of elasticity of the 6061 Al matrix composites increased with increasing volume fraction of the reinforcement, as shown in Fig. 2. 14.

The volume fraction of reinforcement is the dominant factor in increasing the modulus of elasticity. For a given fraction of reinforcement, the modulus tends to be isotropic with nearly equal values obtained from tests in the longitudinal and transverse directions. Moreover, the modulus appears to be insensitive to the type of reinforcement used. The modulus is also independent of the matrix alloy, but heat treatment may have a slight effect upon it if measured as the initial slope of the curve.

The yield strength σ_{yc} or ultimate tensile strength (UTS) of the MMCs is generally found to be higher as compared to the base alloys. McDanels[82] investigated SiC whisker and particle reinforced Al alloys with different matrices with respect to the yield strength and the UTS of the MMCs. It was found that an increase in yield strength and UTS was dependent on the volume fraction of reinforcement, alloy matrix and the heat treatment of matrix. Lloyd[81] studied stress-strain curves for A356 Al alloys and SiC particles reinforced A356 composites with two particle sizes and two tempering treatments. The investigations were consistent with the earlier work[82, 83]. Fig. 2.15

shows the comparison of stress-strain curves of the unreinforced material and the composites. It can be seen that the work hardening rate at low strains is higher in the composites. It implies that work hardening in the composites is extremely rapid at low strains. After strains of about 3% the stress-strain curves of the composite and the

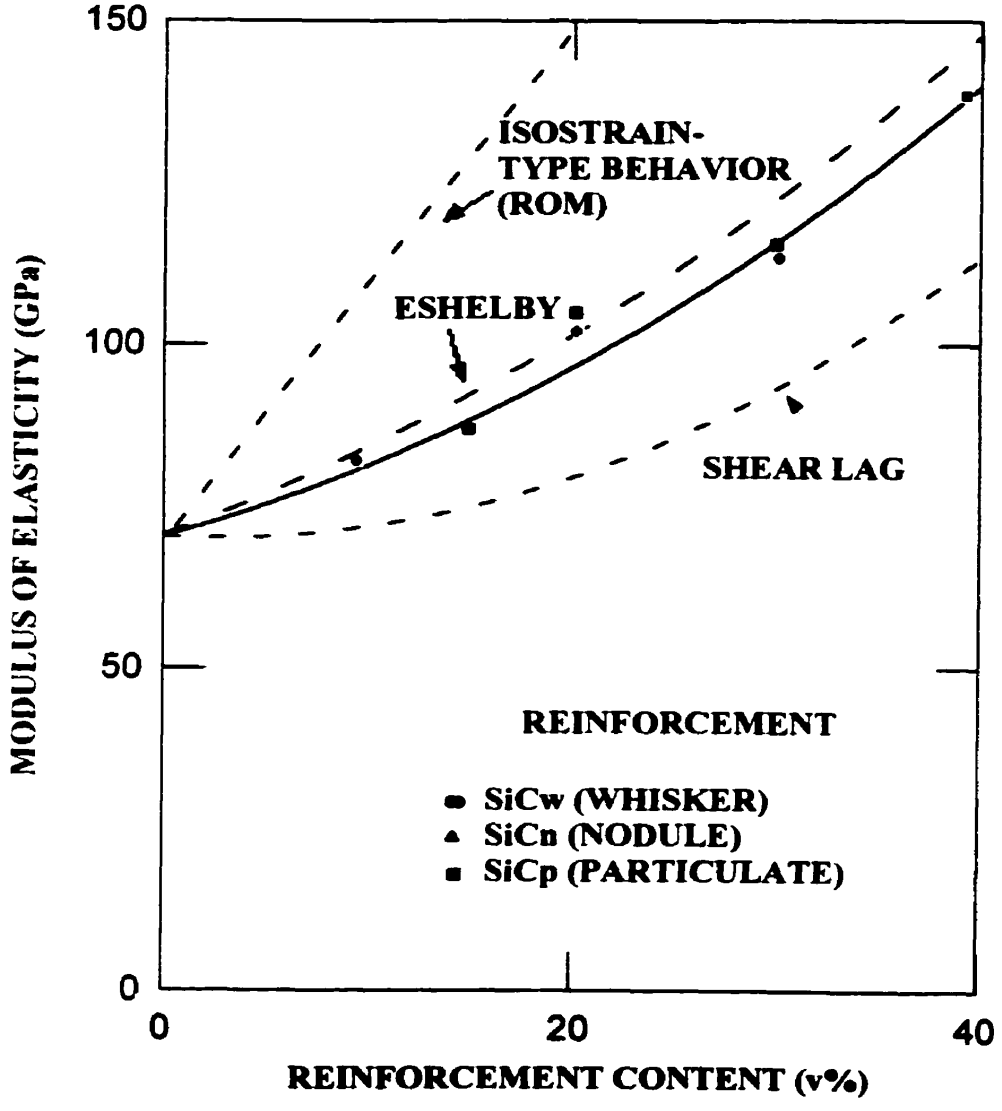

Fig. 2.14 Effect of reinforcement content on modulus of elasticity of SiC/6061 Al composites. After [82].

unreinforced alloy are essentially parallel, so all the strengthening is associated with the first few percent of strain. It can be also observed that the work hardening rate increases with a decrease in particle size. The strengthening mechanisms of the particulate reinforced MMCs have been studied by a number of investigators[84 - 87]. With respect to the interaction between the reinforcement and the matrix, the possible strengthening mechanisms can be accounted for by the following[81]:

1. Orowan strengthening.
2. Grain and substructure strengthening.

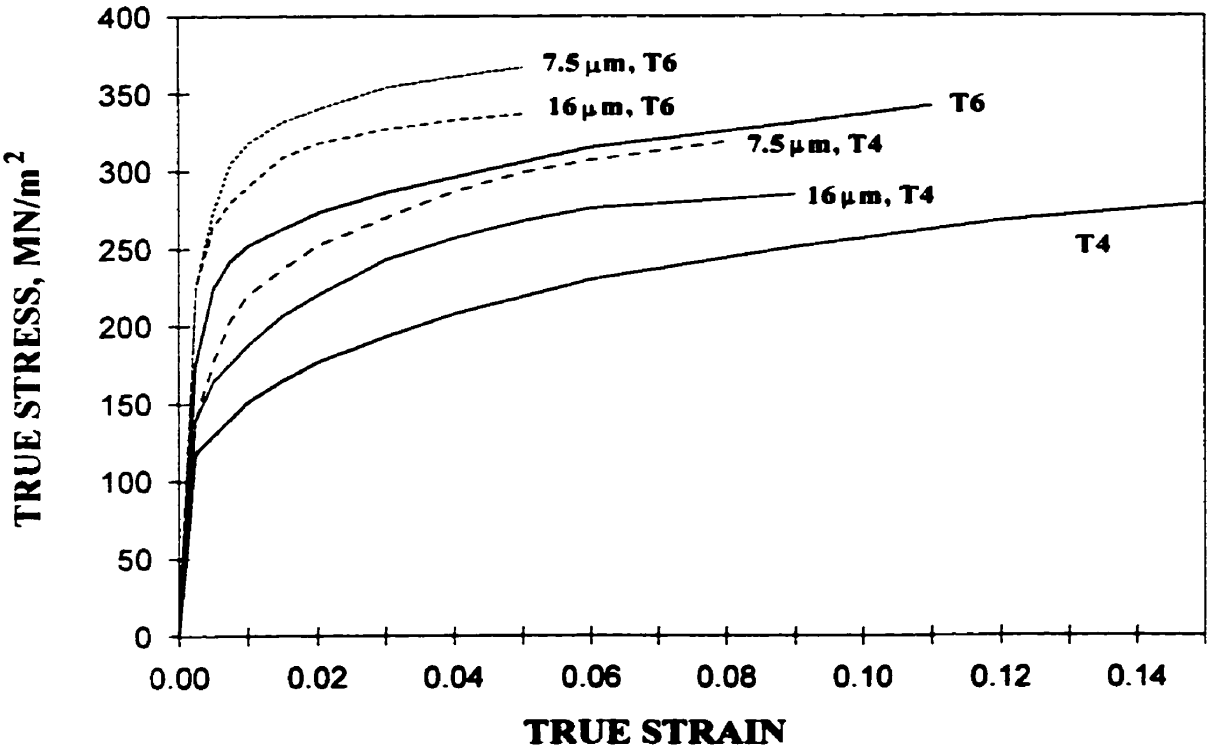

Fig. 2.15 Stress-strain curves for extruded A356(Al-Si) and A356(Al-Si)/SiCp composite with different particles sizes and tempers. After [81]

3. Quench hardening resulting from the dislocations generated as a result of differences in coefficient of thermal expansion(ΔCTE) between the reinforcement and the matrix.

4. Work hardening from the strain misfit between the elastic reinforcing particles and the plastic matrix.

The strengthening mechanisms which operate in a composite will depend upon the microstructure and processing of particular materials. In composites fabricated by powder metallurgy, for example, a very fine grain size can significantly contribute to the increased strength. In melt processed composites, it has been accepted that the matrix can be strengthened by strain misfit and dislocations generated due to ΔCTE. Arsenault[88] has proposed that the strengthening of Al alloys due to the addition of particulate SiC reinforcements occurred as a result of an increase in dislocation density due to the ΔCTE and a reduced subgrain size in the matrix. Based on the concept of ΔCTE, Taya et al[87] have proposed that a back stress, which is the average internal stress in the matrix as a result of particulates resisting the plastic flow of the matrix, also contributes to the strengthening from the addition of reinforcements.

The ability to transfer stress from the matrix to the ceramic reinforcing particles is also critical to the strengthening of the MMCs. As a composite is loaded, the matrix in the vicinity of the stronger reinforcing particles is able to transfer a portion of the load to the particles[89]. This effect can be seen from the fact that an increase in elastic modulus is found in composites compared to the unreinforced alloys, as shown in Fig. 2.14. The

load transfer, however, is dependent upon a stronger interfacial bond between the reinforcement and the matrix. To a large extent, an increase in the mechanical properties of the MMCs is determined by the structure and properties of the interface. Therefore, a number of studies have been conducted on microstructures and properties of the interface including interface reactions[90, 91], crystallographic relationships and interface precipitation[92]. In SiC/Al alloy system[93], it has been shown that Al_4C_3 will form as a result of the reaction between SiC and molten Al, which could be detrimental to the interfacial strength. Other investigations have shown that some oxides such as MgO [92] and $MgAl_2O_4$ [91] could possibly form in the interface, which would certainly affect the properties of the interface.

2.2.2 Fracture in particulate reinforced MMCs

In general, the fracture of the particulate MMCs is considered to be associated with:

1) The type of the reinforcing phase, including its size, volume fraction, and distribution.

2) The properties of the matrix alloy.

3) Interfacial characteristics.

Fracture toughness of the MMCs is considered as the work of fracture, i.e., the dissipation of elastic energy imposed in the specimen by the externally applied load per unit of new crack surface formed. As a crack grows rapidly through the particulate

reinforced composite, many events occur that are potentially related to the fracture toughness, and each of these either makes it easier or harder for the crack to extend. The events, as shown in Fig. 2.16, summarize main mechanisms associated with fracture of the MMCs with respect to the above aspects. As we can see from Fig. 2.16, the energy dissipated around a propagating crack tip of a SiC particle in an MMC is satisfactory with the elastic energy consideration regarding the fracture toughness, but a crack tip in the ductile matrix is readily associated with plastic deformation.

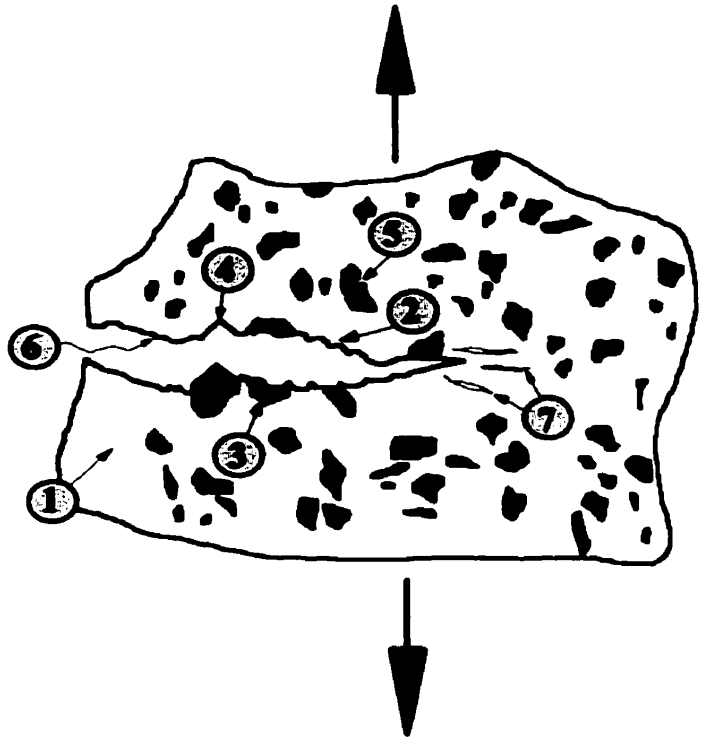

Fig. 2.16 Schematic illustration of events of fracture of metal matrix composites reinforced with particulate. (1) deformation within plastic zone; (2) formation of voids along fracture surface; (3) fracture of SiC particles along crack path; (4) interfacial separation between matrix and SiC; (5) fracture of SiC within the plastic zone; (6) tortuous fracture path increase fracture surface area; (7) matrix cracks near, but not continuous with, the main crack. After [96].

1) Deformation within the plastic zone

Most, but not all, of the energy absorbed within the plastic zone of a growing crack occurs within the matrix. A small amount of energy was absorbed within the reinforcement. The plastic deformation zone was largely influenced by the matrix microstructure and tempering conditions[94,95]. In an Al/SiC composite, Lloyd[94] found that in the T4 temper, strain localization occurred only just prior to fracture, while in the T6 temper strain localization made the major contribution to the fracture strain. In the plastic zone, some of the energy was of elastic nature and would be recovered as the crack passed and the stress concentration associated with the crack tip was diminished[96].

2) Formation and growth of microvoids

This is a very important energy absorption mechanism. Voids which form during fracture are found as dimples on the fracture surface. The energy absorbed in void coalescence and growth is directly dependent upon the size of the voids and their aspect ratio, or depth. Wang and Zhang[97] compared different fracture morphologies of the dimples in the A356 alloys and A356/SiC composites. They found that the size of the dimples was no longer uniform, and nor were their shapes circular, compared to those in unreinforced alloys. More importantly, both the size and shape of the dimples with SiC inside, were found to be associated with the SiC particles. The results suggest that microvoids are likely to be initiated by the particles in the composites, and the interfacial debonding plays an important role in the crack formation.

It has been hypothesized[96] that the presence of a large number of microcracks near the main crack would effectively toughen the material because these microcracks have the effect of blunting the main crack in a sense that the stress field experienced at the main crack tip is lowered. Thus, the stress intensity at the main crack tip caused by an applied external stress would be lowered by the formation of these microcracks. In some particulate composites, microcracks were found to form near the main crack tip, at least at some levels of stress intensity factor, and at least some of these cracks were in the interface between the particles and the matrix.

3) Effects of particle reinforcement on fracture

Addition of hard particles to a ductile matrix can result in the following changes to the material behavior:

(a) Slip characteristics of the matrix alloy is altered. Particles will have the primary effect of blocking the slip lines. However, there may be secondary effects, such as limiting of the operation of secondary dislocation sources and limiting of the extent of cross slip.

(b) Presence of particles near the crack tip could also limit the strain to fracture at the crack tip. This might alter the distribution of strain within the plastic zone.

(c) Debonding of particles near the crack tip to form microcracks not directly

connected to the main crack is another mechanism that has the potential to influence the fracture toughness.

The influence of particulate fracture on composite fracture toughness has also been investigated and discussed[94, 95, 98]. Lloyd[94] proposed that the particle fracture would affect strain behavior of the composite. Particle fracture was also thought to be responsible for the lower ductility of the composite. On the other hand, the particle fracture might increase surface roughness, and that would, in turn, enhance fracture toughness because of the increase in fracture surface area created.

2.3 WEAR OF Al ALLOYS AND Al BASED MMCs

2.3.1 Wear performance

The majority of wear investigations have been carried out on wear performance of the Al alloys (2014, A356, 6061, 7091) reinforced with different particles such as SiC, Al_2O_3 and TiB_2 etc. These investigations have shown that reinforcements have usually been found to improve wear resistance under abrasive and lubricated sliding conditions compared to the wear resistance of an unreinforced alloy under the same conditions[9]. However, some other results of dry sliding and erosion tests performed by various investigators did not show a consistent trend. Among these, Wilson and Ball [14]reported that erosion resistance of 6061 Al-SiC alloys was no different from that of the unreinforced alloys. Wu et al [15]observed that the erosion wear resistance of 2014Al

reinforced with SiC or Al_2O_3 was inferior to that of the monolithic 2014Al. This was attributed to the lack of ductility of the composites. On the other hand, an increase in the dry sliding wear resistance of particulate-reinforced cast or wrought Al alloys was measured by Hosking et al [16] in a pin-on-disc sliding test against 52100 bearing steel at a speed of 100 mm/s. Alpas and Zhang[17] observed similar increased wear resistance of the Al based composite sliding against a bearing steel 52100 using a block-on-ring test at a sliding speed of 0.8 m/s, load range of 1 to 15 kg. Parmila Bai et al[18] explained the increased wear resistance in terms of the generation of iron rich layers on the surfaces of the Al composites sliding against an En 24 steel in a pin-on-disc apparatus at a sliding speed 0.5 m/s, sliding load of 6 to 75 N. Jokinen and Anderson[19] observed a slight decrease in wear rate with an increase in SiC particle size in a wear system of an Al based composite reinforced with SiCp against 52100 steel in a pin-on-disc test at sliding speed 0.2 m/s at a higher load of 39.2 N, while at a lower load (10 N), the wear rate of the composite decreased abruptly with an increase in the SiC particle size. Alpas and Embury[20] showed that under the conditions where SiC particles promoted subsurface cracking and material removal by delamination, SiC reinforcement did not contribute to the wear resistance of a 2024-Al alloy sliding against SAE 52100 bearing steel at a sliding speed of 0.1 m/s, sliding load of 9 N by using a block-on-ring wear tester. Wang and Rack [21] studied transition wear behavior of SiCp (20 vol%) and SiCw (20 vol%) reinforced 7091Al MMCs by doing unlubricated sliding wear on Pin-on-Disc tester. Fig. 2.17 shows the typical wear volume loss as a function of sliding distance at different sliding velocities for unreinforced 7091 alloys, SiCp reinforced and SiCw reinforced composites, respectively. Based on the microstructural observations at different wear

stages for the three samples, they concluded as follows:

(1) Wear rates of both unreinforced and reinforced composites were of the same order of magnitude when the sliding velocity was less than 1.2 m/sec. The mechanisms of wear under these conditions were surface-fatigue-related surface cracking. It implies that SiC reinforcement does not affect wear resistance at low sliding speeds.

(2) At sliding velocities greater than 1.2m/sec, the wear rates of reinforced materials were lower than for the unreinforced matrix. The mechanisms of wear under these conditions were controlled by subsurface-cracking-assisted adhesive transfer and abrasion. During steady state sliding, however, elevated wear rates were maintained only by the unreinforced alloy, while much reduced wear rates were observed with the reinforced composites.

Zhang and Alpas[22] also demonstrated that the rate-controlling wear mechanisms might change abruptly from one to another at certain sliding velocities and contact loads, resulting in an abrupt increase in wear rates. Alpas and Zhang [23] further reported the effect of microstructure (such as particulate size and volume fraction) and counterface material on the sliding wear resistance of particle reinforced Al composites. They found that the wear mechanisms could be divided into three regimes, namely low load regime, high load regime and a transition regime in between the low and high load regimes. The wear rates versus the applied loads are typically shown in Fig. 2.18. The wear rate decreased significantly with an increase in reinforcing particle size at a lower

load, Fig. 2.18(a). Regarding the effect of volume fraction on wear rate, it was observed, Fig. 2.18(b), that the transition ranges between the wear regimes were shifted to higher loads. It suggested that increasing the particle volume fraction had a positive effect on the wear resistance of the Al alloys by delaying the transition to more severe wear rate regimes.

Wear behavior of the Al composites at elevated temperatures is also an important issue since many high temperature tribological applications of these composites are found. for example, some engine components. Only limited investigations of the influence of ambient temperature on wear performance have been reported[24, 25, 26]. Martinez et al[24] and Martin et al[25] studied wear behavior of an Al-Si/SiCp composite and an eutectic Al-Si alloy at ambient and elevated temperatures (20° c to 200° C). They reported that at low temperatures the wear behavior was controlled by the eutectic Si or SiC particulate, and at high temperatures, on the other hand, the wear behavior was controlled by the matrix which underwent large plastic deformations. Both materials experienced a transition temperature at which wear mechanisms changed from mild to severe wear with an increase in temperature, and the transition temperature was increased by the addition of SiC particles. Therefore, they concluded that the main effect of the SiC reinforcement on the sliding wear at high temperatures was to delay the transition from mild to severe wear by about $50°C$. Similarly, Wilson and Alpas[26] investigated the effect of ambient temperature on wear performance of A356 Al and 6061 Al composites in comparison with their base alloys. They found that the reinforcements increased the transition of wear mechanisms from mild wear to severe wear into high temperature and

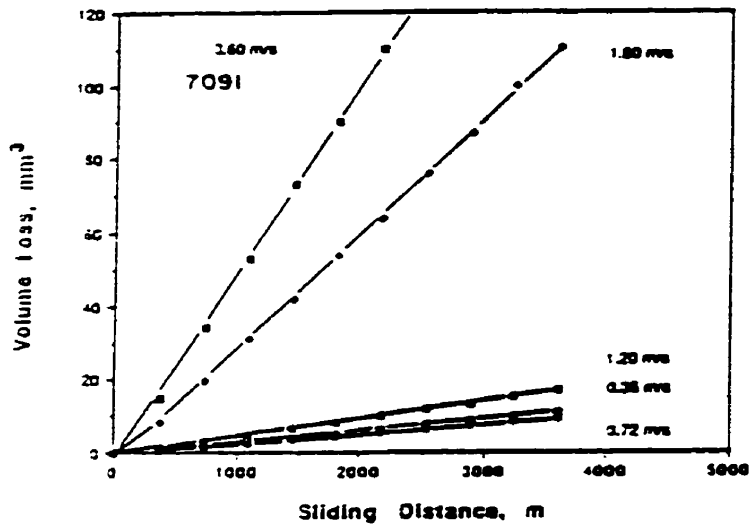

(a)

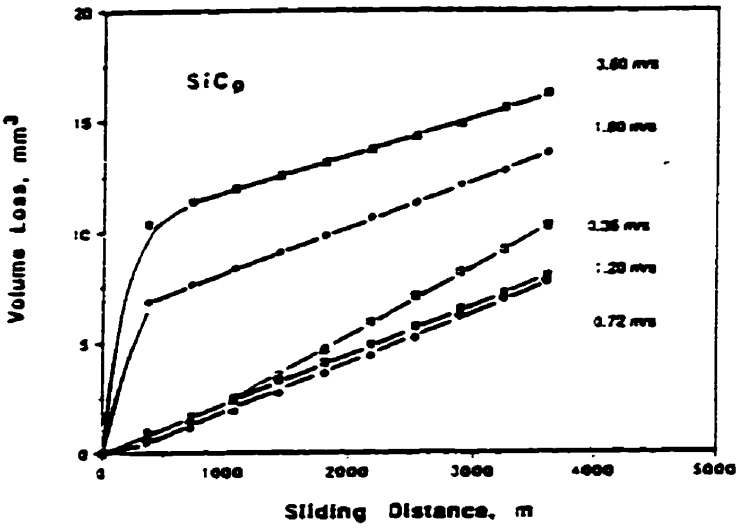

(b)

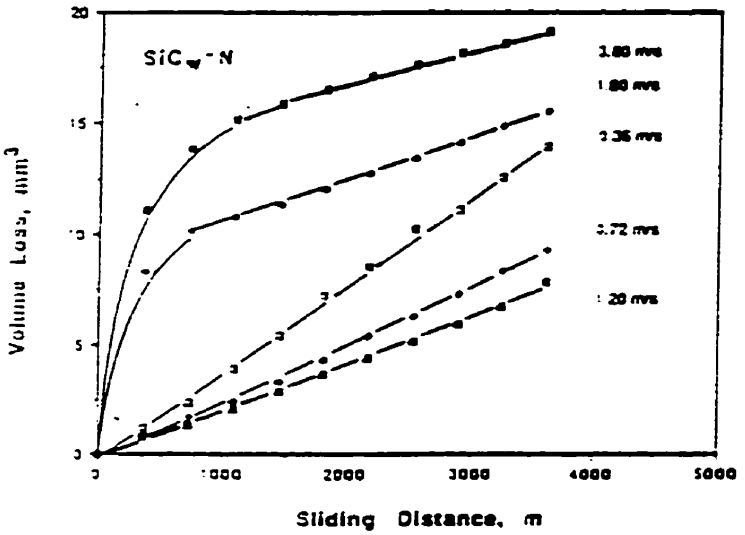

(c)

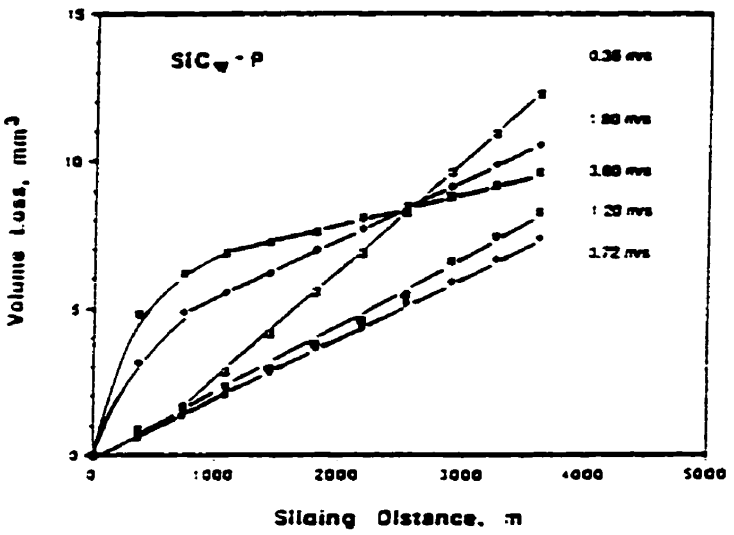

(d)

Fig. 2.17 Wear volume loss as a function of sliding distance at different sliding velocities: (a) unreinforced 7091 alloy; (b) perpendicularly oriented SiCp composite; (c) perpendicularly oriented SiCw composite; (d) parallel-oriented SiCw composite. After[21].

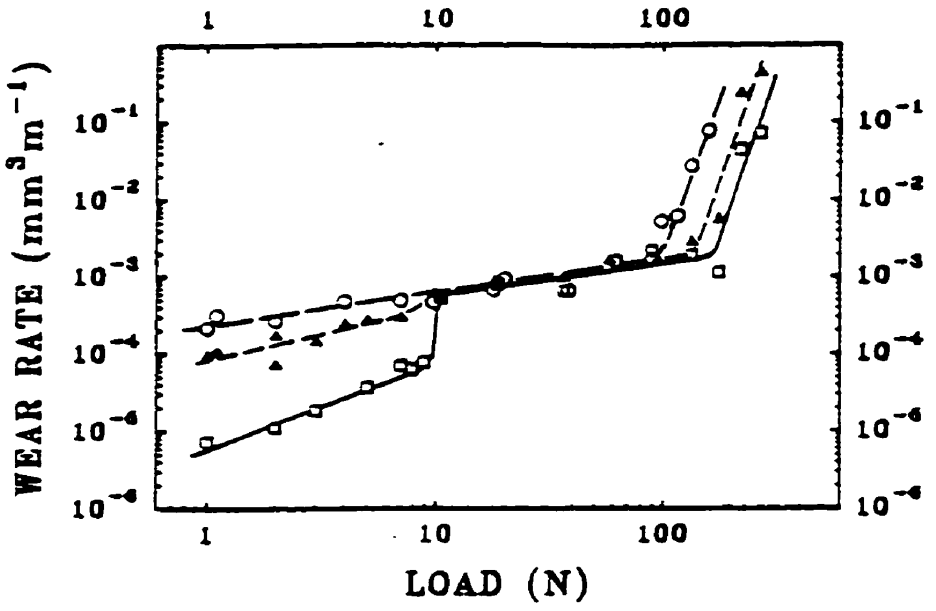

(a)

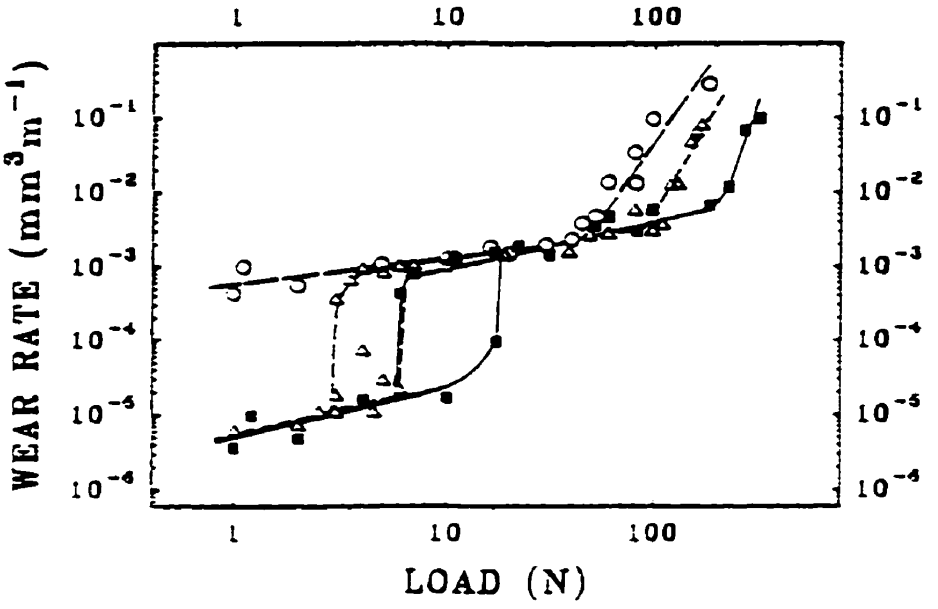

(b)

Fig. 2.18 Wear rate as a function of applied load. Counterface SAE 52100. After [23].
(a) With a base alloy of 2014 Al. (O) 2014 Al; (▲) 2014Al-20 pct SiC(2.4 μm), and (□) 2014 Al-20 pct SiC(15.8 μm).
(b) With a base alloy of 6061 Al. (O) 6061 Al; (△) 6061 Al-10 pct Al_2O_3, and (■) 6061 Al-20 pct Al_2O_3 .

the increase could be 100-200°C higher than that in the unreinforced alloys. They attributed the increase to formation of protective transfer layers of comminuted reinforcing particles and transferred steel debris from slider counterfaces.

2.3.2 Deformation structure of the wear surface

As discussed in section 2.1.2, deformation structures are complex in the worn surface, which could get further complicated during the sliding wear of ductile composite metallic materials reinforced with hard second phase particles owing to the presence of the hard particles. Using SEM, many investigators[21-30] have characterized the subsurface features of the worn surface and discussed the role of reinforcement. Alpas and Zhang[17] proposed that SiC particles acted as load-bearing elements, and at a higher load, decohesion of SiC from the SiC/matrix interface could lead to the formation of cracks causing delamination of the subsurface. Pramila Bai et al[18] suggested that the effect of SiC particles is to resist the plastic flow as obstructions at and near the surface. As well, several researchers [23, 65] have discussed the fragmentation of the reinforcement, which will be discussed in next subsection.

Very few investigations, however, have been conducted on the microstructural characterization of the worn surface in the MMCs by using TEM. Recently, Perrin and Rainforth [99] reported the effect of alumina fiber reinforcement on wear of an Al-43%Cu alloy at a sliding speed 1 m/s, constant sliding distance 10 km, in a load range of 6 to 40 N by using a pin-on-discmachine. They observed that the depth of plastic deformation was significantly greater in the reinforced alloy than in the unreinforced

alloy. The load bearing capacity of the alloy was improved due to the addition of fibers. They extensively studied the microstructural evolution below the worn surface, and found that the spacing and morphology of the fibers dictated local strains in the matrix and imposed changes in the direction of matrix flow up to 45°. The local strain was much higher where the spacings between the fibers were small. They also proposed that a dynamic equilibrium existed between the work hardening due to deformation of new subgrains and recovery mechanisms such as subgrain boundary migration and coalescence. In their study, however, the deformation structure in the reinforced alloys did not show changes systematically as a function of depth below the worn surface.

Age hardening and precipitation in the matrix can influence the microstructure of metal matrix composites and thus influence their wear behavior [28]. A modified precipitation sequence and accelerated aging are found in the MMCs[81, 100]. As mentioned in previous sections, it has been accepted that matrix strengthening mechanisms of the MMCs are mainly due to the high density dislocations generated by the difference between the coefficients of thermal expansion (ΔCTE) of reinforcement and the matrix[85, 86, 88]. The dislocations with an increased density would serve as nucleation site for strengthening precipitates during the aging of the composites. The incubation time for the precipitate nucleation and aging time to achieve peak hardness in the matrix could be significantly reduced for MMCs as compared to the unreinforced matrix[100]. Therefore, work hardening characteristics and precipitation in the worn surface of the MMCs are of much interest and far from complete in understanding the sliding wear behavior where shear strains and friction heating are associated. Pan et

al[28] studied effects of aging on the wear performance of P/M 2124 Al/SiC composites against a 52100 bearing steel at a load 168 N, sliding speed 2 m/s. They found that the overaged composite had the best wear resistance among all the treated conditions (underaged 30 min., peak aged at 191° C for 6 h, overaged at 204° C for 12 h.) It was thought that the decreased wear rate of the overaged composite was due to the easier crack propagation along the incoherent precipitation/matrix interface compared to the matrix/SiC interface.

2.3.3. Mechanical mixing induced by sliding wear

Aluminum alloys undergo a transition from a mild wear to a severe wear, depending mainly upon the sliding load and speed during dry sliding wear against steels at an ambient environment [52, 80, 101, 102]. The main feature of the worn surfaces in the mild wear regime is formation of mixed surface layers that are generally found to be comprised of materials from the sliding surface and the counterpart. These layers are mostly believed to be protective layers that provide the alloys an excellent wear resistance[80, 101]. During the sliding process, these layers are subjected to repeated compaction and fragmentation, and consequently wear debris is detached from the sliding surface. Formation of wear debris is directly related to that of the mixed surface layers. An understanding of the nature of the wear debris and the mixed layer from which the debris is formed, especially their microstructures and composition, could provide important insight into the wear mechanisms of these alloys and development of new materials for tribological applications.

There have been a number of investigations[13, 34, 52, 74, 78, 79, 101] into the formations of the mixed surface layers and nature of wear debris in unlubricated sliding systems, especial in wear of Al alloys sliding against ferrous alloys like steels. Razavizadeh and Eyre[78, 79] reported that the surface layer on the worn surface of Al-Si alloys was formed by the fracture and compaction of Al oxide particles during the sliding wear against a steel at a sliding speed of 100 cm/s in a load range of 2 kg to 18 kg. In a wear study of a 6061 Al alloy sliding against SAE 52100 steel using a block-on-ring configuration within a load range of 1-450 N and a sliding speed range of 0.1 - 5.0 m/s, Zhang and Alpas[52] recently suggested that the surface layers and the debris particles contained an aluminum oxide phase with an amorphous structure, in addition to the original phases of α-Fe and α-Al, based on the results obtained using X-ray diffraction(XRD). In contrast, other workers[34, 80] have found little or no oxide in the wear debris produced in the sliding wear of Al-Si alloys at an ambient environment. By using a pin-on-disc configuration for wear tests of an Al-Si alloy against AISI 4340 steel discs in a load range of 4.4 to 35.4 N and speed range of 0.25 to 1.0 m/s, Antoniou and Borland[34] found that the layers mainly consisted of an ultrafine mechanical mixture of Al, Si, and α–Fe particles created during the sliding process, with no evidence of any oxide or Al-Fe intermetallics. These results are in agreement with those obtained by Pramila Bai and Biswas[80, 101]. Therefore, the nature of the wear debris and the mixed surface layers in an Al alloy/steel wearing system, especially their chemical and microstructural characteristics, remains to be further investigated.

There have long been arguments about the chemical condition of iron and formation of intermetallics generated during dry sliding wear[67 ,78, 79, 103]. Recently, based on the observations of the wear debris using Mössbauer spectroscopy, Antoniou et al [103] inferred that the debris contained ternary Fe-Si-Al phases that were the results of solid state reactions between the two sliding materials. However, their X-ray diffraction results did not provide definite evidence that could support the formation of the ternary phases, even though broadened peaks of α–Fe, which were overlapped by aluminum peaks, were noted, with considerable uncertainty about the microstructural and chemical information in a very fine scale.

Recently, Alpas and Zhang[23], Feng and Tandon[65] and others[13] have found similar mechanical mixing layer in the sliding wear of the MMCs. Not only did the mechanical mixing layer occur in the matrix, but the reinforced particles were fragmented and redistributed in the mixed layer as well. Similarly, the occurrence of the mixed layer was mainly dependent on the normal load and sliding speed. In MMCs, incorporation of the reinforced particles is considered as an enhancement to the formation of the mixed layer during sliding wear[65]. The abrasive action of the hard particles resulted in debris fragments and some loose debris deposited on the contact surface of the composite. As a result, an oxidized mixed layer was formed by an association of strain and friction heating during the sliding wear.

However, microstructural and compositional characteristics of the mixed layer and their formation mechanisms are not yet well understood, in comparison with the

commercial mechanical alloying[70]. The majority of investigations concerning wear induced mixing have not provided an evidence of the formation of intermetallic compounds during sliding wear. Rather, the mixing layers were mainly comprised of mechanical mixture of materials from both the contact surfaces and oxides either from the worn surface or the counterpart.

CHAPTER THREE SCOPE OF PRESENT RESEARCH

As discussed in previous sections, in spite of the extensive data already available on the dry sliding wear behavior of the Al alloys and the Al based MMCs, further detailed study of wear of these materials is needed, not only on their wear performance but also on some fundamental aspects in terms of deformation structures, influence of second phases, reinforcements and precipitation on wear processes. In particular, a comprehensive understanding of mechanically mixed layers of the Al alloys and Al based composites is yet to be achieved in order to fully understand the wear mechanisms of these materials. The present investigation was undertaken to study the wear behavior of Al alloys and Al based metal matrix composite (Al-Si/SiCp). The primary focus of the present investigation was to study the microstructural characteristics of the worn surface and microstructural evolution as a function of depth below the wear surface by using scanning electron microscopy and transmission electron microscopy equipped with energy dispersive spectroscopy as well as x-ray diffraction. Especially, the microstructural characterization of the worn surface was extensively carried out using cross sectional TEM technique as described in Chapter Four, so that a depth profile of microstructural evolution below the worn surface was successfully achieved.

In association with the study of the microstructural characteristics of the worn surface, wear debris detached from the wearing system was also investigated by using the above analytical techniques as well as Mössbauser spectroscopy in terms of the presence of iron coming from the sliding counterpart. In order to investigate the influence of reinforcements and second phases(e.g., eutectic Si), a high purity of Al was also chosen, and parallel tests and analyses were conducted on these materials for a comparison with the Al-Si/SiCp composite and the base alloy. During the course of the present study,

sample preparation methods of the longitudinal cross section of the worn surface and wear debris for TEM studies were developed.

The main objectives of the research were:

1) Investigation of wear behavior of the Al-Si/SiCp composite and the Al-Si base alloy under different tribological conditions (applied load, sliding distance and environment) and different matrix characteristics, i.e., as cast state and T6 heat treatment.

2) Studies on microstructural characteristics of the worn surface and wear debris of the Al base alloy and the Al composite by using the analytical electron microscopy (SEM and TEM) attached with EDS and X-ray mapping. Mössbauer spectroscopy and X-ray Diffraction were used to analyze the nature of wear debris in conjunction with SEM and TEM. The following aspects were mainly addressed in the present research:

i) Deformation and dislocation structures as a function of depth below the worn surface;

ii) Work hardening effects and strain distribution in the worn surface as a function of depth;

iii) Microstructural changes as a result of a combined strain and frictional heating generated during the sliding wear;

iv) Material transfer and mechanical mixing between the sliding surfaces in the near worn surface caused by the sliding wear. The nature of the mechanically mixed layers in the worn surface and wear debris that fell off the wearing system were examined. The formation mechanisms and their influence on the wear behavior were studied as the microstructural characterization and the wear behavior of the Al alloys were correlated.

v) Behavior of the reinforcing and secondary particles in the matrix during the sliding wear.

CHAPTER FOUR MATERIALS AND EXPERIMENTAL PROCEDURES

4.1 MATERIALS

An Al-Si alloy based composite material and the base Al-Si alloy were two main materials studied in the present work. In order to understand the fundamental aspects of wear of multiphase materials and microstructural characterization of the worn surface, pure aluminum (99.99%) was also chosen for study. The wear behavior and microstructural characteristics of the worn surface and debris of the HP Al were compared with the Al-Si alloy and the composite. The MMC was a cast SiC particulate reinforced A356 aluminum-silicon alloy prepared by Duralcan. The reinforcing SiC particles distributed uniformly in the Al matrix, and the volume fraction of SiC was 20% (Vol.). The size of the SiC particles was 5-10 μm. The nominal composition of the matrix of the MMC is shown in Table 4.1:

Table 4.1 Chemical Composition of Matrix of the A356 MMC (wt.%)

Si	Mg	Ti	Fe	Mn	Cu	Cr	Ni	Sn	Al
6.5-7.5	0.17	0.20	0.20	0.10	0.20	0.25	0.5-1.5	0.50	Balance

Table 4.2 Chemical Composition of the unreinforced A356.2 alloy (wt.%)

Si	Mg	Ti	Fe	Mn	Cu	Zn	Ni	Al
6.99	0.34	0.11	0.08	0.01	0.01	0.01	0.01	Balance

The unreinforced Al-Si alloy was A356.2, and the chemical composition of the alloy is shown in Table 4.2. The alloys were fabricated by Alcan Ltd., Kingston, Ontario.

4.2 WEAR TESTS

Sliding wear tests were performed using two kinds of experimental set-ups, i.e., Block-on-Ring unidirectional configuration and Ball-on-Block reciprocating configuration. Unless otherwise specified, most of the wear tests were carried out at an ambient environment (room temperature 22°C and humidity 38-40%). No lubricant was used in all the wear tests which were carried out under a variety of sliding loads ranging from 0.1 kg to 15 kg, while the sliding speed and sliding distance were kept constant. The weight loss of specimen was determined by weighing the specimen before and after the wear test. The weight of specimen was obtained using a digital micro-balance with an accuracy of 0.1 mg. All specimens were polished (down to 0.25 μm) and cleaned by an ultrasonic cleaner before and after wear test.

4.2.1 Block-on-Ring Unidirectional Wear Test

The block-on-ring wear test machine was designed and fabricated according to ASTM standard: G77-91. Fig. 4.1 schematically shows the configuration of the test machine. Basically, the test block (1) is held by the holder (4) which is connected tightly into the loading arm (3), and the test ring (2) is fastened on the shaft of the rotation assembly which can be driven into rotation by the motor. The test block is loaded through the loading arm against the test ring that rotates in a given speed for a give number of revolutions.

The Al alloy and Al MMC specimens were used as rectangular blocks of 9 x 9 x 9 (mm^3), and slid against a tempered M2 tool steel ring with an outer diameter of 35 mm and width of 10 mm. The hardness of the M2 steel ring was 60-64 HRC, and the nominal composition of the M2 tool steel is shown in Table 4.3. The counterpart steel ring was polished to 1 μm *in-situ* by using the same wear tester in a manner that special steel blocks attached with sand papers of different grits and polishing clothes were sliding against the steel rings immersed in a coolant.

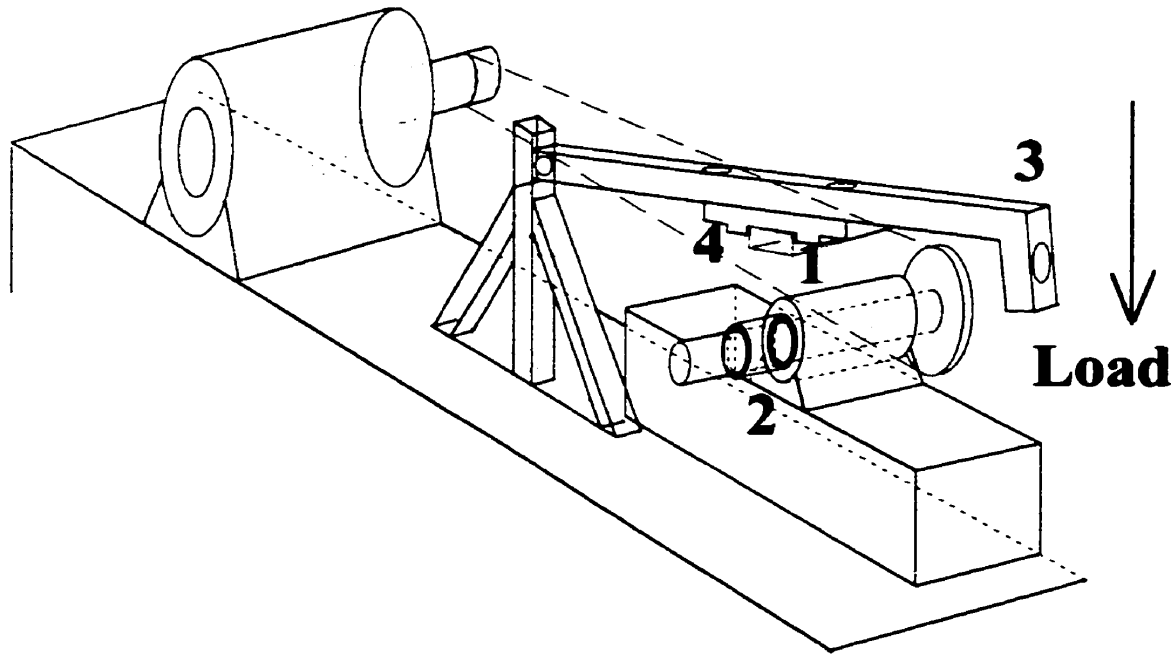

Fig. 4.1 Schematic illustration of Block-on Ring wear tester. (1) Specimen Block; (2) Test Ring; (3) Load Arm; and (4) Block Holder.

Table 4.3 The Nominal Composition of the M2 Tool Steel (wt.%)

C	Mn	Si	Cr	W	V	Mo	S	Fe
0.84	0.25	0.30	4.00	6.50	1.90	5.00	0.20	Balance

Before starting the wear tests, the block and ring were carefully adjusted to ensure full contact, i.e., initially was a line contact. The loading arm was loaded gently. The wear scar on the specimen should be square in shape after the wear tests, and those specimen on which the wear scars were not square were discarded. The sliding speed was kept constant at 20 cm/s by adjusting the rotational speed of the ring, and the total sliding distance was kept at 1000 m. Fig. 4.2 shows an example of the square-like wear scar on a block specimens using the block-on ring wear tester.

4.2.2 Ball-on-Block Reciprocal Wear Test Machine

The ball-on-block reciprocating sliding wear test, as shown in Fig. 4.3, was originally built to simulate the reciprocating sliding in an internal combustion engine[90]. The set-up details can be found in [103]. Wear tests, especially microstructural characterization of worn surface in the reciprocating sliding system, were initiated on the basis of a previous work[65] in which the so called surface mixed layer (SML) was found in the worn surface of the MMC sliding against a bearing steel SAE 52100. According to the previous work, a surface mixed layer was developed in which the SiC particles were fragmented and redistributed during dry wear test. At a fixed load (1 kg), the depth of the SML changed with sliding cycles, and there existed a maxima in the mixed layer depth near 2000 sliding cycles. Therefore, the sliding conditions existing at this maximum point

were chosen for the present work, i.e. load 1 kg, sliding speed 10 cm/sec, total cycles 2000 and sliding track length 25 mm at ambient environment (room temperature $22^{0}C$, humidity 38-40%). Thus the sliding distance was 100 m and the contact stress level was approx. 10 MPa.

4.3 TEMPERATURE MEASUREMENT

The average temperature (bulk temperature) of the block specimen at the surface was measured using spot-welded thermol-couples (NiCr/NiAl-K type) adjacent to the worn surface. Very small wires of the thermol-couples were spot-welded on the sides of block specimen, and the welding spots were close to the wear track (about 1 mm away from the wear track) according to previous wear tests.

4.4 X-RAY DIFFRACTION

Phase identification of the wear debris and determination of the variation of the lattice parameters of the phases at different load levels were carried out using a Rigaku X-ray diffractometer using Cu Kα radiation. In XRD analyses, wear debris was placed as a thick paste using a few drops of acetone on a concave of a glass slide. In all experiments, wear debris were collected and XRD samples were prepared in the shortest time possible for observations with minimum contamination.

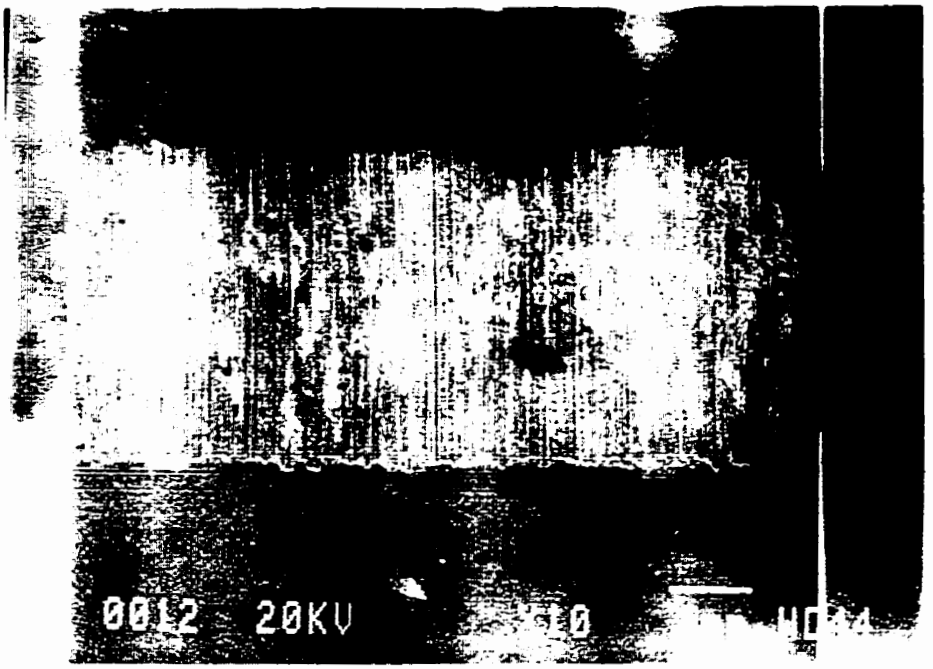

Fig. 4.2 A typical wear scar on a block specimen obtained using the Block-on Ring wear tester.

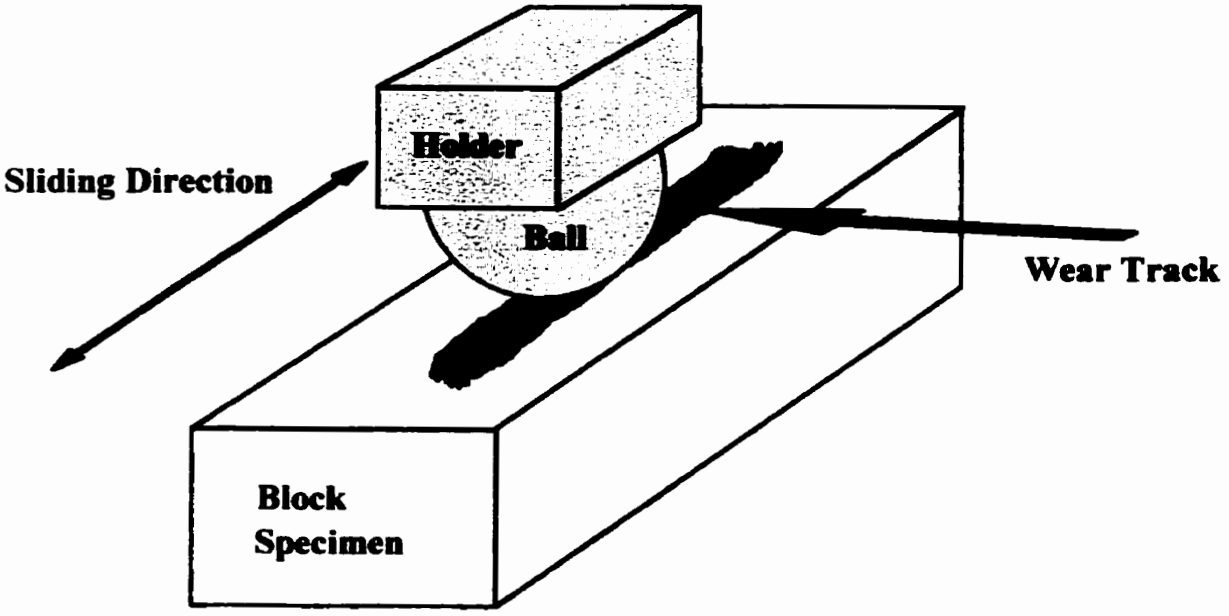

Fig. 4.3 Schematic illustration of Ball-on Block wear test.

4.5 SCANNING ELECTRON MICROSCOPY

The microstructural features of the Al base alloy and the composite prior to and after the wear tests were examined using optical microscopy and scanning electron microscopy (SEM) to determine topographic and microstructural conditions. Characteristic X-ray microanalysis, i.e., Energy Dispersive Spectroscopy (EDS) and X-ray Mapping techniques were also utilized in the study to understand compositional information of the worn surface. A JEOL JXA-840 scanning electron microscope was used in the present work.

In SEM studies, both secondary electron emission mode (SE) and back scattered electron emission mode (BE) were used, which provided topographic and compositional images, respectively. EDS was conducted with a JEOL EDS system (Si detector, and Norvar plastic window) equipped with a Tracor Northern TN-5500 X-ray analyzer. The Norvar plastic window makes it possible that the EDS spectra have a better detectivity for light elements such as C, O in terms of qualitative analysis.

4.5.1 Worn surface and cross section of the worn surface

In addition to the surface morphology of the worn specimens, cross-sections of the worn surfaces were investigated to characterize the wear surface and the subsurface. Two kinds of cross sections were used in this study, namely, transverse cross section and longitudinal cross section. The longitudinal cross-section is referred to as a section normal to the wear surface and parallel to the sliding direction, and the transverse cross section is a section normal to the wear surface and perpendicular to the sliding direction, as schematically illustrated in Fig. 4.4.

Two kinds of methods were used to prepare the cross section samples from the wear specimens.

Method 1:

The worn specimens were first electro-plated with a Cu layer to protect the worn surface from other damages. The Cu plated specimens were cut half into either longitudinal or transverse cross sections, and then mounted and polished according to standard metallographic specimen preparation method[104]. The polished cross section samples (down to 0.05 μm) were slightly etched using a Keller Reagent (2.5 ml HNO3, 1.5 ml HCl, 1.0 ml HF, and 95 ml water) prior to optical and SEM observations.

Method 2:

Two half blocks from the wear specimens were polished down to 0.25 μm, and the polished sides were joined, face to face, tightly together using a small bolt. The joint sample was then polished in such a way that the side to be polished, was perpendicular to the joint surfaces. The joint sample was then ready for wear test with the polished side being slid against the steel and the joint surfaces being either parallel (longitudinal) or perpendicular (transverse) to the sliding direction. During the wear test, the joint surfaces near the wearing contacts would friction weld and be displaced. After the test, the joined blocks were simply broken apart, and worn surfaces were also broken into two parts. Thus, fracture cross-sections of the worn surfaces were produced. These fracture cross-sections were expected to provide some unique information compared to those obtained from the Method 1. As well, no any contamination on the fracture cross-sections was present since the fractured cross-sections were put into SEM for observation immediately after being fractured.

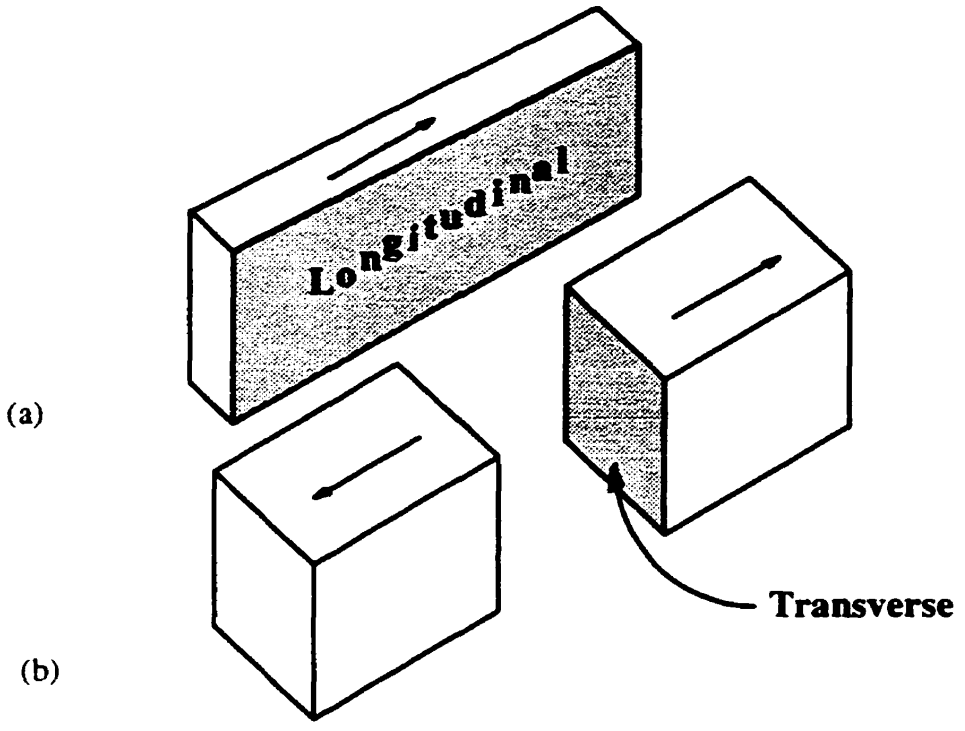

Fig. 4.4 Schematic illustration of two kinds of cross-sections. (a) Unidirectional sliding wear; and (b) Reciprocal sliding wear.

4.5.2 Wear Debris

Microstructural characterization of wear debris was also conducted using SEM and EDS examinations. During the wear tests, the debris was collected on a Cu plate which was then placed in the vacuum chamber of the SEM immediately after it was collected. There was no other physical contact on the wear debris. In doing so, contamination or other influence on wear debris would be minimized, especially in the case that transfer and mixing of materials during the sliding wear were studied.

4.6 TRANSMISSION ELECTRON MICROSCOPY

Surface and subsurface microstructures of the worn specimens and wear debris are of most interest in the present work. Therefore, transmission electron microscopy(TEM) was used extensively. A JEOL 2000FX Transmission Electron Microscope with an EDS attachment was used for the study. The conventional selected area electron diffraction(SAD) and image analyses were carried out by using an acceleration voltage of the electron source of 200 kV. The convergent beam electron diffraction (CBED), by which crystallographic symmetry can be determined, was obtained at the acceleration voltage of 125 kV and with low camera constant.

The most important step in a TEM study of the worn surfaces and wear debris was the preparation of thin foils. Ion milling was mainly utilized as a thinning technique of the TEM thin foils. A Gatan ion milling machine was used with a cooling system using liquid nitrogen. Complicated preparation procedures for the thin foils of the worn surface and wear debris were carefully carried out with great patience and confidence.

4.6.1 The Worn Surface And Cross Section Of The Worn Surface

In order to investigate the microstructural features near the worn surface, longitudinal cross section specimens were prepared for TEM. The worn specimens were cleaned to remove loosely adherent debris and then were electroplated with a Cu layer as a protective layer prior to being sliced for thin foils. An epoxy was then used as a protection and as a glue by which two pieces of half-disc (diameter of 3 mm) from the cross section were put together supported by a standard copper ring of 3 mm in diameter. In doing so, two worn surfaces, opposite and parallel to each other, were set up in the center of the copper ring. The process is schematically shown in Fig. 4.5. In order to

obtain high quality electron transparent area in the cross section thin foils, two rotational speeds were chosen during the ion milling, so that the thinning along the glue line between the two half discs (at a higher rotation speed) would be less than that perpendicular to the glue line (at a lower rotation speed). Fig. 4. 6 demonstrates a typical close-up morphology of a cross section sample, showing the centre area with perforation.

The planar view specimens, i.e. the electron beam was normal to the worn surface in TEM, were prepared as well. In order to obtain planar view thin foils, single side milling method, which was done successively for TiN coated sample by the author[105], was used for the worn surface characterization by modifying in a way that one ion gun was applied with a high voltage(6 KV) to achieve sufficient thinning from the un-worn side of the foil and another gun was applied a low voltage (1 KV) to prevent the worn surface from deposition of contaminants during the ion thinning process. As well, the un-worn side was upward setting on the thin foil holder, while the worn surface side was downward, in order to minimize the redeposition of contaminants during the thinning.

4.6.2 Wear debris

The specimens of wear debris for TEM studies were prepared using Gatan G-1 epoxy that is specially made with an enhanced resistance to electron radiation in TEM. At first, the collected debris powder was mixed with the epoxy, and then transferred into a brass tube of 3mm in out-diameter and cured for 20 min at an elevated temperature below 80°C. The tube was sliced into a series of discs in thickness of about 500μm using a thin diamond saw. The discs were ground to achieve a thickness of 80 to 100 μm and dimpled on the centers of both sides of the thin foils prior to ion milling. Finally, the dimpled foils

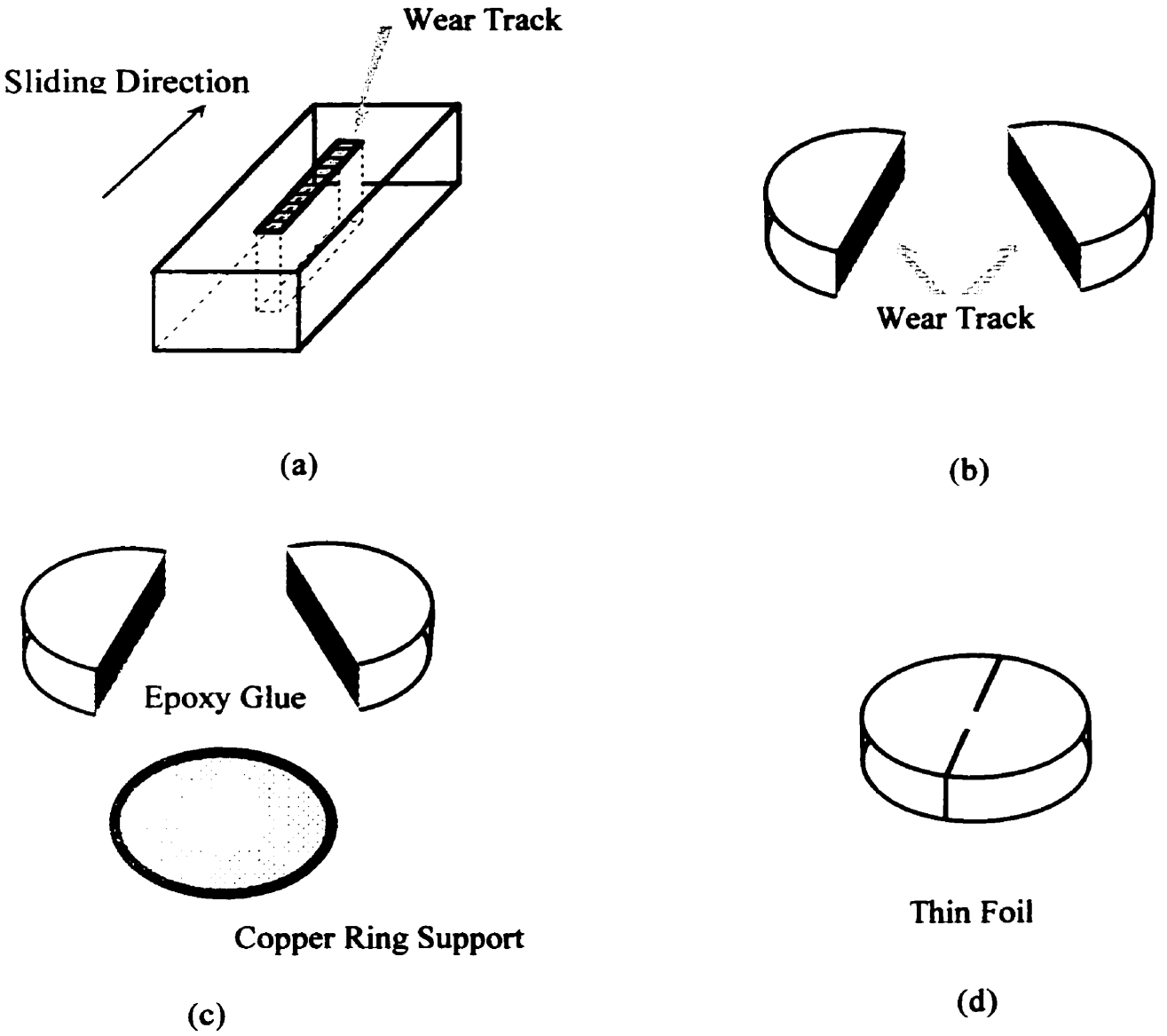

Fig. 4.5 Schematic illustration of preparation of TEM thin foils of longitudinal cross section of worn surface. (a) A longitudinal cross section is cut from a specimen; (b) and (c) Two pieces of the sections is put together with epoxy and supported by a Cu ring of 3 mm; (d) The thin foil.

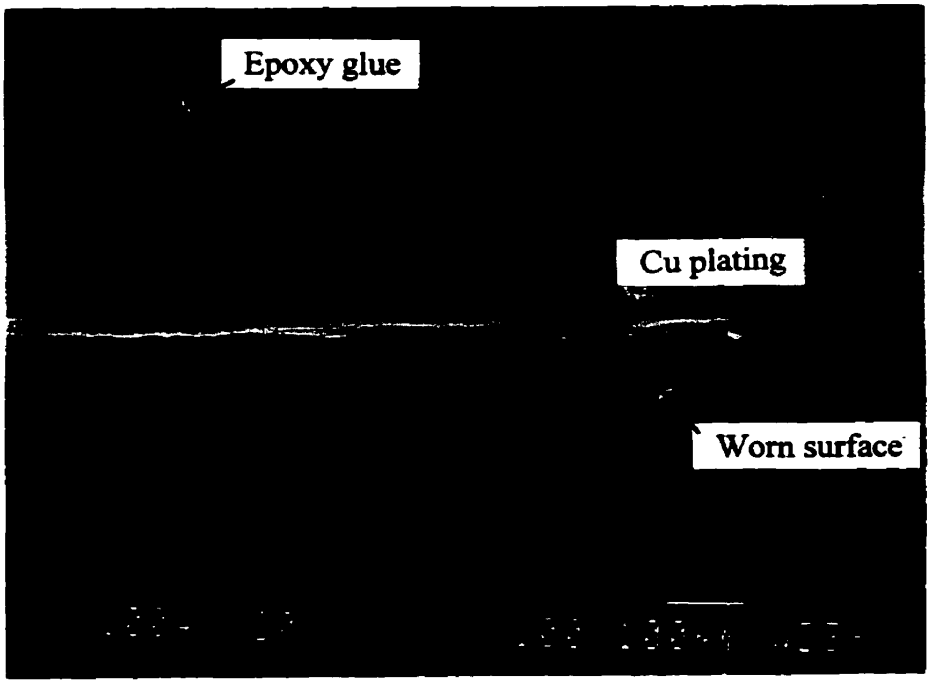

Fig. 4. 6 SEM morphology of a cross section thin foil for TEM studies, showing a perforation including the worn surface, mixed layer and subsurface.

were subjected to ion milling for 4 hrs at 5 KeV and half hrs at 2 KeV, using a Gatan ion milling machine at an angle of 12^0 with a cooling system using liquid nitrogen. Fig. 4. 7 schematically shows the preparation process for the wear debris samples for TEM observation.

4.7 MÖSSBAUER SPECTROSCOPY

Since a significant amount of iron was found in the wear debris, Mössbauer spectroscopy was also used. The Mössbauer spectroscopy is a useful method for the

phase analysis of alloys containing Fe or Sn, and is extensively used in the studies of Al alloys and Ti alloys that contain a variety of amount of Fe, especially obtained by mechanical alloying [106-108]. Some fundamentals and applications of the Mössbauer spectroscopy regarding the Al-Fe system is briefly summarized in Appendix 1.

In the present study, the wear debris specimens for Mössbauer Spectroscopy were prepared as thick plates by compacting a mixture of the debris (approx. 100mg) and Benzophenone powder (100mg). The specimens contained about 8-10 mg/cm^2 of Fe. The spectra were obtained using a γ–ray emission with ^{57}Co in a matrix of Rh source at room temperature. Isomer shifts in the spectra were given relative to α-Fe. The spectra were evaluated by standard least-square fit of lines.

The Mössbauer spectroscopy experiments were conducted at the Magnetic Materials Lab in the Department of Physics, the University of Manitoba.

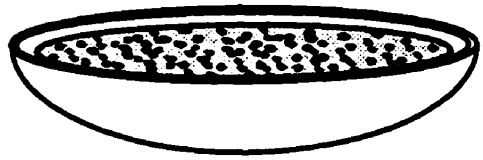

Step 1 Mix wear debris with G-1 epoxy resin

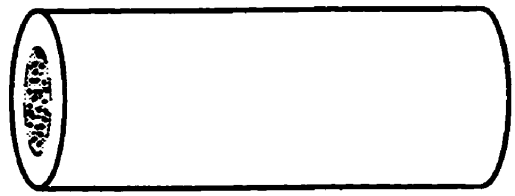

Step 2 Cure resin mixture in a 3 mm diameter brass tube

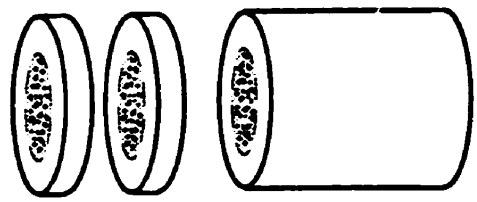

Step 3 Slice the tube into discs and grind the discs

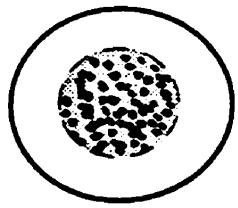

Step 4 Dimple and ion milling the discs

Fig. 4. 7 Schematic illustration of the preparation procedures of wear debris samples for TEM observation.

CHAPTER FIVE WEAR BEHAVIOR AND MICROSTRUCTURAL CHARACTERIZATION OF WORN SURFACE

5.1 MICROSTRUCTURAL CHARACTERIZATION OF AS-RECEIVED Al-Si ALLOY AND Al-Si/SiCp COMPOSITE MATERIAL

Fig. 5.1 shows a typical microstructure of the Al-Si alloy (A356) obtained using SEM. During solidification of the alloy, dendrites of aluminum (α solid solution) solidify first. Then the spaces between these dendrites are filled with aluminum-silicon eutectic. When the eutectic freezes, it decomposes into aluminum and Si. The eutectic Si is acicular and randomly distributed. Mg is a major alloying element that makes the alloy heat treatable.

Fig. 5.2 shows a typical microstructure of the Al-Si alloy reinforced with SiC particulates. The average size of SiC particles is approximately 10 μm, and the volume fraction of the SiC particles is 20 %. During the solidification process, reinforcing particles are generally rejected at the solid/liquid interface and pushed by the moving interface and then segregate in the interdendritic regions which solidify last[32 , 109].

In as-cast conditions of the base alloy and the composite, the matrix is free of precipitates and is mainly single phase of α-Al solid solution with the presence of the secondary particles Si and the reinforcing particles SiC.

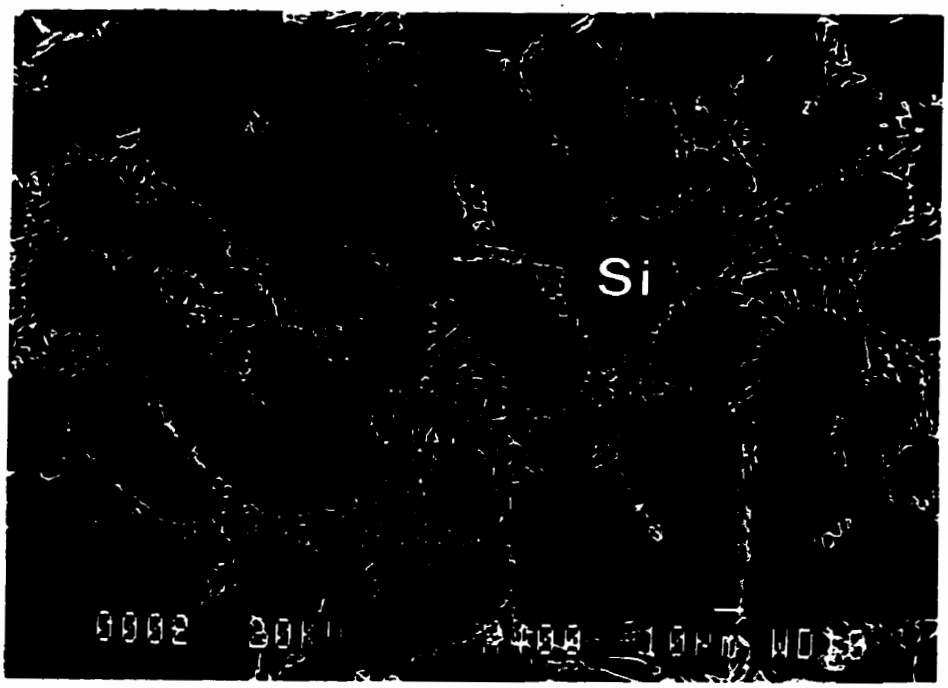

Fig. 5.1 Microstructure of A356 Al-Si alloy.

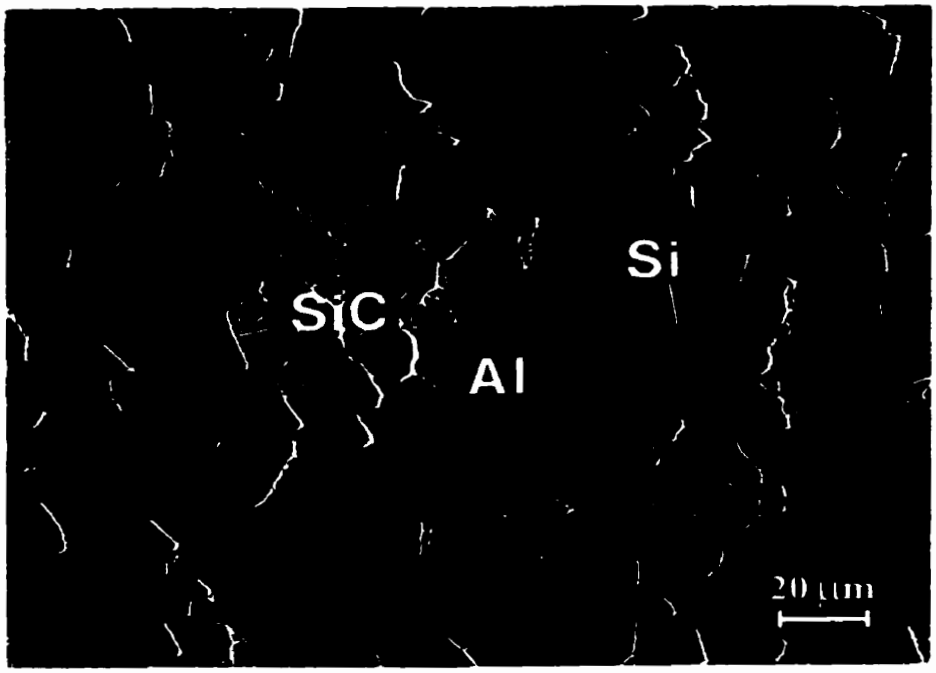

Fig. 5.2 Microstructure of A356 Al-Si alloy reinforced with SiC particulate.

5.2 HEAT TREATMENT OF THE BASE ALLOY AND THE COMPOSITE

5.2.1 Heat treatment

T6 heat treatments of both the Al-Si base alloys and the SiC reinforced composites were carried out using a single solution temperature and a series of thermal aging temperatures in order to find out the peak aging conditions for both materials. The T6 heat treatments were as follows:

(1) Solid solution at 540° C for 8 hours;

(2) Quenching in warm water at 50° C;

(3) Subsequent aging at 155° C for several aging periods;

(4) Air cooling.

The hardness for the samples before and after the heat treatments for different thermal aging time was measured using Vickers hardness tester at a load of 20 kg. Fig. 5.3 shows the effect of the thermal aging time on the hardness of both the base alloy and the composite. It is seen that the peak hardness occurs at aging time of 16 hours for both the base alloy and the composite. Therefore, all heat treated samples for the wear tests were chosen to be thermally aged for 16 hours.

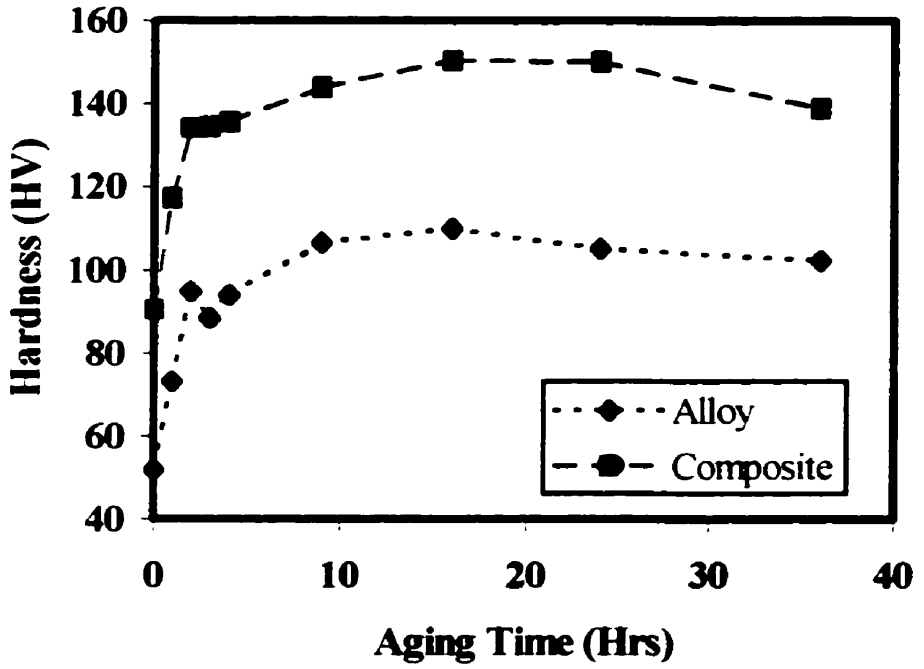

Fig. 5.3 Dependence of the microhardness of the Al base alloy and the Al-Si/SiC composite on the thermal aging time at the aging temperature of 155° C.

5.2.2 Microstructures of the heat treated samples

When subjected to the T6 heat treatment, the Si particles in the Al alloy agglomerated and changed their shape and size in the solid solution process. As shown in Fig. 5.4, the Si particles were rounded as a result of the agglomeration and the average size was approximately 5 μm. During the age hardening process, precipitation occurred in the supersaturated solid solution of the matrix. Depending on the aging temperature

and time, the sequence of the precipitation in Al-Si-Mg ternary alloys has been generally considered to be as follows[110-112]:

(1) Needle-shaped Guinier-Preston zones along <001> matrix;

(2) Rod-shaped metastable precipitates β';

(3) plate-shaped equilibrium precipitates $\beta(Mg_2Si)$.

Fig. 5.5 shows a typical microstructure of the T6 aged Al-Si/SiCp composites in the present work. It can be seen that two types of precipitates are present in the matrix: (1) needle or rod shaped precipitates β' and equiaxed precipitates of Si. The β' precipitates are uniformly distributed in the matrix. The average size of the β' precipitates is about 100 nm in length.

5.3 WEAR BEHAVIOR

The wear rate of the alloys used in the wear tests were determined using the following expression:

$$w = \frac{Wear\ Loss(g)}{Sliding\ Distance(m)}$$

Fig. 5.6 shows the wear rate as a function of the sliding load for the base alloy (T6) and the composite at the as-cast and T6 conditions. The data were plotted using Logarithmic scale to get a better view of the dependence of the wear rate on the sliding loads. Considering Curve 1, it is seen that the wear rate of the base alloy increased gradually with an increase of the sliding load, from 3.2×10^{-6} g/m at a load of 0.1 kg and

slightly accelerated at 3 kg until a transition to severe wear is observed starting at 10 kg. In comparison, the wear rates of the composites in both the as cast and the T6 condition were considerably lower than that of the base alloy at the Zone I as indicated in Fig. 5.6, i.e., at a load range of 0.1 kg to 3 kg. For example, the wear rate of the composites (at 10^{-7} g/m) was one order of magnitude lower than that of the base alloy at a load of 0.1 kg. The significant increase in wear resistance resulting from the incorporation of the reinforcing SiC particles is mostly manifested at this load range. It can also be seen that at Zone II, the wear behavior for the three kinds of samples was similar, and the reinforcing SiC seemed not to offer any significant improvement to the wear resistance of the composites.

It should be noted that only a slight decrease in the wear rate was found in the age hardened composite as compared to that of the as cast composite. This implies that the wear resistance was not enhanced significantly as a result of the T6 heat treatment compared to the increase in hardness resulting from the heat treatment, even though the hardness was increased by almost factors of two due to the age hardening. The composite samples in both conditions showed very similar wear behavior at a low load range (Zone I). In Zone II, wear loss of the as cast composite samples slowed down slightly in contrast to that of the T6 composite samples, but still was slightly higher than that of the T6 samples. However, the wear rate of the former was noticeably lower than that of the latter at high load range, i.e. in Zone III. The wear rate of the as cast composite samples was also lower than that of the base alloy in Zone III. As will be discussed later, these interesting findings are the result of different wear mechanisms and microstructural changes generated during the sliding wear.

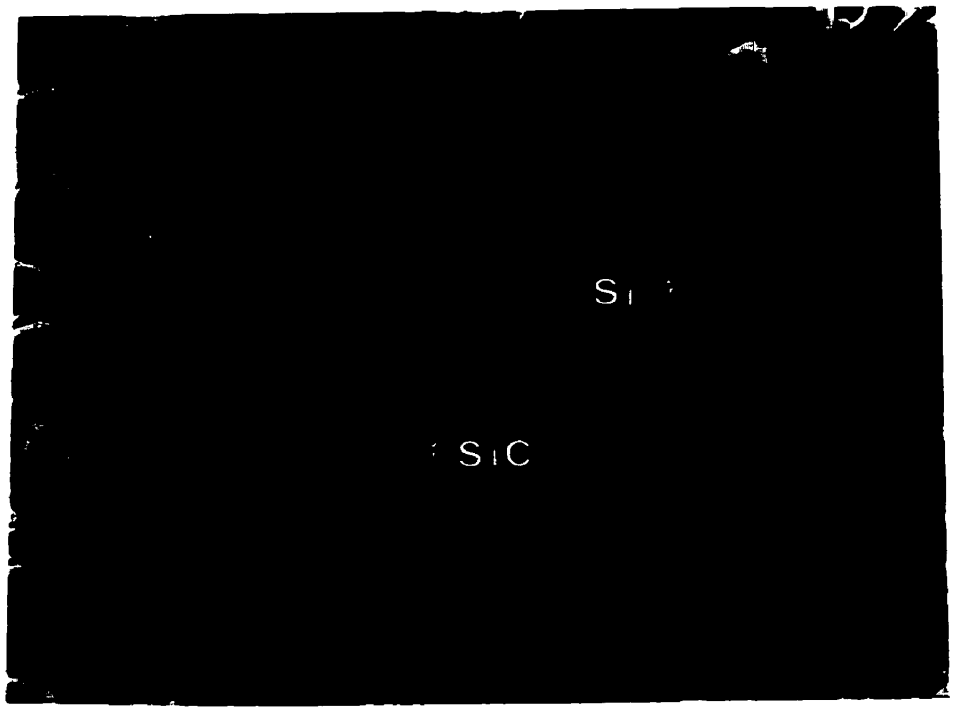

Fig. 5.4 SEM Micrograph of the T6 treated Al-Si alloy reinforced with SiC particulate.

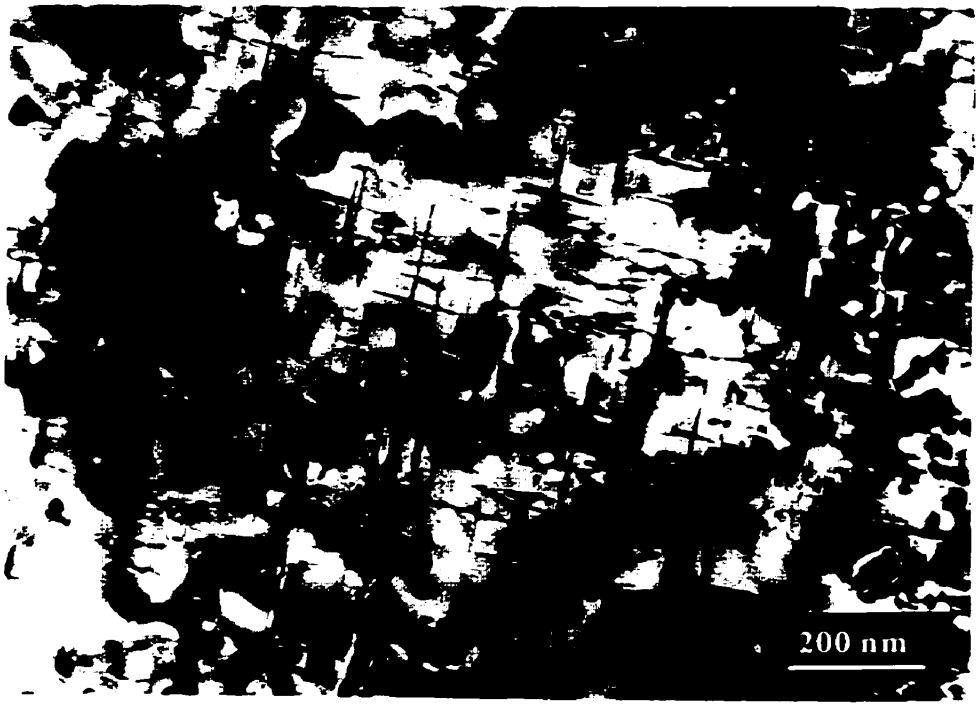

Fig. 5.5 TEM Micrograph of the T6 treated Al-Si alloy reinforced with SiC particulate.

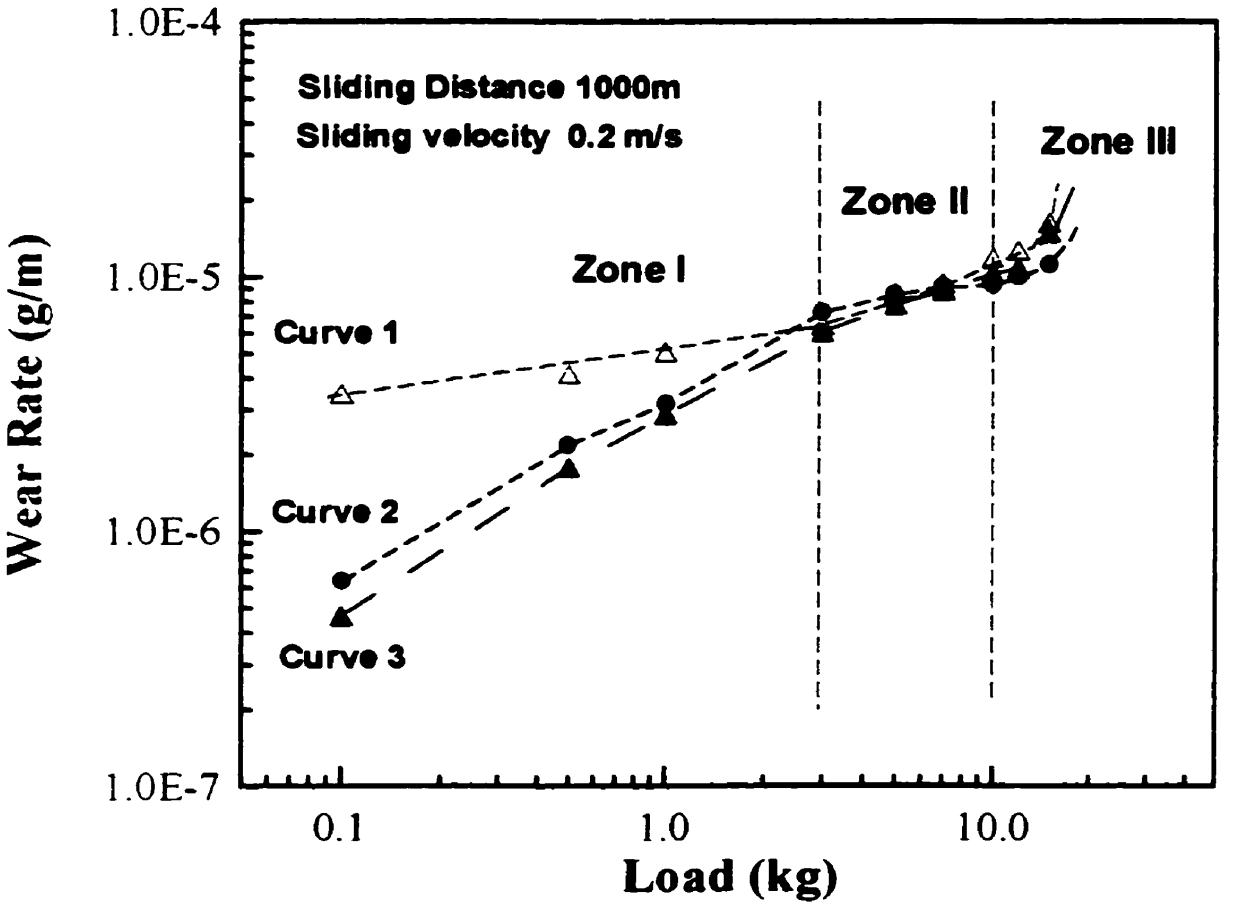

Fig. 5.6 Wear rate of the Al base alloy (T6) and the Al-Si/SiC composites at both the as cast and T6 conditions. Curve I: T6 Al-Si Alloy, Curve II: As-cast Al-Si/SiC composite, and Curve III: T6 Al-Si/SiC composite.

5. 4 MICROSTRUCTURAL CHARACTERIZATION OF THE WORN SURFACES—*Scanning Electron Microscopy Studies*

5.4.1 Morphology of the worn surfaces

The worn surfaces of the unreinforced alloy showed two distinct regions: smooth and crater regions, at a load range of 3 kg to 10 kg using the unidirectional block-on-ring configuration. Typical SEM morphology of a worn surface of the Al-Si alloy at a load of 5 kg is shown in Fig. 5.7. The worn surface of the reinforced composites also showed similar morphology at the same load range, as shown in Fig. 5.8. It can be seen that ploughing and scoring along the sliding direction were mainly present in the smooth region. Observed at a high magnification, the surface morphology showed the presence of microcracks at directions both parallel and perpendicular to the sliding direction in the smooth region (Fig. 5.9). It is seen that large flakes and extruded lips were adjacent to crater regions. In comparison with the extruded lips and adjacent craters, it seems that the smooth regions were the last contact areas before the sliding stopped. It also appears that the material had been detached in the crater region, probably before the slider passed through the adjacent smooth region or at least before the extruded lips were formed under the compressive stresses.

It was generally observed that equiaxed particles were predominantly present in the crater areas of the worn surfaces at this load range, as shown in Fig. 5.10 and Fig. 5.11. From the topographical features in the crater regions, it appears that fracture surface in the crater areas did not show a typical fracture feature, such as dimples, that take place in a normal tension test of a ductile material such as bulk Al alloys [97, 98]. At worn surfaces with a short sliding distance (100 m), it was observed that the worn surface was

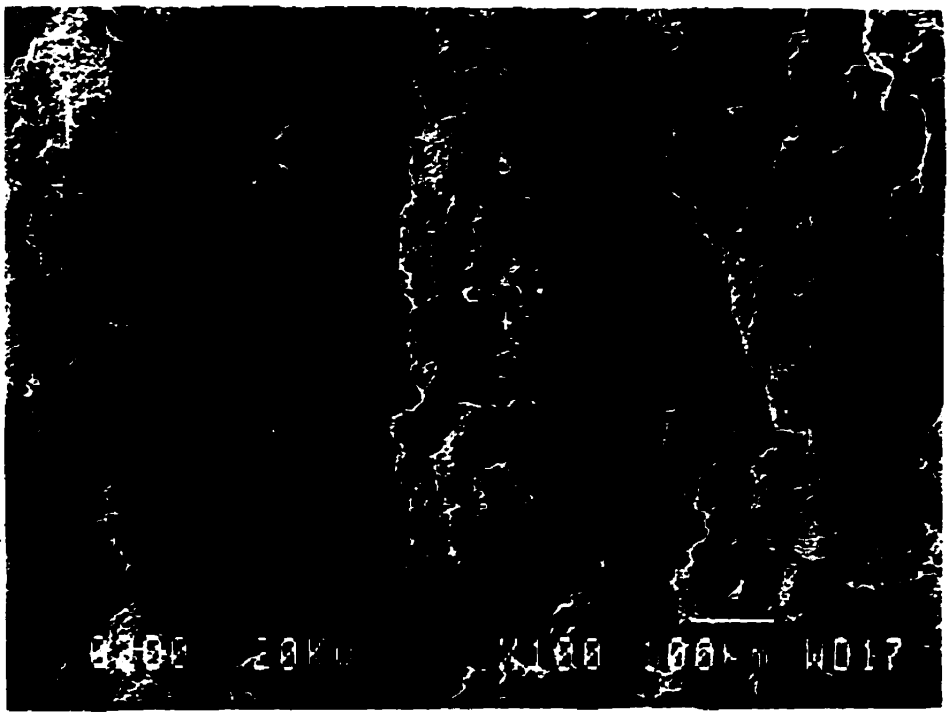

Fig. 5.7 Typical SEM morphology of worn surface of the Al-Si alloy at a load of 5 kg using the block-on-ring configuration.

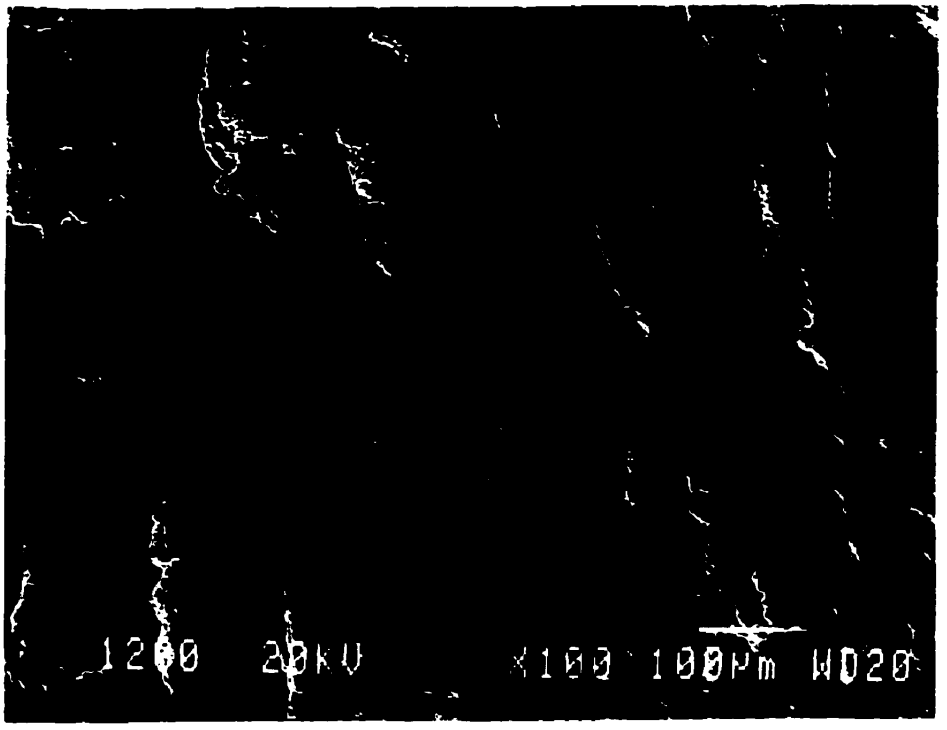

Fig. 5.8 Typical SEM morphology of worn surface of the Al-Si/SiC composite at a load of 5 kg using the block-on-ring configuration.

relatively flat and some areas showed fracture features similar to those in a normal tensile test, as shown in Fig. 5.12. It can be seen that there were "dimples" or fresh interfaces due to detachments of SiC. It is likely that the matrix material including the second phase particles Si or SiC was detached from the subsurface, so that the "dimples" were formed as a result of removal of the second particles. It is interesting to note that a considerable amount of elemental iron was found on the worn surface by using EDS analysis. Fig. 5. 13 shows x-ray maps of Al and Fe elements on the worn surface with the two distinct regions. It is seen that iron was present in both the smooth region and crater areas. It is obvious that the iron was transferred from the sliding ring. It should be mentioned that the crater areas with fine equiaxed particles were found to contain a larger amount of Fe than in the smooth regions.

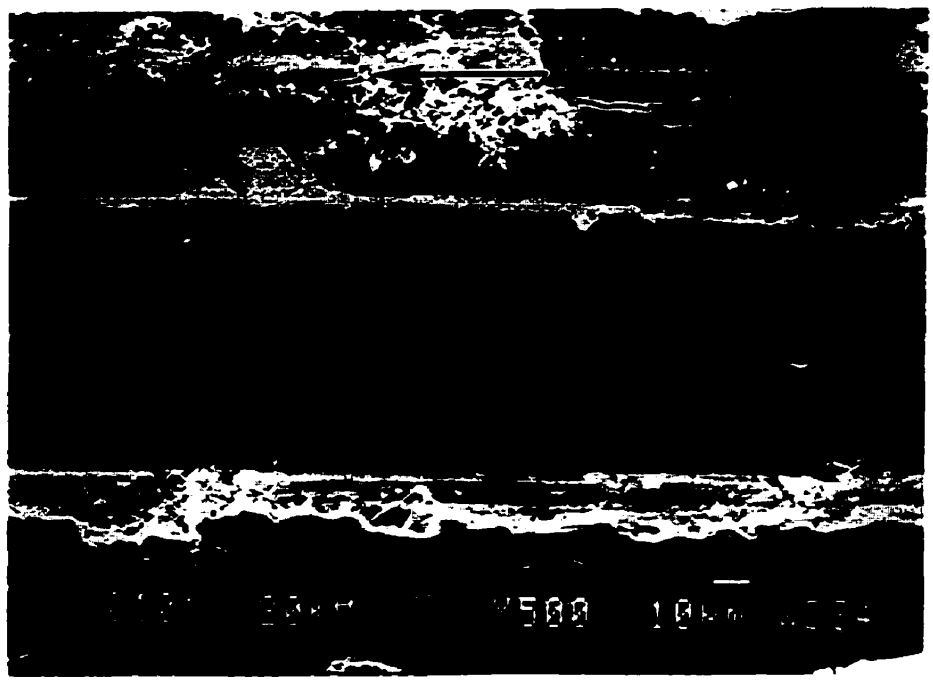

Fig. 5.9 Microcracks parallel and perpendicular to the sliding direction in the smooth region in the worn surface of the Al-Si alloy at a load of 3 kg using the block-on-ring tester.

Careful SEM examination of the crater areas also indicated that there were different microstructural features present on the equiaxed particles in the craters in the worn surfaces of the Al-Si alloys at different sliding loads. As shown in Fig. 5.11, the size of the equiaxed particles in the crater in the worn surface at a load of 5 kg was much larger than that of the particles in the crater area at a load of 10 kg as shown in Fig. 5.10. The particle size ranged between 0.2 to 1 μm in the former, and the size was about 2 -5 μm in the latter. In addition, EDS analysis showed that the amount of Fe in the very fine particles was higher than that in relatively bigger equiaxed particles in the crater areas.

Fracture in the subsurface below the worn surface was also noted. In the bottom of a crater shown in Fig. 5.14, it is evident that extensive cracking occurred in the subsurface as a result of severe deformation and heavy strains caused by the sliding wear. Fig. 5.15 shows a crater with very sharp edges, from which debris very likely had detached by adhesion. In a montage micrograph shown in Fig. 5.16, it was noted that in area A, the bottom of the crater seemed to be very flat with extensive cracks, and no particles similar to those in Fig. 5.10 were present. Furthermore, Flake B as marked in Fig. 5.16, did not show direct evidence of being detached from adjacent areas, and there were gaps between Flakes B and C and the subsurface below Flake B. It suggests that Flake B might be displaced during the sliding motion, and Flake C might be smeared on the former in a subsequent event.

During the wear process, loose debris were detached from the worn surface, and some of debris were compacted into the surface again. This can be confirmed by the observation as shown in Fig. 5. 16. In the smooth region, some of flakes were found to be

Fig. 5.10 SEM Micrograph of a crater area in the worn surface of the Al-Si alloy at a load of 10 kg, showing very fine particles in the crater.

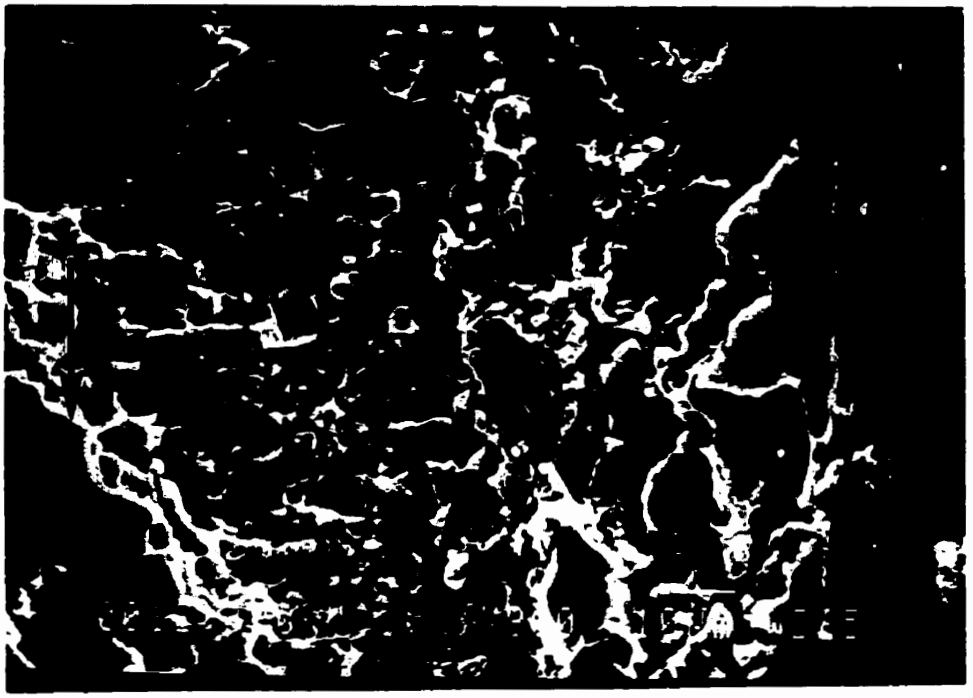

Fig. 5.11 SEM Micrograph of a crater area in the worn surface of the Al-Si alloy at a load of 5 kg, showing relative larger particles in the crater.

comprised of small particles embedded in the large flakes (smooth region A), as shown in Fig. 5.16. This feature can be observed more clearly on the worn surface of HP Al at a load of 3 kg, as shown Fig. 5.17. The worn surface was comprised mainly of small fragments or agglomerates with a size of 2 μm. It is likely that the cracks, either perpendicular or parallel to the sliding direction, occured at the boundaries or interfaces of the small fragments. It was noted that these segments consisted of a large amount of Fe.

Fig. 5.18 shows the comparison of surface morphologies for the Al-Si alloy and the MMC at the ends of the wear track at the same sliding condition at a load of 3 kg. It is obvious that the extruded lips are much larger in the unreinforced alloys than in the reinforced composites, and the grooving is smoother in the former than in the latter. It

Fig. 5.12 Surface morphology of worn surface at a sliding distance of 100m, showing "dimple" features and fresh interface due to detachments of SiC.

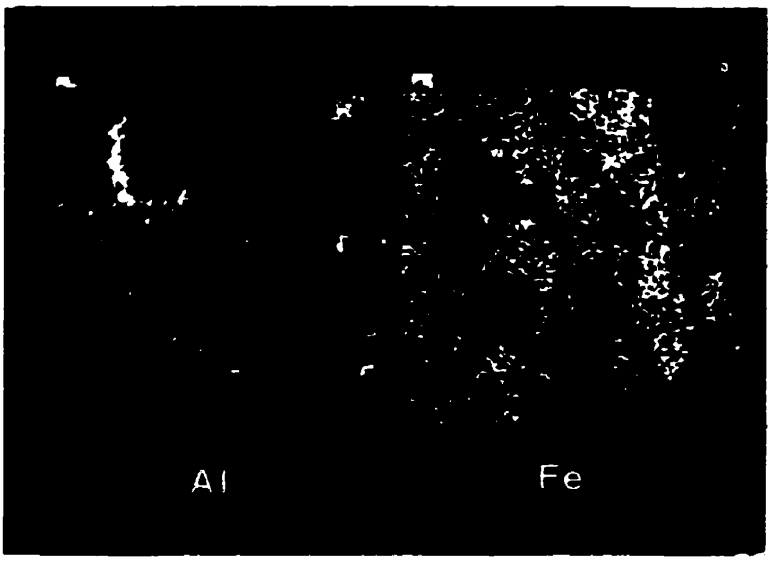

(a)

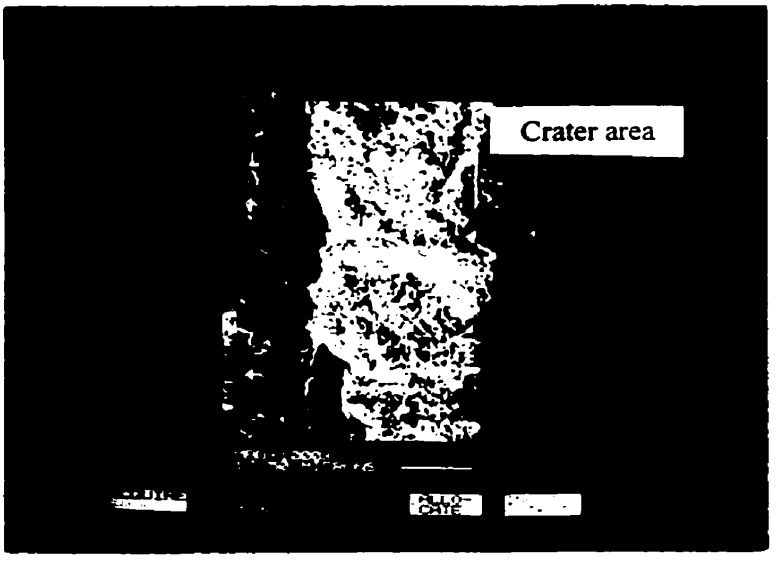

(b)

Fig. 5.13 Elemental distributions of Al and Fe on the worn surface of Al-Si alloy at 7 kg. (a) X-ray mapping; and (b) Morphology of the corresponding worn surface.

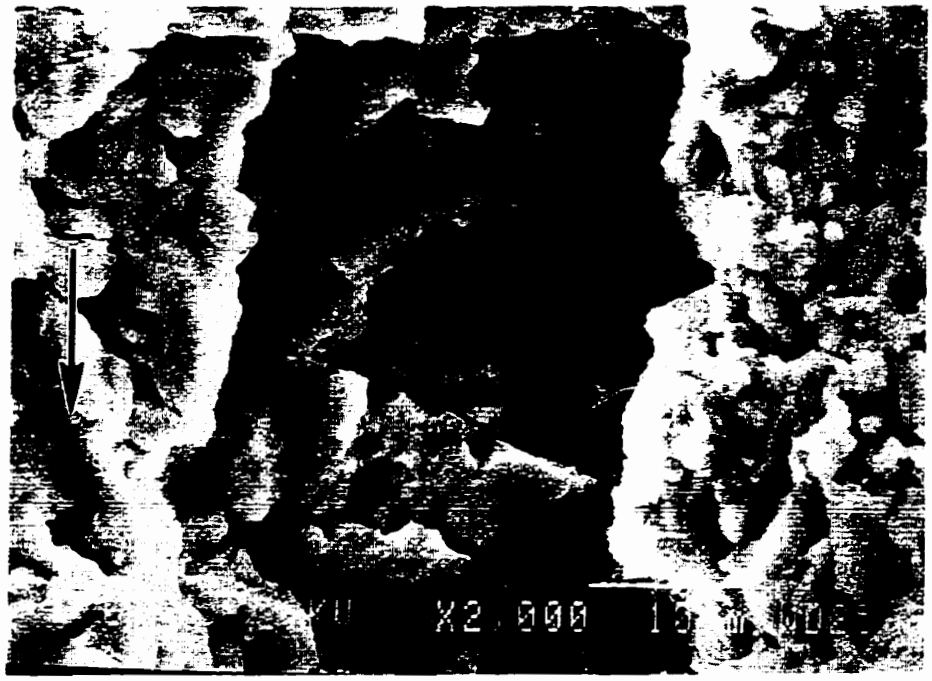

Fig. 5.14 Subsurface cracks in the worn surface of the Al-Si alloy at a load of 10 kg. The arrow shows the sliding direction.

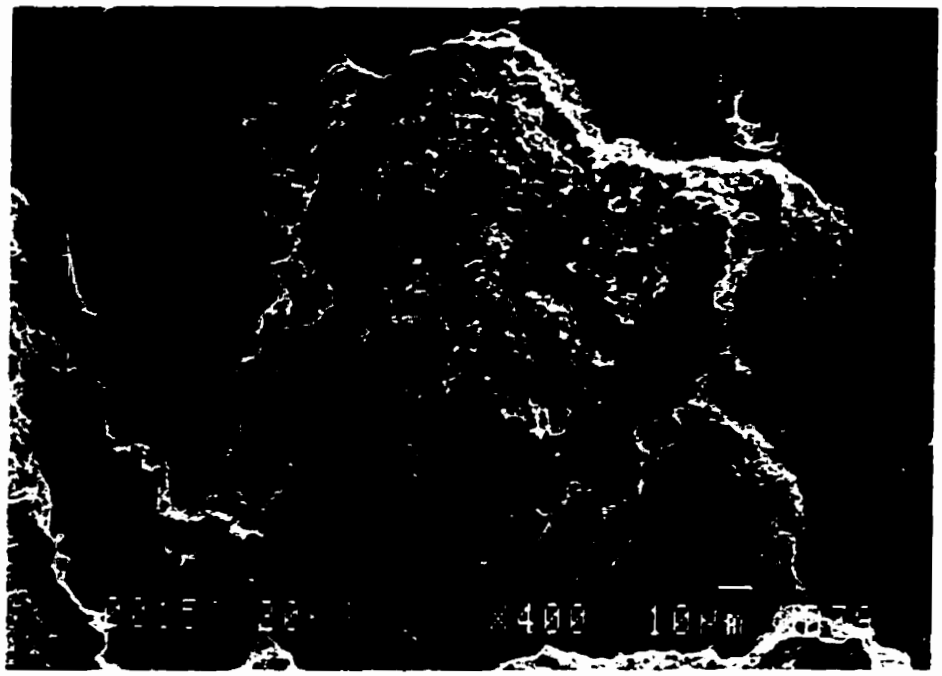

Fig. 5.15 A crater region with sharp edges in the worn surface of the Al-Si alloy at a load of 7 kg, an indicative of adhesive wear.

Fig. 5.16

SEM Micrograph of a flat crater area (A) and wear flakes (B) and (C) in the worn surface. The formation of the flat crater area and the wear flakes might not be occurring at the same time. See text for details.

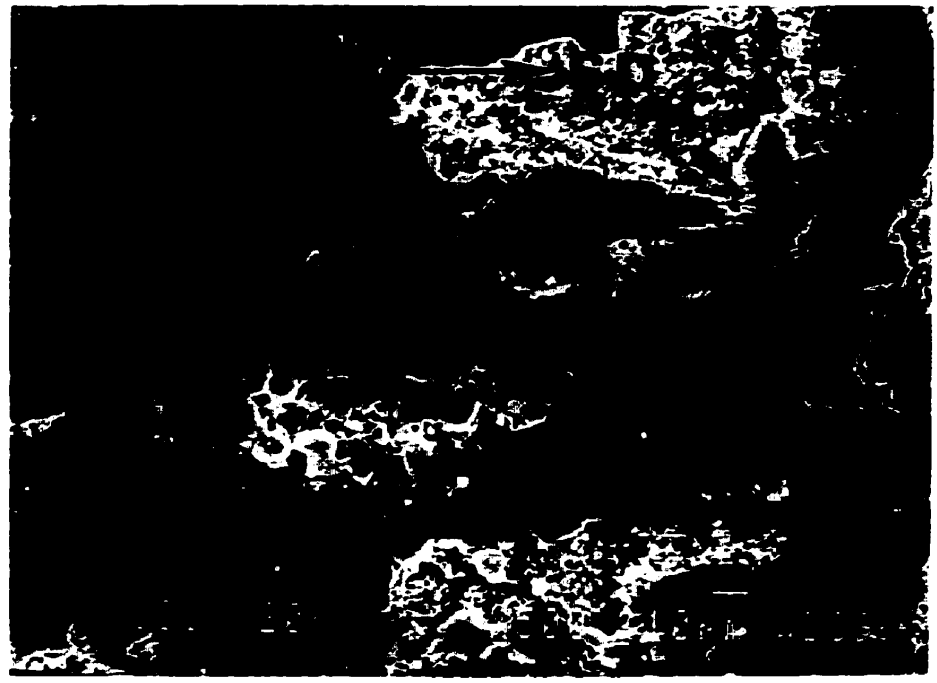

(a)

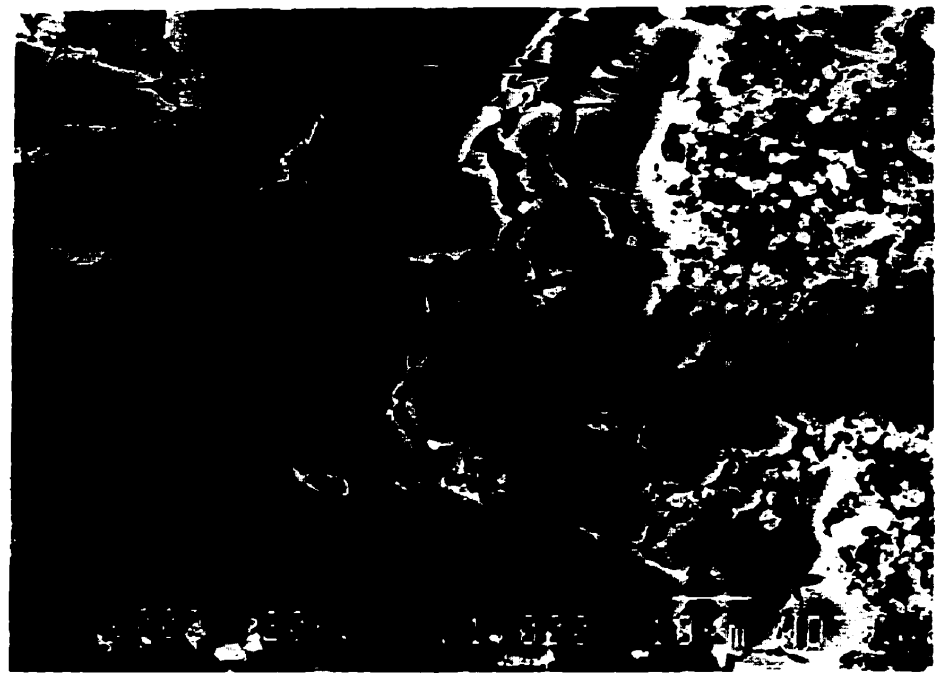

(b)

Fig. 5.17 Morphology of the worn surface HP alloy at a load of 5 kg, showing small fragments or agglomerates embedded in the worn surface. (a) At a low magnification; and (b) At a higher magnification. S.D. Sliding Direction.

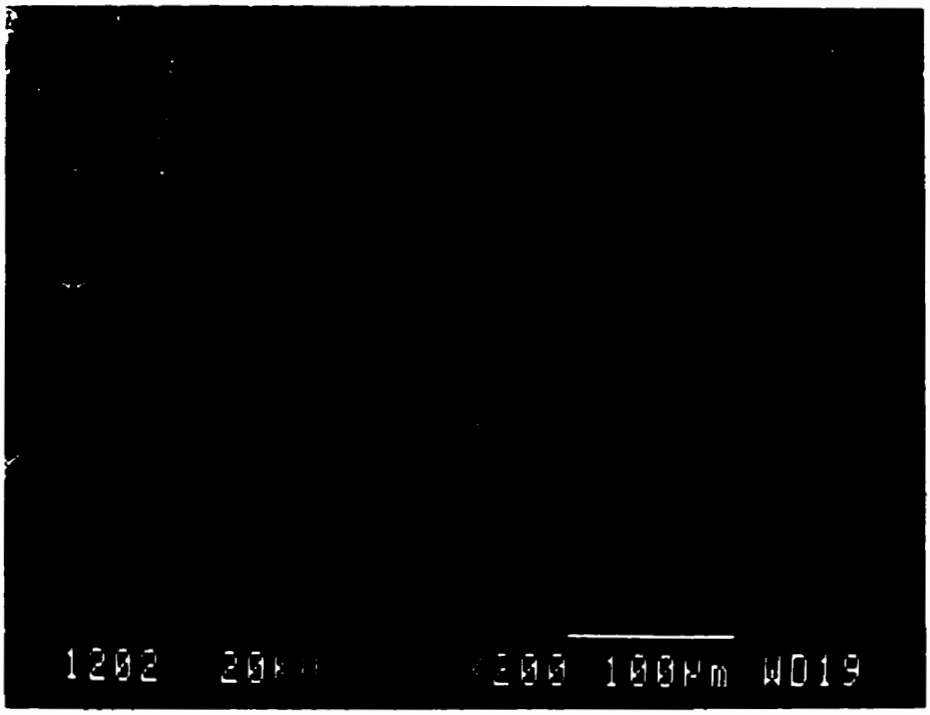

(a)

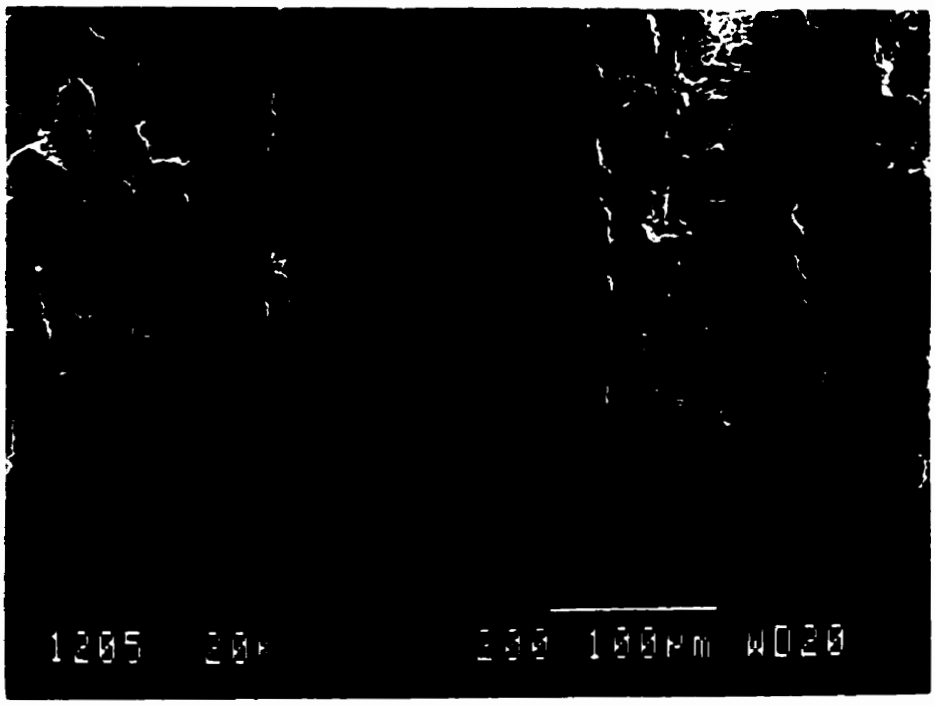

(b)

Fig. 5.18 Ends of wear tracks at a load of 3 kg, showing extruded lips. (a) Al-Si alloy; and (b) Al-Si/SiC composite. The arrow indicates the sliding direction.

(a)

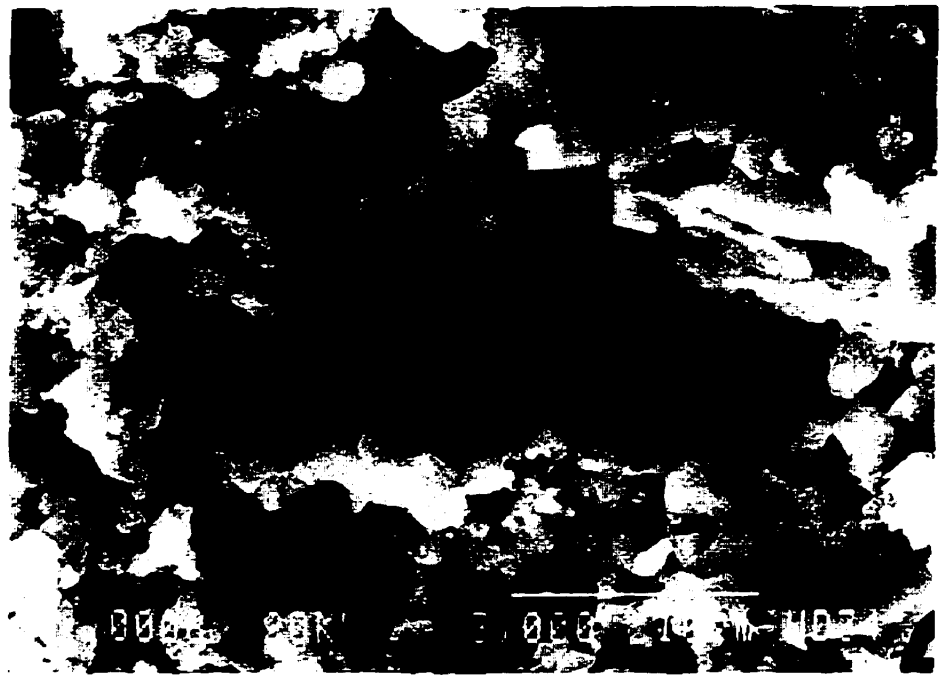

(b)

Fig. 5.19 (a) Debonding of SiC particles to the Al matrix; and (b) Fracture and fragmentation of SiC particles in the worn surface of the Al-Si/SiC composite.

suggests that plastic deformation was much severe in the unreinforced alloys than in the composite at a lower load.

At the worn surface of the composite, bare SiC particles were less frequently found in the smooth grooves. Within the crater areas, evidence of fracture and debonding of the SiC was found, as shown in Fig. 5. 19. As will be discussed later, fragmentation and fracture of the SiC particles were frequently observed in the cross section of the worn surfaces of the MMC.

In summary, two distinct regions, namely smooth region and crater regions, were observed in the worn surfaces of the Al-Si alloy and the MMC at a variety of sliding loads under the unidirectional dry sliding condition. It was found that the material transferred from the sliding steel, i.e., the major element of iron, was present in the worn surface, and the amount of iron element was found to be more in the crater regions than in the smooth region. Presence of the fine equiaxed particles containing iron were found to be the major feature of the crater regions in the worn surfaces of the Al-Si alloy and the MMC.

5.4.2 Cross-sections of the worn surfaces

5.4.2.1 Al-Si alloy

Fig. 5. 20 shows a longitudinal cross section of the worn surface of the Al-Si alloy. The cross section was obtained using the fracture method (Method 2) described in

section 4.5.1. The cross sections obtained by this unique method accentuate the highly-strained region and the plastic deformation in the subsurface created during the sliding wear. It can be seen that the cross section of the worn surface can be divided into three regions. The first region is the top surface layer in which fine fragmented particles were found. As will be discussed later, this layer was comprised of elements from both the Al alloy and the slider steel, and thus called a mechanically mixed layer (MML). The second region just below the MML was the subsurface with highly deformed structures. Severe plastic flow and material displacement occurred in the subsurface region. The third region is below the highly deformed second region, and it was just slightly deformed with a transition to the unaffected matrix. Hence, the third region is less important in the present study.

From Fig. 5. 20 and Fig. 5. 21, it can be observed that severe plastic flow occurred in the subsurface. The narrow band-like structures of material flow bent over towards the sliding direction and approach the near surface. As indicated in Fig. 5.21, the thickness of the band structure was about 1 to 3 μm, and the extended length of the shear band was quite long as compared to the thickness. This implies that the shear deformation process was very intensive.

The transverse fracture cross section also demonstrated similar features in the subsurface of the worn surface, as shown in Fig. 5.22 and Fig. 5.23. In conjunction with the longitudinal cross section, it appears that the subsurface underneath the worn surface was comprised of band structures in 3D. Since the surface of the cross section was originally polished before being joined and subjected to the sliding wear, the layered features in it evidently showed the extent of shear deformation.

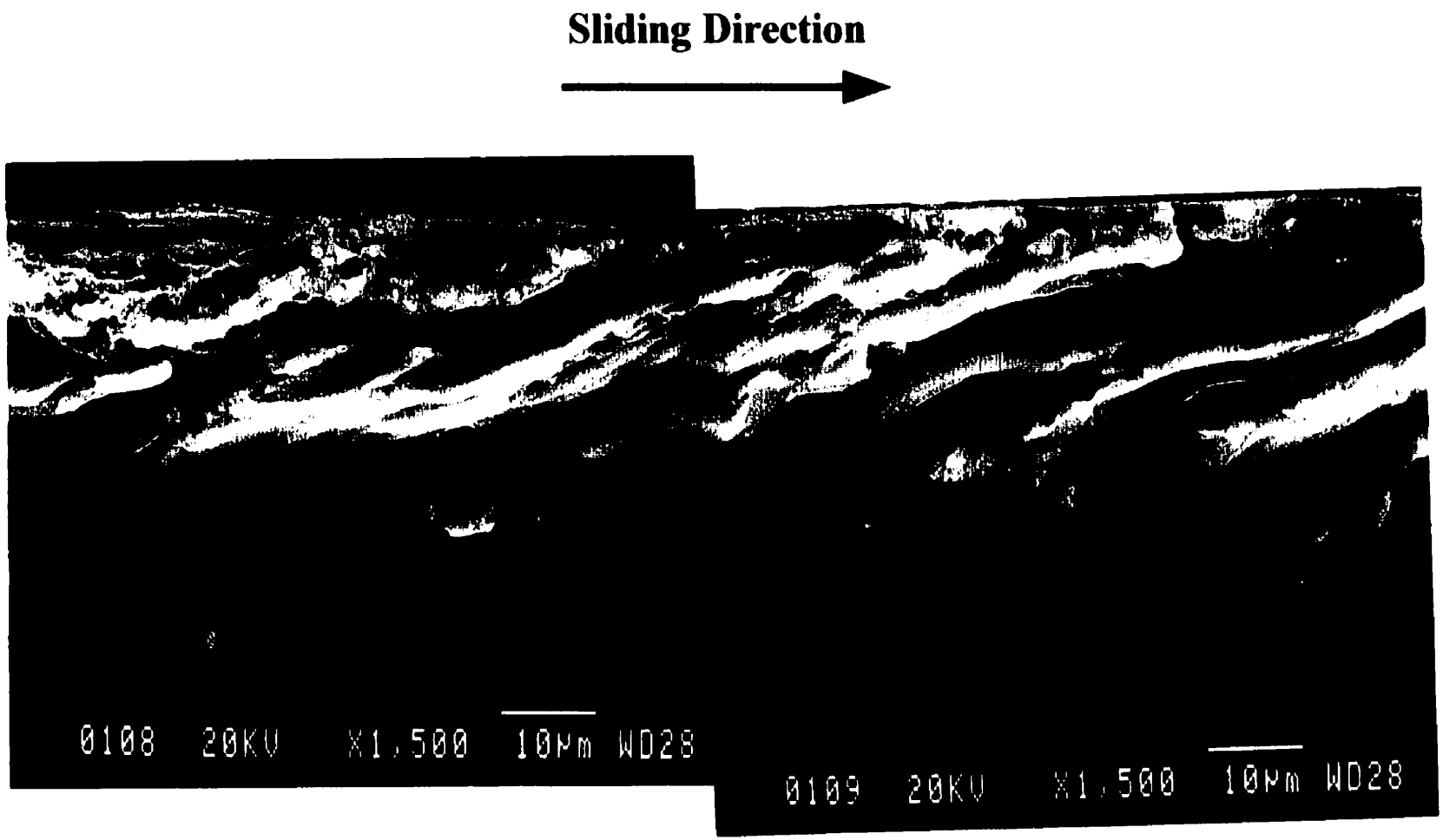

Fig. 5. 20 Longitudinal fracture cross section of the worn surface of Al-Si alloy at a load of 5 kg, showing highly strained regions and the plastic flow of matrix in the subsurface of the worn surface.

As mentioned above, very fine particles were observed in the top layer of the worn surface. Figs. 5. 24 and 25 show ultrafine structures in the top layers in transverse cross sections of the worn surfaces at a load of 7 kg. From the morphologies of the fine equiaxed particles, it appears that these particles are the same as those observed in the crater areas in the worn surface. EDS analysis also indicated that the top surface layers contained a considerably high amount of Fe from the slider steel, as found in the worn surface. The elemental Fe was found to distribute over all the areas that contained ultrafine particles. Fig. 5.24 (b) shows both Al and Fe distributions in the cross section corresponding to Fig. 5.24 (a) by using X-ray mapping. Fig. 5.25 shows a polished cross section of the worn surface at a different sliding load (7 kg).

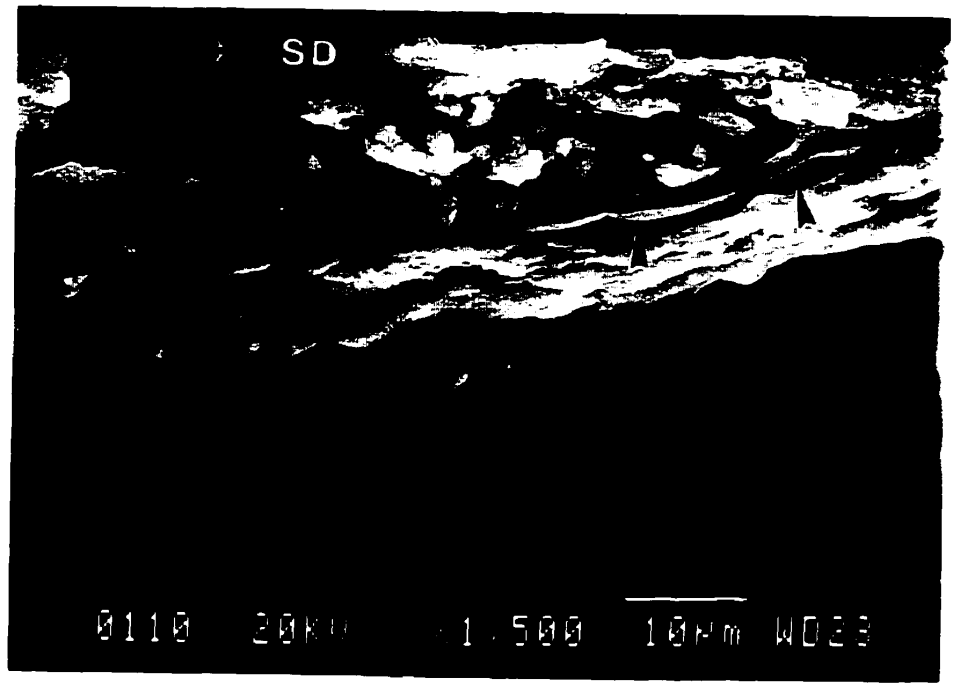

Fig. 5. 21 Longitudinal fracture cross-section of the worn surface of Al-Si alloy at a load of 5 kg, showing shear bands in the highly strained subsurface and mechanical mixed layer above the shear banded structures.

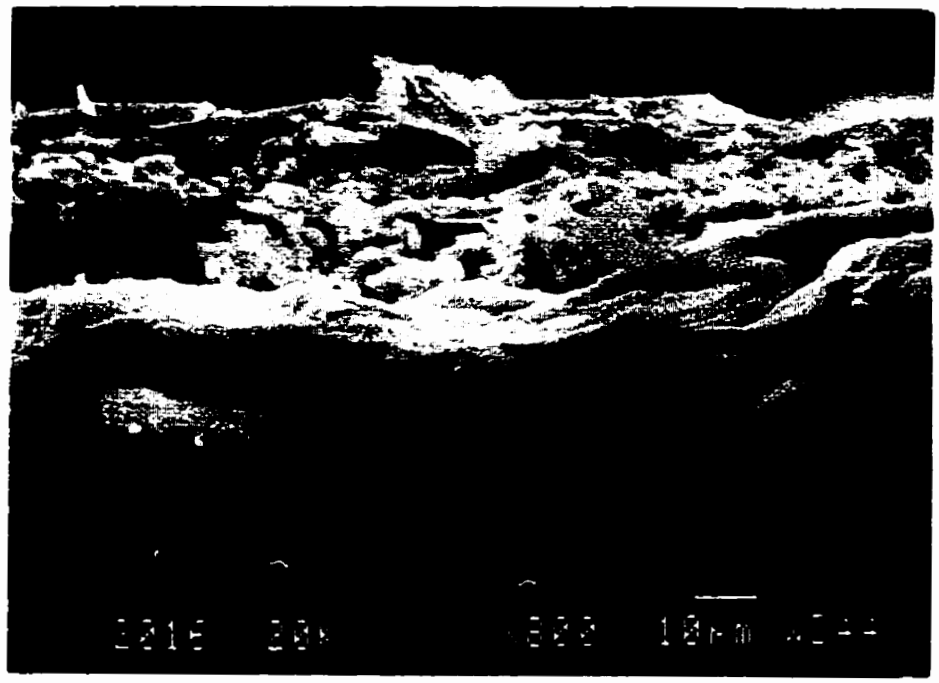

Fig. 5.22 Transverse fracture cross section of the worn surface of the Al-Si alloy at a load of 5 kg, showing the shear bands in the subsurface.

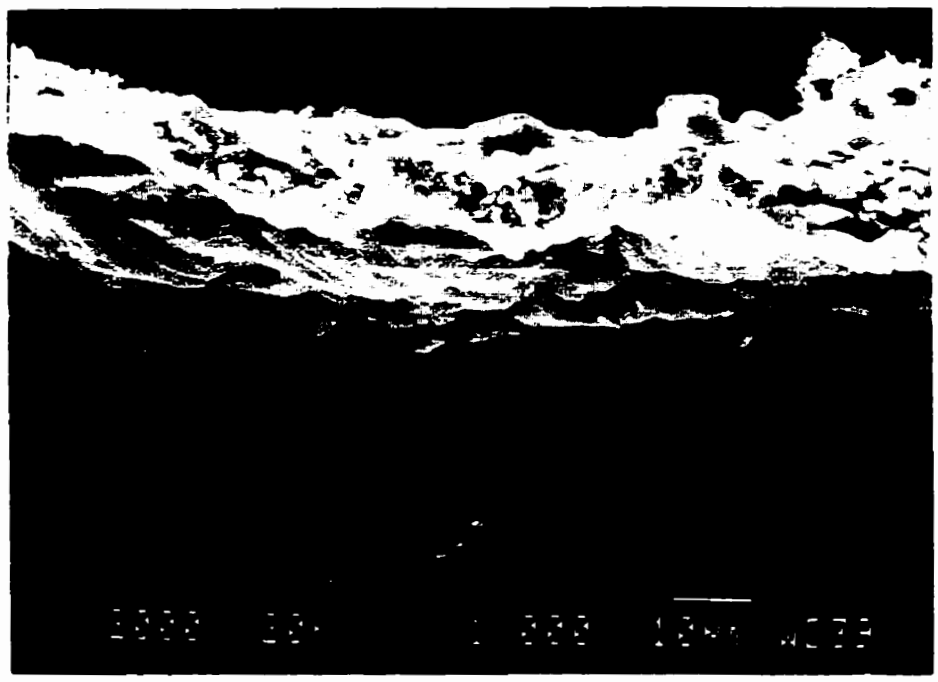

Fig. 5.23 Transverse fracture cross section of the worn surface, opposite to the Fig. 5. 22, showing trace due to shearing displacement in the subsurface.

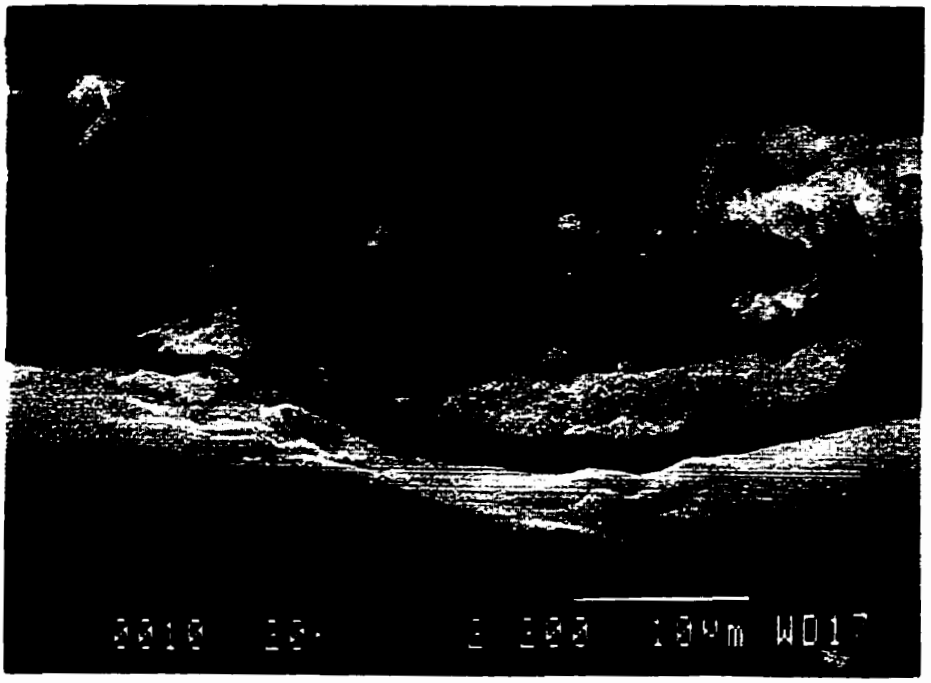

(a)

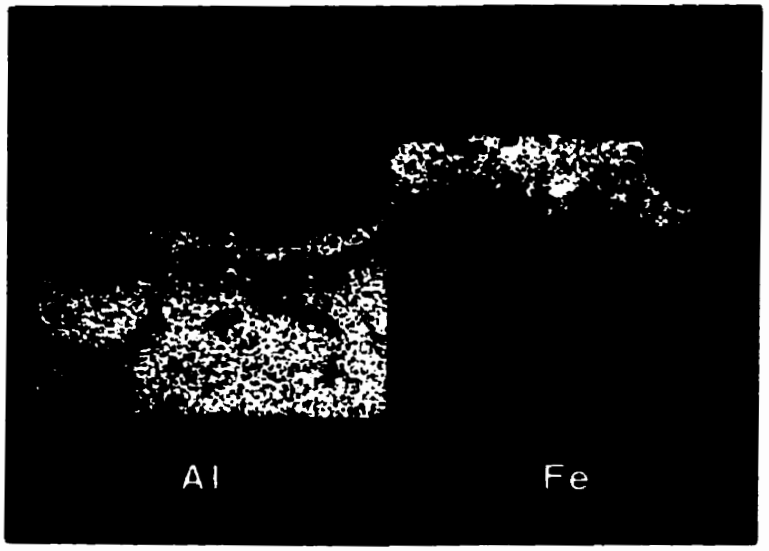

(b)

Fig. 5.24 Mechanically mixed layer in the transverse fracture cross section of the worn surface of the Al-Si alloy at a load of 7 kg. Note a subsurface crack below the MML. (a) SEM micrograph, and (b) X-ray mapping.

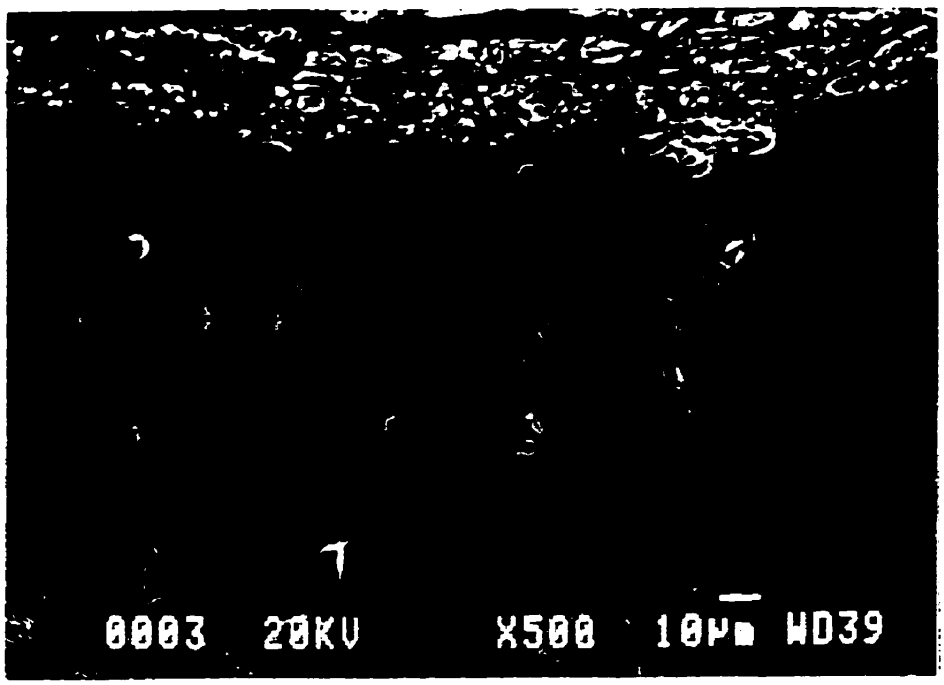

(a)

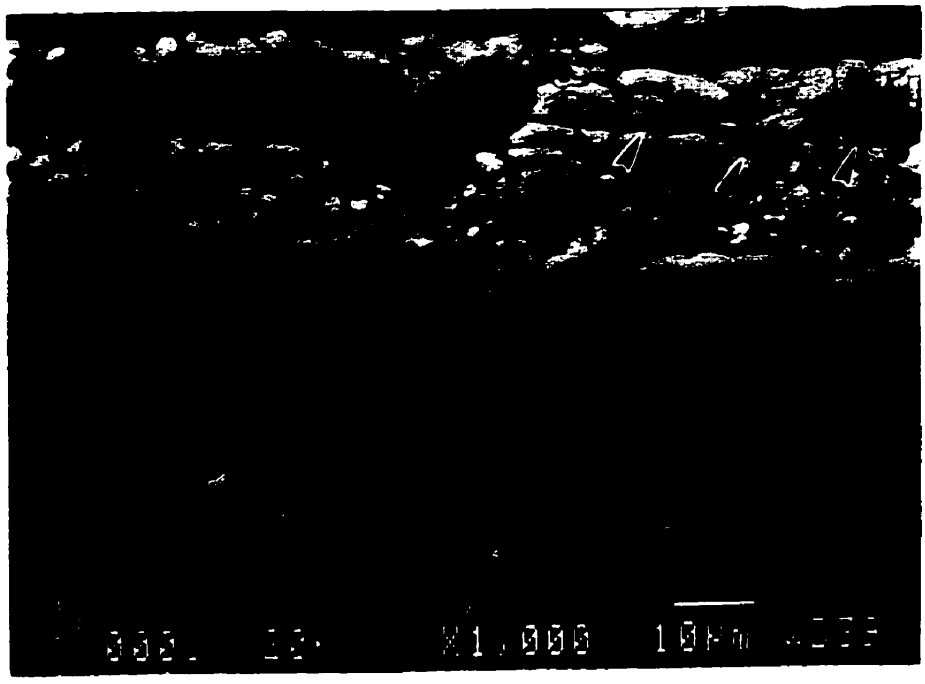

(b)

Fig. 5.25 *(continued)*

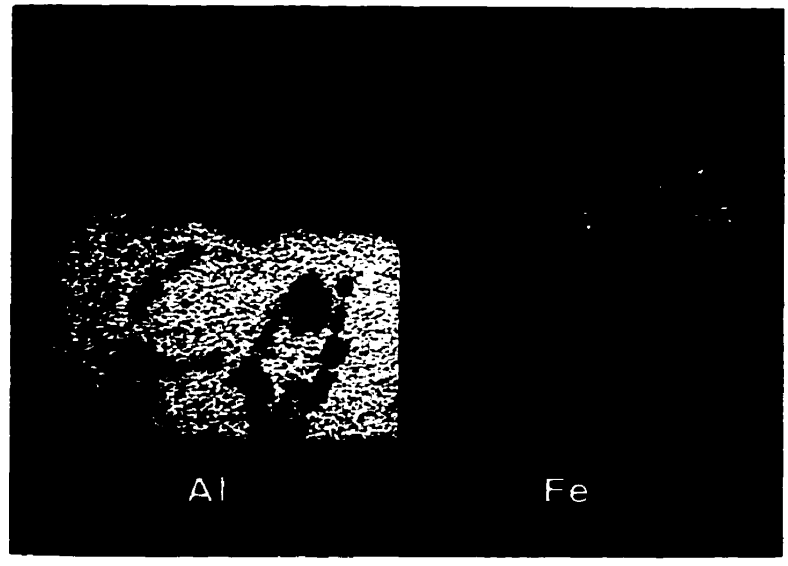

(c)

Fig. 5.25 Longitudinal cross section of the worn surface of the Al-Si alloy at a load of 7 kg, showing presence of a mechanically mixed layer (MML) and plastic flow in the subsurface. SD stands for the sliding direction.
(a) At a low magnification;
(b) At a higher magnification, the arrows indicate cracks parallel to the sliding direction.
(c) X-ray mapping corresponding to (b), showing Fe distribution in the MML.

Microcracks were also noted in the MML and some of which might have propagated and formed large cracks that appeared to be parallel to the sliding direction, as can be seen from the micrograph at a higher magnification as shown in Fig. 5.25 (b). Presence of plate-like subsurface crack underneath the fragmented particle layer was another evidence of subsurface delamination. As well, X-ray mapping showed mechanical mixing of Fe from the slider steel into the top surface layer. Together with the EDS analysis conducted on the worn surface, the X-ray mapping results strongly suggest that an extensive mechanical mixing took place between the Al alloy and the slider steel, and a mechanically mixed layer (MML) containing the elements from the two sliding counterparts was formed in the worn surface.

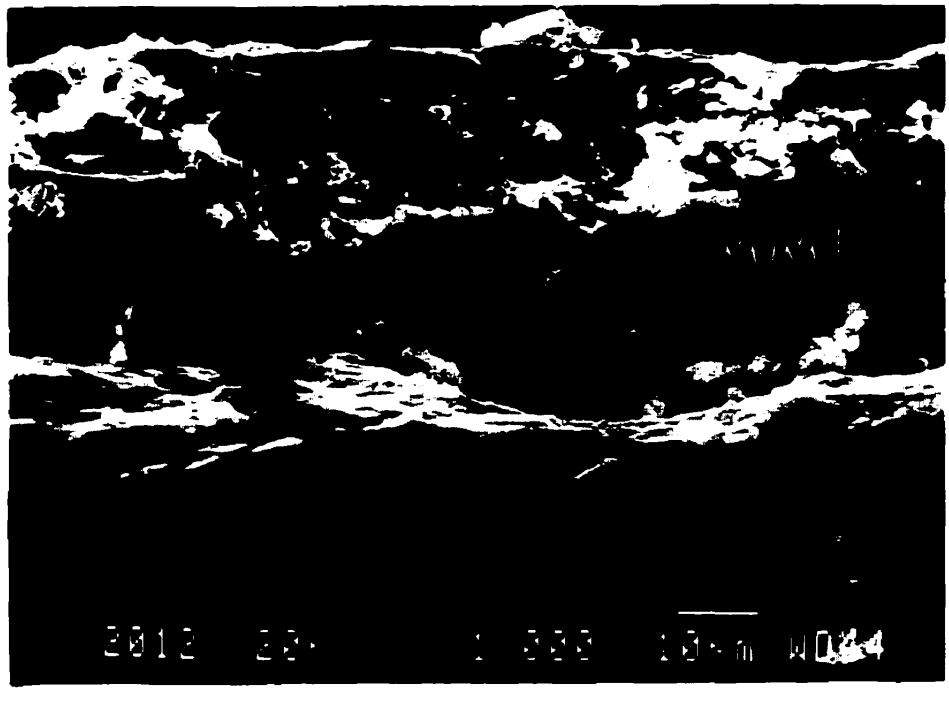

Fig. 5.26 Fracture cross section of the worn surface of the Al alloy at a load of 5 kg, showing a layered structure in the MML. **Layer 1** is a layer without ultrafine particles and mainly contains Al, and **Layer 2** is a subsurface layer with ultrafine particles containing a considerable amount of Fe.

Fig. 5.26 shows another example of the MML in the transverse fracture cross section. It was noted that there were two distinct sublayers in the fracture cross section, i.e., 1) very top surface without ultrafine particles; and 2) subsurface with ultrafine particles in an average size of 1 μm, as indicated in Fig. 5.26. EDS analysis indicated that the first top layer consisted mainly of Al, while the subsurface layer with ultrafine particles contained much more Fe than the first top layer. It is very likely that the Fe-rich sublayer was smeared and covered by a thin "fresh" film of Al alloy in subsequent events during the mechanical mixing process. This layered structure or a Sandwich Structure was formed as a result of mutual transfer of materials and mechanical mixing processes generated by the sliding wear and would be subjected to further compaction, fragmentation and mixing if the sliding was to continue.

It was also noted that the MML was formed almost at all sliding loads used at the sliding speed and distance in the present work. The thickness of the MML, however, was found not to be uniform across the entire wear track. At some locations, the MML was very thin and the fresh matrix of the Al alloy almost approached to the top worn surface, for example in the center area shown in Fig. 5.20.

5.4.2.2 Al-Si/SiC Composite

The morphologies of the worn surface of the Al/SiCp composite were basically similar to those in the Al-Si alloy. However, important differences resulting from the presence of the SiC particles were noticeably observed at the worn surface of the composite. Fig. 5.27 shows cross sections of the worn surface of the composite. It can be

seen that the worn surface was primarily divided into the deformation area and mechanically mixed area. In the fracture cross section, it is clear that a large amount of shear strain and plastic deformation flow of the matrix occurred in the subsurface, as shown in Fig. 5.27(a). The SiC particles were constrained by the plastic strain, and some of the particles were noticed to be fractured due to the heavy strain. The matrix flow had developed around SiC particles, and the direction of the matrix flow changed just in front of the SiC.

Extensive mechanical mixing was also found in the worn surface of the MMC. Fig. 5.28 shows a cross section of the worn surface at a load of 10 kg. It was noted that across the entire cross section of the worn surface, the mechanically mixed layer was not uniform in thickness, and it showed a wavy pattern in depth, as seen in Fig. 5.28(a). At a higher magnification, shown in Fig. 5.28(b), the MML was comprised of two sub-layers, i.e., a top sublayer in which very fine particles were embedded in the matrix, and a compacted layer rich in Fe underneath the first top layer. The major element distributions obtained using X-ray mapping showed a clear picture of the layered structure in the subsurface, in Fig. 5.28 (c). In the Fe rich mixed layer in the subsurface, it is noted that extensive cracking developed either parallel or perpendicular to the sliding direction. The layered or sandwich structure feature was one of the common features in the MML at various loads. Fig. 5.29 (a) and (b) show another typical morphology of the sandwich structure and the corresponding x-ray maps, respectively. It can be seen that the entire MML consisted of alternate sublayers either rich in Fe (white layers), or rich in Al (dark layers). The alternation of the two kinds of sublayers was not uniform across the entire cross section of the wear track. It can also be observed that in the Al rich sublayers there were quite a few small particles containing Fe embedded in the Al matrix material. These features of the MML provided evidence how the mechanically mixed layers were replenished with new fresh matrix material as the wear debris was removed from the

MML. A "fresh" matrix material was detached from some locations where the matrix approached in the near surface, and the detached material was further mixed with previously formed mixture. These "new" mixtures were not only compressed by the normal load, but also extended longitudinally by the shear strain during further sliding. Through this way, "new" material was replenished into the MML and the alternate layers formed. The alternate layers could be further fragmented and mixed if the sliding motion continued.

Fig. 5. 30 shows the morphologies of the alternate structure in the MML at high magnifications. It is noted that there were microcracks in the Fe rich sublayers. The microcracking could be the result of high residual stress in the MML. As shown in Fig. 5. 30(b), the microcracks could possibly develop and coalesce into large cracks contributing to subsequent detachment from the MML. Fig. 5. 31 shows extensive crack propagation in the MML, which was very likely to lead to subsequent delamination and formation of wear debris.

It was also noted that large SiC particles with the same size as in the original material were less frequently observed in the MML compared to those in the original matrix of the composite. Fig. 5. 32 shows a fracture transverse cross section of a worn surface of the composite. SiC particles of the original size can be observed below the MML that was about 10 μm in thickness, while SiC particles of the same size were absent in the MML. This can be clearly observed in the X-ray mapping of Si element in the cross section, as shown in Fig. 5.32 (b). This phenomenon can also be found in the MML discussed above (Fig 5. 28 to Fig. 5. 31). Actually, SiC particles smaller than the original size can be found; for example, a SiC particle with a size about 5 μm, half as the original size, is shown in Fig. 5. 28 (b). Compared to the original material, most of SiC particles found in the MML were smaller, with the presence of a few of large particles as

shown in Fig. 5. 33. The backscattering electron image in Fig. 5.33(b) shows clearly the contrast of the SiC particles to the matrix and the MML. It suggests that the SiC particles were fractured and fragmented in the subsurface during the sliding wear, and it is very likely that fragmented SiC particles were subsequently redistributed in the worn surface as the sliding progressed.

In the subsurface, fragmentation of the reinforcing particles was frequently observed. As shown in Fig. 5. 34, cracks were observed in particles A and B. In the particle A, the crack was running perpendicular to its longer axis, while in particle B, the cracks oriented along the sliding direction as a result of large shear stress generated during the sliding wear. It is seen that the fragments of the fractured SiC particles had moved apart considerably. In particular, for example, particle A was fractured into pieces and the fragments moved away from each other. Refilling of the gaps between the fragments by the surrounding materials or microvoids occurred, as shown in Fig. 5.35 (b) at a high magnification. This provides evidence of a mechanism that the microvoids were formed in the subsurface of the worn surface. The microvoids would serve as sites resulting in cracks in the subsurface. Cracks could possibly be initiated at the interface between the SiC particles and the matrix, as confirmed by the observation that some cracks grew between SiC particles as in Fig. 5. 36.

It should be noted that eutectic Si particles in the matrix were also found to be fragmented in the worn surface as shown in a transverse cross section in Fig. 5.37. The compositional image obtained using Backscattering Electron mode clearly shows the contrast of Si, SiC and the matrix, and confirmed the fragmentation of Si particles. It is seen that the Si particles became much finer by fragmentation in the near worn surface.

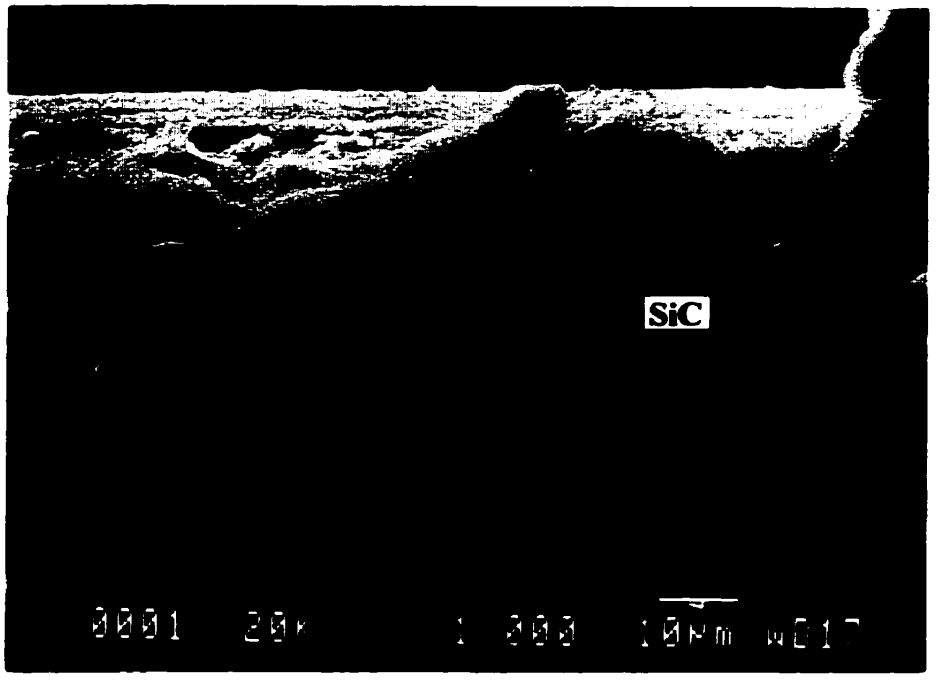

(a)

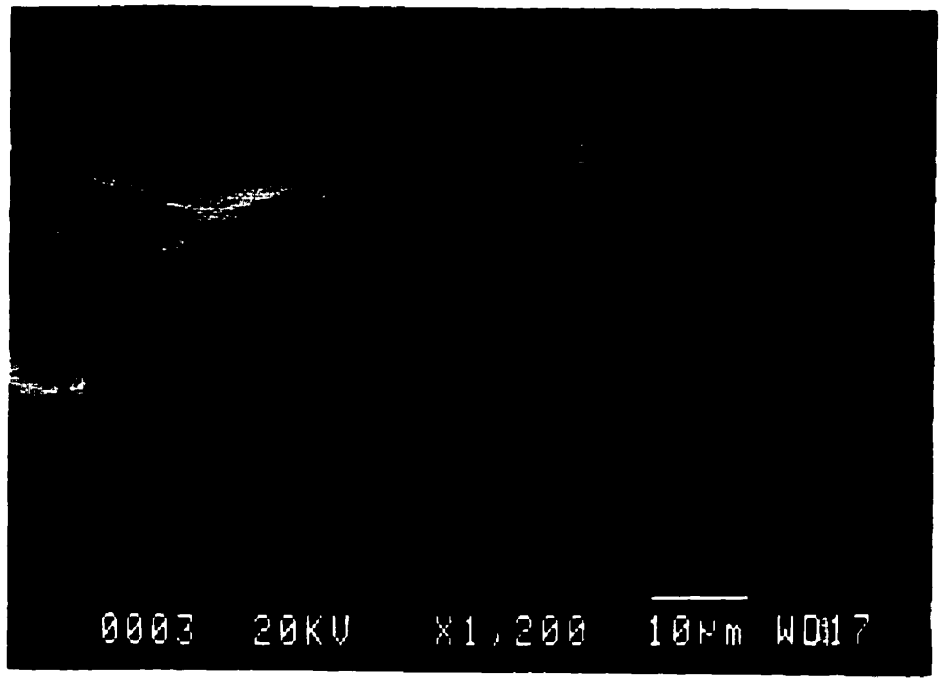

(b)

Fig. 5. 27 Longitudinal fracture cross section of the worn surface of Al-Si/SiC composite at a load of 7 kg. (a) Showing that plastic flow of matrix was impeded by the presence of SiC particles. (b) Showing fragmentation of the SiC particles and the features similar to those in (a).

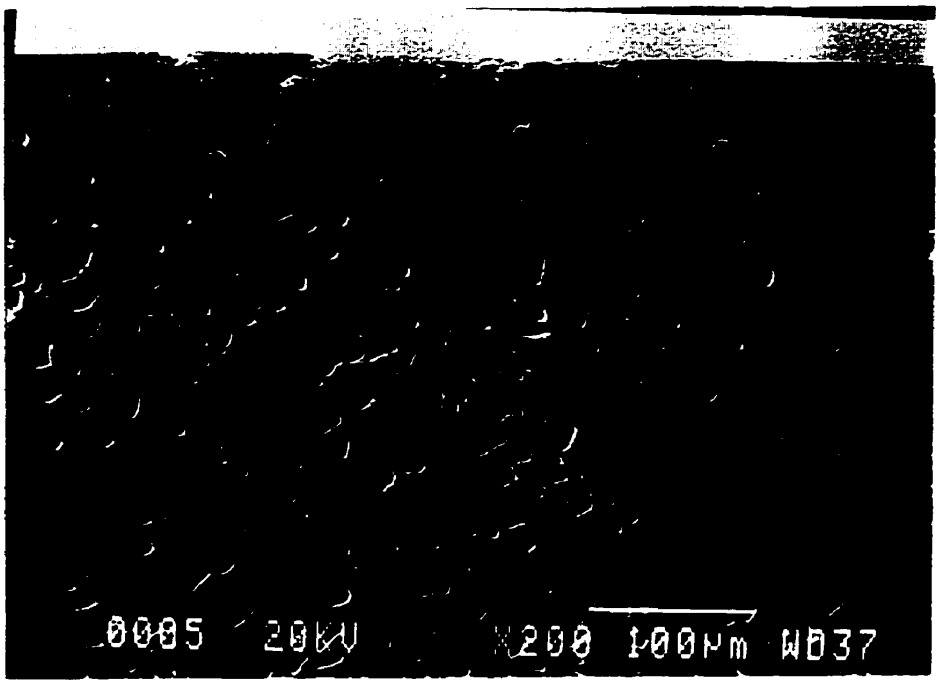

(a)

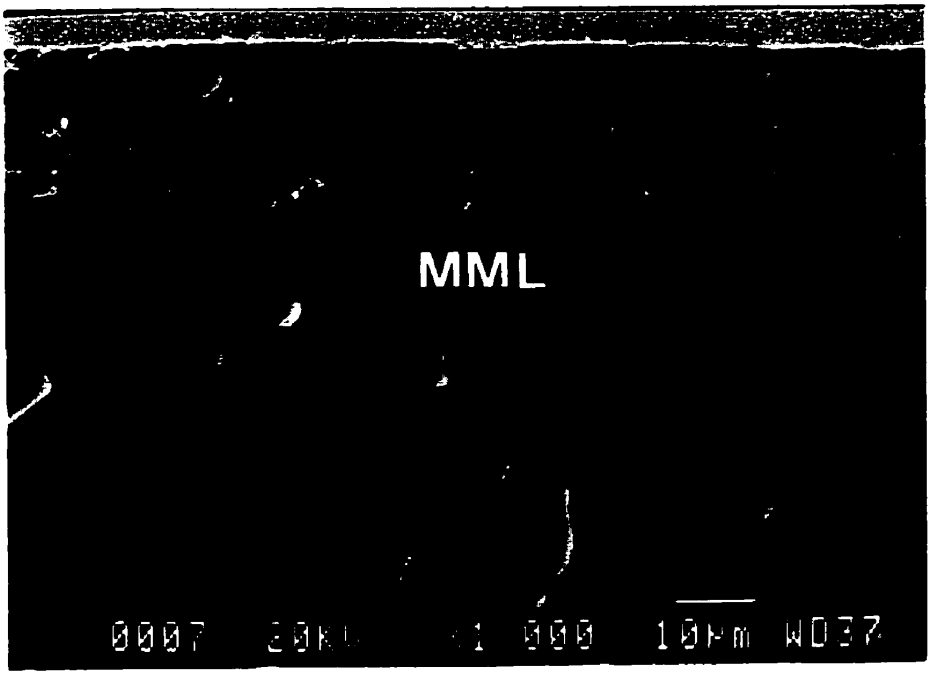

(b)

Fig. 5.28 *(continued)*

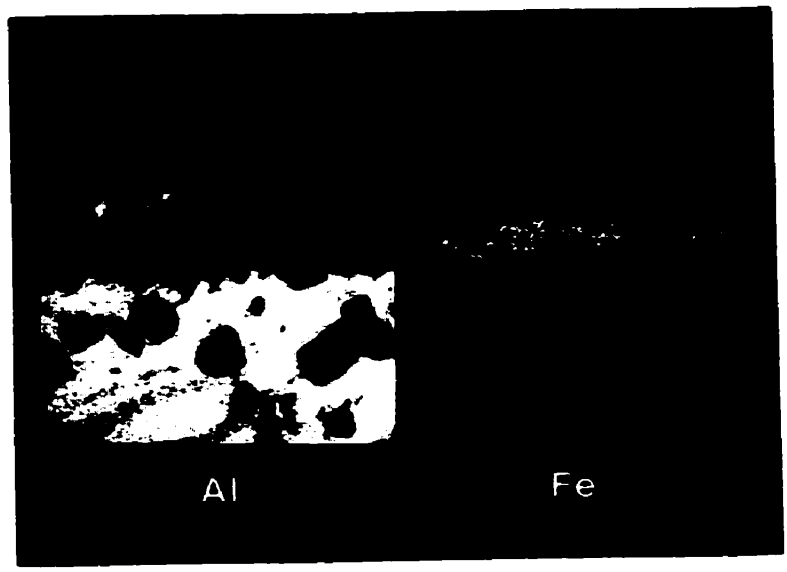

(c)

Fig. 5.28 Mechanically mixed layer in a longitudinal cross section of the worn surface of the Al-Si/SiC composite at a load of 10 kg.
(a) At a low magnification;
(b) At a high magnification;
(c) X-ray mapping corresponding to (b), showing Fe distribution in the MML.

(a)

(b)

Fig. 5. 29 A sandwich structure of the MML in a longitudinal cross section of the worn surface of the Al/SiC composite at a load of 10 kg, in which sublayers either rich in Fe or Al alternatively exist. SEM micrograph, and (b) X-ray mapping of worn surface showing Fe and Al distributions in the MML.

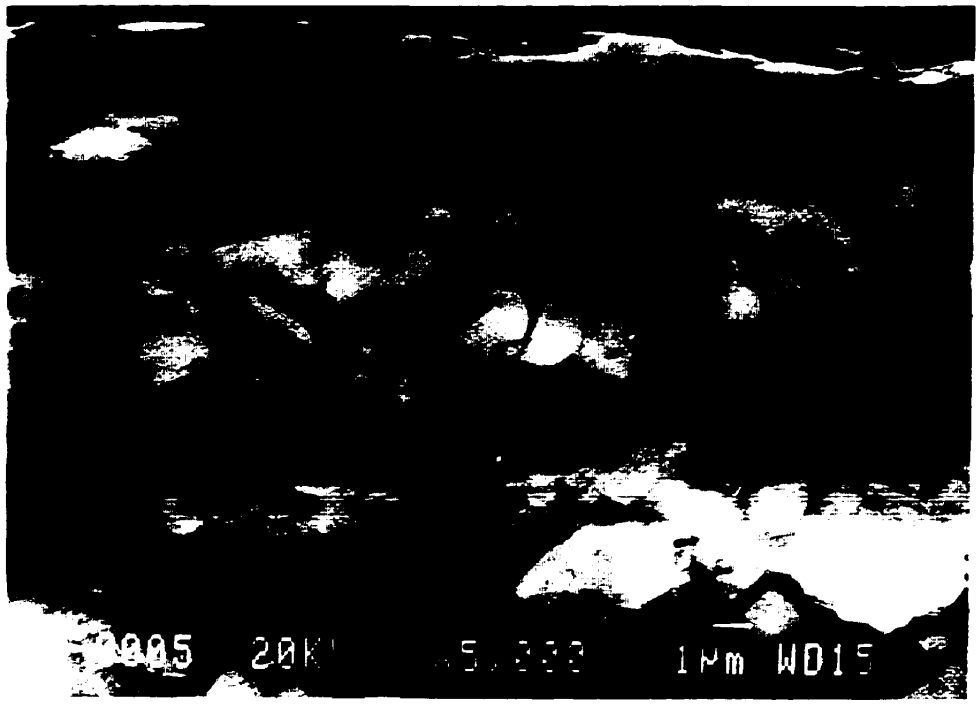

(a)

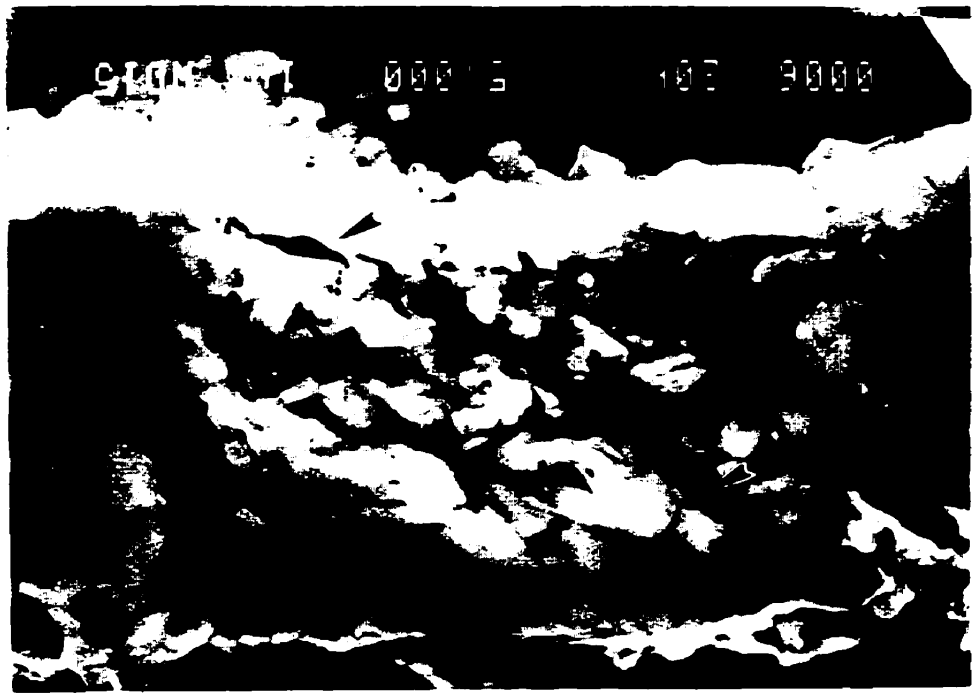

(b)

Fig. 5. 30 (a) The alternative sublayers in the MML of the worn surface of the Al/SiC composite at a higher magnification. (b) Microcracks in the MML as indicated by arrows.

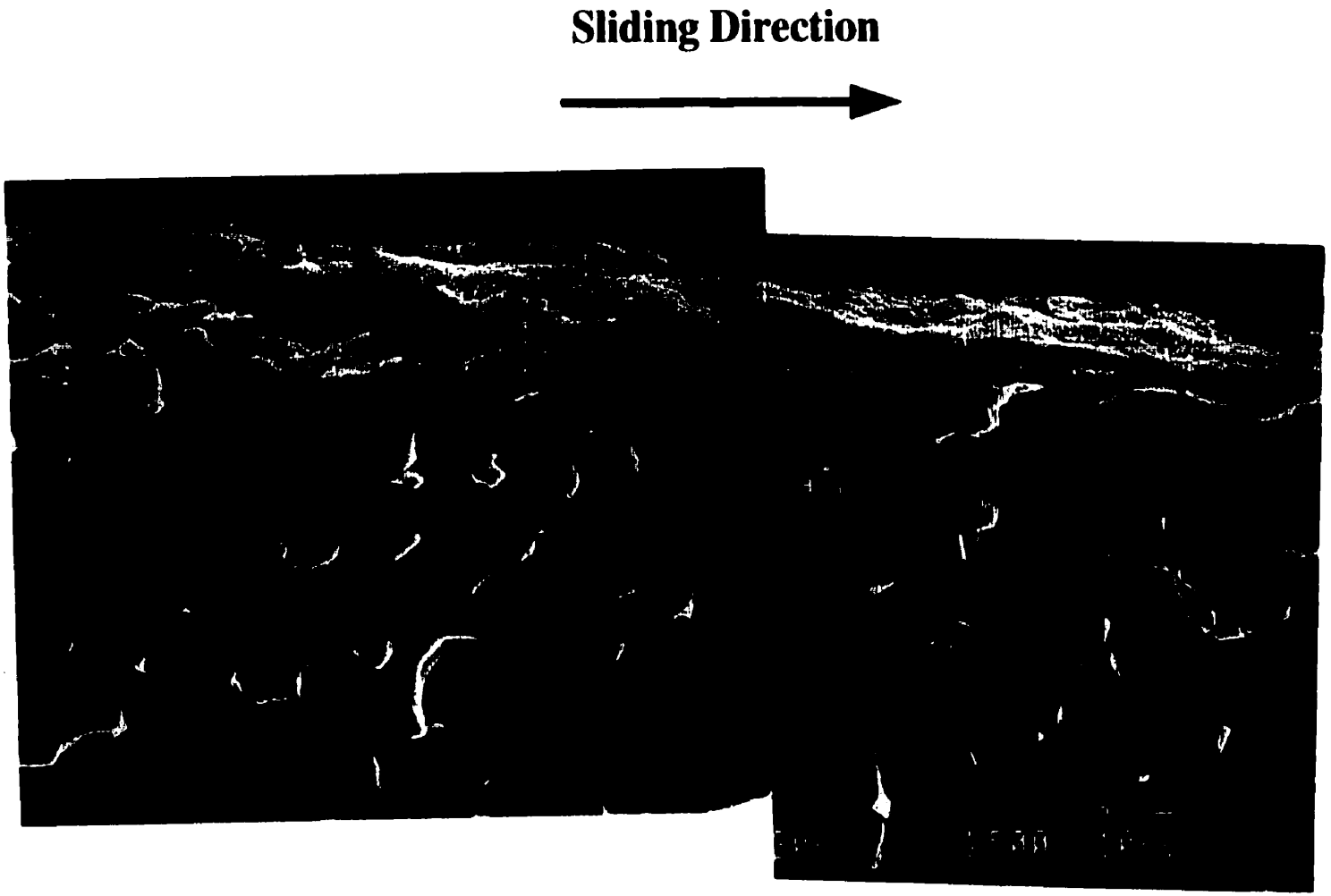

Fig. 5.31 Extensive subsurface cracks in the MML of the Al-Si/SiC composite at a load of 7 kg.

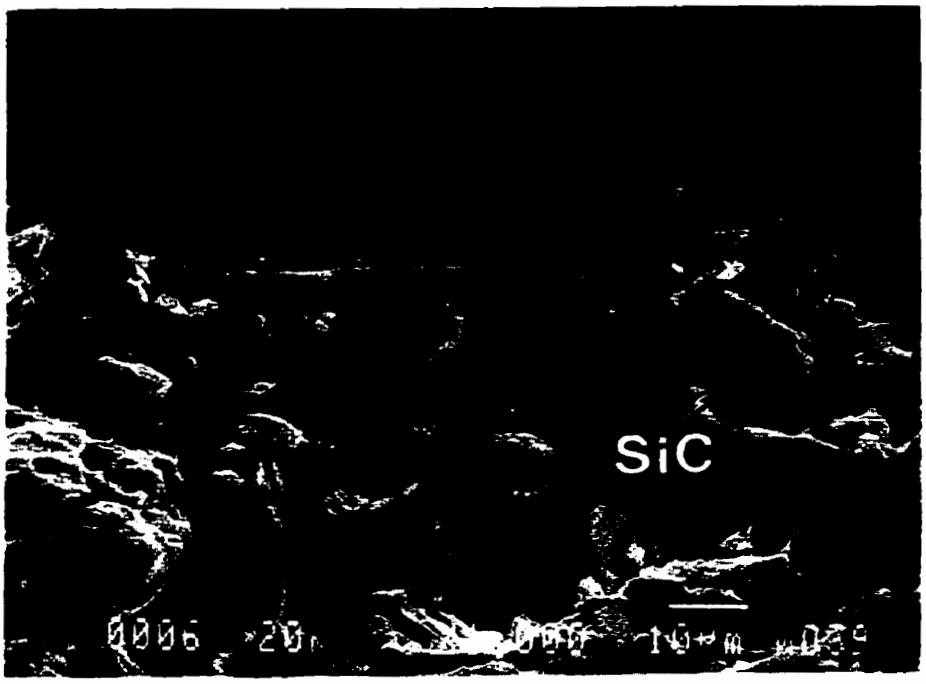

(a)

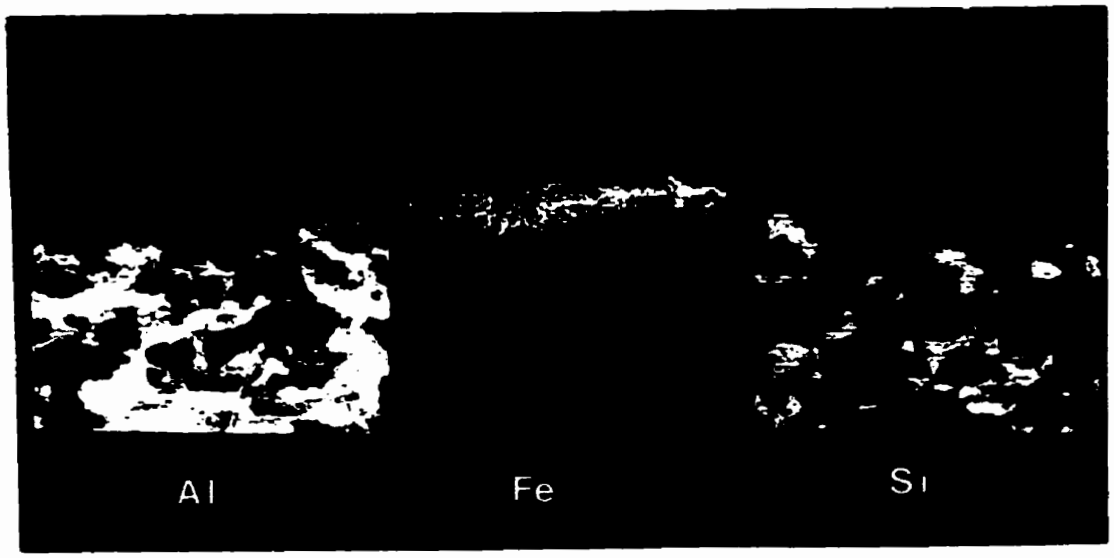

(b)

Fig. 5. 32 Transverse fracture cross-section of worn surface of Al-Si/SiC composite at a load of 7 kg, showing a layered structure in the MML and absence of SiC particles in the original size in the MML. (a) Micrograph, and (b) X-ray mapping in the cross section.

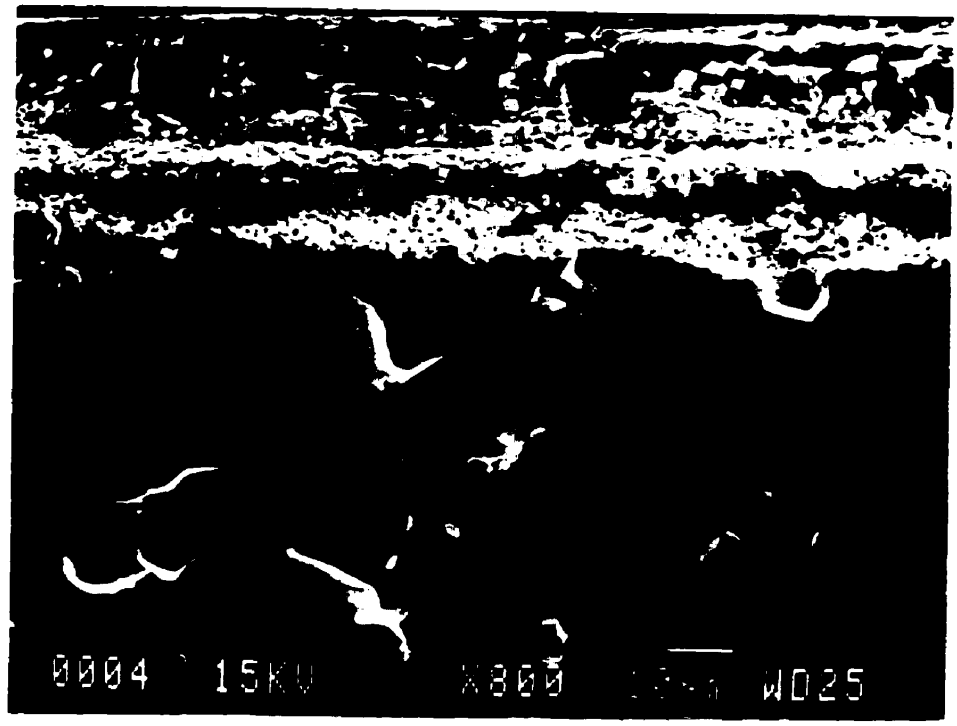

(a)

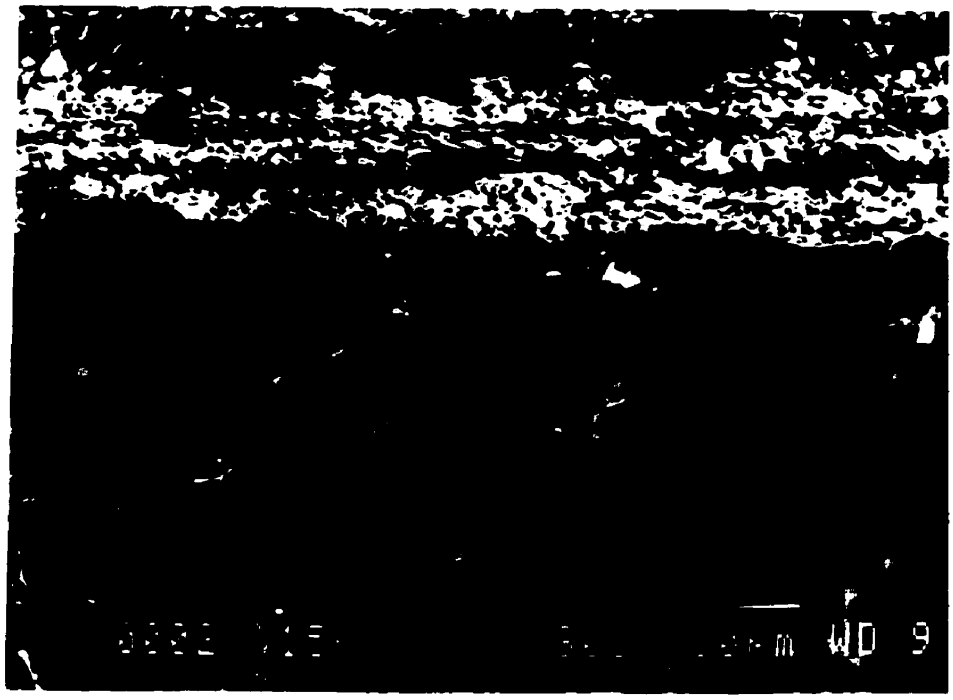

(b)

Fig. 5. 33 Mechanically mixed layer in a longitudinal cross section of worn surface of Al-Si/SiC composite. (a) Secondary electron image; and (b) backscattering electron image. Note that the cross section was polished using ion milling.

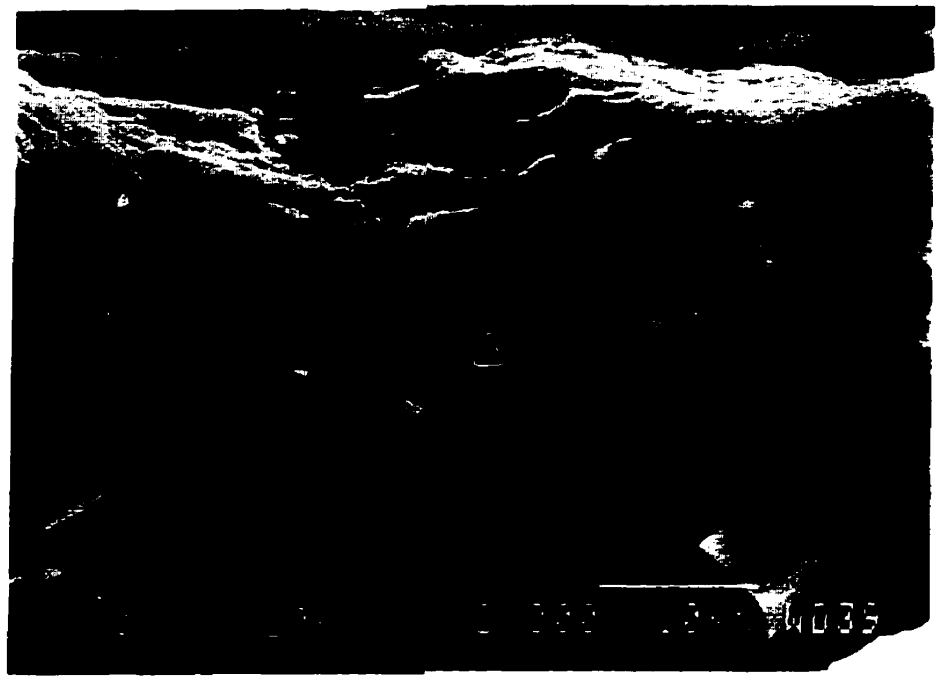

(a)

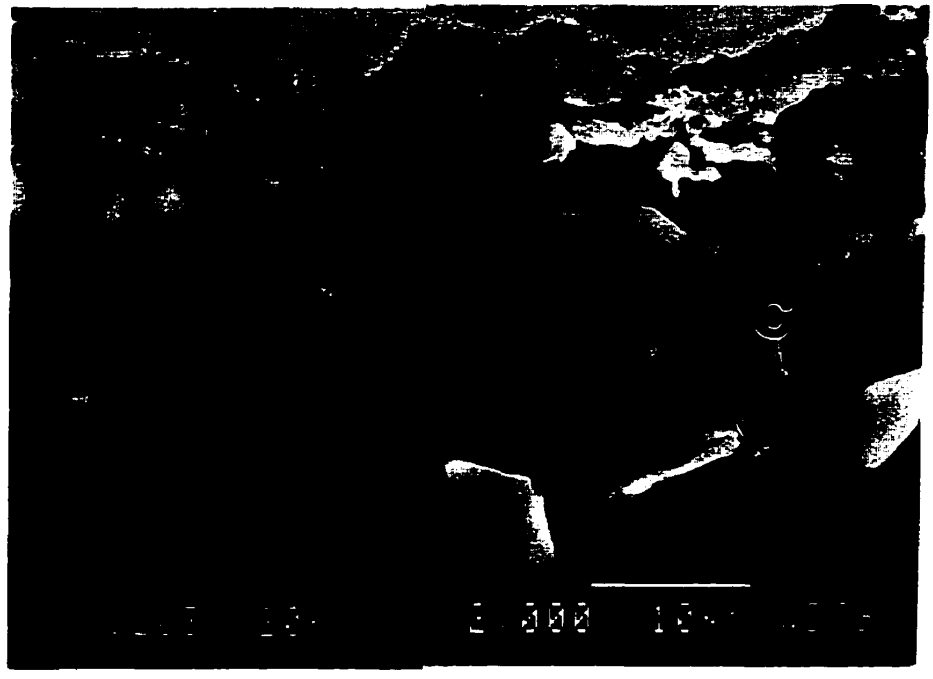

(b)

Fig. 5. 34 Fracture and fragmentation of SiC particles in the subsurface of the worn surface of the Al-Si/SiC composite at a load of 7 kg. (a) Cracking perpendicular and parallel to the sliding direction in the particle A and B, respectively; (b) Transparticle cracking of SiC. Particle C was broken into three parts as indicated by the arrow.

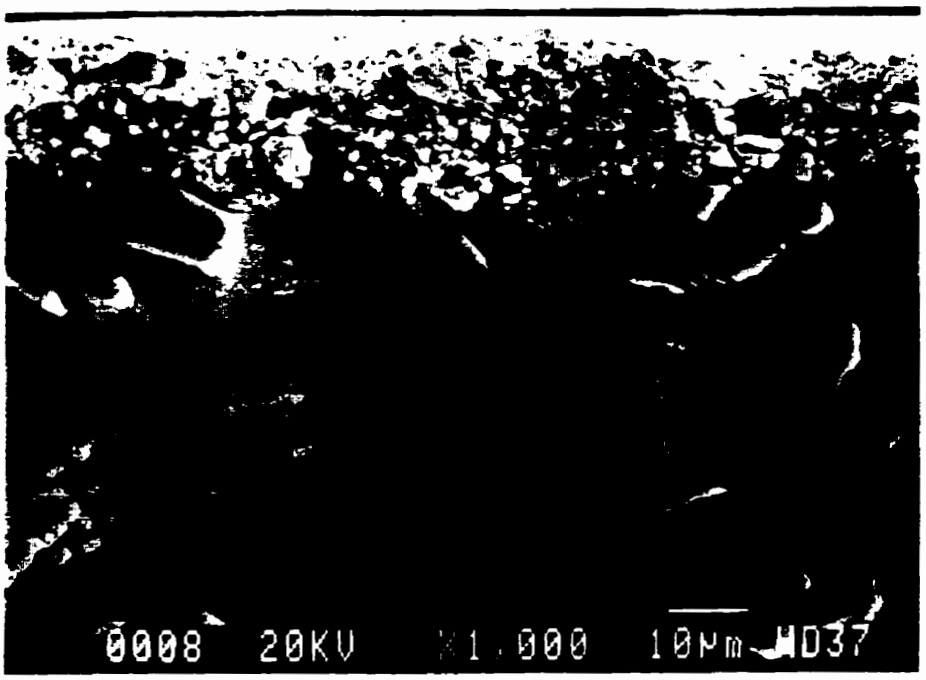

(a)

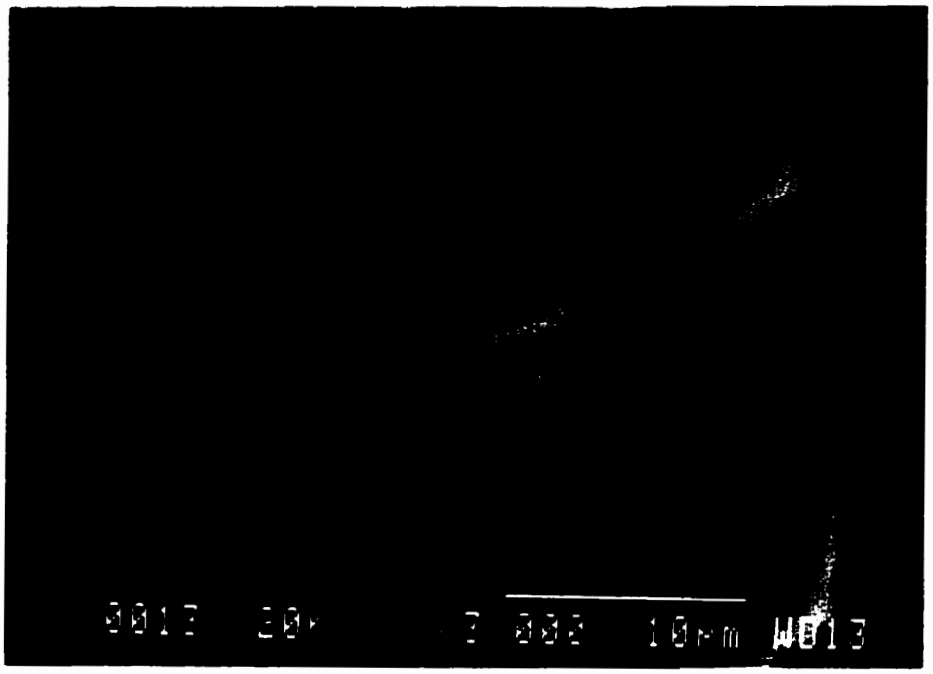

(b)

Fig. 5. 35 Fracture and fragmentation of SiC particles in the worn surface of Al-Si/SiC composite at a load of 10 kg. Particle A was fractured into five parts with microvoids in between the broken parts.

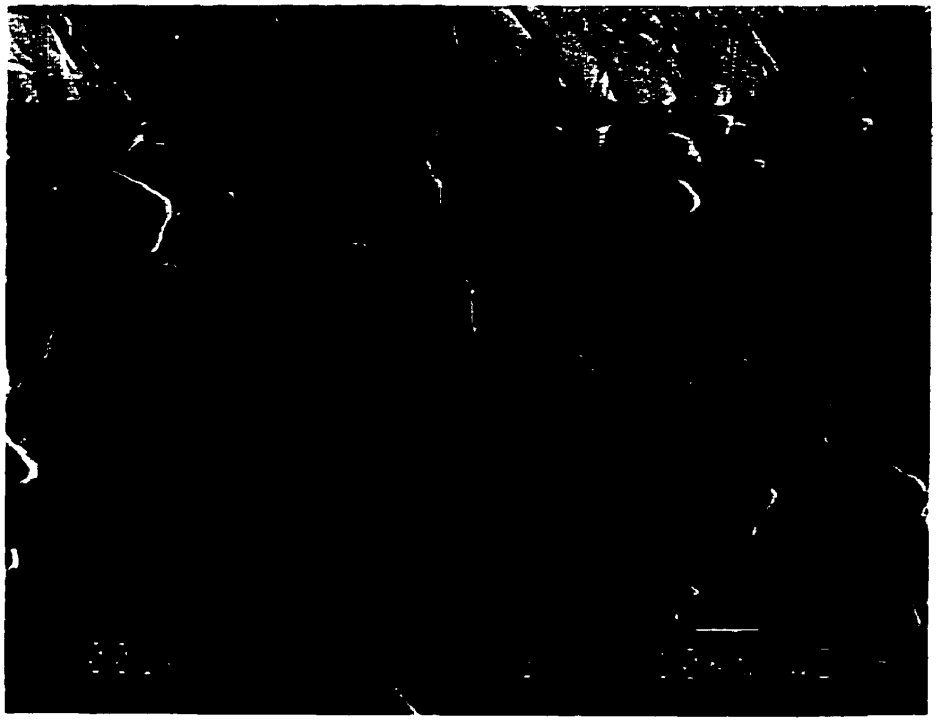

Fig. 5. 36 Longitudinal cross section of the worn surface of the Al-Si/SiC composite at a load of 5 kg, showing cracks grown between SiC particles.

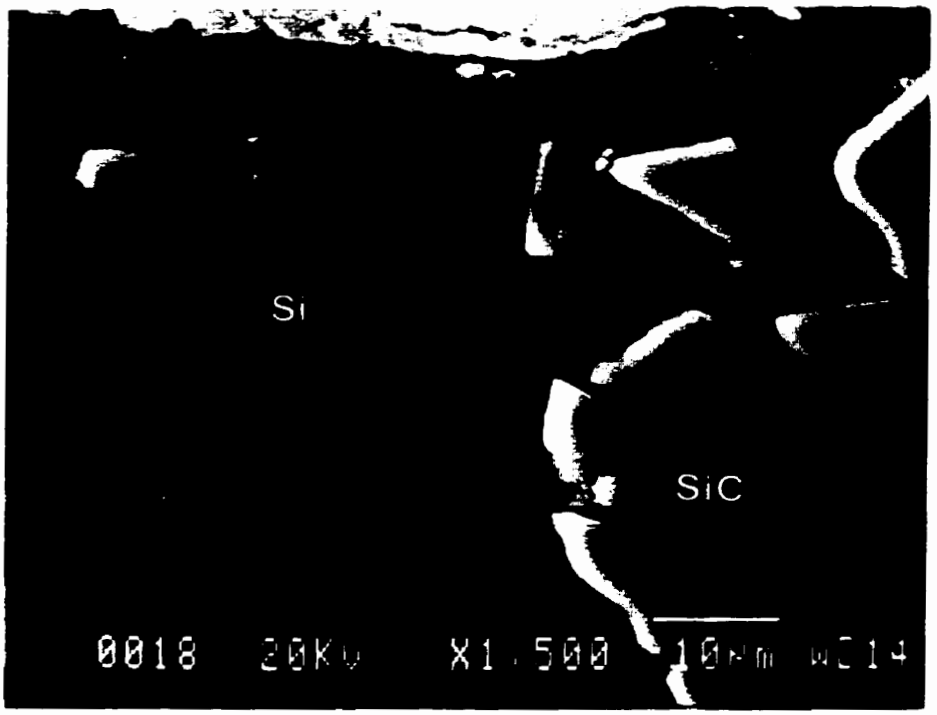

(a)

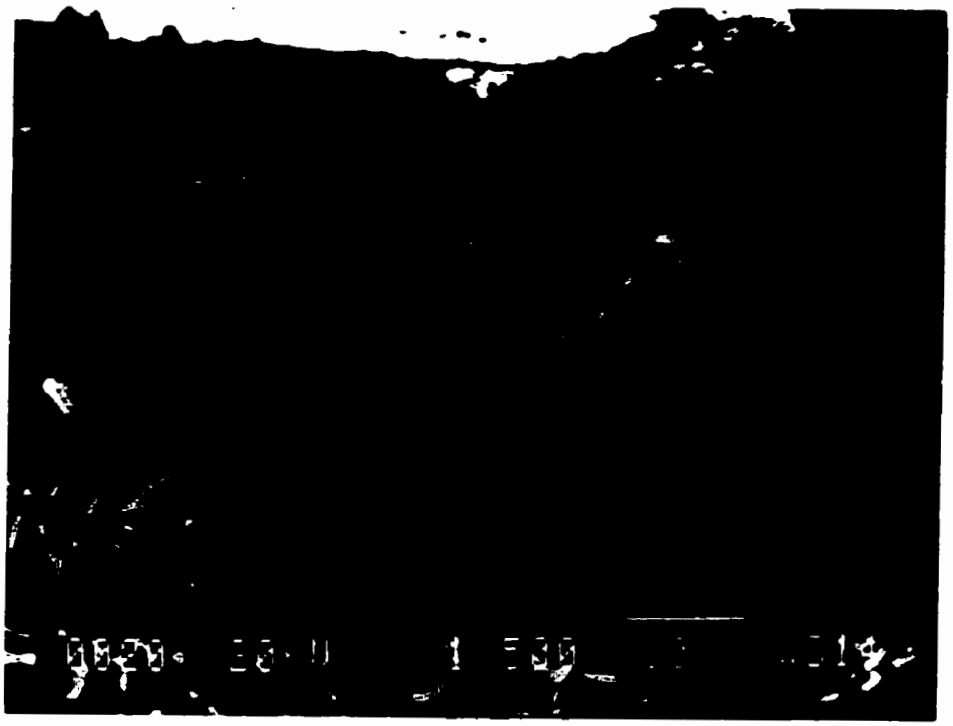

(b)

Fig. 5. 37 Fracture and fragmentation of eutectic Si particles in a transverse cross section of the worn surface of the Al-Si/SiC composite at a load of 7 kg. (a) Secondary electron image; and (b) backscattering electron image.

5. 5 MICROSTRUCTURAL CHARACTERIZATION OF THE WORN SURFACE — *Transmission Electron Microscopy Studies*

5.5.1 The high purity aluminum

Longitudinal cross sections of the worn surface of HP Al at a load of 5 kg were examined using TEM. Fig. 5.38 shows a TEM profile of the sample observed at low magnification, showing a part of the perforation of the thin foil just underneath the top worn surface. As discussed in the previous section of SEM results, the strain profile changes with the depth from the worn surface from low strains at a deeper depth to a severe strains in the subsurface adjacent to the worn surface. Therefore, the microstructural features of the worn surface of the HP Al are discussed here for low strained depths to the highly strained layers near the surface.

Fig. 5.39 shows a typical micrograph of the microstructure between positions A and B indicated in Fig. 5.38, i.e., at a depth of about 300 - 400 μm. It can be seen that dislocations became tangled and cells started to form. A number of individual dislocations can still be observed in the interior of the cells. However, the number of these dislocations in the interior of cells gradually decreased as the top near surface was approached, as shown in Fig. 5.40. The average size of the cells at these depths was about 2.0 μm to 3.0 μm.

With further approaching the top surface in the zone between positions B and C corresponding to Fig. 5. 38, i.e., at a depth of about 50 μm to 300 μm, as shown in Fig.

5.41 to Fig. 5.44, the cells became further refined and the number of dislocations in the interior of cells decreased in most of the cells, as some of arrays of dipoles developed to cell walls in the substructures (for example, dislocation arrangement as indicated in Fig. 5.41). The reduction of the number of dislocations inside the cells continued, and some of the cell walls were still quite thick and the spacing of dislocations in the cell walls decreased. The average size of the cells was about 1.5 μm to 2.0 μm, as can be seen from a low magnification micrograph in Fig. 5.44. At a depth less than 50 μm, the cells became somewhat sharp and started to get elongated, as shown in Fig. 5.45. Some of the cells started to develop very thin and line shaped boundaries, for example as indicated in Fig. 5.45. Near the top surface, the walls developed into elongated subgrains with an aspect ratio of about 1:4.

Very narrow band-like substructures were also noted near the worn surface. As can be seen in Fig. 5.46, the aspect ratio of the narrow band was quite large, and the thickness of the band was about 0.03 μm. These bands were similar to those found in the worn surface of an aluminum in a pin-on-disc wear test in vacuum by Kou and Rigney[4]. It is very likely that these bands were formed as a result of lower shear strength in comparison with stress intensity[4] and strain heterogeneity due to shear instability[128]. The shear bands, delineated by two sharp and parallel walls, oriented almost parallel to the sliding direction. Interestingly, it seemed that the shear bands run through the subgrains as shown in Fig. 5.46.

In summary, the microstructural evolution along the depth below the worn surface is very much similar to rolled materials [113] at high strains in which formation and development of cell structures are more pronounced according to work hardening theory[114].

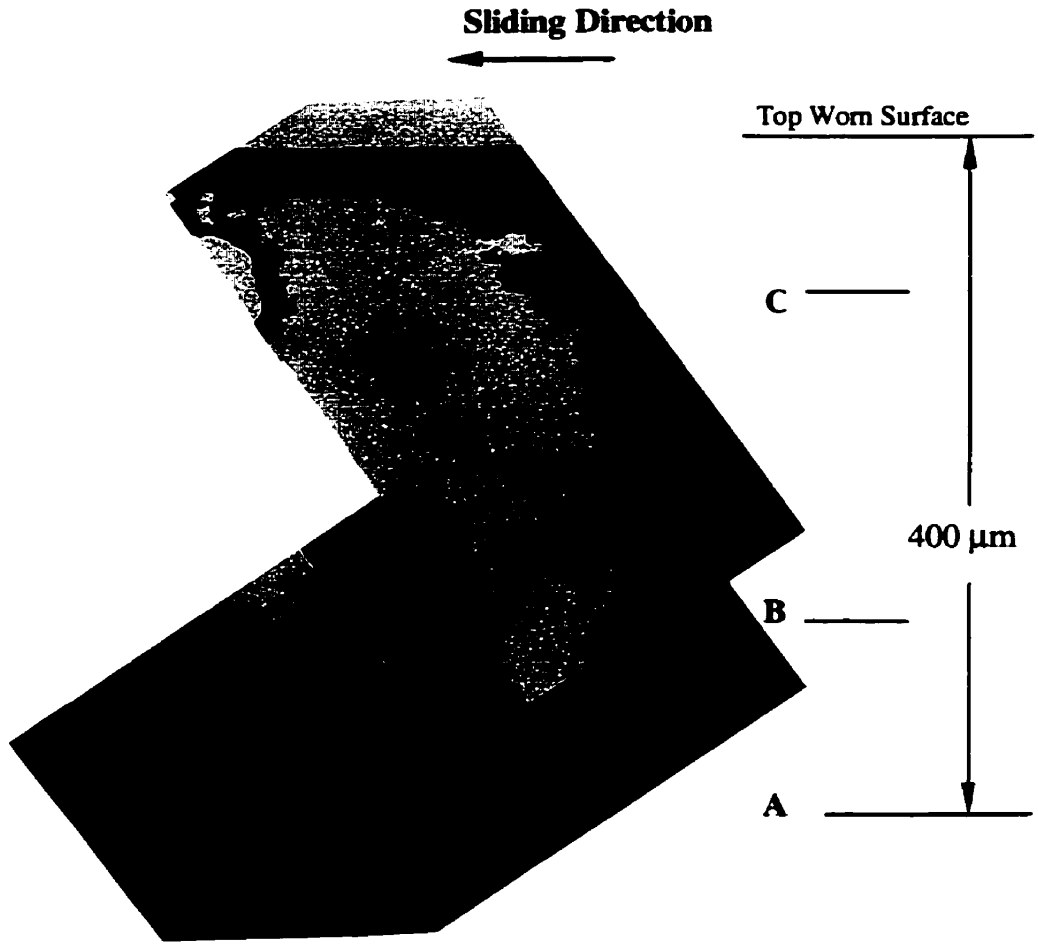

Fig. 5. 38 TEM profile of the longitudinal cross section specimen of HP Al worn surface, showing a partial perforation of the thin foil. Zone A, B, C will be discussed in following figures. See text for details.

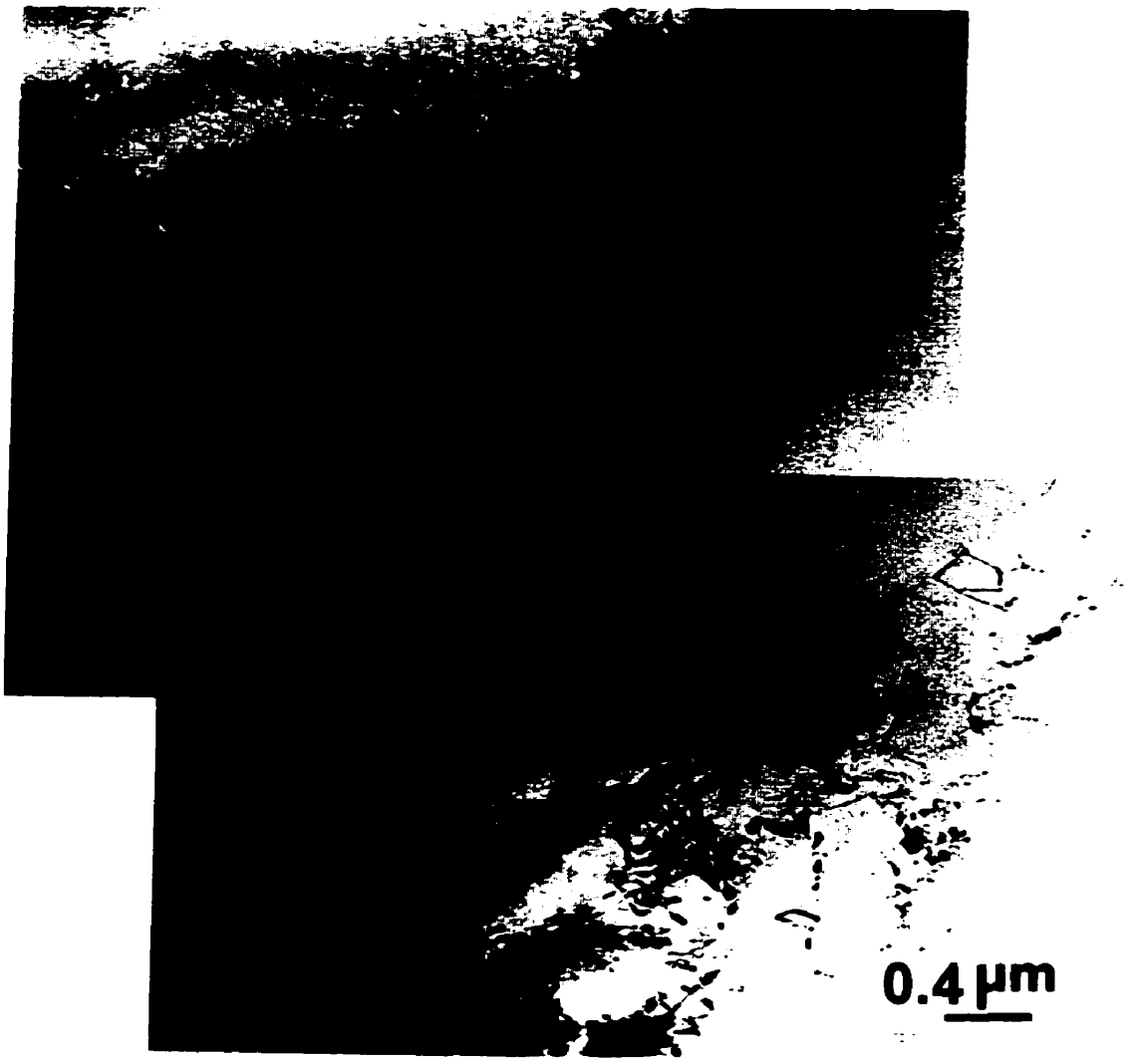

Fig. 5. 39 Microstructure of the worn surface of the HP Al at a depth of about 300-400 µm. (Zone between position A and position B). Sliding load: 5 kg.

Fig. 5. 40 Microstructure of the worn surface of the HP Al at a depth of about 300-400 µm, showing the cells with very few dislocations in the interior of the cells. Sliding load: 5 kg.

Fig. 5. 41 Microstructure of the worn surface of the HP Al at a depth of about 50-300 μm. (Zone between position B and position C). Note that arrays of dislocation dipoles developed into cell walls. Sliding load: 5 kg.

(a)

(b)

Fig. 5. 42 (a) and (b) Microstructures of the worn surface of the HP Al at a depth of about 50-300 μm, showing reduction of dislocation inside the cells, and presence of thick walls of cells. Sliding load: 5 kg.

Fig. 5. 43 Cell structures in the worn surface of the HP Al at a depth about 100 μm from the top surface.

Fig. 5. 44 Cell structures in the worn surface of the HP Al at a depth about 100 μm from the top surface. (Low magnification) Note that the average cell size was about 1.5 to 2 μm.

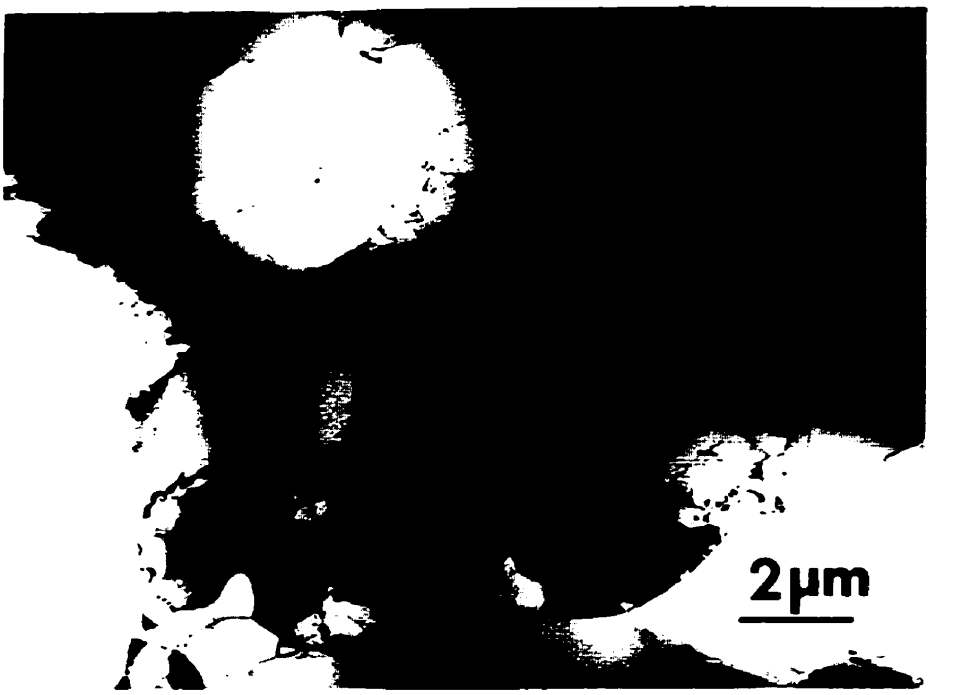

(a)

(b)

Fig. 5. 45 Subsurface structures in the worn surface of the HP Al at a depth less than 50 μm from the top surface, showing the cells started to get elongated, and that thin and line shaped boundaries formed as indicated by arrows.

(a)

(b)

Fig. 5. 46 Microbands in the near surface of the worn surface of the HP Al. The thickness of the microbands is about 0.03 μm. The tilting angle is about 10° between (a) and (b).

5.5.2 The Al-Si Alloy

Fig. 5.47 shows a panoramic view of a cross section of the worn surface of the Al-Si alloy (T6) at a load of 5 kg at a low magnification. It can be seen that the subsurface structures changed as a function of depth below the worn surface. At the very top worn surface, a mechanically mixed layer (MML) was present, which contains Fe transferred from the steel slider and will be separately discussed later. Just below the MML, a mixed structure of equiaxed and elongated subgrains was found. As indicated as Zone 1, which is about 4 to 8 μm below the top worn surface, equiaxed subgrains were present with an average size of 0.2 to 0.5 μm. At a depth of 10 to 20 μm below the worn surface, (Zone 2), the substructure transition to elongated subgrains was noted, and the aspect ratios of the elongated subgrains were about 5 to 10. In Zone 3 (about 30 μm below the top worn surface), it can be observed that the thickness of the elongated subgrains became large and so did the aspect ratio. Below this depth, the substructure transited into a poorly developed structure. Fig. 5.48 (a) to (c) shows the substructure at a higher magnification.

Careful examination of the subgrains, especially the equiaxed subgrains near the top worn surface indicated that the dislocation density in the interior of the subgrains was at a very low level. This is in agreement with other investigations involving the recovery and recrystallization of many deformed Al alloys[116-118]. In the present work, it was also found that in some subgrains there were still a considerable number of dislocations at the elongated structures, as shown in Fig. 5.48. More detailed dislocation structures in the interior of the subgrains are shown in Fig. 5.48 (b) and (c). This implies that the

subgrains might undergo further severe deformation during the recrystallization process, i.e., the recrystallization might be a dynamic process instead of a static one.

Influence of the eutectic Si particles was also noted in the subsurface in the cross section of the worn surface. Fig. 5.49 shows that the local plastic deformation in the matrix was controlled and obstructed by the presence of a Si particle, and the flow of the elongated subgrain structures was running around the Si particle. Some of the equiaxed subgrains with sharp boundaries could also be observed near the Si particle. In all the deformed zones below the worn surface, extensive fragmentation of Si particles was frequently observed, as shown in Fig. 5.50. The fracture locations were found to be associated with the sliding direction, suggesting that the fractures mainly resulted from the plastic deformation caused by the sliding wear. The fractures in these Si particles did not necessarily happen in association with the stacking faults although the stacking faults were observed very frequently in Si particles.

It is also of interest to note that fracture of the Si particles occurred coincidentally with fractures in the Al matrix, as can be seen in Figs. 5.51 and 5.52. This implies that the fracture of the Si particles could be a source of initiation of cracks in the matrix since Si particles were more brittle than the matrix. Similar to the observations by SEM, microvoids were also frequently observed between the Si particles and the matrix, as shown in Fig. 5.53. The microvoids could also be observed in Figs. 5.50 and 5.52. The microvoids could result from debonding at the interface between the Si particles and the matrix and from coalescence of cracks mentioned above during the further deformation generated by the sliding wear.

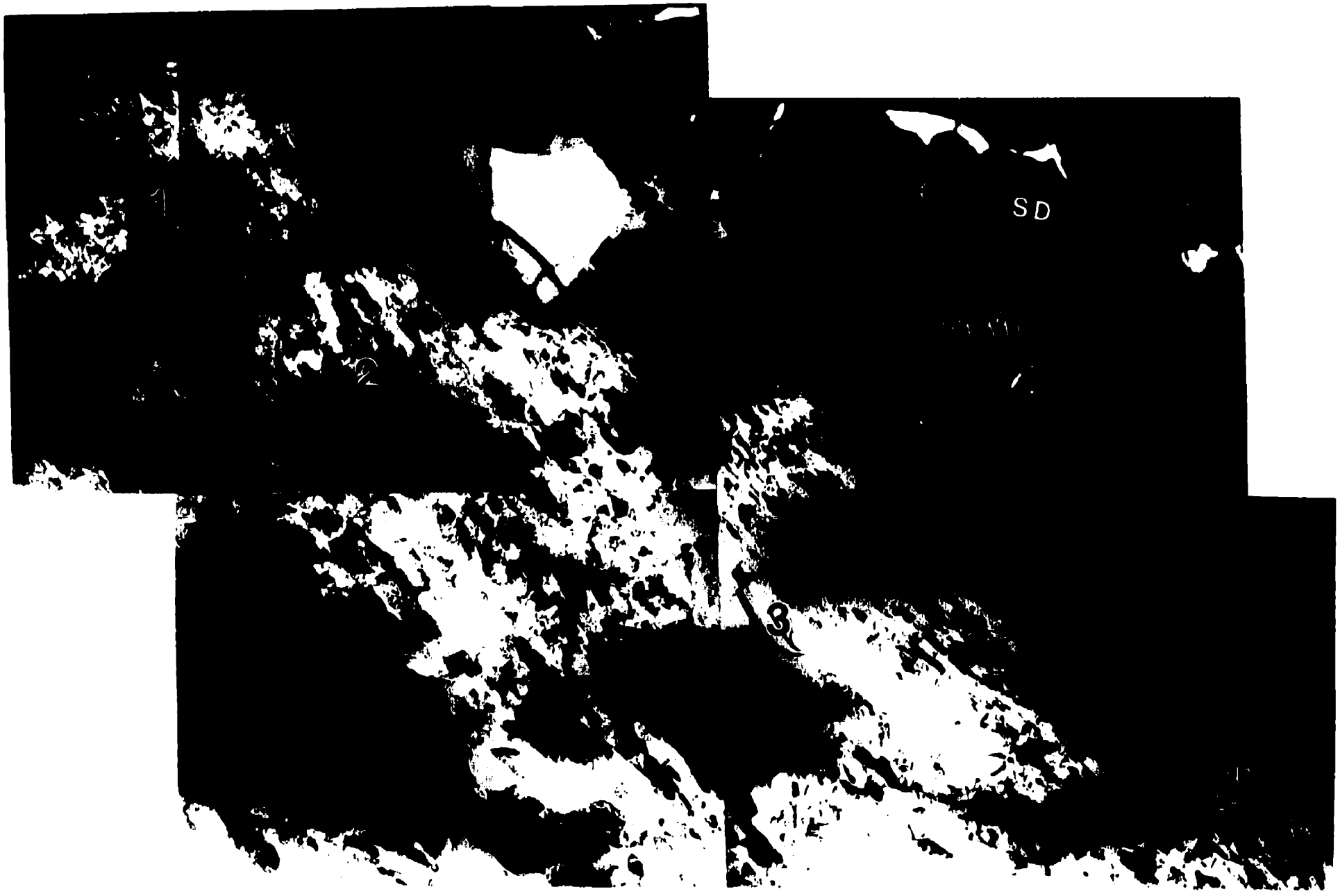

Fig. 5.47 Longitudinal cross section of worn surface of Al-Si alloy at a load of 5 kg. Zone 1, approx. 4 to 8 μm from the top surface; Zone 2, 10 to 20 μm; and Zone 3 approx. 30 μm. Note that voids occur in the MML.

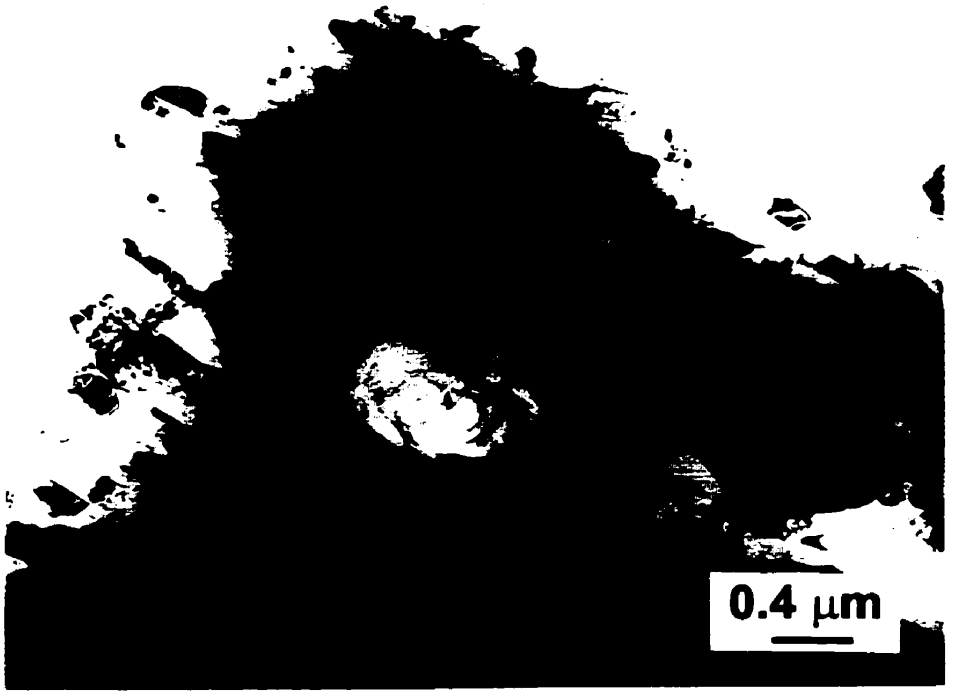

(a)

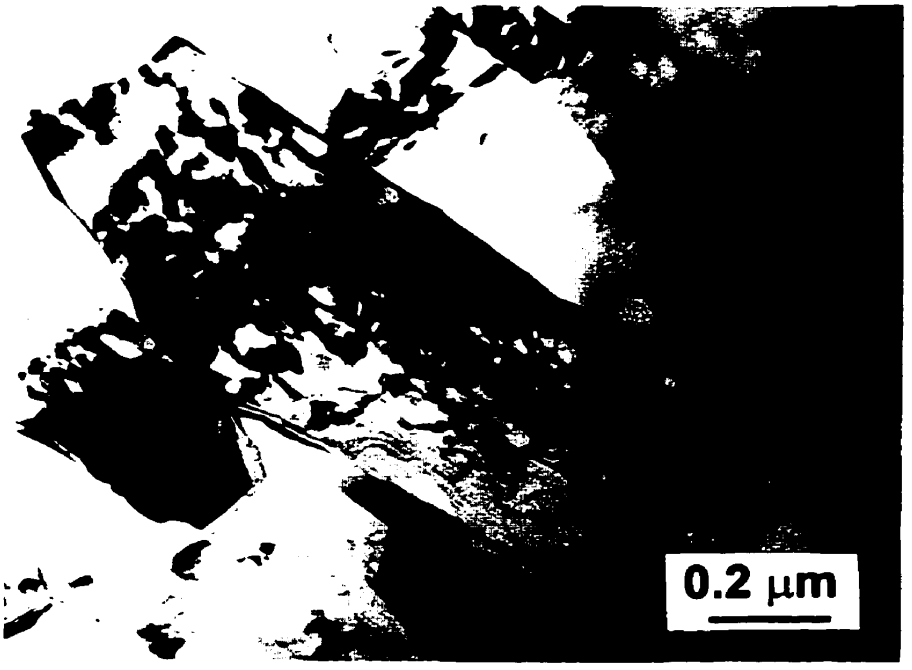

(b)

Fig. 5.48 *(continued)*

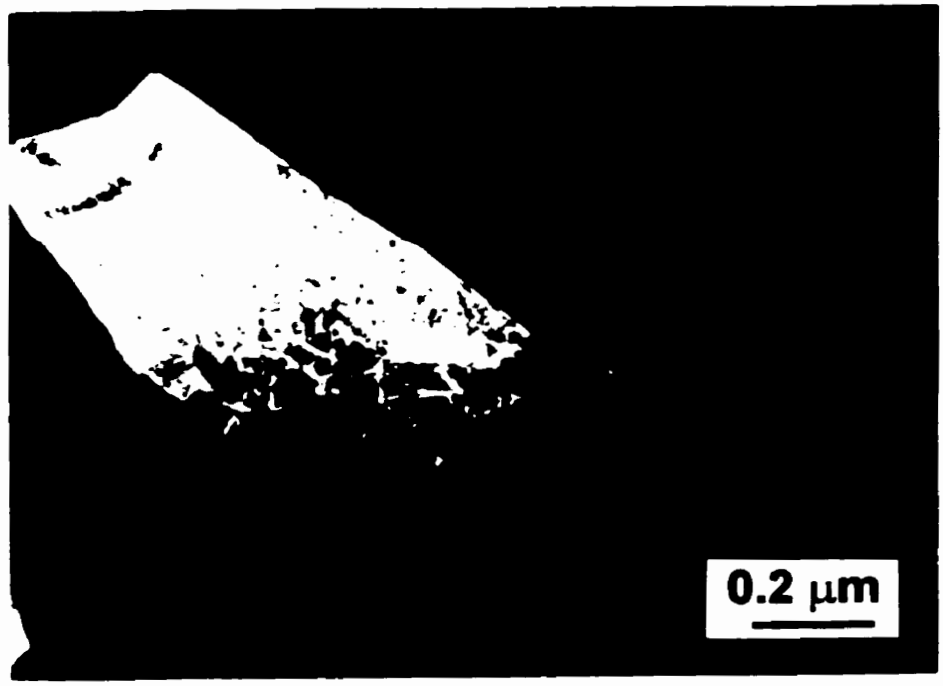

(c)

Fig. 5.48 Subsurface microstructure of worn surface of the Al-Si alloy (T6) at a load of 5 kg. (a) showing the elongated substructures, and dislocation structures within some subgrains. (b) Bright field image of dislocations in the elongated subgrains at a higher magnification. (c) Dark field image of dislocations in the elongated subgrains.

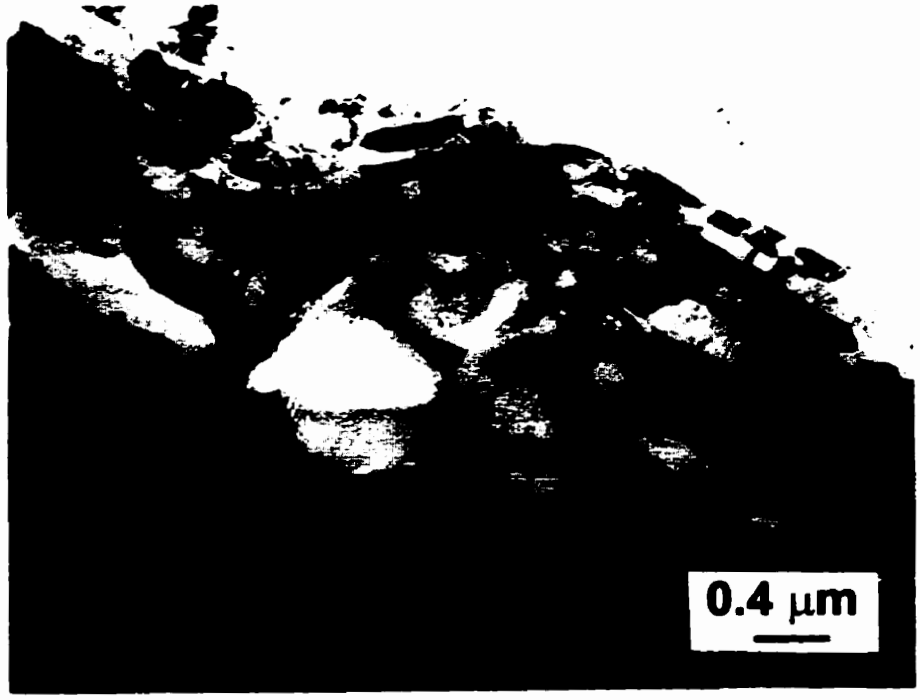

(a)

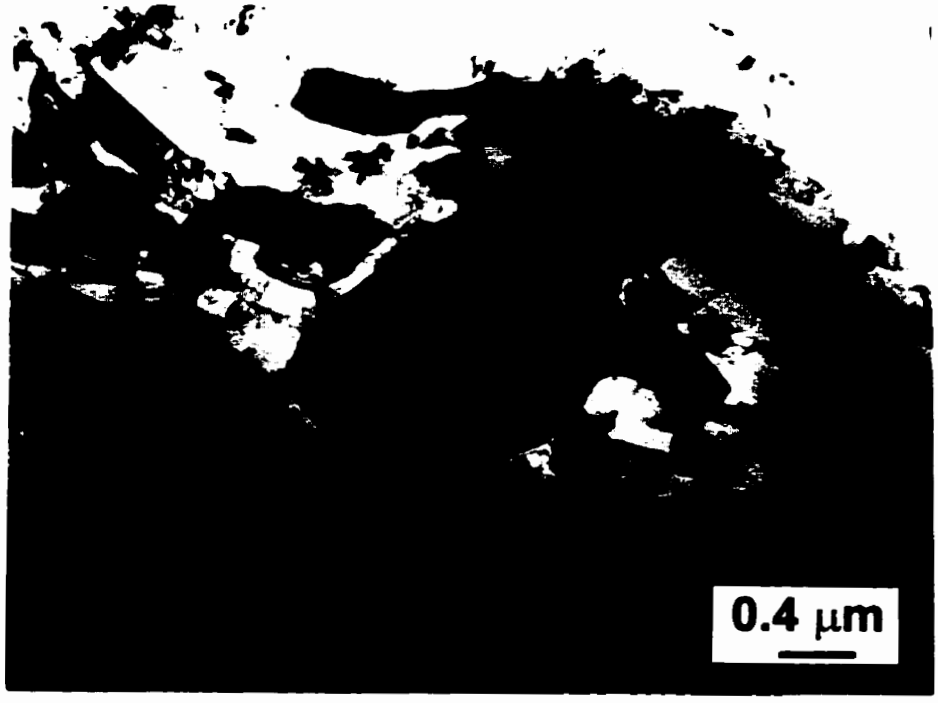

(b)

Fig. 5.49 (a) and (b) Extensive matrix flow of elongated subgrains were impeded by the presence of Si particles.

Fig. 5.50 Fracture of Si particles in the cross section of the worn surface of the Al-Si alloy. Note that the crack orients towards the sliding direction.

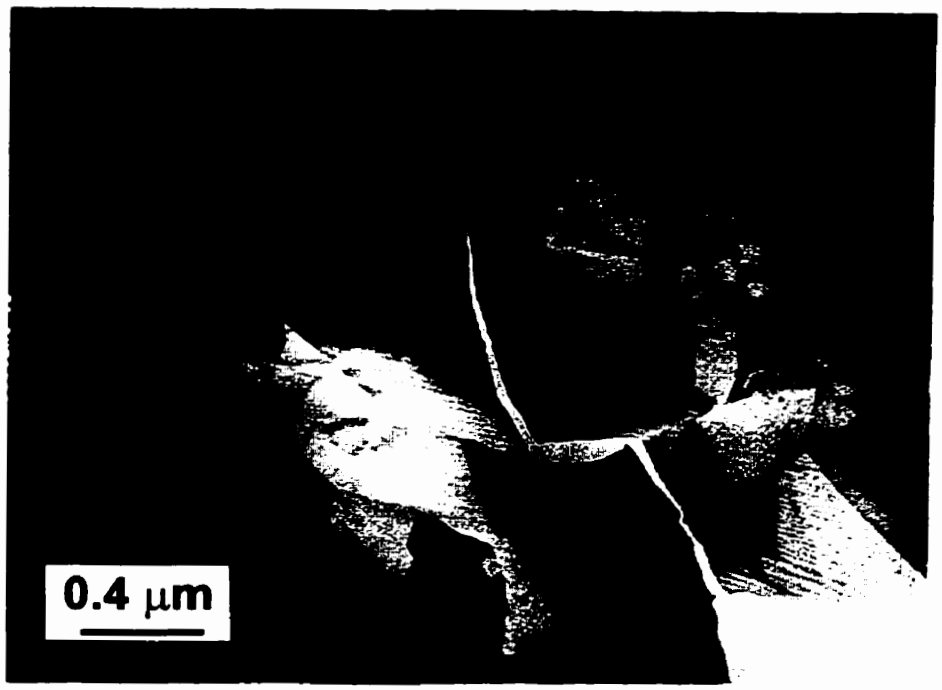

Fig. 5.51 A crack in the Al matrix is associated with the crack in the Si Particle in the subsurface of the worn surface of the Al-Si alloy.

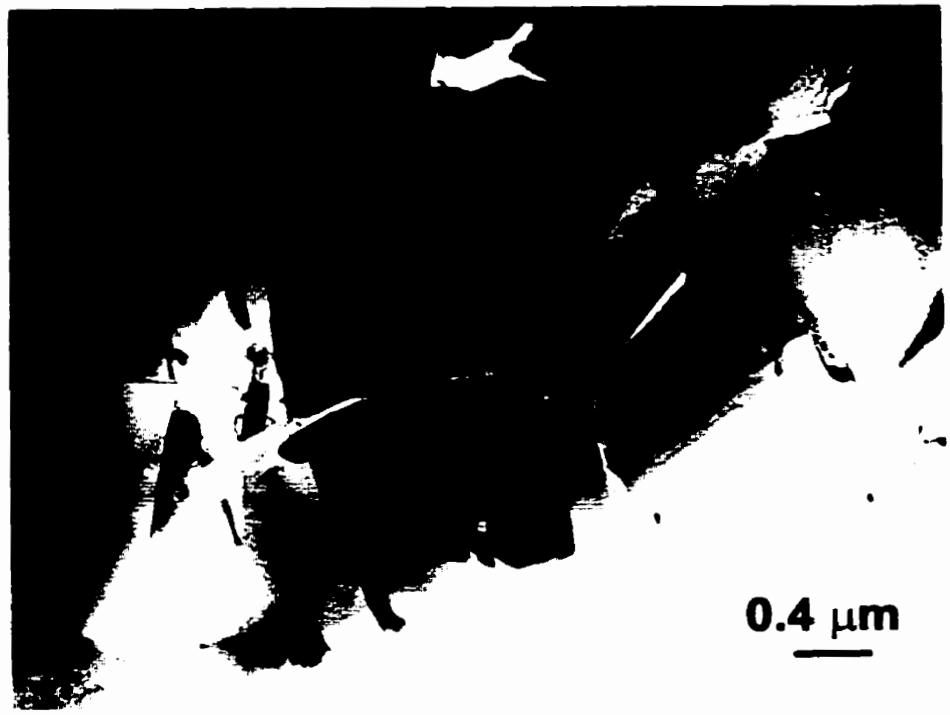

Fig. 5.52 Fracture of the Si particle leads to fracture in the matrix in the worn surface of the Al-Si alloy (T6).

Fig. 5.53 Microvoids were observed at the interface between the Si particles and the Al matrix.

5.5.3 The Al-Si/SiC Composite

5.5.3.1 Deformation substructures

A micrograph of TEM a specimen prepared in a manner that the TEM thin foil was parallel to the sliding wear surface shows the microstructure of the very top worn surface was mainly comprised of equiaxed subgrains in a size of about 0.05 to 0.1 μm, as shown in Fig. 5.54. Since the parallel specimen could not reveal the detailed information, longitudinal cross section TEM specimens were again used to investigate the microstructural evolution of the worn surface in the composites. Fig. 5.55 shows the changes in the subsurface microstructure as a function of depth below the worn surface at a load of 5 kg. It can be observed that the microstructural evolution of cell structures in the Al matrix was similar to that observed in the Al-Si alloy in terms of deformation generated during the sliding wear. In the near surface, equiaxed subgrains could be observed near SiC particles, and then a sharp transition to elongated subgrains occurred. It should be mentioned that the elongated subgrains were less well developed as compared to those observed in the unreinforced alloys, and high dislocation densities could be observed in the interiors of the subgrains. Fig. 5.56 shows a typical micrograph of the elongated subgrains in the worn surface of the reinforced composite at a high magnification. From a depth about 30 μm below the top worn surface, the cell structures were poorly developed, and actually they were still at incipient stage, as can be seen in Fig. 5.55.

It was found that the deformation substructures of the worn surface were similar at loads of 5 kg and 10 kg, and the deformation depth at the load of 10 kg was significantly bigger than that at 5 kg. The subsurface microstructure at a depth of about 60 μm at a load of 10 kg is shown in Fig. 5. 57. It can be seen that there was a high density of dislocations in the cell structures, some of which started to get elongated. By tilting the thin foil in the TEM, a subboundary could be observed when the foil was tilted about 5° from Fig. 5.57 (b) to (c). The dislocation arrays on the sub-grain boundaries imply that the dislocations had undergone a rearrangement. Some dislocation loops could also be observed in the cell structures with a high density of dislocations in the interiors. These phenomena suggest that the deformation was most likely taking place at a relatively high temperature. Fig. 5.58 shows another example of the dislocation structures in the subsurface of the worn surface. With an increase in the strain level approaching the top surface, the number of dislocations in the interior decreased and the cell walls of the subgrains were sharp and became elongated subgrains, as shown in Fig. 5. 59. The orientation between the elongated subgrains seemed to be larger.

The elongated subgrains were oriented conforming to the shape of the SiC particle, as shown in Fig. 5.60 and 5.61. It is obvious that the direction of the elongated substructure flow in the matrix was imposed to change by the presence of the SiC particle. It can be seen that the elongated subgrains gradually turned the flow direction until the direction was almost vertical to the original direction, Fig. 5. 61. The aspect ratio of the subgrains seemed to decrease probably because of dynamic recrystallization within the stress field of the SiC particle.

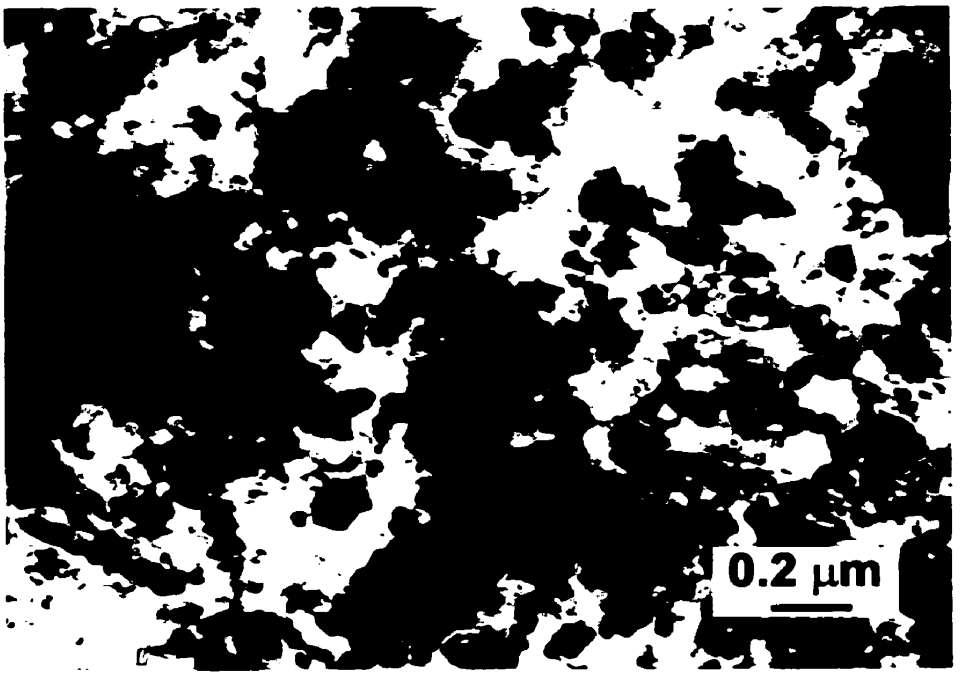

Fig. 5.54 Microstructure of the worn surface in the extreme worn surface of the Al-Si/SiC composite (as-cast) at a load of 10 kg. The thin foil was prepared parallel to the worn surface.

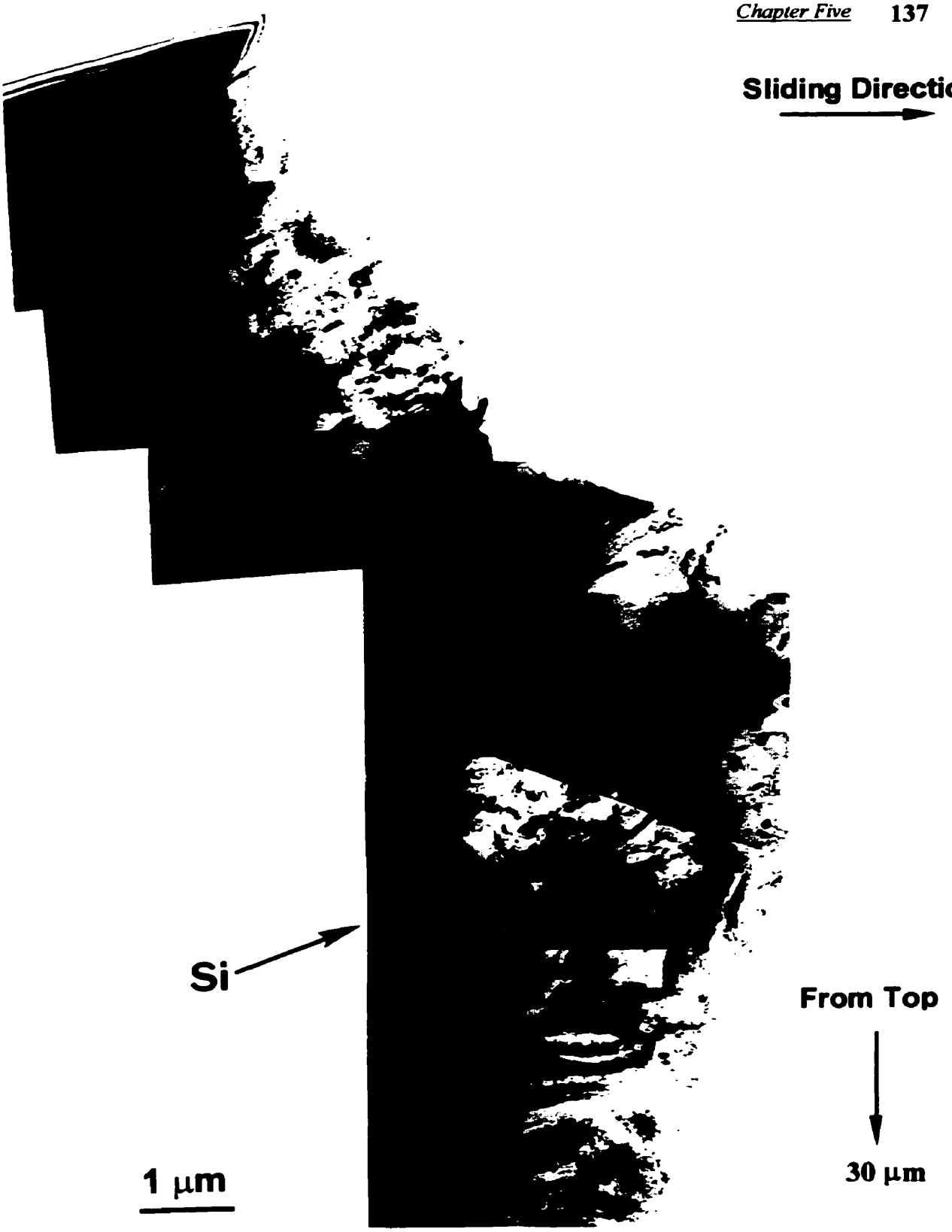

Fig. 5.55 Subsurface microstructure changes as a function of depth below the worn surface in a longitudinal cross section of the Al composite at a load of 5 kg. Note the microstructure transition from elongated subgrains to a structure that contains incipient cells.

Fig. 5.56 Subsurface microstructure of elongated subgrains in the worn surface of the Al-Si/SiC composite (as-cast) at a load of 5 kg.

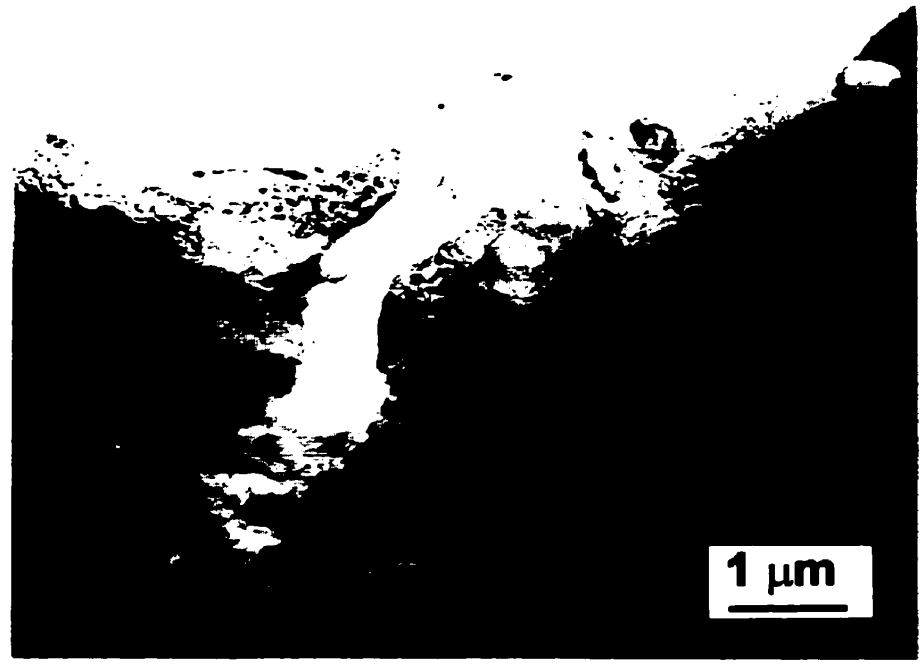

(a)

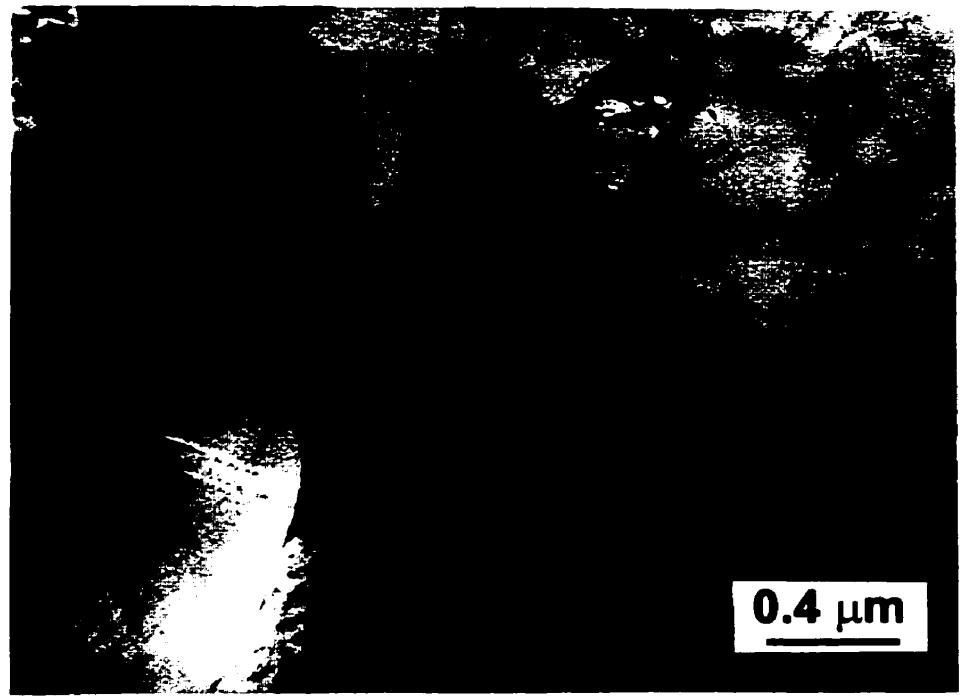

(b)

Fig. 5.57 Subsurface microstructure in a longitudinal cross section 60 μm below the worn surface of the Al composite (as-cast) at a load of 10 kg. (a) at a low magnification (b) high magnification. *(continued)*

(c)

(d)

Fig. 5.57 Subsurface microstructure in the cross section about 60 μm below the worn surface of the Al composite (as-cast) at a load of 10 kg. (c) Bright field image that was tiled about 5° from (b); (d) Weak beam dark field from (c).

5.5.3.2 In-situ precipitation during the sliding wear

It was found that fine precipitates were present in the subsurface below the worn surface of the as cast composites which were originally precipitate free before the sliding wear. This finding of in-situ precipitation was noted to occur at high loads (> 5 kg). The microstructure in the subsurface about 60-70 μm below the top worn surface at 5 kg is shown in Fig. 5. 62. It can be seen that dislocations with high density were tangled, and cells started to form. Careful examination indicated that a large number of needle-like precipitates occurred in the matrix. Figs. 5.63 and 5.64 show the subsurface microstructures of the worn surface at a high magnification. It is seen that the cells oriented towards the sliding direction. By using two-diffraction-beam technique in the TEM, images of the dislocations and the precipitates could be clearly observed in the weak beam dark fields, as shown in the figures. The electron diffraction pattern, for example, using the two-beam diffraction as shown in the insert in Fig. 5.63, confirms the presence of the precipitates. At this depth, it can be seen that the size of the precipitates is approximately 80 nm in length. The orientations of the needle-like precipitates were in agreement with those found in the literature[111, 112] i.e., parallel to $<001>_{Matrix}$ directions, as shown in Figs. 5.63 and 5.64.

At the depth about 40 to 50 μm below the worn surface, a large number of coarse precipitates were present, coexisting with highly dense dislocations in the matrix. The thick straight parallel line images, for example as shown in the upper left side in Fig. 5. 62, were identified as coarse precipitates. In addition to the presence of fine precipitates mentioned above, rod -shaped particles were noticeably observed in the subsurface and their size was comparatively larger than that of the precipitates in T6 treated composite as shown in Fig. 5.5 in Section 5.2.2. Figs. 5.65 (a) and (b) show the subsurface

microstructures at the depth of approximately 40 μm below the worn surface. On the zone axis of <101> of the matrix (the foil was approximately {101}), the precipitates were observed to be lying on the directions of [010] and $[\bar{1}01]$, respectively. It was noted that the precipitates were frequently decorated with dislocations, which can be seen more clearly using weak beam dark field as shown in Fig. 5. 65(b). As can also be observed, a large number of dislocation loops were present in the subsurface, implying that the local temperature was considerably high during the process. In order to understand the mechanisms responsible for the substructure and interaction of strain fields of the precipitates and matrix in the worn surface, further study of the nature of the precipitates and dislocations in the subsurface was conducted.

Figs. 5.66 to Fig. 5.72. show the nature of coarse precipitates at high magnifications using different operation vectors $\bar{g}$. It seems that the precipitates were not coherent with the matrix and misfit dislocations were present in the interface between the precipitates and the matrix. By using different operation reflection $\bar{g}$ at "two diffraction beam" conditions, the interface structures could be observed clearly. Dislocation lines were found to be along and parallel to the lath-like precipitates. Almost vertical to the lath-like precipitates, rod-shaped precipitates were found to be accompanied with misfit interfacial dislocations. By tilting the thin foils and using invisibility criterion of dislocations, the nature of the dislocations was determined, as shown in Figs. 5.66 to Fig. 5.72. It can be seen that the dislocations along the sides of the rod precipitates were invisible when the operation $\bar{g} = [1\,\bar{1}\,\bar{1}]$ and $[\bar{1}\,\bar{1}\,1]$ at zone axis B=[101], Figs. 5.66 and 5.67, respectively. Fig. 5.68 shows another example of the invisibility of the dislocations at $\bar{g} = [\bar{1}\,\bar{1}\,1]$, with the foil being tilted to zone axis B=[112]. At $\bar{g} = [0\bar{2}0]$ and $[\bar{2}20]$, the dislocations along the sides of the rod precipitates were visible. Fig. 5.69 to Fig. 5.71 demonstrate the images of the dislocations at $\bar{g} = [0\bar{2}0]$ with different zone axis, and Fig.

5.72 shows the dislocation structures at $\bar{g}$ = [$\bar{2}$20], B=[112]. As a result, the Burgers vector of the dislocations should be $\frac{a}{2}$[101] according to the invisibility criterion. These dislocations therefore have the nature of edge dislocations since they lie in the direction of [$\bar{1}$01], perpendicular to their Burgers vector. It can also be observed that by tilting the foil, interfacial structures of the precipitates, for example, Moire patterns, were present because of the misfit between the precipitates and the matrix. As shown in Fig. 5.73, closely spaced dislocation loops were found along the length of the precipitates, indicating the interaction between the strain field of the dislocations and the elastic strain field of the precipitates. These phenomena are similar to those found by Weatherly and Nicholson[113] in Al-Cu-Mg alloys which were simultaneously aged and plastically deformed under creep conditions. According to them[113], during the coarsening of precipitates under creep conditions, dislocations initially climb to the particles, and lie along the interface of the particles or loop around the particles. The dislocations then break up to form prismatic loops. In the present wear process, a similar mechanism of dislocation climb could also be responsible for the formation of the interfacial structures, due to the heavy plastic strain in association with the frictional heating.

On the other hand, the initial nucleation and formation of the precipitates could also occure at dislocations [118]. It was observed that the rod precipitates were frequently decorated by dislocations. Fig. 5.74 shows the precipitates along the dislocation lines when the above foil was tilted to zone axis of [001]. It is shown that the images of the precipitates changed into equiaxed particles, showing end-on images. The end-on images of the precipitates, in turn, confirm that the precipitates lay on the planes of (100) or (010). The presence of the precipitates preferably at the dislocation networks becomes evident as shown in Fig. 5.75. This is not surprising, and the phenomenon that dislocations in the matrix serve as nucleation sites for strengthening precipitates have

been reported in the studies on strengthening mechanisms of composite materials [118, 119]. The higher dislocation density in the worn surface of the composite generated during the sliding wear would provide many preferential nucleation sites for precipitates as the strain field associated with the precipitates could interact with the dislocations to reduce the strain component in the activation energy for the precipitates[119, 120].

5.5.3.4 Mechanically mixed layer

As discussed in the SEM observations in Section 5.4, mechanically mixed layers were found on the worn surfaces of the materials studied, at a variety of sliding loads in the present work. The MML contained the elements from both the sliding counterparts and a significant amount of Fe was present in the MML. Therefore, it is of great interest to study the microstructures of the MML using TEM.

Fig. 5.76 shows a longitudinal cross section of the worn surface of the base alloy at a load of 10 kg. It can be seen that relatively large aggregates (marked as MML) were just lying above the subsurface with elongated subgrains. It was also noted that microvoids were present between some aggregates, for example, a void as indicated by the arrow in Fig. 5.76. At higher magnifications, it was observed that the aggregates were actually comprised of ultrafine particles with a size of a few nanometers, as shown in Fig. 5.77. It is of interest to note that the ultrafine particles in some aggregates seemed to congregate along the plastic flow. In Fig. 5.77, for example, the ultrafine particles oriented in a direction towards the elongation direction of the substructure in the matrix below the mixed layer, i.e, towards a direction parallel to the sliding direction.

Similar structures of the aggregates in the MML were also found in the extremely worn surface of the composite (Fig. 5.78) and in the high purity Al (Fig. 5.79). Fig. 5.78 shows the mixed structure in the worn surface of the composite at a load of 10 kg. The aggregates with ultrafine structures coexisted with the recrystallized grains of the Al matrix. It should be noted that some aggregates were mixed and impressed into the Al matrix, and some of the matrix grains were mixed in between the aggregates, as indicated in Fig. 5.78 (b). The interfaces between the aggregates and the matrix grains remained clear and sharp. From the microstructural characteristics of the MML, it is evident that the MML were formed by compaction and incorporation of wear debris into the deformed subsurface.

EDS analyses conducted on the ultrafine particles in the MML of the worn surface exclusively indicated that a significant amount of iron was present in the aggregates, and the amount of iron was in excess of the solubility of iron in the α-Al solution, as shown in Fig. 5.80. Moreover, in some particles, especially at a high load, oxygen was also noticeably present in the aggregate. Since the size of the nanocrystallites was much smaller than that of the focused electron beam used in the EDS mode, it was not possible to differentiate whether the particles contained some iron or they were "pure" iron particles. It is certain, however, that the iron element was transferred from the counterpart and got mixed either mechanically or chemically with the Al alloys mainly depending on the sliding load in the present work. The results are consistent with the observations using SEM.

The selected area electron diffraction (SAD) revealed that the crystal structures of the ultrafine particles were different from one location to another in the MML. Since the microstructural features of the aggregates with ultrafine grained structures in the MML were found to be very similar to those in the wear debris, the detailed studies of the crystallographic characterization of the ultrafine grained structures of the debris will be discussed separately in Chapter Seven using TEM, X-ray diffraction and Mössbauer spectroscopy. The results show that the microstructures of the ultrafine grained structures were basically comprised of a mixture of different phases. Depending mainly on strains and temperatures caused by sliding friction, the mixture included the constituents from both the sliding materials such as α-Al, α-Fe, and iron aluminum intermetallic compounds as a result of solid state reaction between both the sliding materials, as well as oxidation products with the environment, such as α-Al_2O_3.

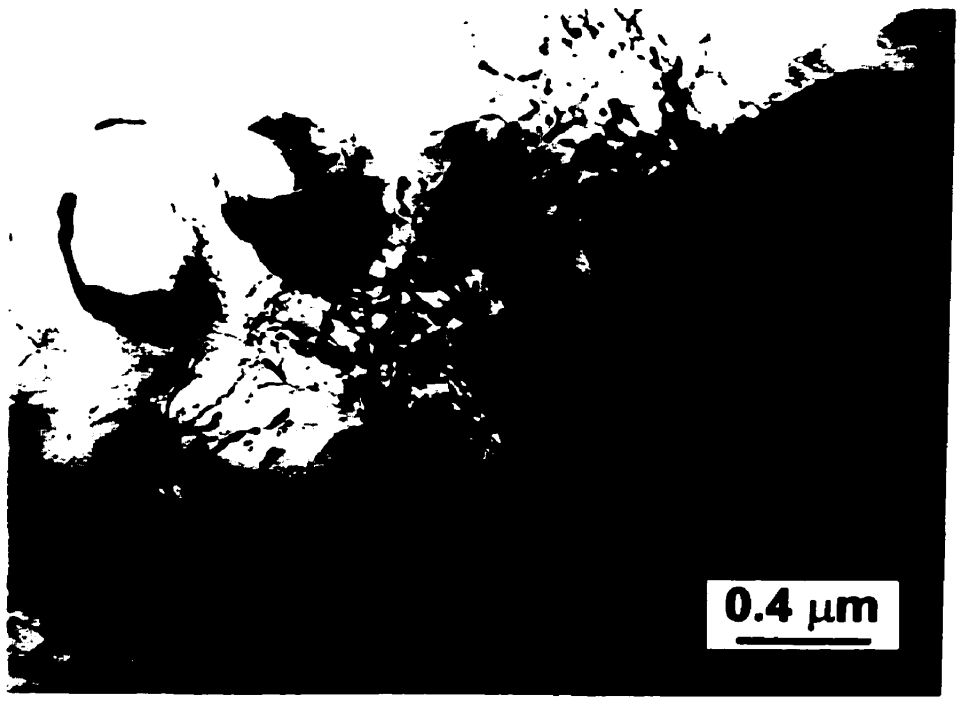

(a)

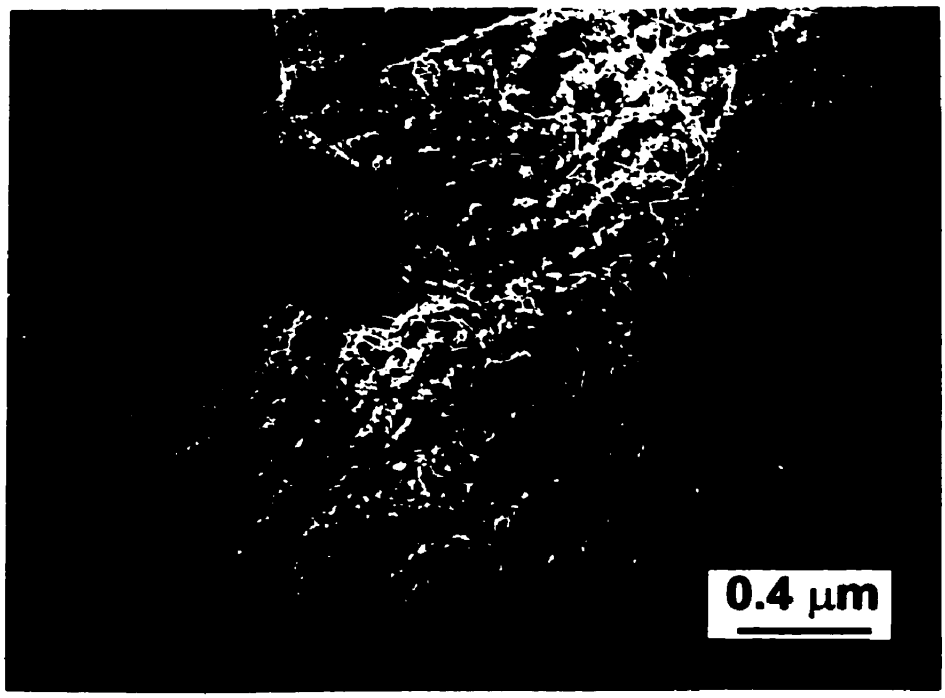

(b)

Fig. 5.58 Dislocation structures in the subsurface about 60 μm below the worn surface at a load of 10 kg. (a) Bright field image; (b) Weak beam dark field image. **B**={101}.

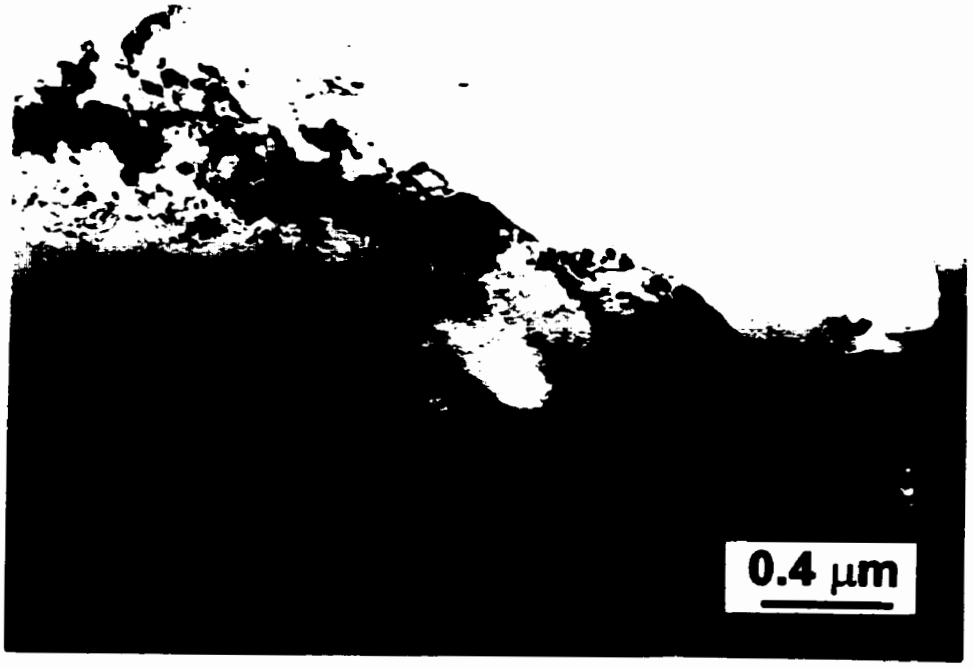

(a)

(b)

Fig. 5.59 Elongated subgrains and dislocation structures at a depth about 40 μm below the worn surface of the Al-Si/SiC composite (as-cast). (a) Bright field image; and (b) Central dark field image.

Fig. 5.60 Direction of the plastic flow of the matrix with elongated subgrains was changed due to the presence of the SiC particle.

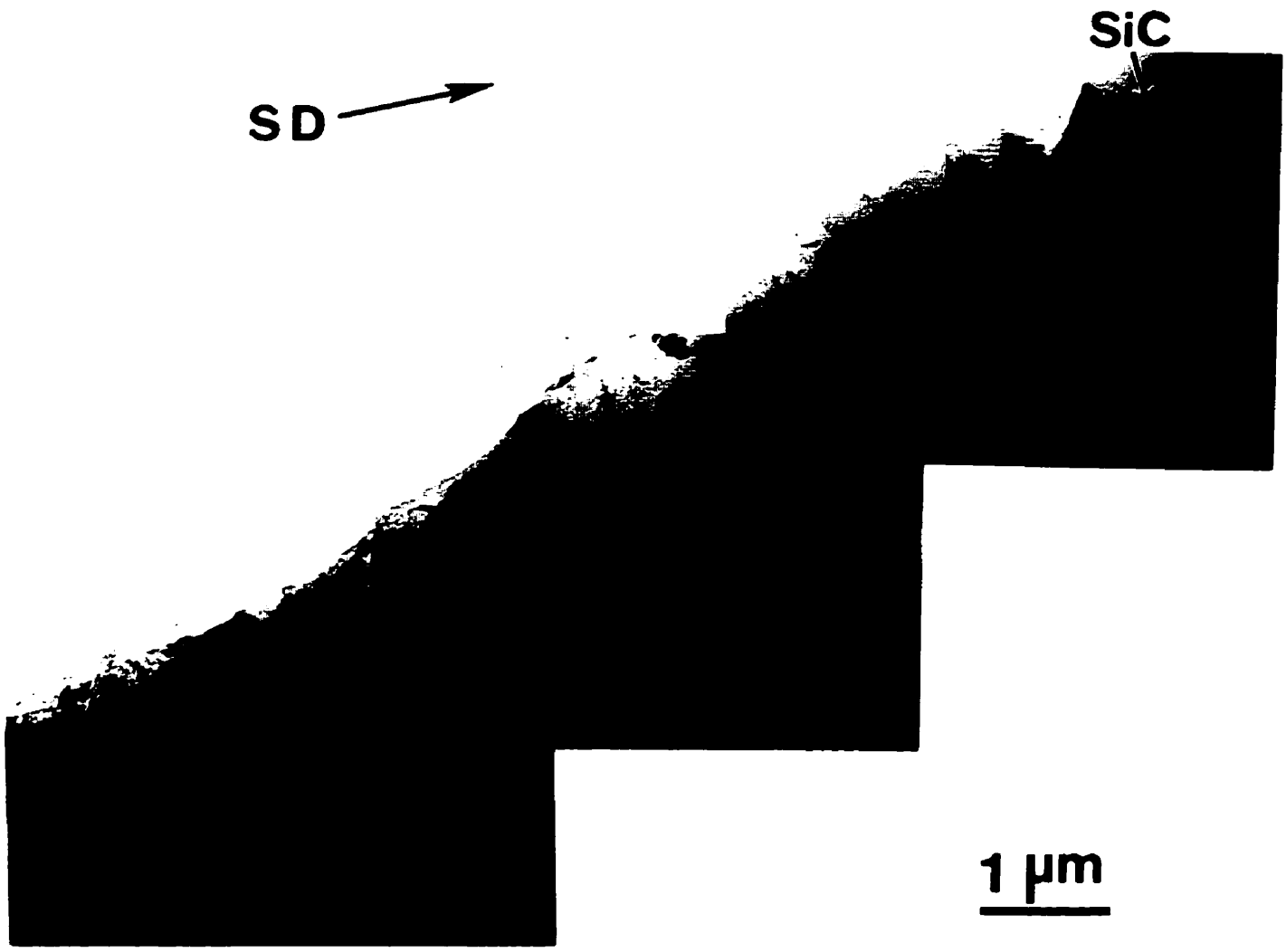

Fig. 5.61 Elongated subgrains were impeded and the matrix flow of the subgrains was constrained due to the presence of the SiC particle in the worn surface of the Al-Si/SiC composite (as-cast) at a load of 10 kg .

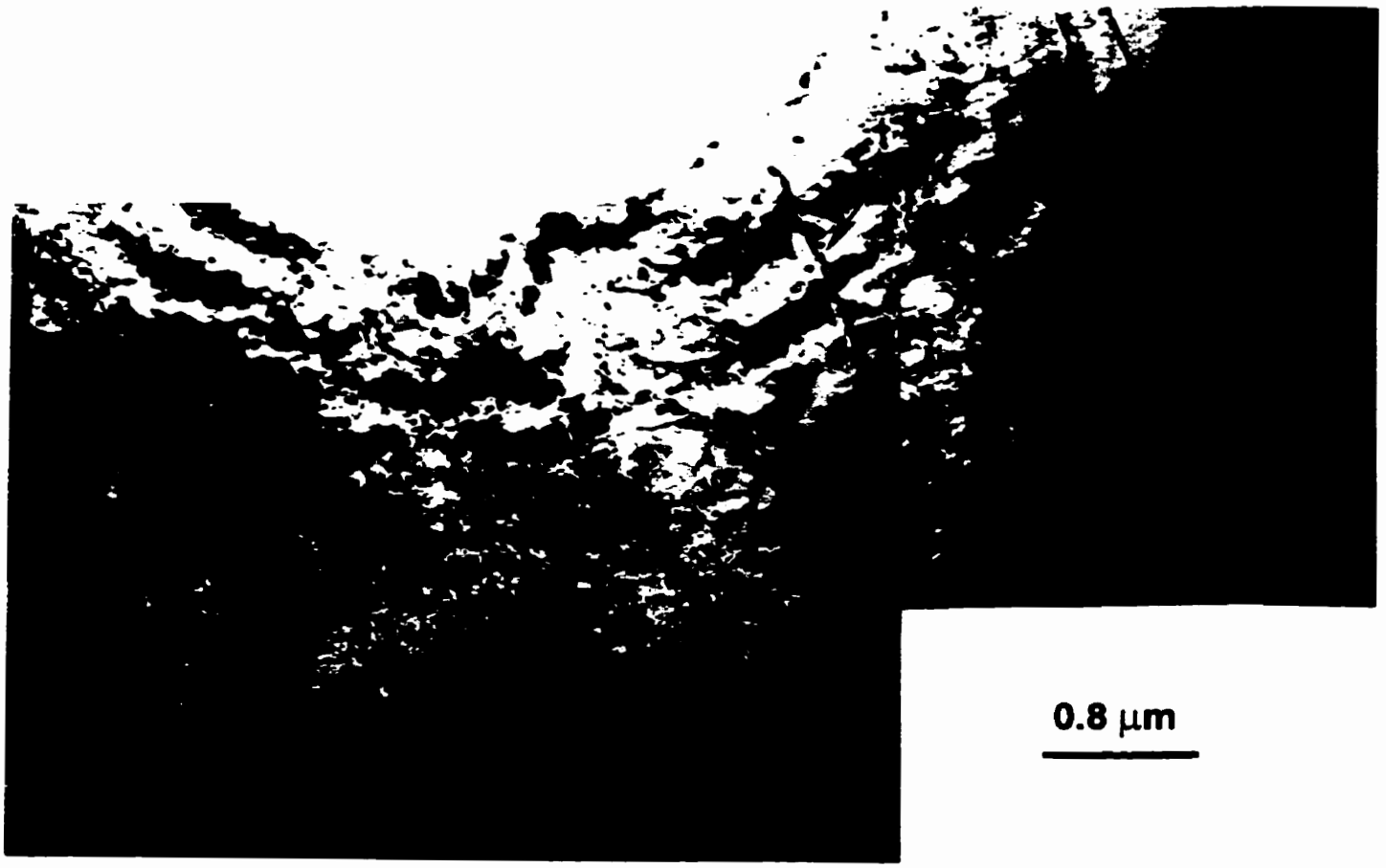

Fig. 5.62 Subsurface microstructure about 60 -70 μm below the worn surface of as cast Al-Si/SiC composite at a load of 5 kg. Note that high density dislocations were tangled and cells started to form. Coarse precipitates were also noticed.

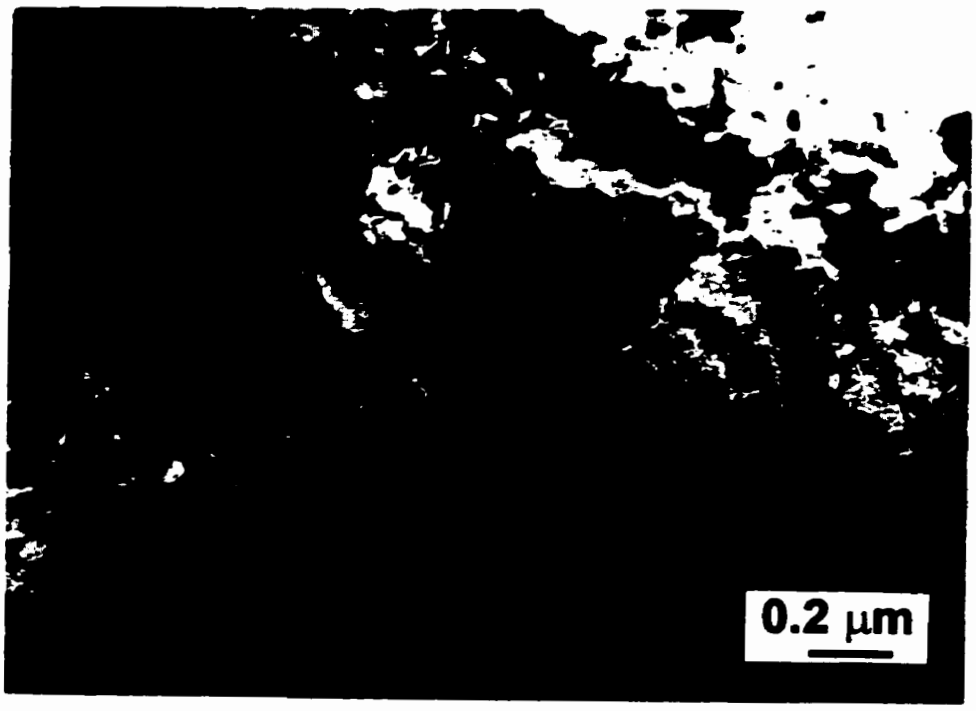

(a)

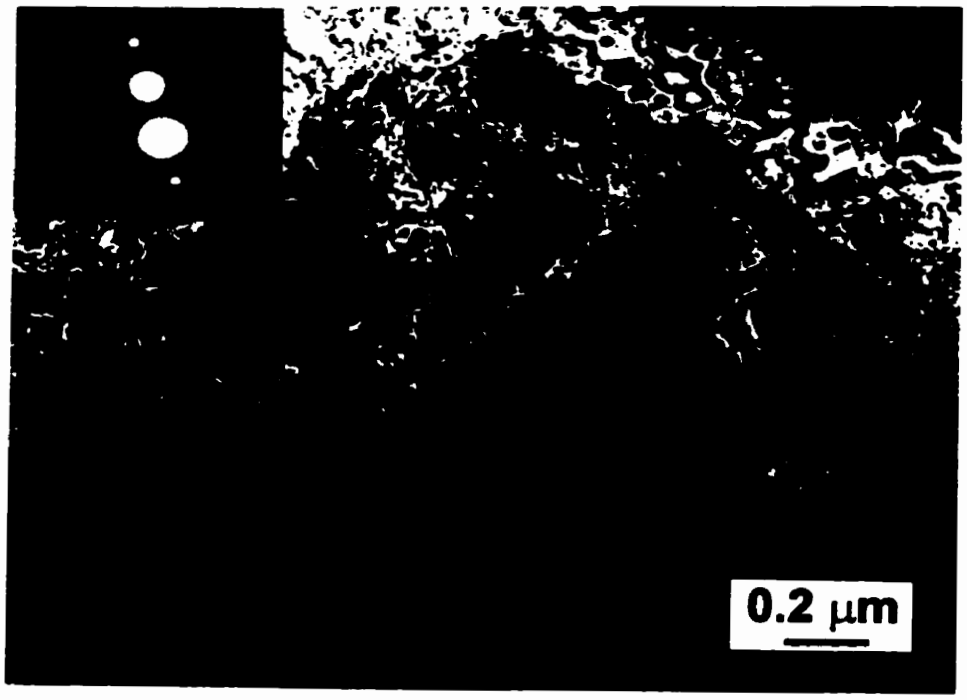

(b)

Fig. 5.63 Needle-like precipitates and dislocation structures in the worn surface of the as cast Al composite at a load of 5 kg. The insert shows two-beam condition of the matrix and electron diffraction pattern of the precipitates. (a) Bright field; (b) Weak beam dark field. B=[101], $\vec{g} = [\bar{1}01]$.

(a)

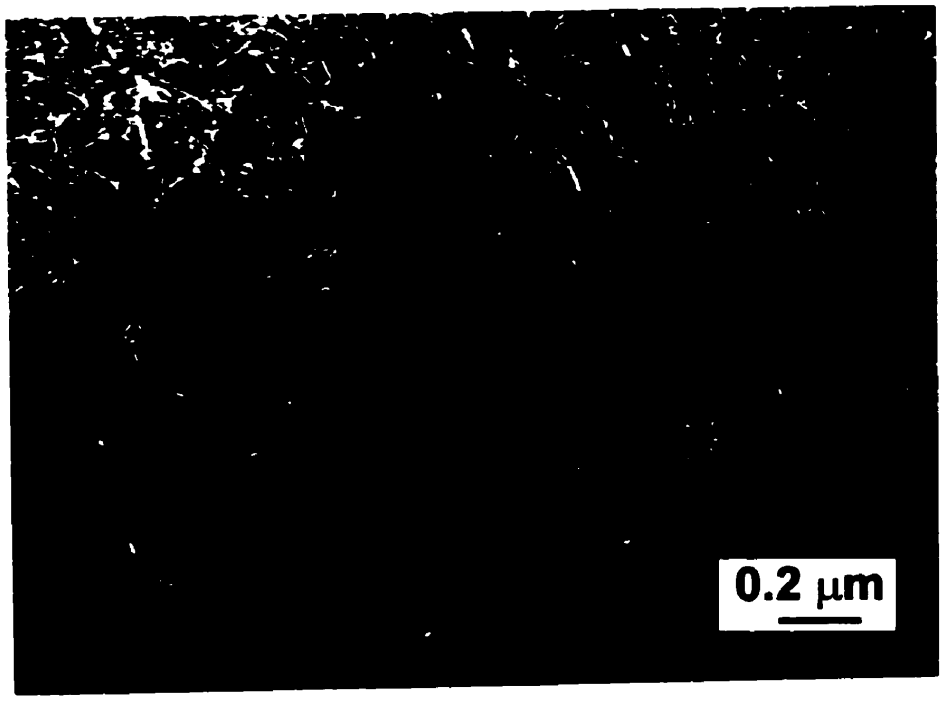

(b)

Fig. 5.64 As in Fig. 5.62, needle-like precipitates and dislocation cell structures in the worn surface of the as cast Al composite. (a) Bright field; (b) Weak beam dark field. B=[101].

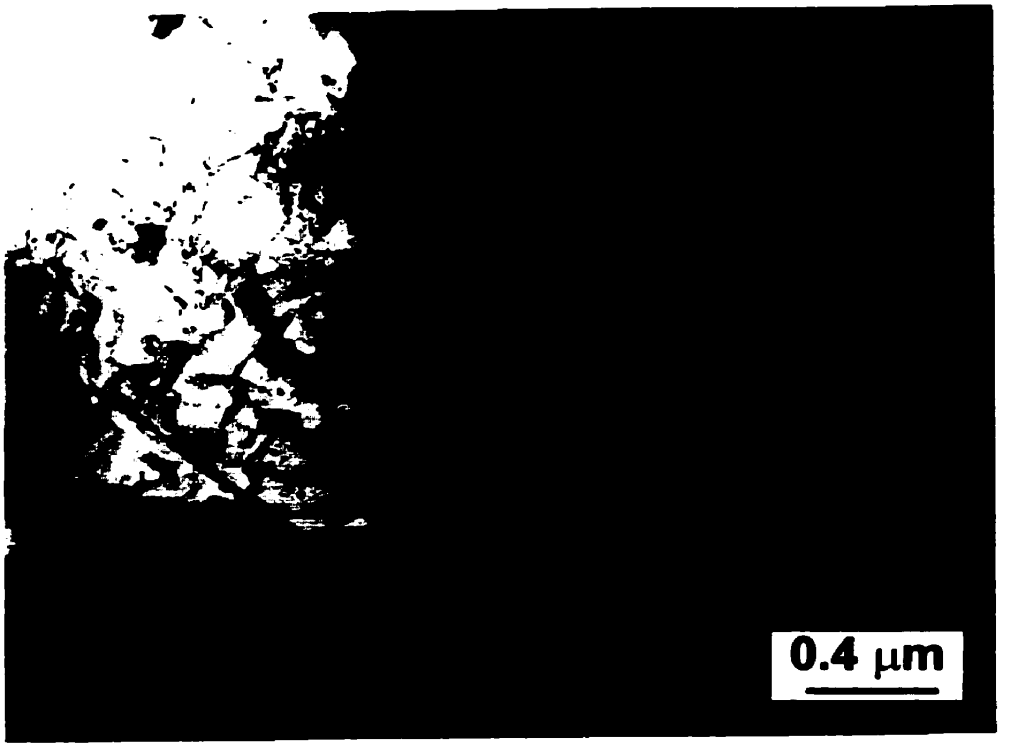

(a)

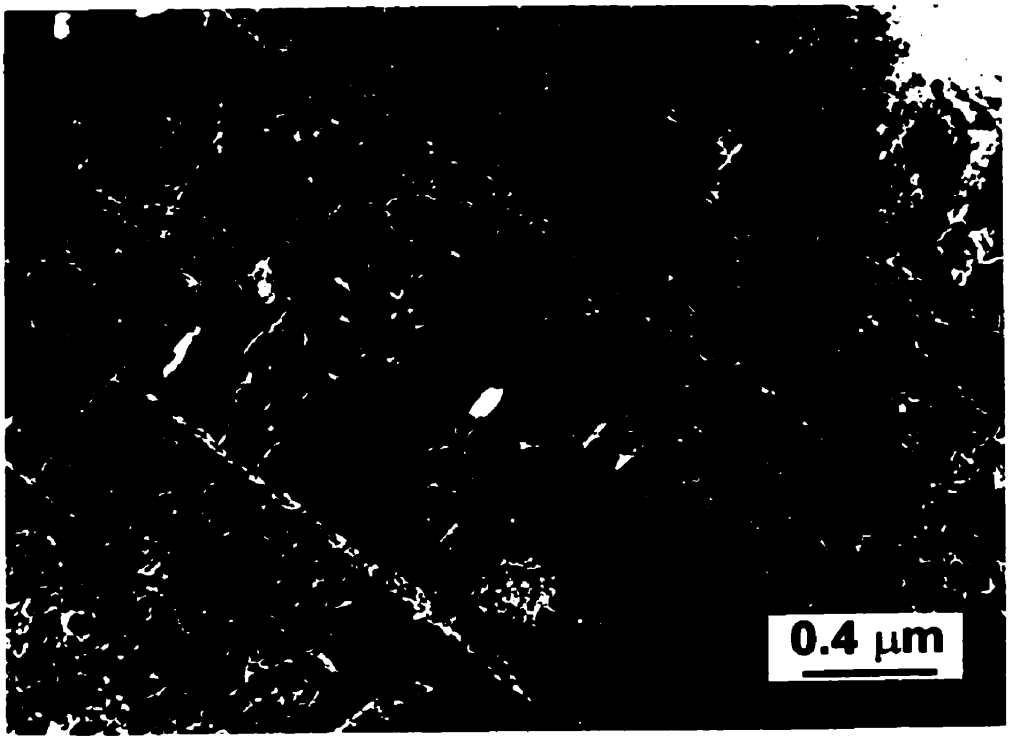

(b)

Fig. 5.65 Subsurface microstructure at a depth about 40 μm below the worn surface of the as cast composite, showing coexistence of high density dislocations and rod precipitates. B=[101], $\vec{g}$=[$\bar{1}$ $\bar{1}$ 1]. (a) Bright field; (b) Weak beam dark field.

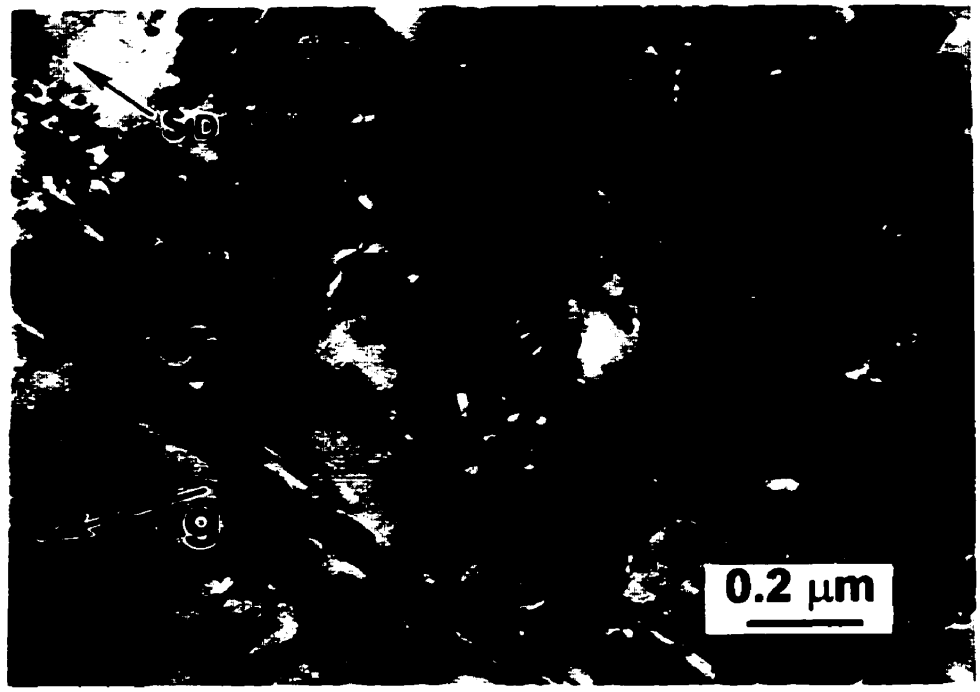

(a)

(b)

Fig. 5.66 Dislocation structures and the in-situ precipitates in the subsurface of the worn surface of the as cast composite. $B = [101], \bar{g} = [1\,\bar{1}\,\bar{1}]$. (a) Bright field; (b) Weak beam dark field.

(a)

(b)

Fig. 5.67 As in Fig. 5.66, the image was obtained using different $\bar{g}$. $B = [101], \bar{g} = [\bar{1}\,\bar{1}\,1]$. (a) Bright field; (b) Weak beam dark field.

(a)

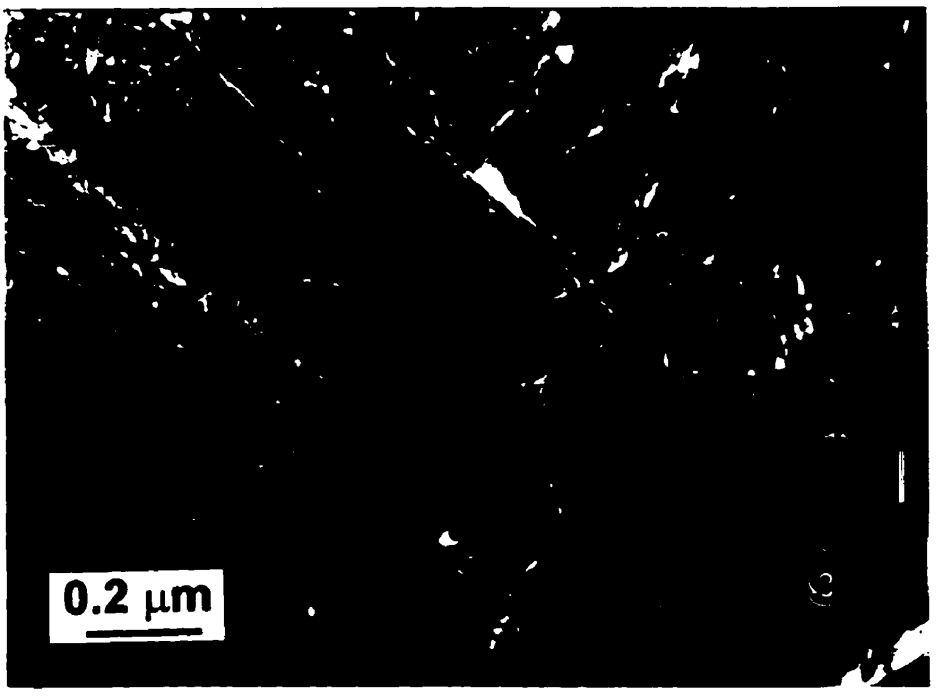

(b)

Fig. 5.68 As in Fig. 5.66, the thin foil was titled to Zone [112]. $B = [112]$, $\bar{g} = [\bar{1}\,\bar{1}\,1]$. (a) Bright field; (b) Weak beam dark field.

(a)

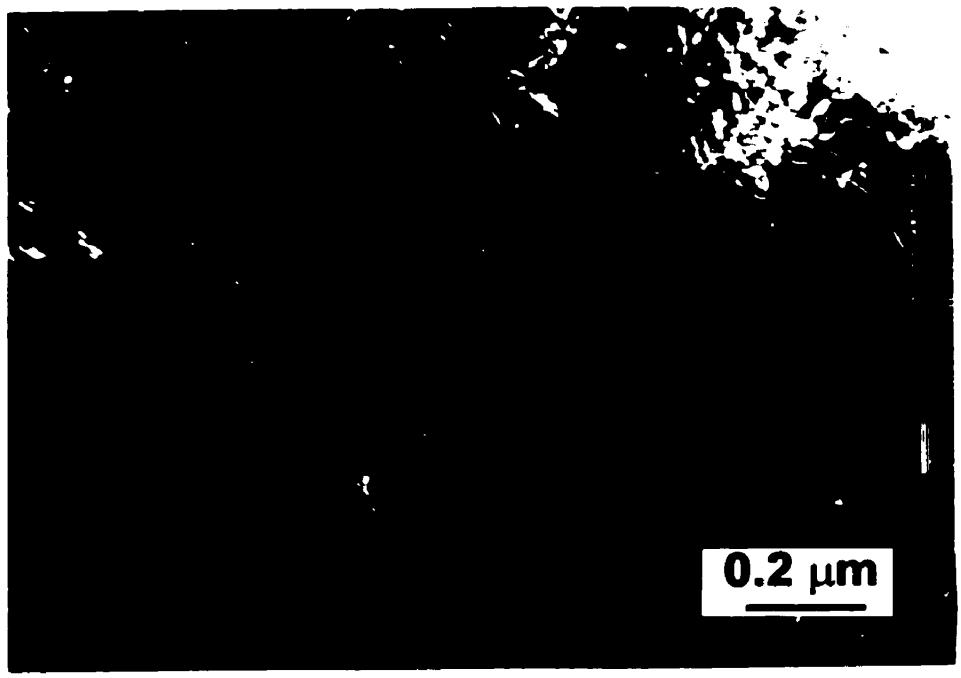

(b)

Fig. 5.69 As in Fig. 5.66, the thin foil was titled to Zone [101] but with different $\bar{g}$. $B = [101]$, $\bar{g} = [0\bar{2}0]$. (a) Bright field; (b) Weak beam dark field.

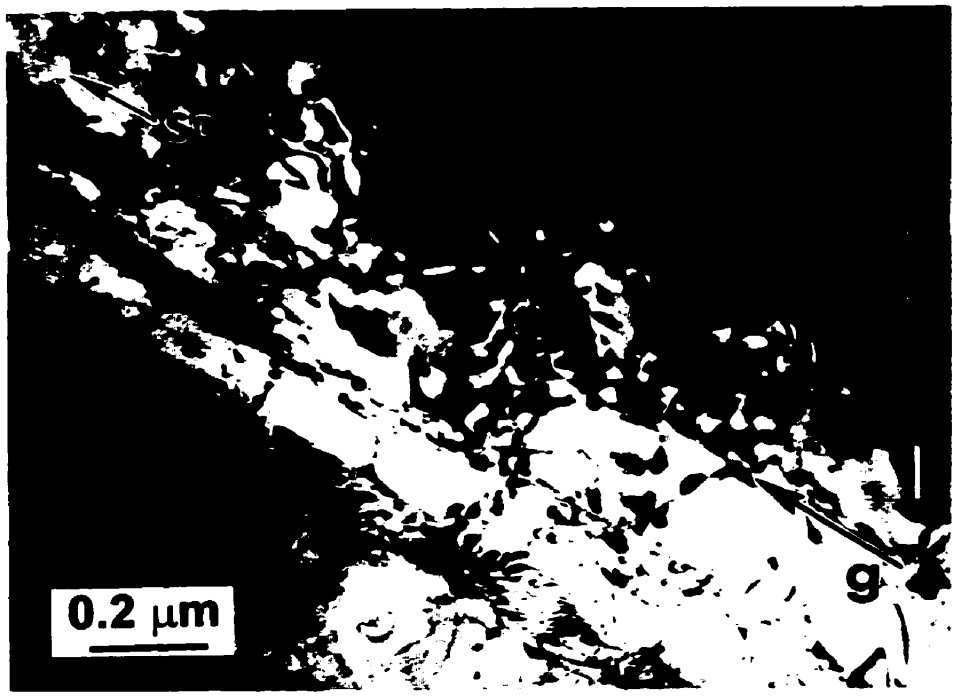

(a)

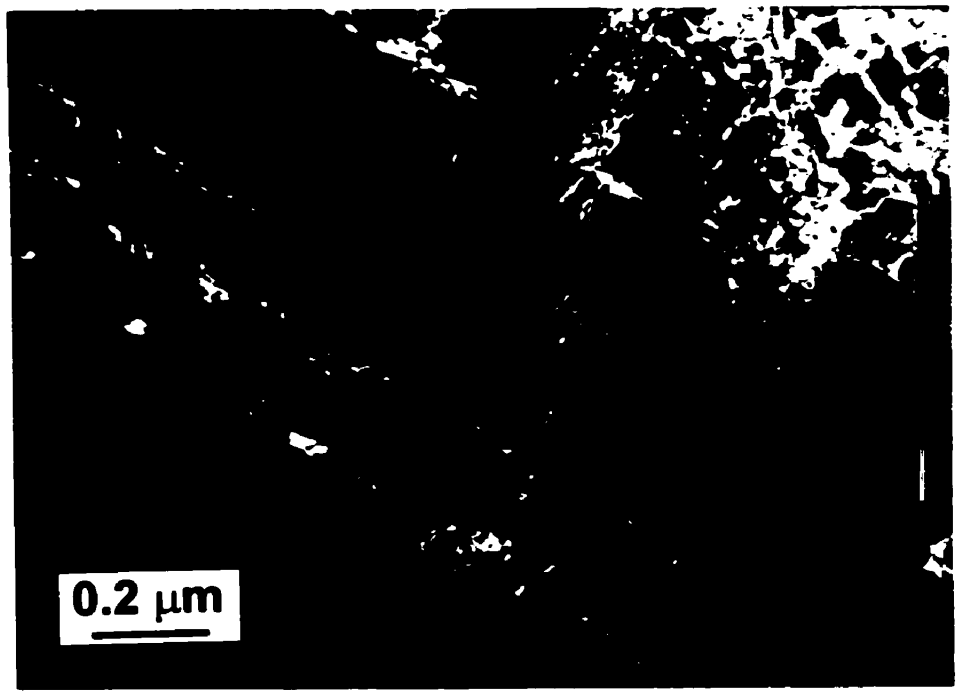

(b)

Fig. 5.70 As in Fig. 5.66, the thin foil was titled to Zone [301]. $B = [301]$, $\bar{g} = [0\bar{2}0]$. (a) Bright field; (b) Weak beam dark field.

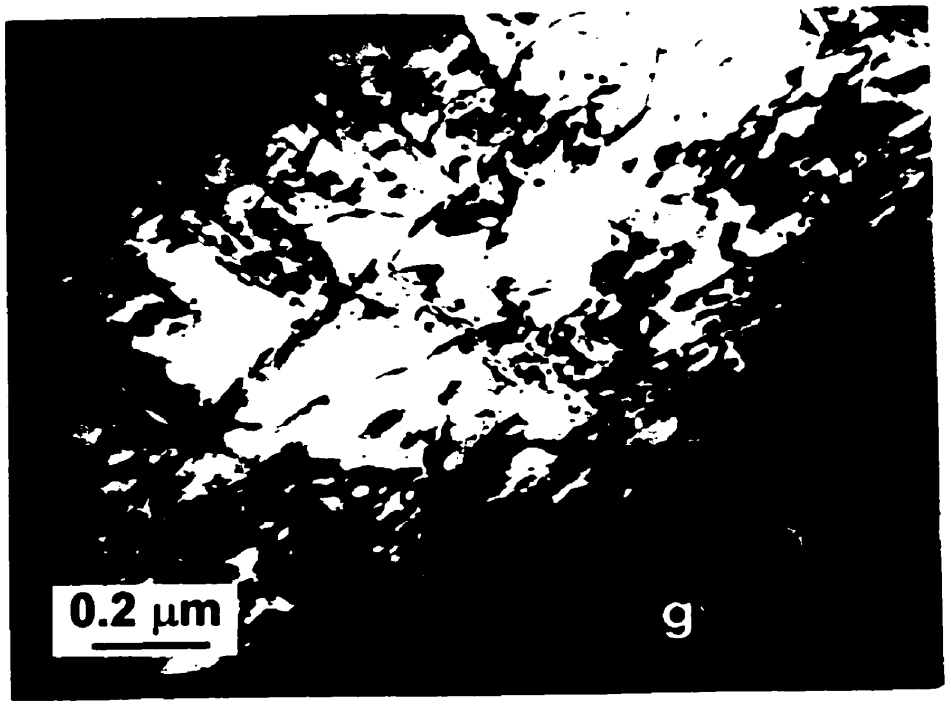

(a)

(b)

Fig. 5.71 As in Fig. 5.66, the thin foil was titled to Zone [100] and different $\bar{g}$. $B = [100]$, $\bar{g} = [0\bar{2}0]$. (a) Bright field; (b) Weak beam dark field.

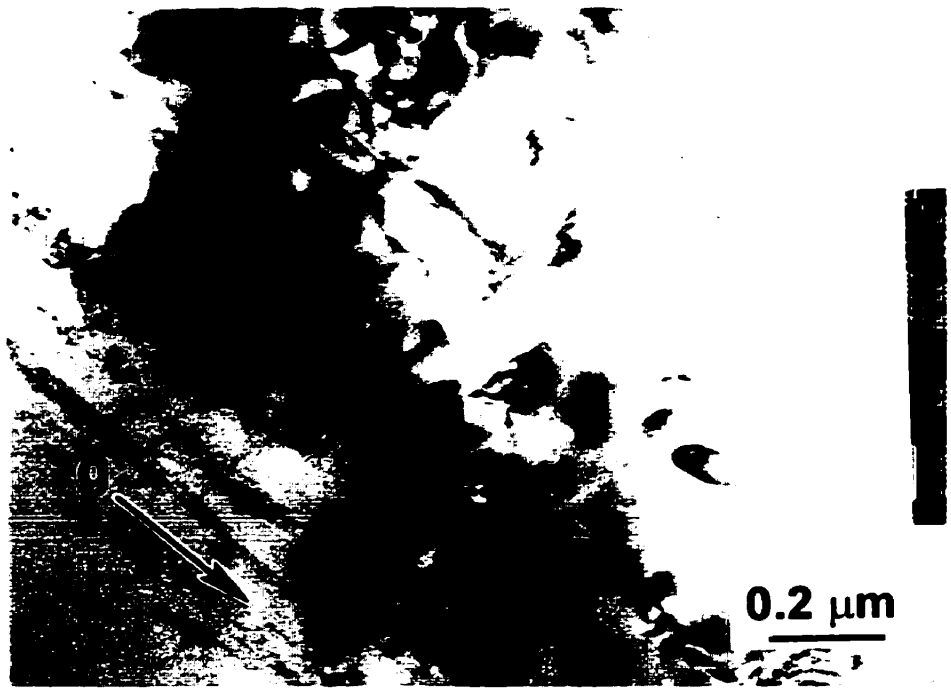

(a)

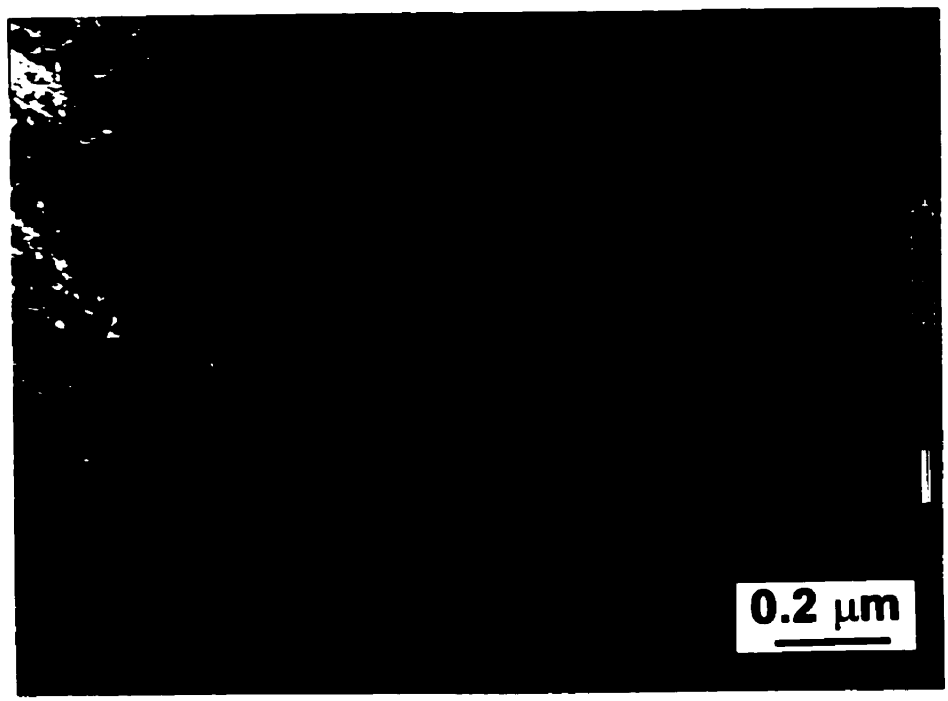

(b)

Fig. 5.72 As in Fig. 5.66, the thin foil was titled to Zone [112] but with different $\bar{g}$. $B = [112], \bar{g} = [\bar{2}20]$. (a) Bright field; (b) Weak beam dark field.

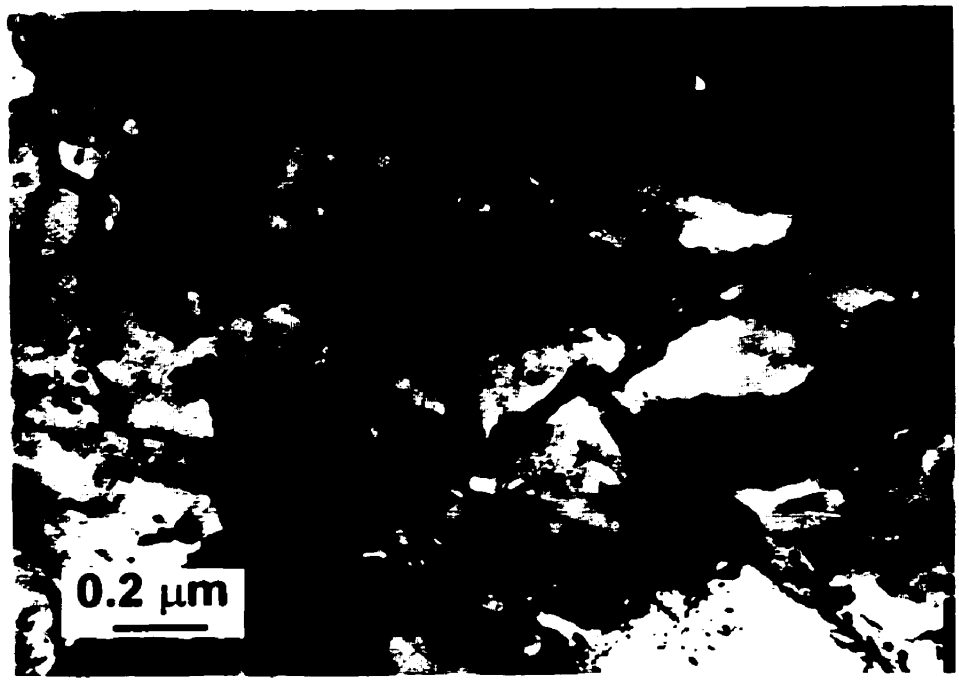

(a)

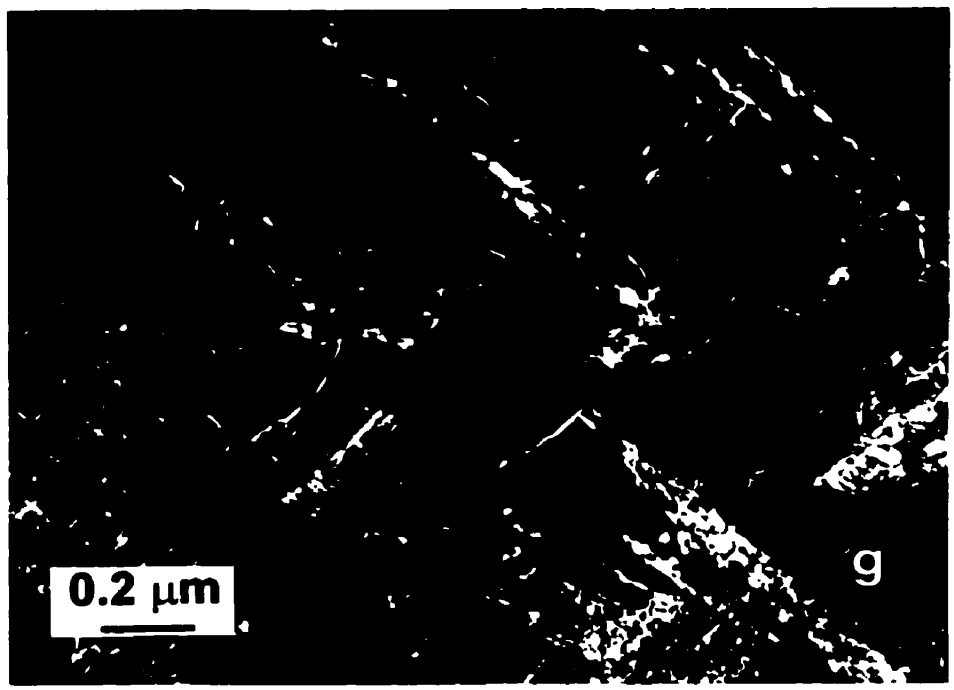

(b)

Fig. 5.73 Dislocation structures and the precipitates in the subsurface. Note that closely spaced dislocation loops at the interface between the matrix and the precipitates lying on direction $[\bar{1}01]$. $B = [101]$, $\bar{g} = [0\bar{2}0]$. (a) Bright field; (b) Weak beam dark field.

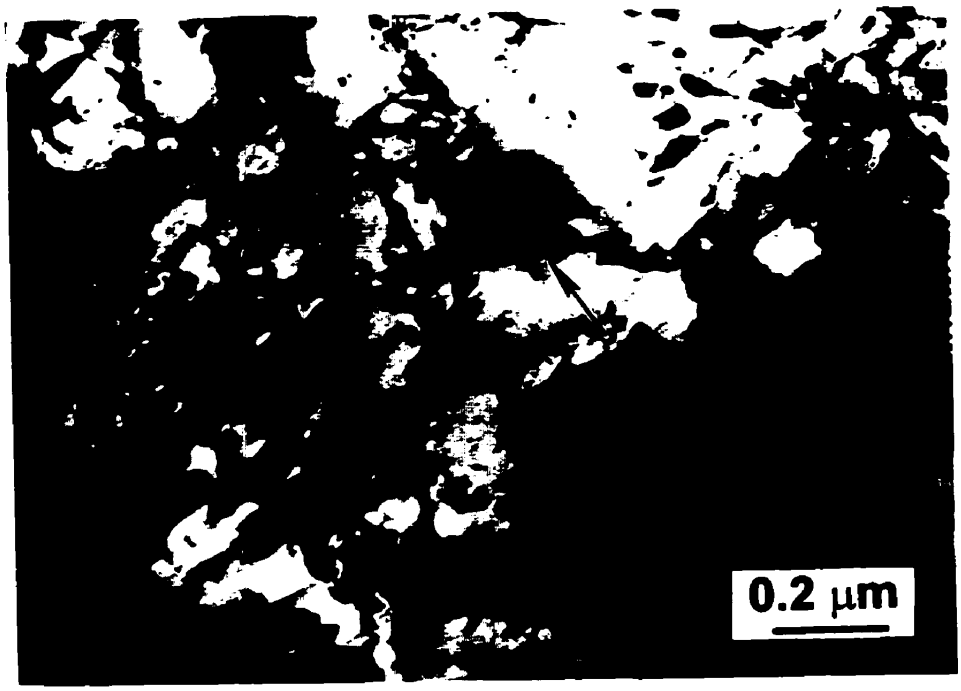

Fig. 5.74 Dislocation structures and the precipitates in the subsurface. The foil was titled to Zone axis [001]. The precipitates showed end-on image decorated with dislocations. $B = [001], \bar{g} = [0\bar{2}0]$.

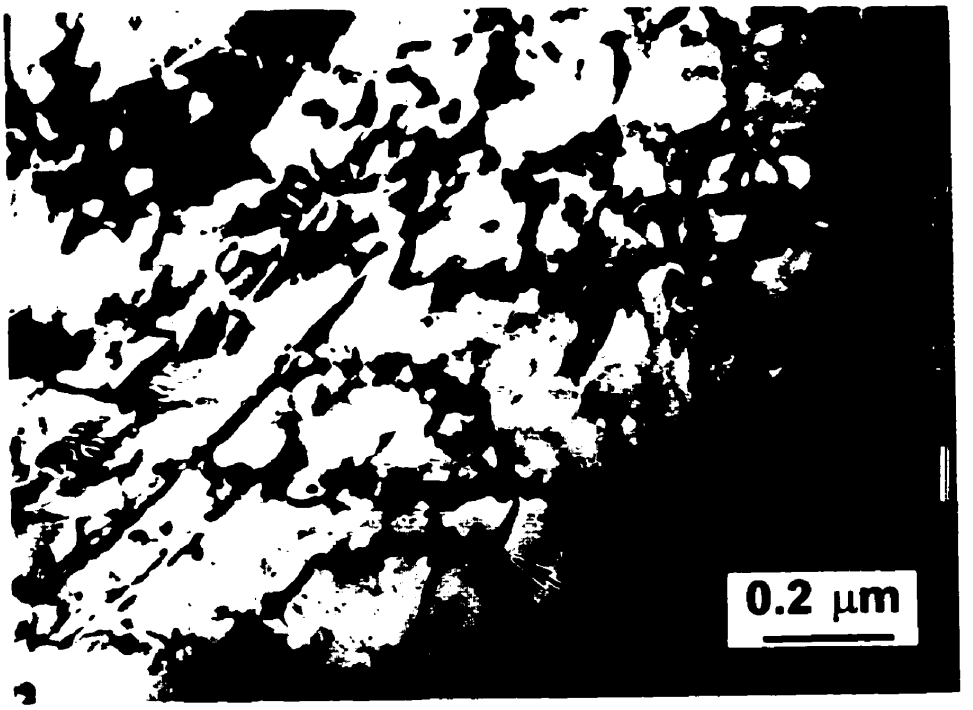

(a)

(b)

Fig. 5.75 Precipitates with end-on images were decorated with dislocation network. The foil was titled to Zone axis [001]. $B = [001], \bar{g} = [0\bar{2}0]$. (b) At a high magnification.

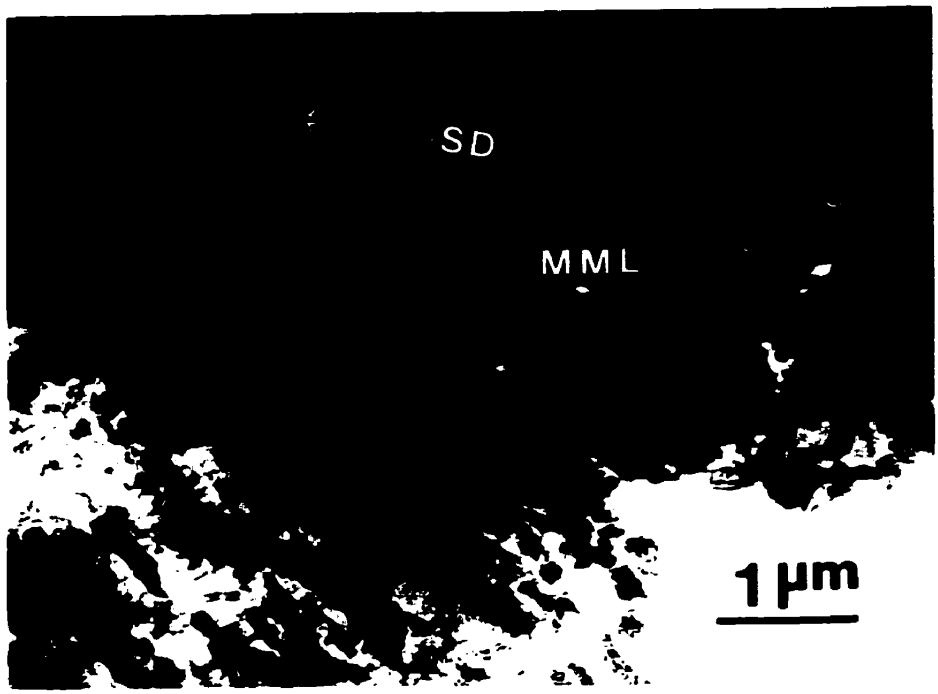

Fig. 5.76 TEM micrograph of a longitudinal cross section of the worn surface, showing the mechanically mixed layer(MML) and elongated subsurface structure at a load of 10 kg. The small arrow indicates a microvoid between aggregates in the MML.

(a)

(b)

Fig. 5.77 The ultrafine grained structure in the MML in the longitudinal cross section of the worn surface of the Al-Si alloy at 10 kg. Note that the ultrafine particles congregated along the plastic flow in the aggregates. (a) At a low magnification ; (b) At a high magnification.

(a)

(b)

Fig. 5.78 Mechanically mixed structures of the ultrafine grained aggregates and subgrains of the matrix in the MML. Subgrains of the matrix mixed in the ultrafine grained aggregates should be noted as indicated by arrows.

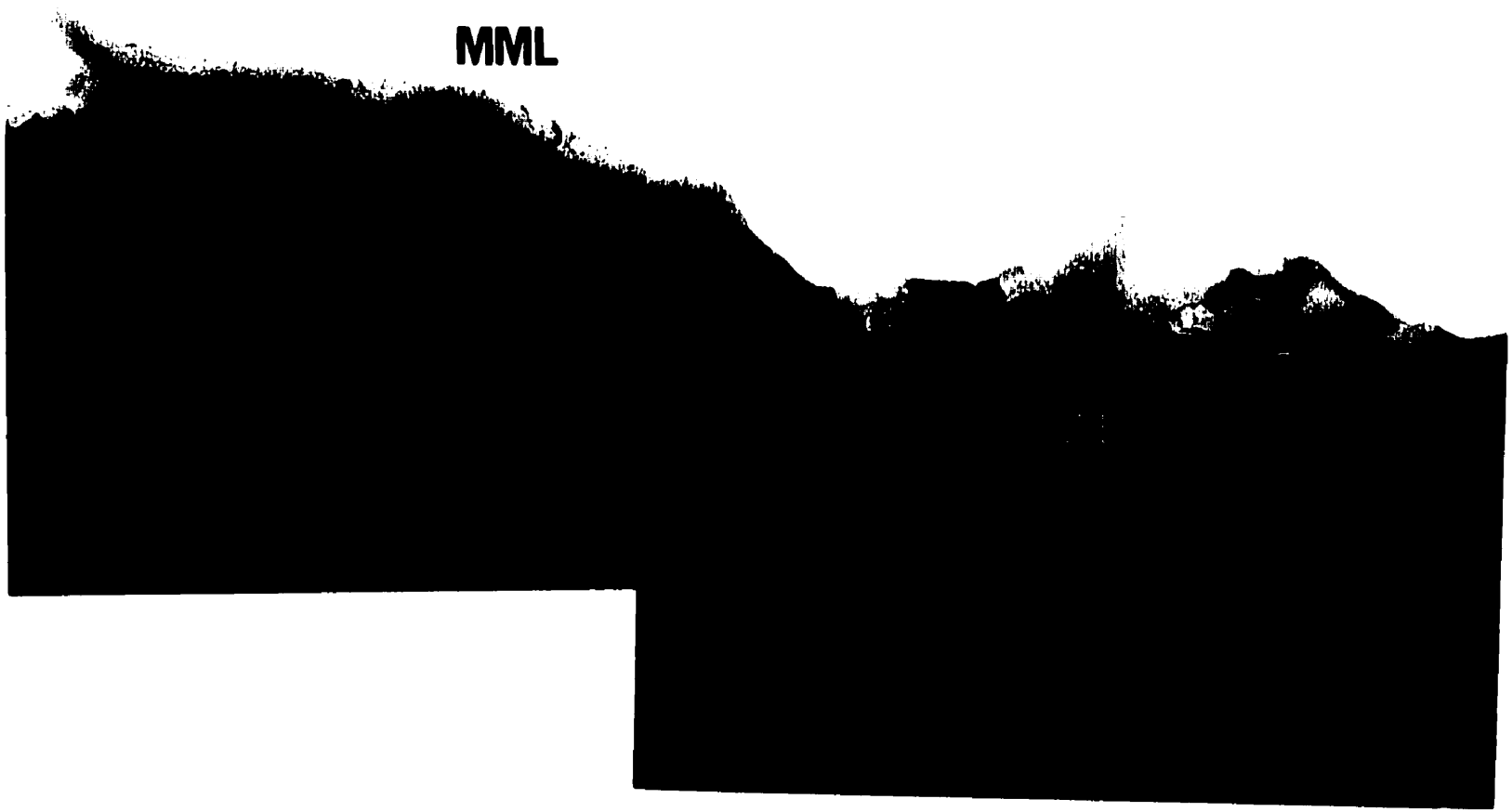

Fig. 5.79 The ultrafine grained structure in the MML in the longitudinal cross section of the worn surface of HP Al.

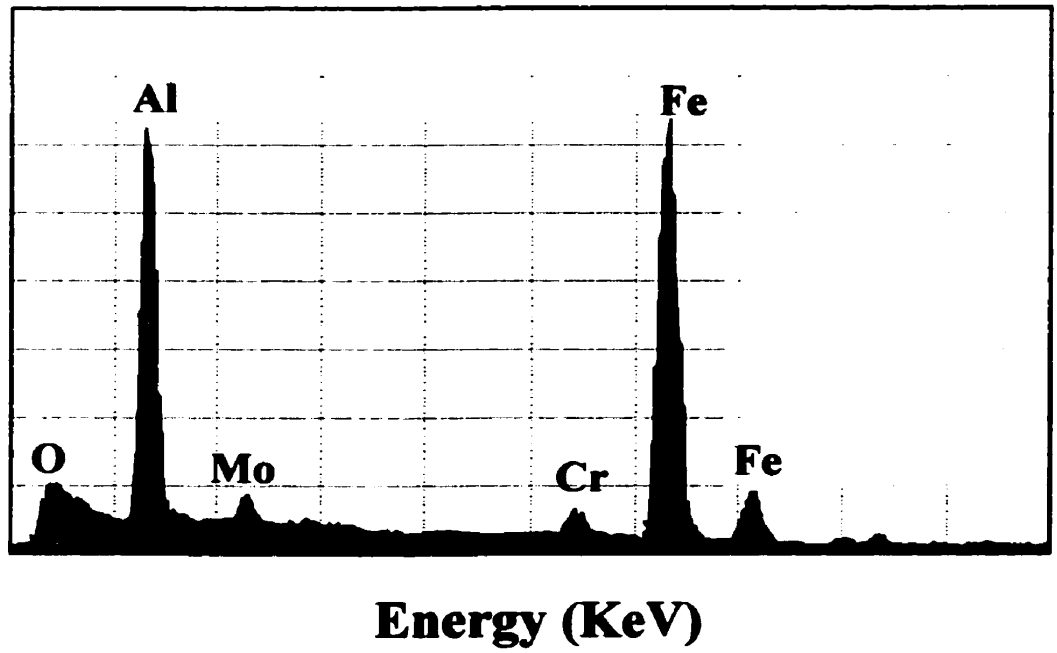

Fig. 5.80 EDS analysis of the ultrafine grained structures in the MML, showing a considerable amount of Fe and Al.

5. 6 DISCUSSION

5.6.1. Plastic deformation below the worn surface

From the microstructural observations using SEM and TEM as discussed above, it can be generally concluded that in addition to the loose debris, the worn surface can be divided into different sublayers along the depth below the worn surface. The first or top layer is the actual contact surface with the sliding counterpart and contains a mixture of materials from both the sliding contact surface, i.e, mechanically mixed layer (MML). Underneath the MML is the highly deformed sublayer in which strong shear deformation is dominant as a high degree of shear plastic flow is observed. Just between the shear deformed layer and the undeformed bulk material is the plastically deformed sublayer.

In the highly shear deformed sublayer, as observed by the SEM examination, the passage of the shear band layers was aligned or parallel to the sliding direction, especially at the depth approaching the near surface. This may suggest that the maximum shear stress was parallel to the surface during the sliding motion. This phenomenon is in agreement with other observations in different sliding systems such as stainless steels [6] and Cu alloys [58] as well as Al alloys[4]. According to the shear instability model proposed by Rosenfield [120-122] and later modified by Kou and Rigney[4], shear localization could occur at a depth below the worn surface in the competition of the flow strength of material and the stress intensity caused by the sliding wear. The stress intensity was associated with a force acting on the surface above a shear crack as a result

of combined effect of normal load and friction force during the sliding wear as defined by Rosenfield[120, 122]. Shear localization could occur in the case of HP Al as a result of severe shear stresses in the worn surface, as micro-shear bands were evidently observed in the present work. The initial flow strength of the HP Al was lower and could be raised after sliding for some distances due to the work hardening effect that was pronounced in the HP Al. In the case of the base alloy and composite, no shear localization was noted in the TEM microstructural observations in the present work. Instead, elongated subgrains were the predominant features in the subsurface of the base alloy and the composite at the depth range corresponding to the shear banded structure observed in the worn surfaces of the base alloy and composite in SEM.

Kuhlmann-Wilsdorf [2] and other researchers [123, 124] have suggested that a linear hardening law is most likely to be applicable in sliding wear from the theoretical viewpoint in terms of strain distribution at a worn surface [2]. According to this model, the flow stress rises linearly with the logarithm of the strain. The model was compared to the work of Dautzenburg and Zaat[123] from which the experimental data fitted the strain distribution model following an exponential relation:

$$\gamma = \gamma_s \exp(-kz)$$

where γ_s is the shear strain at the surface.

In the present work, the work hardening effects can also be observed through microhardness profile and/or strain profile along the depth below the worn surface, and these profiles are thus compared to the microstructural features obtained using SEM and

TEM. Fig. 5.81 shows the microhardness profiles along the depth below the worn surface of the HP Al and the Al base alloy. These values were obtained through an average of at least five readings, and no values that obtained from the mechanically mixed layer were included, since the hardness values (170 HV) in the MML were generally found to be much higher than those in the subsurface. The increased hardness in the near subsurface confirms that the flow stress was raised as a result of work hardening caused by the sliding wear, and deformation depth was quite deeper in the HP Al than in the Al base alloy, in agreement with the observations in TEM. Due to the difficulty of measurement of hardness below the worn surface of the Al composite with the presence of the SiC particles, an estimated strain distribution along the depth can be used to evaluate the plastic deformation behavior of the Al base alloy and the Al-Si/SiC composite. A strain profile along the depth was obtained using a method in which the equivalent plastic strain ε was calculated from shear angles between the plastic flow line and the normal to the

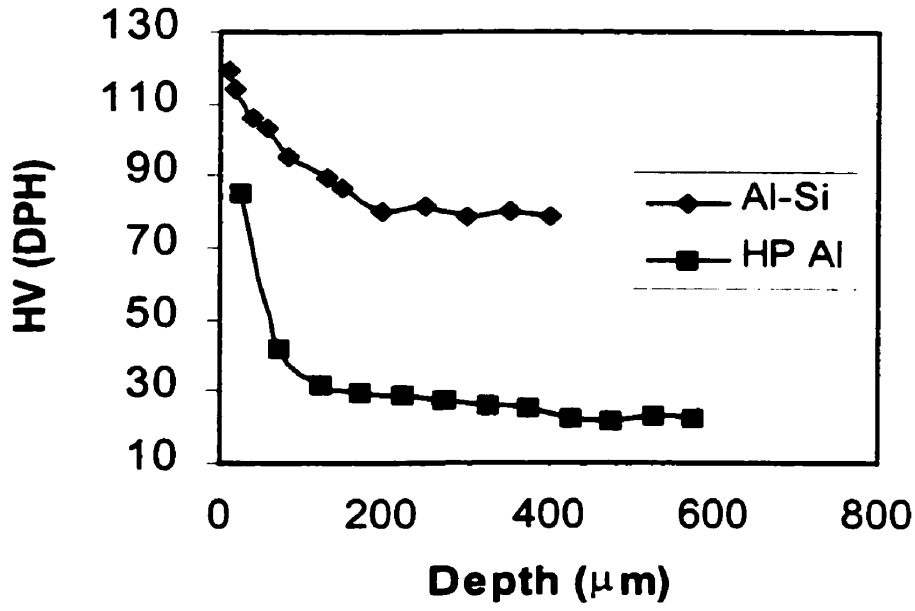

Fig. 5.81 Microhardness profile as a function of depth below the worn surface of the HP Al and Al-Si alloy at a load of 5 kg.

worn surface θ [13, 50, 55, 123], as reviewed in Chapter 2 and Fig. 2.11, i.e.,

$$\varepsilon(z) = \frac{\sqrt{3}}{3}\tan[\theta(z)]$$

at a depth z from the top surface. The plastic flow line was approximately traced using longitudinal cross sections of the worn surface. Fig. 5.82 shows the equivalent strain as a function of the depth below the worn surface of the Al-Si alloy and the Al -Si/SiC composite at a load of 5 kg using the above mentioned method. Since the work hardening behavior in the extreme surface would be affected by the presence of MML, the measurement at the very near surface was ignored. The curves were obtained using a fitting software [125] to fit the raw data. From the logarithm of the strain as a function of depth shown in Fig. 5.82(b), it appears that the nature logarithm of the strain is linearly related to the depth, i.e.,

$$\ln \varepsilon(z) = z_s - kz$$

or

$$\varepsilon(z) = \varepsilon_s \exp(-kz)$$

This is in agreement with the well-known Voce equation proposed to account for the relation between the plastic stresses and strains in compression tests [126]. This is also in good agreement with the model proposed by Kuhlmann-Wilsdorf [2], and in good agreement with the results obtained in different sliding systems by other researchers[2, 6, 22, 127]. The strain distributions are also consistent with the microstructural evolution along the depth below the worn surface, as observed using TEM in the present work.

Since many equiaxed subgrains were observed in the near surface, for example, the microstructure just below the mechanically mixed layer as shown in Fig. 5.77 and

Fig. 5.78, demonstrates that the recrystalization of the deformed structures may have been occurring in the worn surface. This is not surprising since large gradient shear strains and temperature rise as a result of frictional heating exist in the worn surface. With respect to the frictional heating, many investigators [44, 46, 47, 51, 52] have made great efforts to estimate and calculate temperature rise at the sliding surface. Lim and Ashby[44] and Ashby et al [51] have developed a model to estimate the bulk surface temperature and flash temperature at real contact asperities for steels. Zhang and Alpas[52] applied the similar method to estimate the surface temperature of an Al alloy (6061) sliding against a bearing steel using Block on Ring sliding configuration, and developed a temperature map for the sliding system of the Al alloy. They found that the surface temperature of the worn surface could reach up to about 430 K, at a load of 98 N, sliding speed 1.0 m/s, which is below the melting temperature of the 6061 Al alloy (Tm=925 K). In the present research, the sliding speed was lower (0.2 m/s), so that the surface temperature as a result of frictional heat would be considerably lower as compared to that obtained in [52]. The average temperature on the surface was measured using spot-welded thermal couples adjacent to the worn surface at a load of 10 kg, as shown in Fig. 5.83. Although the bulk surface temperature was not very high because of the low sliding speed, the local flash temperature at real contact asperities could be much higher. This could also be estimated using microstructural features in the subsurface, since a large number of dislocation loops were noted and precipitation occurred in the worn surface of the as cast matrix. Therefore, the surface temperature rise would be favorable to the recrystallization of the deformed structure in the worn surface.

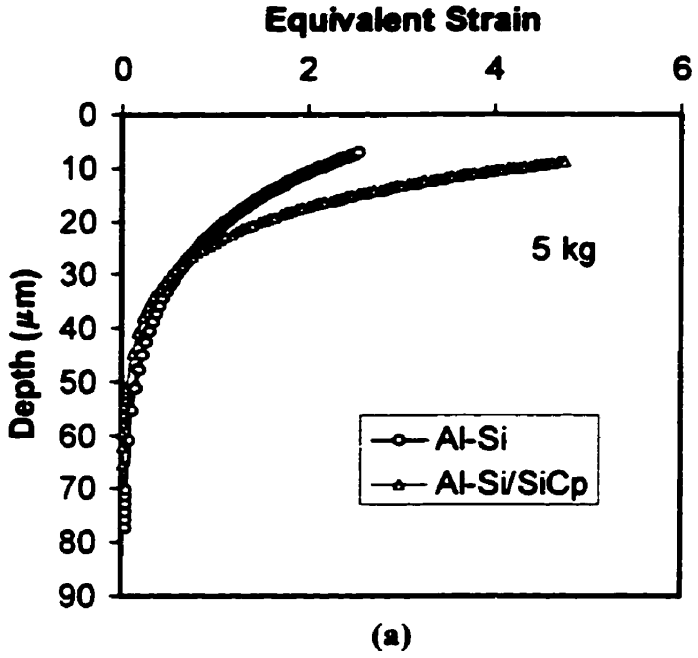

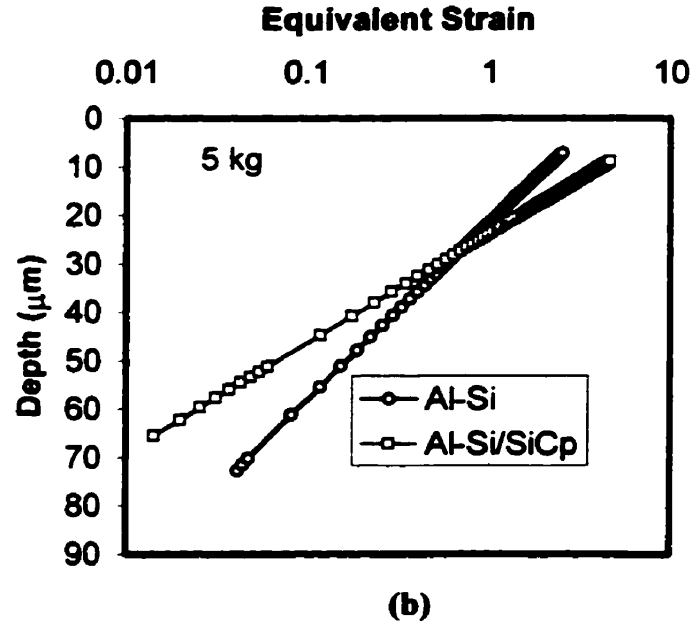

Fig. 5. 82 Equivalent strains as a function of the depth below the worn surfaces of the Al-Si alloy and the Al-Si/SiC composite at a load of 5 kg.

Recrystallization of deformed structures in the worn surface have been discussed by many researchers[3, 4, 117]. Dautzenberg [3] reported a dynamic recrystallization in the worn surface of copper, and proposed that the dynamic crystallization was only process that could satisfy the different properties in the worn surface, and it could occur at a lower temperature because the crystallization temperature could probably be lowered by the heavy deformation generated during the sliding process. Rao and Kosel [117] and Kou and Rigney[4] provided good evidence for dynamic recrystallization in the worn surface of Al alloys. However, there are still some uncertainty whether it is dynamic or static recrystallization because static recrystallization would take place very quickly if an aluminum specimen was kept at an elevated temperature after hot working had stopped with respect to friction-induced-heating during the sliding wear[4, 128]. It is generally considered that dynamic recrystallization is unlikely to occur in aluminum and its dilute alloys because its high stacking energy makes it very easy for dynamic recovery to occur. However, there is evidence of dynamic recrystallization in aluminum deformed to large strains at an elevated temperature. McQueen et al[128] reported a change in the flow stress of Al alloys, i.e., there were peaks in the stress-strain curves that was different to the plateau, characteristic of a material which undergoes only dynamic recovery [129]. Similar results were also observed and reviewed by Kassner et al[130] in which subgrain remained equiaxed and their size appeared to be approximately constant over a large range of strains which were attributed to geometric dynamic recrystallization. Gottstein et al [131] suggested that extensive dynamic recovery could initiate dynamic recrystallization if the dislocation density were sufficiently high.

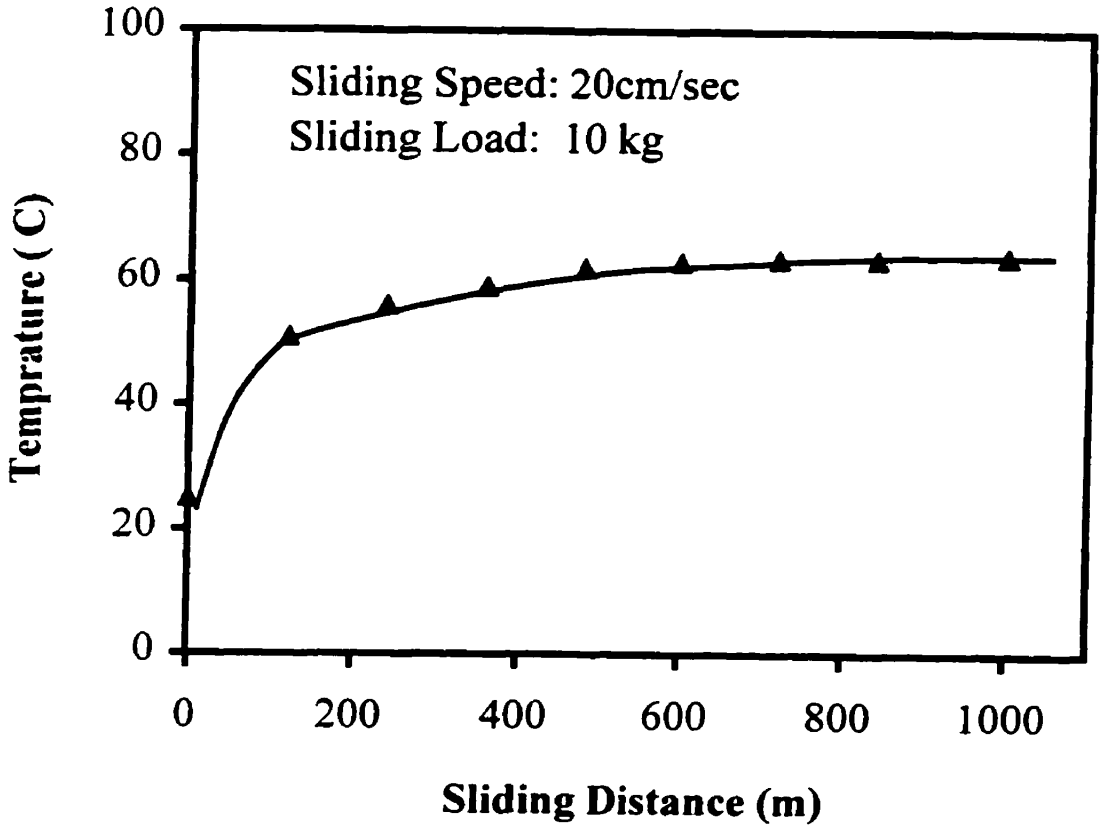

Fig. 5. 83 Average temperature on the worn surface of the Al composite as a function of sliding distance at a load of 10 kg.

In the present research, large angle boundaries between the elongated grains in the near surface of the worn surface were observed, suggesting that recrystallization did occur in the subsurface in the near surface. Although internal dislocation densities were low in many grains, some of the elongated grains were not completely dislocation free, for example Fig. 5.49 in which a considerable number of dislocations could be clearly observed in the elongated subgrains. This strongly suggests that the recovery and recrystallization were a dynamic process in the worn surface in the present work. There might be a dynamic equilibrium of work hardening and recovery mechanism, which

could be attributed to the frictional heating in association with a large amount of strains caused by the sliding wear. The TEM observations made on small flake wear debris indicated that there were also substructures in the equiaxed subgrains, as shown in Fig. 5.84 and 5.85. These small grains were identified as α-Al and did not result from the mechanical mixing process since no Fe was found in the flake debris. This is another strong evidence of dynamic recrystallization since cooling was extremely rapid once the small flake became loose from the sliding surface, so that static recrystallization had little time to occur.

It is interesting to note that the strain distribution along the depth below the worn surface exhibited great discrepancy for the base alloy and the composite, although their microstructural evolution along the depth was similar to each other as discussed above. Under the same sliding load, for example at 5 kg, it was noted that the equivalent strain was relatively smaller for the composite than for the base alloy in the subsurface below a depth away from the top worn surface (i.e., below approx. 30 μm from the top surface in Fig. 5.82). This result is in agreement with the observation in uniaxial tensile tests of the A356 composite and the control alloy [97] in which an increase in stress strength was attributed to the presence of SiC particles. On the other hand, it was also noted that the surface strain appeared to be greater in the composite than in the base alloy in the near surface, as shown in Fig. 5.82, despite the fact that the yield stress of the composite was substantially higher than that of the base alloy. This could partly be attributed to the void formation in the near worn surface. As will be discussed in Section 5.6.3, the void

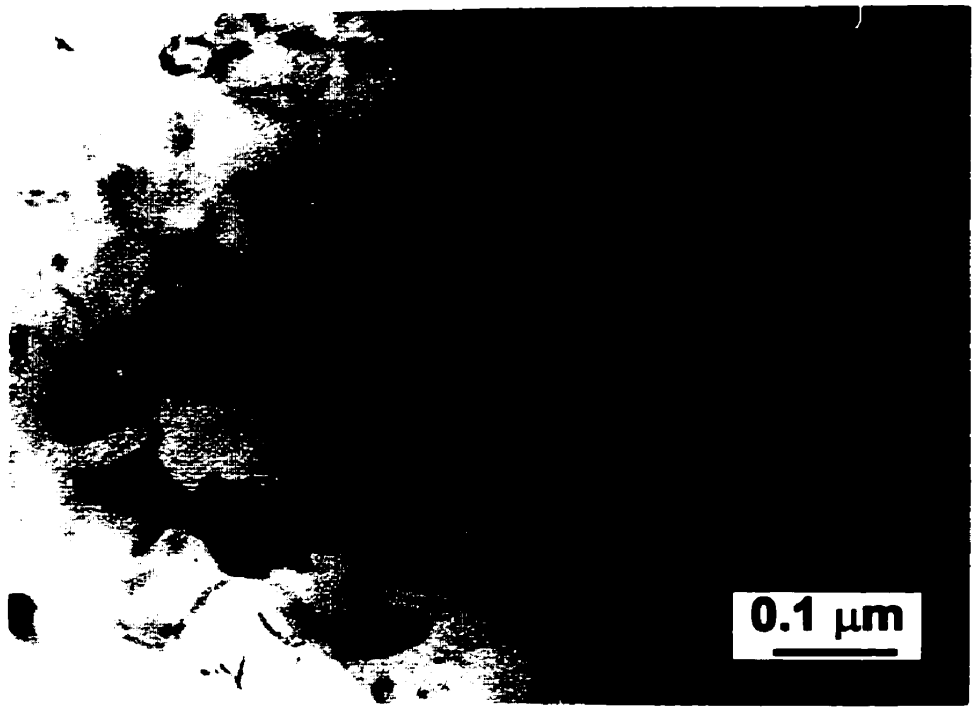

(a)

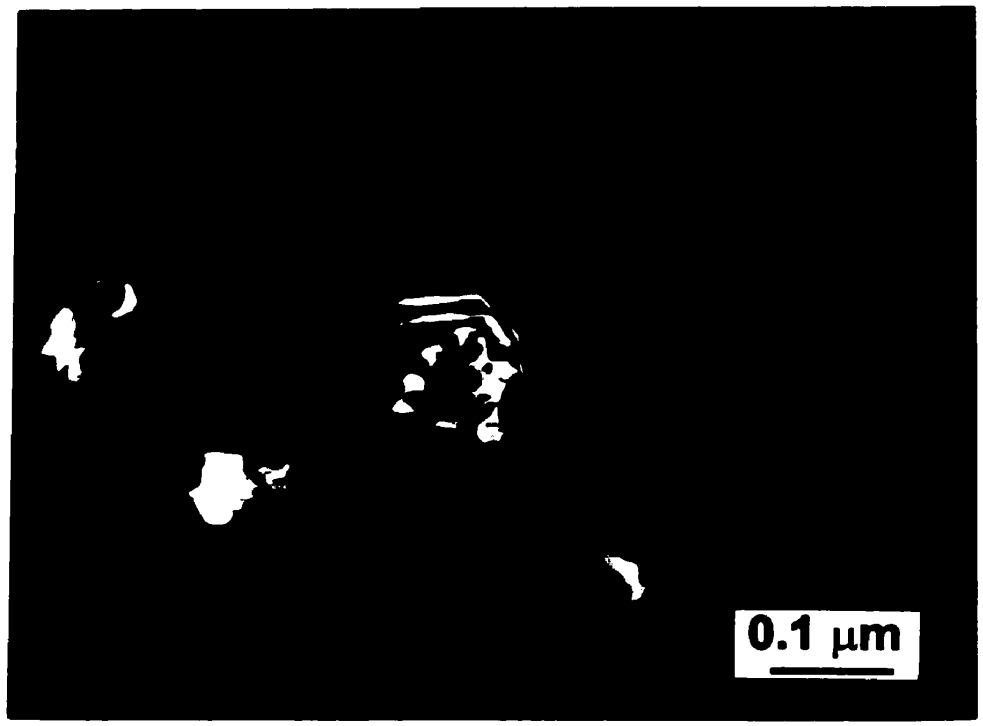

(b)

Fig. 5. 84 Recrystallized subgrains in a flake wear debris of the Al-Si alloy at a load of 10 kg. (a) Bright field, and (b) Dark field.

formation in the matrix and transparticle void formation as a result of fracture and fragmentation of the secondary particles or reinforcing particles, as observed using SEM, would contribute to an increase in local strains in the near surface. Moreover, the friction coefficient of the composite might be higher due to the addition of reinforcing particles in comparison with the base alloy [132]. As a result, the tangential force would be accordingly higher, so that a larger amount of strain would be formed in the near surface.

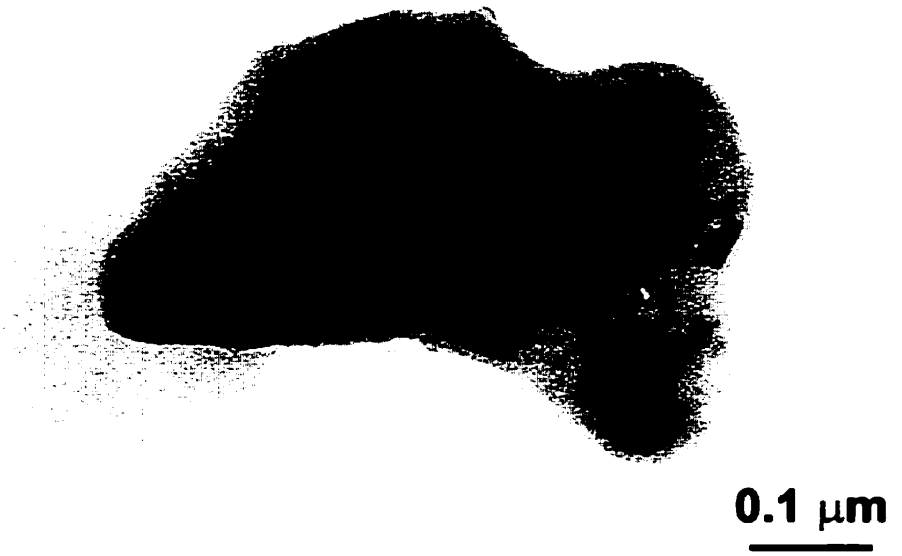

Fig. 5. 85 Subgrain structures in a flake-like wear debris of the Al-Si alloy.

5. 6. 2 The Mechanically mixed layer

The present work has provided evidence that a mechanically mixed layer was formed in the sliding wear of the HP Al, Al-Si alloy and Al-Si/SiC composite against the M2 steel under dry condition. The MML contained elements from both the sliding materials, and at a high sliding load, partial oxidation also took place in the MML. As observed in the present work, the MML was much harder than the bulk material. Fig. 5.86 shows a MML cross section of the worn surface of the HP Al at 5 kg, in which indentations were made along the depth using a microhardness indenter at a load of 15 g. The microhardness was about 170 HV, which was about 8 times higher than that of the bulk HP Al and was comparable with that of the MML in the base alloy. As will be discussed in Chapter 7, wear debris detached from the wear system were found to contain a significant amount of Fe which was obviously transferred from the steel counterpart, suggesting that the formation of wear debris was most likely related to the formation of the mechanically mixed layer. Therefore, the MMLs played a vital role in governing the wear performance of the materials.

It is well known that the transfer of materials from one component to another is quite common in a sliding system, and the importance of transfer phenomenon in understanding of wear mechanisms has been acknowledged [70-72]. At the initial stage of sliding wear, the actual contacts between the sliding surfaces are at some individual spots, i.e., asperities, on the microscopic scale. Friction caused by the sliding motion is actually dependent on the local asperity contacts. The conditions of sliding wear,

especially in unlubricated states, produce a high compressive pressure and large shear strains in the asperities. As confirmed in the present work and in other recent investigations [4, 56, 61, 77] on different material wear systems, it is evident that the heavy plastic deformation and shear strains in the worn surface gave rise to a large number of dislocation cells and elongated subgrains. The local fragmentation and fracture at some asperities could take place as the shear stress was sufficiently higher than the strength of the materials. Therefore, individual fragments could be detached as discrete particles from the surface. A similar process could also occur at the surface of the counterpart, especially in the Al-Si alloy and the composite where hard secondary particles of Si and SiC could act as microcutters and result in fine fragments of iron from the ring surface.

The transfer and mechanical mixing have been found in many sliding wear systems of Al alloys and Al based composites [4, 23, 72, 74, 78-80, 132-135]. Antoniou and Borland[34] reported that the mechanically mixed layers mainly consisted of an ultrafine mechanical mixture of Al, Si, and α–Fe particles during the sliding process, with no evidence of any oxides or Al-Fe intermetallics. Zhang and Alpas[52] recently suggested that the surface layers and the debris particles contained an aluminum oxide phase with an amorphous structure, in addition to the original phases of α-Fe and α-Al, based on the results obtained using X-ray diffraction(XRD). Venkataraman and Sundararajan[13] also reported formation of a mechanically mixed layer in the wear of Al reinforced with SiC particles and attributed the formation of the MML to a turbulent plastic flow as proposed by Rosenfield [122]. They emphasized that the formation of the

MML required a reinforcing particle that was harder than the mating material, based on their observations that the MML was found in the Al-SiC composites and no MML was noted in the case of Al in their wear system. Their statement seems rational and could be used to explain similar observations in the Al-Si alloy and the Al-Si/SiC composite in the present work. However, it is not in agreement with other findings in the present investigation as a mechanically mixed layer was also present in the worn surface of the HP Al and a considerable amount of Fe was noted in the MML using EDS. Fig. 5.87 shows the MML in the worn surface of the HP Al at a sliding load of 5 kg, and Fe distribution in the cross section of the worn surface can be clearly seen from the X-ray mapping as shown in Fig. 5.87(c). This is in agreement with the observation by Kou [136] in which Fe transferred from the counterpart was observed after a prolonged sliding cycle of Al. Based on the observation in the present work, it is evident that the presence of reinforcing particles with a higher hardness in the original materials is not a necessity for MML to occur during the sliding wear.

As pointed out by Rigney et al [70, 72] and Chen[71], fragmentation and transfer of materials could occur at a very early stage during sliding wear. The earlier fragments from both the contacting surfaces were likely to occur on local asperities, and subjected to a complicated process of mixing, compacting and smearing under the normal load and frictional force between the contacts during further sliding. These initial transfer fragments were highly strained [71], and work hardened [67]. As discussed earlier, although the bulk surface temperature was not very high because of the low sliding speed used, the local flash temperature at real contact asperities could be substantially higher.

Since the flash temperature was accumulated at real asperities that were very small, fragments mentioned above could be hot spots before they lost contact with the surfaces. Therefore, the elevated local temperature could be thermodynamically favorable for the interdiffusion during the mixing process caused by the sliding. With the heavy strain and frictional temperature rise, a possible oxidation and solid state reaction between the transferred particles could occur, and consequently, the reaction products of particles containing the transferred elemental Fe and oxides would be present in between the sliding contacts.

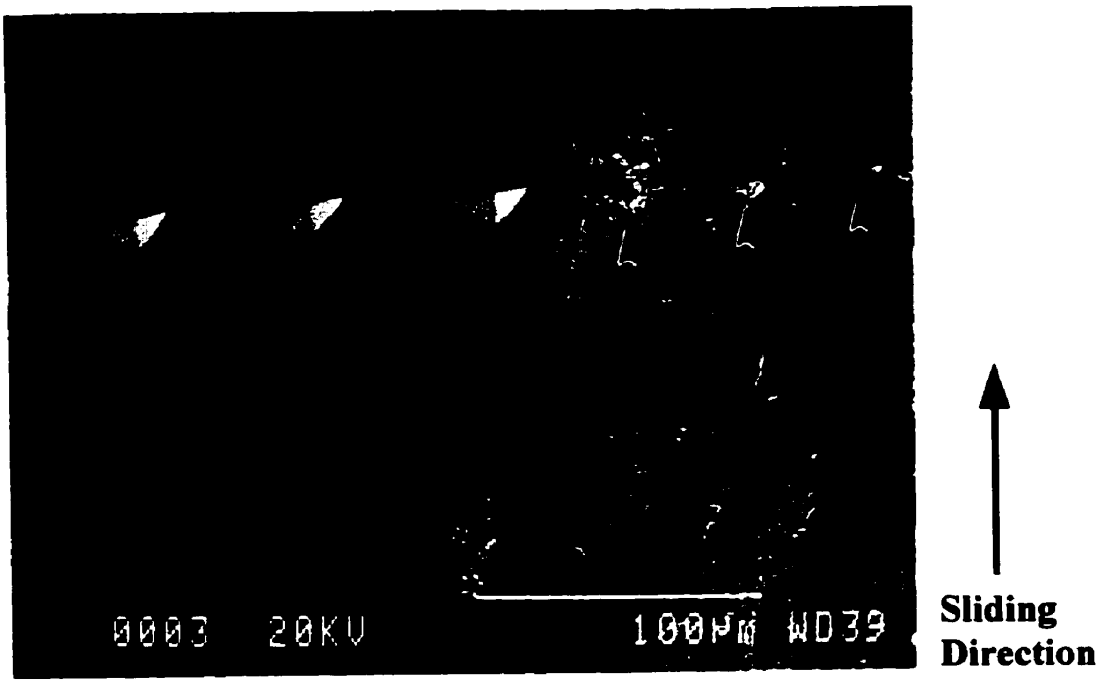

Fig. 5. 86 Microhardness indentation profile along depth below the worn surface in a cross section of HP Al at a sliding load of 5 kg. The indentation was made at a load of 15 g.

(a)

(b)

Fig. 5. 87 *(continued)*

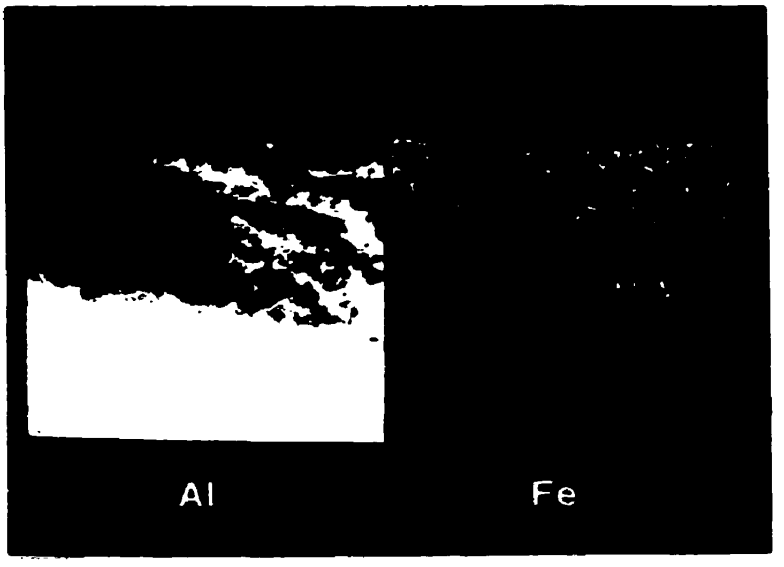

(c)

Fig. 5. 87 Mechanically mixed layer in the worn surface of the HP Al at a sliding load of 5 kg. (a) Secondary electron image; (b) backscattering electron image; and (c) X-ray mapping, showing presence of elemental Fe in the MML.

These in-situ formed particles could "reinforce" the MML as they were compacted and incorporated into the MML. Thus, a further transfer and mechanical mixing would be generated in the worn surface. Actually, a layered subsurface structure or a sandwich structure, in which alternate layers of a fresh Al matrix and mixed material (containing Al and Fe) were found to be present in the MML as shown in Fig. 5.29, has provided evidence of the above events. These mixed and compacted small elements would progressively accumulate and mix up in the worn surface, and as a result, transfer layers would be created. At this stage, fragments and the transfer layer could be a major load-bearing component since they were at direct contacts, and extremely high strains

acting on them could give rise to further fracture and fragmentation. With further sliding, extensive mechanical mixing of materials from both contact surfaces would be involved in more areas in the worn surfaces.

Based on the above discussion, i.e. the heavy shear strain in association with the frictional heat, the mechanical mixing process during the sliding wear is very similar to commercial mechanical alloying (MA) of metallic powders in a high energy ball mill [73], in which high strain deformation, fine cell substructure formation and diffusion-induced grain boundary migration resulted in the formation of intermetallic compounds. The microstructure and morphology of the nanocrystalline aggregates in the wear debris in this research work, as will be discussed in Chapter 7, also showed very similar features to those of nanocrystalline Fe-Al prepared by mechanical alloying [137,138]. Therefore, the α-Al solid solution with iron dissolved and the Fe-Al intermetallic phase formed in the wear debris can be reasonably attributed to similar mechanisms that occurred in the mechanical alloying.

The present results have also shown that with an increase in the sliding load, Al oxides coexisted with other phases in the MML and wear debris. This is an expected phenomenon since the wear system was exposed to air, and the strain level and frictional heat were enhanced as a result of the increased loads. The oxides could provide microstructural stability as a second phase in the ultrafine grained structures in the MML and wear debris, as proposed by Rigney[67, 72]. The oxides formed in the manner mentioned above were fractured and comminuted as they were brought into the further

sliding movement. Participating in the mechanical mixing process, the crushed oxides dispersed into the mixed surface layer, and acted as pinning source of the grain boundaries in the ultrafine mixture in the MML and in the wear debris.

From the examination of microstructural characteristics and formation mechanisms of the MML, it appears that the mechanical mixing played a vital role in the dry sliding wear of the Al alloys at the sliding loads used in the present work. Once the mixed surface layer formed, it provided a protection due to its high hardness. The mixed structures in the MML are similar to a reinforced composite, which could modify the surface properties of the sliding materials. Under further sliding, loose debris was detached or delaminated from the mixed layer as similarities of microstructure and chemistry in the MML and the wear debris were found. It is likely that the sliding wear took place by removal of materials in the mixed layer since cracks were observed in the subsurface and the MML in the present work. As mentioned above, the MML was not uniform across the entire wear track, and actually, it exhibited a wavy pattern in the cross section of worn surface. At some locations, "fresh" Al matrix was actually approached in the very near surface. This phenomenon is very likely related to the plastic flow during sliding induced deformation. As the plastic flow proceeded along the sliding direction, it was impeded by the material in front, and the material that had the maximum strain was often at a location where it was approaching the near surface. When the shear stress was in excess of the shear strength of the material, loose debris would be formed from the "fresh" local surface. Thus, the mixed layer could be replenished with "fresh" base materials with a large plastic flow in a manner mentioned above. As a result, the wear

performance was largely determined by the properties of the MML, and the wear rate could be influenced by the detachment or delamination of the MML and *in-situ* formation of new MML as the sliding continued.

5. 6. 3 The effect of reinforcement and second phase particles

As was shown previously, no significant increase in the wear resistance of the Al composite due to the reinforcement was observed at sliding loads above 5 kg, as compared to the Al-Si alloy. The wear behavior of the Al base alloy and the Al composite were similar at a load range from 5 kg to 15 kg. In this load range, it was often observed that the reinforcing SiC particles were fragmented and fractured in the subsurface of the worn surface (Fig. 5.34 and Fig. 5.35). Debonding of the reinforcing particles was noted occasionally as well (Fig. 5.19). The microcracks could propagate and consequently, delamination of the subsurface occurred. These observations are in agreement with many other researches [12, 13, 17-23]. Zhao et al [139] observed that at an elevated temperature tensile test, a particle reinforced composite failed with a predominant feature of voiding at the ends of reinforcing particles as a result of decohesion of the interface between the reinforcement and the matrix. While at a low temperature, particle fracture was the main damage prior to final fracture of the material, and the void nucleation might be formed in between the fragmented particles. Alpas and Zhang[17] proposed mechanisms of subsurface crack initiation and growth in the worn surface of an Al-Si/SiC particulate reinforced composite, based on their observations. The mechanisms involved (i) void nucleation around silicon particles; and (ii) crack formation by

decohesion of the SiC-matrix interface. The interfaces also provided preferential paths for the growth of subsurface cracks. The present work supports their mechanisms. Furthermore, cross sectional TEM studies of the worn surface have clearly shown evidence that fracture of the particles Si or SiC served as nucleation source of microcracks in the matrix and resulted in crack formation in the matrix. In this work, the crack formation as a result of decohesion of the SiC-matrix interface was found to be less than the transparticle void formation (Fig. 5.35). Once a particle cracked, additional local strain in the region surrounding the particle could be accommodated by growth of the transparticle voids. Upon further sliding, these fragments could be separated probably because of further mechanical mixing process and, consequently, the SiC particles became finer. The size reduction of the SiC particles may reduce the load-bearing ability of the particles, and thus the composite did not provide a superior wear resistance at a high load as compared at a low load.

5. 6. 4 The *in situ* precipitation during the sliding wear

The present results have shown that an *in-situ* precipitation occurred in the subsurface of the as-cast composites during the sliding wear. As mentioned above, extensive plastic deformation was generated in the worn surface. It is well accepted that the surface strains and associated changes in microstructure may be more salient by the sliding wear than those generated by conventional deformation processes [56]. It is energetically favored that the strain energy produced by sliding friction could be a driving force for the nucleation of precipitates and the precipitate coarsening. In terms of

work hardening theory, a large number of cells and dislocations are produced in the deformed layer. In the present study, it is evident that high density dislocations and dislocation loops coexisted with the precipitates (Fig. 5.65). The highly dense matrix dislocations were frequently decorated with the precipitates. Therefore, it is reasonable to assume that the preferential nucleation and growth of precipitates at dislocation sites could be occurring during the deformation process caused by the sliding wear. This has been confirmed by the present work that the initial nucleation and growth of the precipitates were found to be occurring preferably at dislocations in the worn surface of the composite (Figs. 5.74 and 5.75). This phenomenon is in agreement with the observations in other composite materials, for example 2124 aluminum alloy reinforced by SiC whisker conducted by Christman and Suresh[100].

With respect to the influence of the reinforcing particles, it has been shown that the addition of the hard particles increased the dislocation density of the matrix due to differential thermal contraction of the matrix and SiC on cooling [85-88, 140]. Arsenault and Fisher [85] proposed that the increased strength observed in Al-SiC composites could be accounted for by a high dislocation density in the aluminum matrix. By means of an in-situ TEM, they later confirmed that the increased dislocation densities were attributed to the difference of the coefficients of thermal expansion (ΔCTE) between the matrix and the reinforcing particles [88, 140]. Christman and Suresh[100] also reported that the increase in dislocation density due to SiC reinforcement might lead to an accelerated aging of the Al composites. In sliding wear of Al MMCs, some recent investigations have discussed the flow stress below the worn surface [13] and the presence of a deformation layer gradient[99]. In the present work, TEM results show that the dislocation density was very high in the subsurface of the worn surface, and that the precipitates were

frequently associated with the matrix dislocations. These features substantiate the existence of an interaction between the dislocations and the precipitates in the worn surface of the Al composite. It should be mentioned that no similar phenomenon of precipitation was noted in the worn surface of the unreinforced Al base alloy at the same sliding conditions. On the other hand, dislocation activities could provide channels for diffusion in such a way that diffusion rate through dislocations was very high, as proposed by other researchers [141] in sliding wear. The enhanced diffusion could also lead to precipitation and subsequent coarsening of the precipitates.

Strain effects on an enhanced precipitation were reported by Cottu et al [142] in Al composites in a tensile test at elevated temperatures (up to $565^{\circ}C$). The precipitation and dislocation behavior in the unreinforced alloy and the composite were compared. They found that the rod shaped precipitate density was higher in the composite than in the unreinforced material. The nucleation of the precipitates during the high temperature deformation was favored by the reinforcement. They attributed the precipitation phenomenon to a combined effect of strain and temperature. As discussed earlier, the bulk surface temperature during the sliding wear was directly measured by using a thermocouple welded to the specimen in this work. It was found that even at a load of 10 kg, the temperature rise showed an insignificant increase higher than the aging temperature, and was far below the solutionizing temperature, since the sliding speed used was very low. This result is in agreement with the estimation using the method provided by Lim and Ashby[44] and other investigations of dry sliding wear on Al-Si alloys and Al base/SiCp composites[12, 52, 101] in which bulk surface temperatures were estimated to be around 300K or less, at the load of 1.5-20 kg and at a sliding speed of 0.8m/s. These values are much higher than those used in the present work. As a result, it is reasonable to assume that the temperature rise resulting from frictional heating cannot significantly contribute alone to the precipitation and subsequent coarsening found

in the present work. The evidence that a number of dislocation loops were formed in the matrix and at the interface between the precipitates and the matrix, implies existence of interactions between the strain field of the dislocations and the strain field of the precipitates; and local flash temperature could also be higher. It, therefore, suggests that the formation of the *in-situ* precipitates could be due to the high stress in association with frictional heating.

As indicated in the wear tests, the wear resistance of the aged composite did not show significant enhancement due to the age hardening of the matrix, as compared to the wear resistance of the as-cast composites. Based on the above results and discussions, this could be partially attributed to the *in-situ* precipitation during the sliding wear of the as-cast composites, with respect to matrix hardening. It seems reasonable to propose that during the sliding wear, high shear stresses associated with the frictional heating induced an *in-situ* precipitation and work hardening through matrix dislocations. The precipitates acted as obstructions during the further plastic deformation, and the interactions between the precipitates and the dislocations in turn influenced the work hardening behavior of the matrix during the sliding wear. Such an effect may be similar to that resulting from the thermal aging of the composites. On the other hand, the existing precipitates could be coarsened as a result of the frictional temperature rise during the sliding wear of the previously T6 treated composite, as observed by the present author[143]. This suggests that overaging actually occurred in the worn surface of the previously T6 aged composite, and as a result, wear resistance of the T6 composite seemed to be higher than that of the as-cast composite at a higher load, for example, in Zone 3 as shown in Fig. 5.6.

CHAPTER SIX AMORPHIZATION AND PRECIPITATION WITHIN THE AMORPHOUS LAYER INDUCED BY RECIPROCATING DRY SLIDING WEAR OF Al-Si/SiCp COMPOSITE

6.1. INTRODUCTION

From the SEM observations, it has been shown that severe deformation and large plastic strains were present in the near surface below the worn surface of the Al-Si alloy and the Al-Si/SiCp composite as well as the HP Al, and mechanical mixing occurred in the sliding wear surface. Moreover, these features got enhanced during sliding wear of the ductile composite materials reinforced with hard second phase particles owing to the presence of the hard particles. Under certain conditions (load, sliding velocity etc.), wear of a metal matrix composite(MMC) can be treated as a three-body abrasive system (MMC, sliding ball and the fragmented particles) as the hard particles are forced away from the matrix and settle in the wear track during wear. In recent studies on the wear behavior of MMCs, Alpas and Zhang[23, 144] and Feng and Tandon[68] reported that a surface mixed layer (SML), in which the reinforcing particles SiC get fragmented and redistributed, was found during the wear of Al/SiC metal matrix composites. The mixed layer is very similar to the "transfer layer" defined by Alpas and Zhang[23] in which fragmented Al_2O_3-reinforcing particles were observed. These findings are in agreement with the observations of the mechanically mixed layer in the present work as discussed in the previous Chapter. It is therefore suggested that not only the reinforcing particles were fragmented and fractured, but also the presence of these particles resulted in large shear stresses and strains in the matrix, due to the fact that the hard particles constrained the plastic flow of the matrix during dry sliding wear. It is very likely that much stronger mixing of materials could occur under dry sliding wear conditions, and the resulting effects would be similar to the effects observed in mechanical alloying[73, 145]. The

effect would be more pronounced in the sliding wear of the materials with hard reinforced particles than in the unreinforced materials. This may possibly induce some non-equilibrium phenomena in the worn surface as well.

In this Chapter, a presence of an amorphous phase that was formed in the near surface of worn surface of the Al-Si/SiC composite during a reciprocating sliding wear under dry condition is reported and discussed. It has been reported in a few investigations that amorphous or nanocrystalline phases were induced by sliding wear[75, 76]. Recently, Bednar and D. Kuhlmann-Wilsdorf[77] reported that an amorphous film was found in sliding wear of silver on copper. They proposed that the formation of the amorphous alloy was due mainly to the severe plastic deformation rather than rapidly quenching [75] resulting from the frictional heating[44]. This consideration is more pertinent to the present work. As discussed in [77, 146, 147], potential applications of the amorphous tribofilms are most likely to be achievable as they could reduce friction and increase wear resistance. However, formation mechanisms of the wear-induced amorphous phases and related phenomena are still open to question, especially not only for the pure metal tribo-system, but also for multiphase materials. The present work discusses the formation of an amorphous phase and precipitation accompanying the formation of the amorphous phase in the near surface of the worn surface of the Al-Si/SiCp composite during a reciprocating unlubricated wear. By means of transmission electron microscopy (TEM) with an EDS attachment, the microstructural features of the amorphous and the crystallographic structure of the precipitates were characterized and identified. The internal twinning and the formation mechanisms of the precipitates as well as the amorphous phases are also discussed. The present work was initiated on the basis of a previous work[68] in which a mixed layer was found in the worn surface of the Al-Si/SiC composite in reciprocating dry wear. The experimental details have been reported in Chapter 4.

6.2. MORPHOLOGY OF THE AMORPHOUS PHASE AND PRECIPITATES

Fig. 6.1 shows transverse cross section of the worn surface of the Al composite under the dry reciprocating sliding conditions. It can be seen that the reinforcing particles SiC were fractured and fragmented in the near worn surface, and the α−Al solid solution of the matrix was fragmented into fine equiaxed particles in the worn surface. The phenomenon is similar to that of the MML reported in the previous chapter. It is also similar to those in the sliding wear of Al-Si alloy reinforced with Al_2O_3 or SiCp [17, 21, 23], and those in the sliding wear of other Al based alloys[4, 34, 148]. By using TEM, an amorphous phase intermixed with certain precipitates, was observed in the near worn surface, as shown in a longitudinal cross section of the worn surface in Fig. 6.2. The amorphous layer was found to be in thickness of about 0.5 μm- 3 μm parallel to the sliding direction. As is well known, there is no obvious contrast in the image of an amorphous phase under the conditions of electron microscopy. The foils were tilted by various angles over a large range($\pm 40^0$) in the double goniometer in TEM, however, no change in the contrast of the images of the amorphous phase was noted. The electron diffraction pattern of the amorphous region showed a typical diffusive ring or halo pattern, as shown in Fig 6.3(a). The EDS analysis of the amorphous area indicated that the phase was comprised of Al, Si and oxygen as shown in Fig. 6.4 (spectrum b). A similar spectrum (Fig. 6.4, spectrum a) consisting of Al, Si and O, was observed for the region B in Fig. 6.2, where the matrix was found to get smashed into fine grains, for which a polycrystalline diffraction ring pattern of a FCC structure feature was observed as shown in Fig. 6.3(b). The oxygen peak for the amorphous region was higher compared

to that in the polycrystalline region B. This is an expected phenomenon since Al in the very near surface was exposed to air during the wear process. It should be mentioned that no significant amount of Fe that may possibly come from the counterface was noted in the amorphous and ultrafine phases.

At a high magnification, as shown in Fig. 6.5, it can be seen that the area B was overlapped or intermixed with the amorphous phase and the ultrafine particles of the matrix, because the contrast of the images was changed by tilting the specimens in various angles and the corresponding diffraction patterns were shown as polycrystalline rings. It was also observed that some microcracks occurred in the crystallized area, and the microcracks were oriented parallel to the sliding direction. However, as mentioned above, no change in contrast was noted in the amorphous area except the larger precipitates, when the foil was tilted from (a) to (b) in Fig. 6.5.

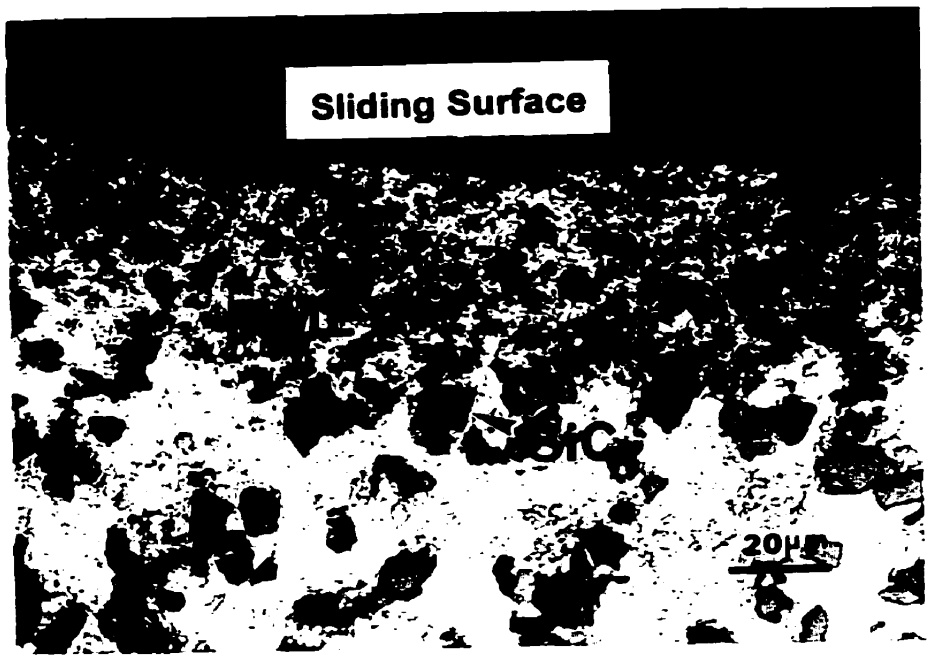

Fig. 6.1 Optical micrograph of the transverse cross section of the worn surface of Al-Si/SiC composite at a load of 1 kg, showing fragmentation of SiC in the near surface.

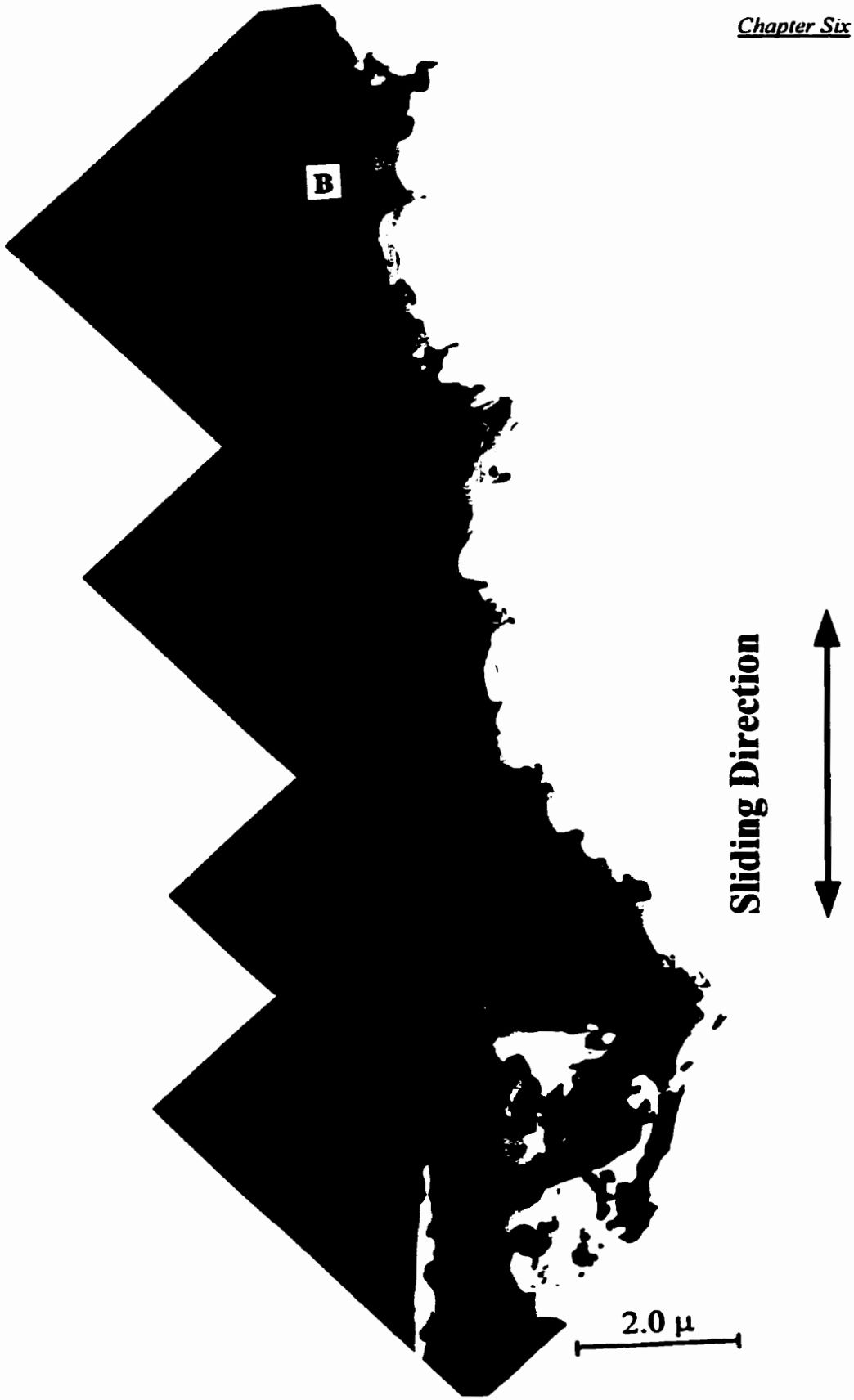

Fig. 6.2 An amorphous layer of Al-Si formed in the extreme worn surface of Al-Si/SiCp composite during the reciprocating sliding wear.

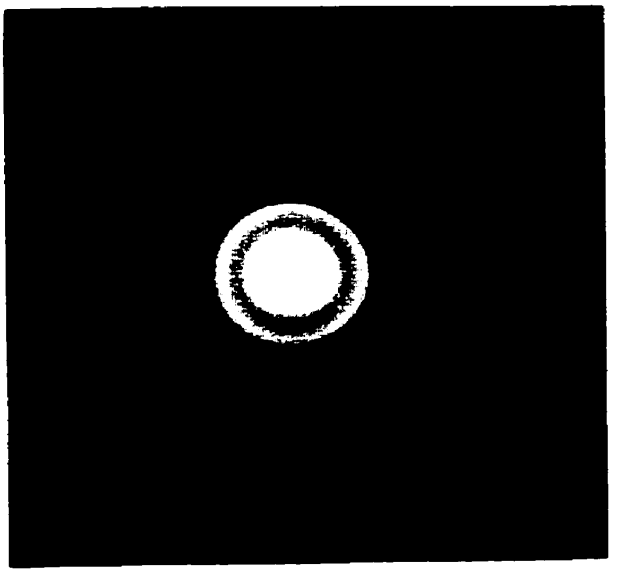

(a)

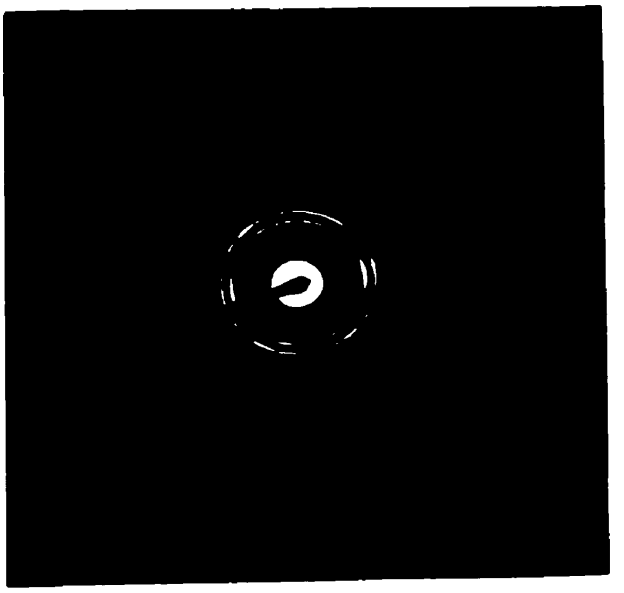

(b)

Fig. 6.3 Diffraction patterns of the amorphous phases (a) and polycrystalline phases (b) of very fine grains of Al(Si) in the worn surface.

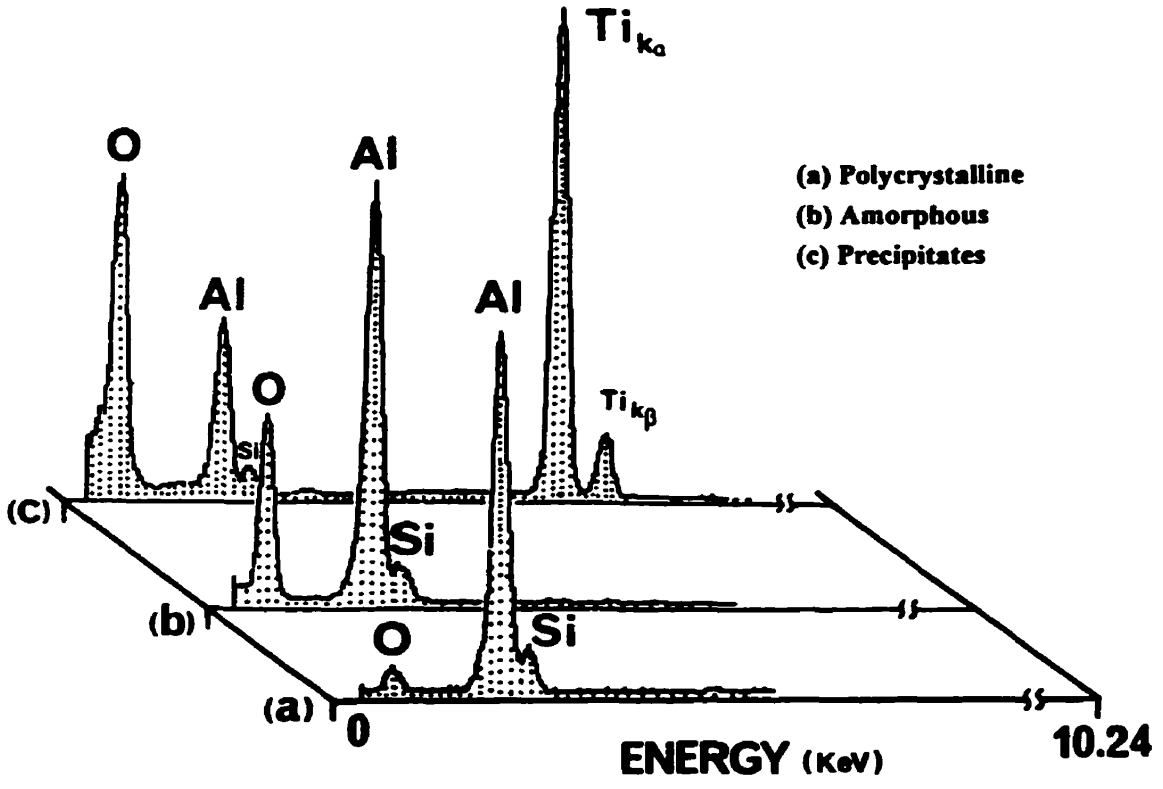

Fig. 6.4 EDS analysis of the ultrafine grained structure (a), amorphous (b) and the precipitate (c) phases in the near worn surface.

Moreover, it is of interest to note that a number of well distributed precipitates were present in the amorphous layer shown in Fig. 6.2. The morphology of the particles indicates equiaxed grains or square-like grains of the size of about 0.2 μm as viewed in the cross section and planar view of the specimens, as shown in Fig. 6.5 and Fig.6.6, respectively. It was also noted that cracks occurred in some particles, for example, a fractured particle is shown in Fig. 6.5(a). Furthermore, these particles were located within the amorphous layer and were not observed outside the amorphous layer which was localized in the near worn surface, about 6 μm below the top worn surface of the specimen. These features indicated that these particles might have been produced in

conjunction with the formation of the amorphous phase during the dry sliding wear. It is noticed (Fig. 6.4) that the EDS analyses of these particles showed two main peaks of titanium and aluminum in the spectrum c shown in Fig. 6.4. The EDS spectrum c was different from those of the amorphous phase (spectrum b) and the polycrystalline phase (spectrum a) of the α-Al solid solution corresponding to the area B in Fig. 6.2 where the matrix was fragmented into very fine grains during the sliding wear. It implies that these precipitates were not recrystallized grains from the amorphous phase because of the different compositions. It should also be noted that the oxygen peaks in the amorphous zone and the precipitates are higher compared to that in the polycrystalline zone. As far as the composition of the precipitates is concerned, EDS analyses show averaged atomic ratio of Ti/Al(Si) as 70:30 obtained from several particles. As is known, EDS analysis is relatively adequate for a quantitative analysis of higher -*Z* elements such as higher than Mg, Al, Si and Ti etc. But it is relatively insensitive to radiation from low *Z* elements and the results are only semiquantitative for C, N, O[149], Therefore, it is impossible to determine quantitatively the amount of oxygen by EDS in the present work. Based on the above observation, it is imperative to further investigate nature of the precipitates in order to understand the formation mechanism of the amorphous phase and the precipitates generated in the dry sliding wear.

6.3. CHARACTERIZATION OF THE PRECIPITATES

Fig. 6.7 (a) to (e) show the selected area electron diffraction patterns of a precipitate which were obtained when the particle was titled in TEM by keeping the

(a)

(b)

Fig. 6.5 Morphologies of the precipitates within the amorphous layer in the longitudinal cross section of the worn surface. The tilting angle of the thin foil was about 10° between (a) and (b). Zone A is the amorphous phase, and Zone B contains mainly fine crystalline grains.

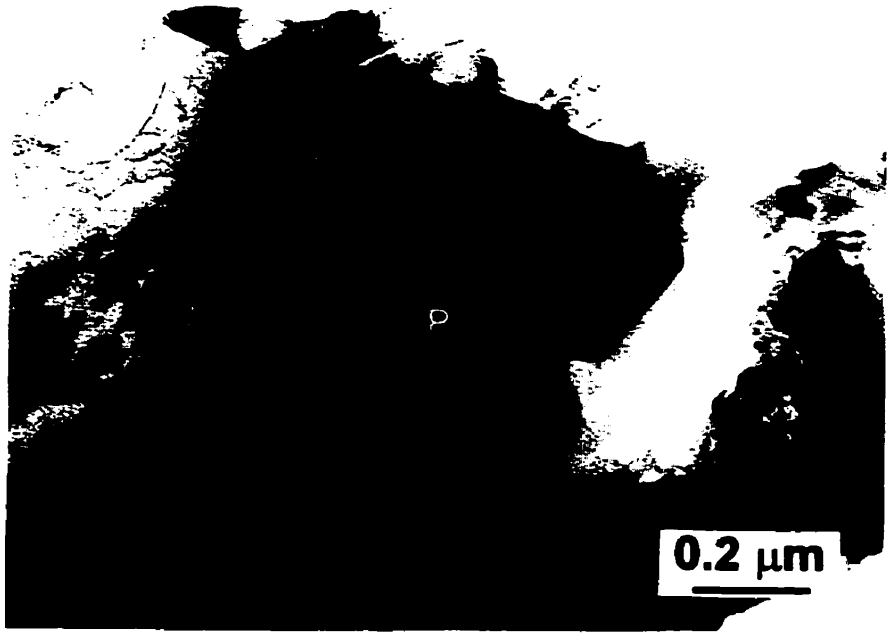

Fig 6.6 Morphologies of the precipitates within the amorphous layer in the planar view specimen of the worn surface, i.e., the thin foil was parallel to the worn surface.

shortest reciprocal lattice vector unchanged. By calculation and comparison of the symmetrical features according to the electron diffraction theory[150] and the method discussed below, these diffraction patterns could not correspond to those of any known phases [151] present in similar composite materials. Since a significant amount of Ti was present in the precipitates, crystallographic features of the diffraction patterns of the precipitates were also compared with intermetallic compounds such as γ- TiAl (L10 structure), $\alpha_2 - Ti_3Al$ ($D0_{19}$ Hexagonal structure)[152] and metastable Ti_2AlN (Hexagonal structure)[153], and TiO_2[154] as well, by using careful calculations and making comparisons. They are not found to be consistent for this precipitate with the

above mentioned compounds. It has also been noted that there exist several Ti-Al oxides listed in the X-ray powder diffraction standards(JCPDS, 1993 version). Namely, they are Al_2TiO_5(file No. 18-68), Al_2TiO_5(file No. 26-40, Orthorhombic, symmetry Cmcm), Al_2TiO_5(file No. 41-258, Orthorhombic, symmetry Bbmm), and Ti-rich phase $Al_2Ti_7O_{15}$(file No. 39-52, Monoclinic, symmetry C2/m). However, the diffraction patterns of the precipitates in the present work can not be interpreted in terms of those above phases, and the compositional information is also different even though $Al_2Ti_7O_{15}$ is close to the ratio of Al and Ti in the precipitates. The diffraction patterns of the precipitates suggest that it may have tetragonal feature based on the observation of the geometric features of the reciprocal lattices.

The suggested tetragonal symmetry was confirmed by convergent beam electron diffraction (CBED). Corresponding to the SAD patterns of [001] and <011>, the CBED patterns indicate 4mm whole pattern symmetry in zone [001] and 2mm whole pattern symmetry in zone <011> as shown in Fig. 6.8(a) and 6.8(b), respectively. It is well known, as indicated and reviewed for each of 32 crystal point groups by Buxton et al [155], that 4mm whole pattern symmetry in [001] and 2mm whole pattern symmetry in <011> are exclusively consistent with 4/mmm point group symmetry as cubic crystallographic features are easily excluded according to the observed SAD patterns. Correspondingly, the diffraction group and zone axis symmetries for the tetragonal structure are 4mm1R and 2mm1R for the [001] and <011>, respectively.

Based on the above crystallographic symmetry analyses, the SAD patterns of the tetragonal structure can be indexed in the light of reciprocal lattice geometry [150] and

the measurement of interangles between zone axes in TEM. The real space lattice can also be deduced from the reciprocal lattice as the camera constant was calibrated by the known metals Al and Cu. As a result, it was determined that the tetragonal lattice parameters are $a = b = 4.423$ Å, $c = 2.844$ Å.

Table 6. 1 **Comparison of Theoretical and Measured Parameters of Diffraction Geometry corresponding to Fig. 6.6.**

	Measured Values		Calculated Values				
Fig .No.	R2/R1	θ (°)	R2/R1	θ (°)	$(h_1k_1l_1)$	$(h_2k_2l_2)$	B=[uvw]
a	1	90	1	90	100	010	001
b	3.25	90	3.268	90	100	012	$0\bar{2}1$
c	1.83	90	1.848	90	100	011	$0\bar{1}1$
d	2.57	90	2.534	90	100	021	$0\bar{1}2$
e	3.44	90	3.384	90	100	031	$0\bar{1}3$

Table 6.2 **Comparison of theoretical and measured angles between different zone axes in Fig.6.6**

$\angle B_1 \wedge B_2$	Θ (Calculated)	Θ' (Measured)
$[001]\wedge[0\bar{2}1]$	72.18	69.71
$[001]\wedge[0\bar{1}1]$	57.25	56.96
$[0\bar{1}1]\wedge[0\bar{1}2]$	19.38	19.65
$[0\bar{1}2]\wedge[0\bar{1}3]$	10.47	10.28
$[001]\wedge[0\bar{1}3]$	27.40	26.72

Even though the camera constant was calibrated, errors in the lattice parameter calculations from electron diffraction patterns may arise from instrumental variations and some physical factors[150]. In the present work, the calculated lattice parameters were justified by following calibrations: (1) the reciprocal lattice should be self-consistent, i.e., the calculated reciprocal vectors should be consistent with the measured ones regarding

both the angles and plane spacing; and (2) more importantly, the interangles between two different zone axes should also be consistent with each other in comparison with

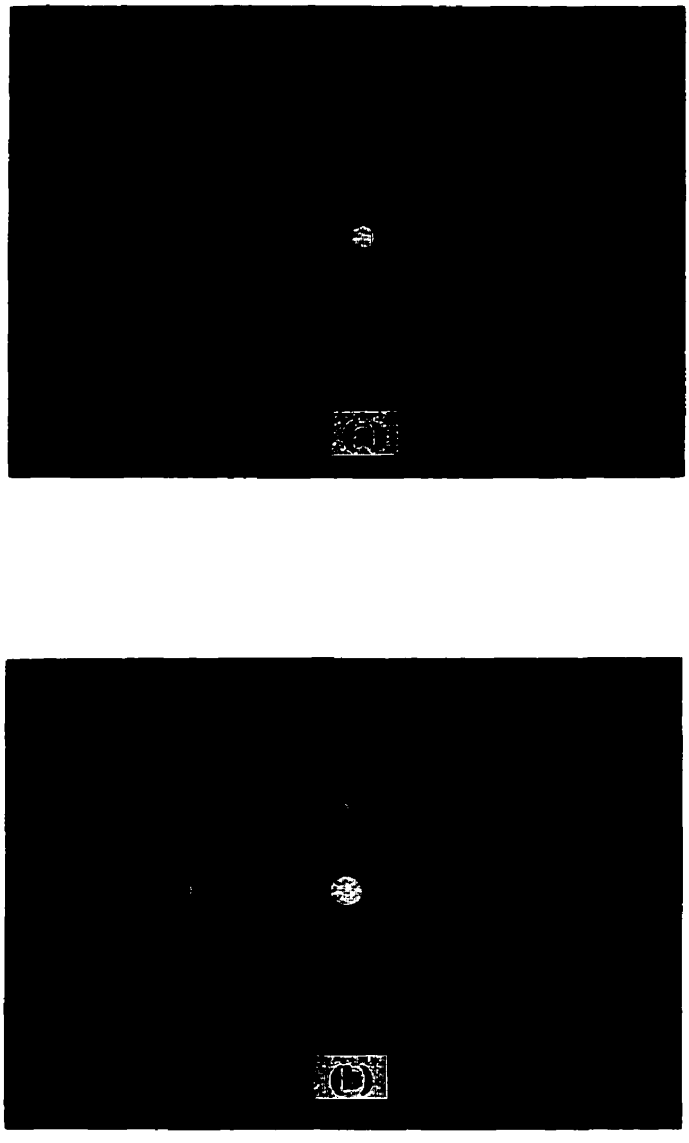

Fig. 6.7 *(continued)*

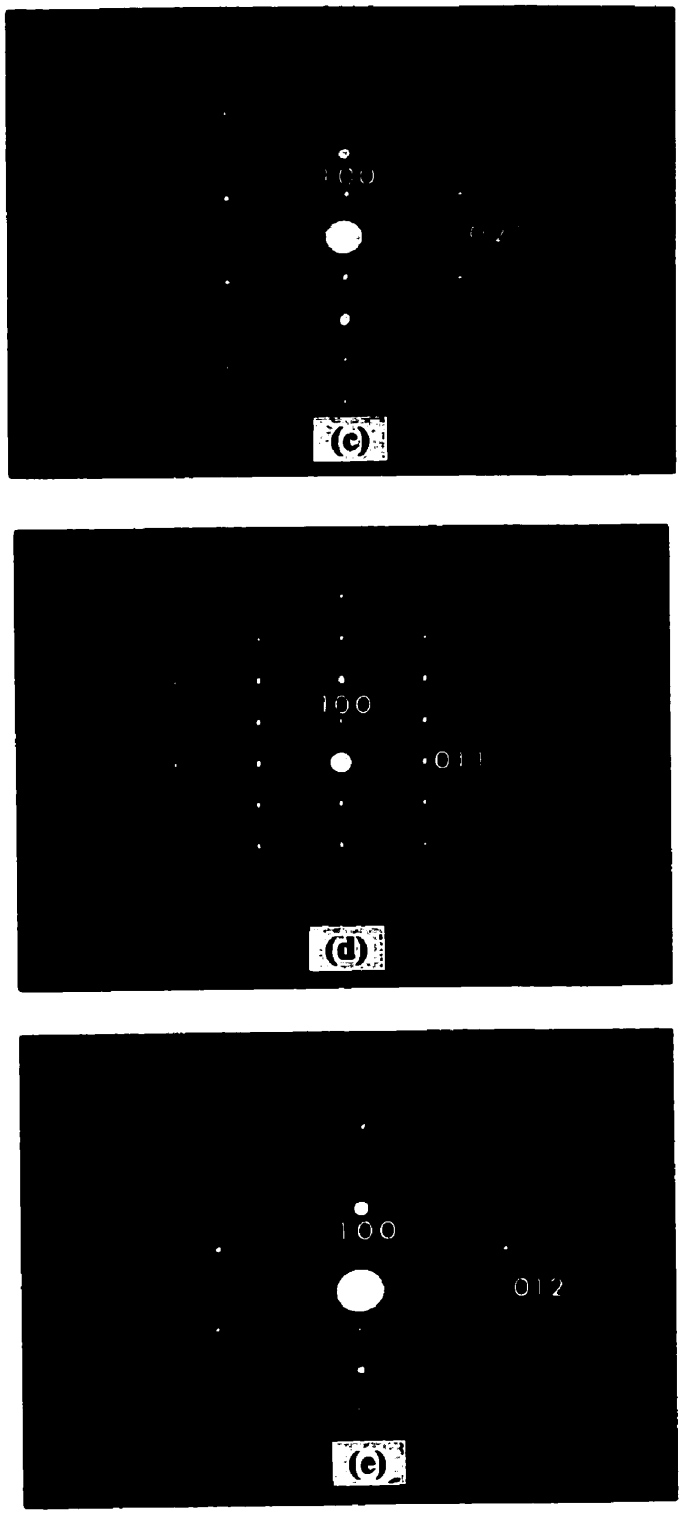

Fig. 6.7 Selected area diffraction patterns of the precipitates. (a) Zone [001], (b) $[0\bar{1}3]$, (c) Zone $[0\bar{1}2]$, (d) $[0\bar{1}1]$ and (e) Zone $[0\bar{2}1]$.

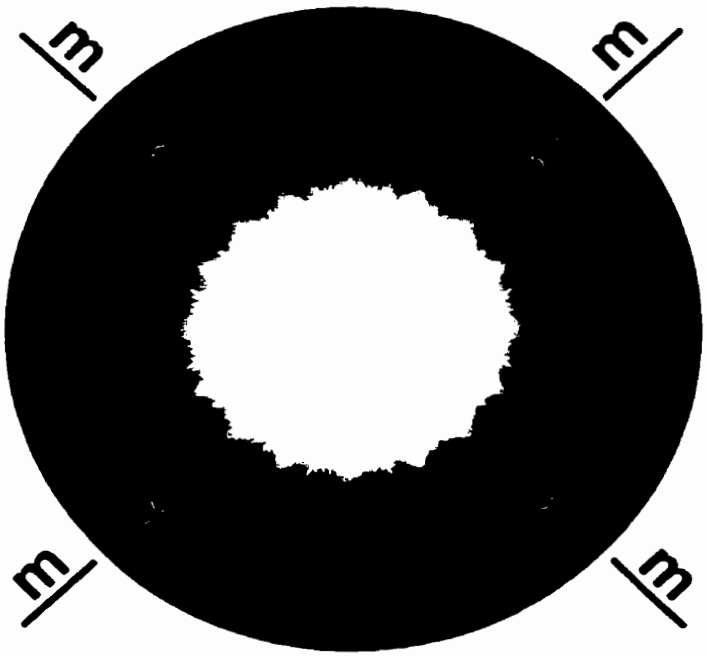

(a)

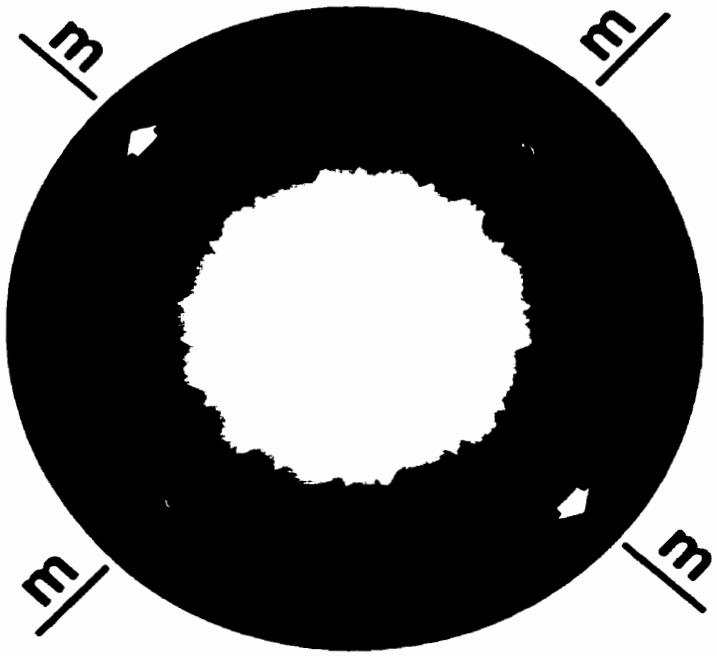

(b)

Fig. 6.8 Convergent beam electron diffraction of the zone axes [001] and [0 $\bar{1}$ 1] in the precipitates. (a) [001] showing 4mm whole pattern symmetry, and (b) [0 $\bar{1}$ 1] showing 2mm whole pattern symmetry.

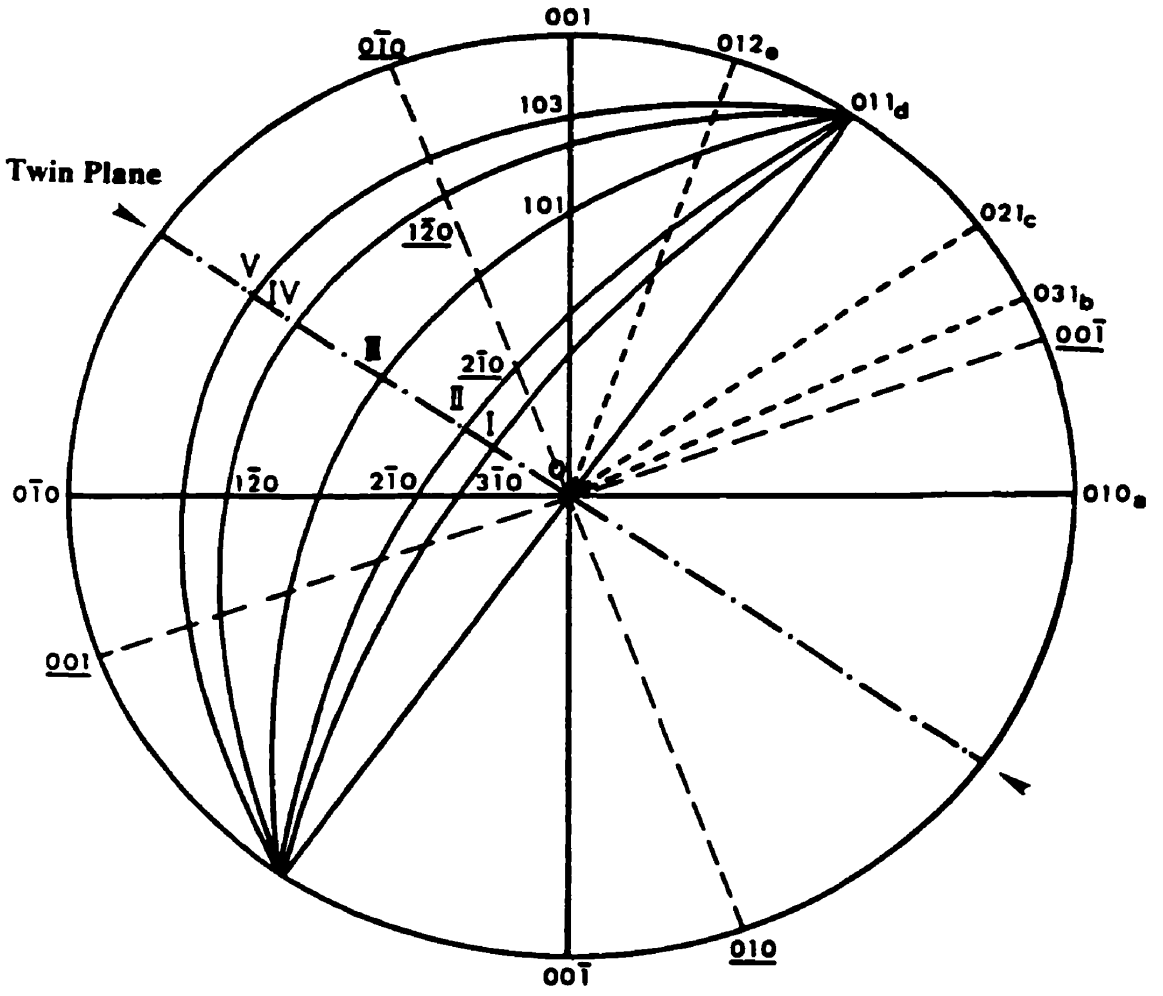

Fig. 6.9 (100) stereographic projection of the precipitates. Diffraction patterns in Fig. 6.7 are corresponding to the zones (a)-(e) in the projection, respectively. The internal twining is also shown in the projection, i.e., zones I-V correspond to zones (a) -(e) in Fig. 6.12.

the calculated values and the values measured by the double tilting goniometer in TEM. The measured and calculated values are listed in Table 6.1 and Table 6.2, where $\vec{R}_1$ and $\vec{R}_2$ are the shortest vectors of the two dimensional reciprocal planes, θ is the angle between $\vec{R}_1$ and $\vec{R}_2$ respectively. Θ is the calculated angle between two different zone axes, and Θ' is the measured angle in the double tilting goniometer when the crystal particle was rotated to get the diffraction patterns in different zone axes. The calculated values of the structure of the precipitate are in good agreement to the measured values as seen from the tables. The diffraction patterns in other zone axes shown in Fig. 6.9 and discussed below, are also consistent with the suggested structure by using calculations in the above manner. Fig. 6.10 shows the stereographic projection (100) and the rotating sense corresponding to the Fig. 6.6(a) to (e).

6.4. INTERNAL TWINNED GROWTH

Internal twinning was also observed in many precipitates. Fig. 6.10 shows the morphological features of the internal twinning. As shown by arrows in Fig. 6.11, the internal twins were apparently observed in this random orientation of the specimen to the electron beam in TEM. The corresponding diffraction patterns of the internal twins are shown in Fig. 6.12 in a manner such that the twin plane was kept parallel to the electron beam and twinning axis perpendicular to the electron beam with respect to zone axis changes from zone O to zones I, II, III, IV and V in the stereographic projection (100) of the tetragonal structure shown in Fig. 6.9. Therefore, it is determined that the twin element of the precipitates is (011)[011]. Again, as discussed above, the diffraction patterns corresponding to the internal twinning were verified with the tetragonal structure

by carrying out two ways of calibration, i.e., of reciprocal plane self-consistent in a zone axis, and interangle agreement of two different zone axes in comparison of the calculated and measured values. They were found to be consistent with each other.

6.5. DISCUSSION

As described above, the amorphous phase was formed in the mixed layer of the worn surface where fragmentation of SiC particles was observed, and the precipitation of the tetragonal structure phase most probably coincided with the formation of the amorphous phase during sliding wear of the composite. The sliding between the two counterparts can produce heavy deformation of surface layers, in addition to the frictional heat. Actually, the bulk surface temperature of the sliding parts can be estimated by using the approach developed by Lim and Ashby[44]. In some investigations of dry sliding wear on Al-Si alloys and Al-base/SiCp composites[12, 101], the bulk surface temperatures of the Al matrix were estimated to be around 300 K or less, where the normal loads(1.5 kg to 20 kg) and the sliding speed (0.8 m/s) were much higher than those in the present work. The sliding speed (0.1 m/s) in the present work was slow so that no appreciable frictional heating (T_F) higher than the melting point (T_M) of the matrix occurred at the normal load (1 kg), i.e., $T_F << T_M$. As a result, the solid state amorphization and the related phenomenon are very likely to be attributed to the heavy plastic deformation induced by the sliding wear. It has been accepted that the wear induced deformation generates a large number of defects such as vacancies, interstitials, dislocations and subgrain boundaries, as discussed in Chapter 5. The reinforcing SiC particles were fragmented and redistributed in the mixed surface layer during the wear as indicated in Fig 6.1. This led to changes in morphology and microstructure of the mixed surface layer of the composite in the sliding wear, which was also confirmed by the

(a)

(b)

Fig. 6.10 Morphology of the internal twin particle within the amorphous layer. (a) Bright field, and (b) Dark field.

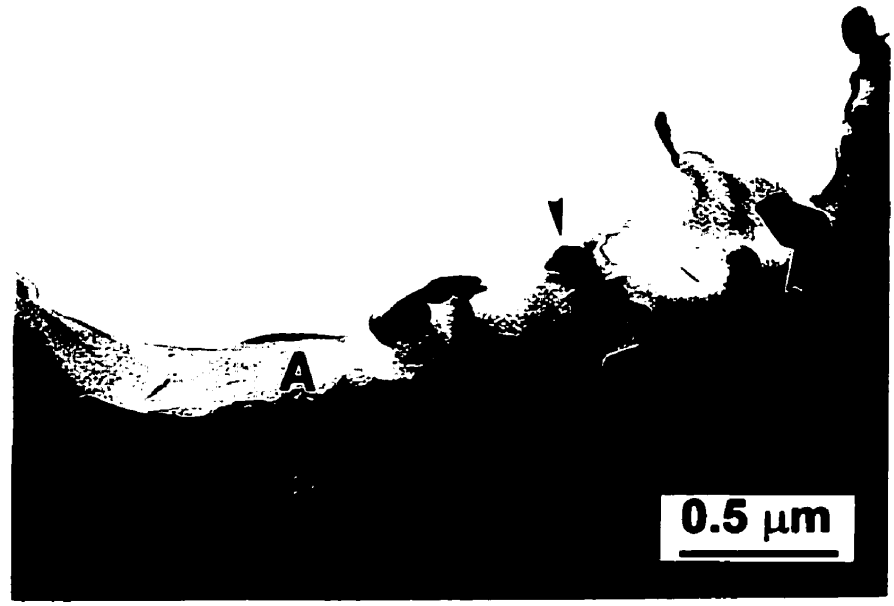

Fig. 6.11 TEM micrograph of the amorphous layer coexisting with the precipitates. Note that internal twining occurred in some of the precipitates as indicated by arrows.

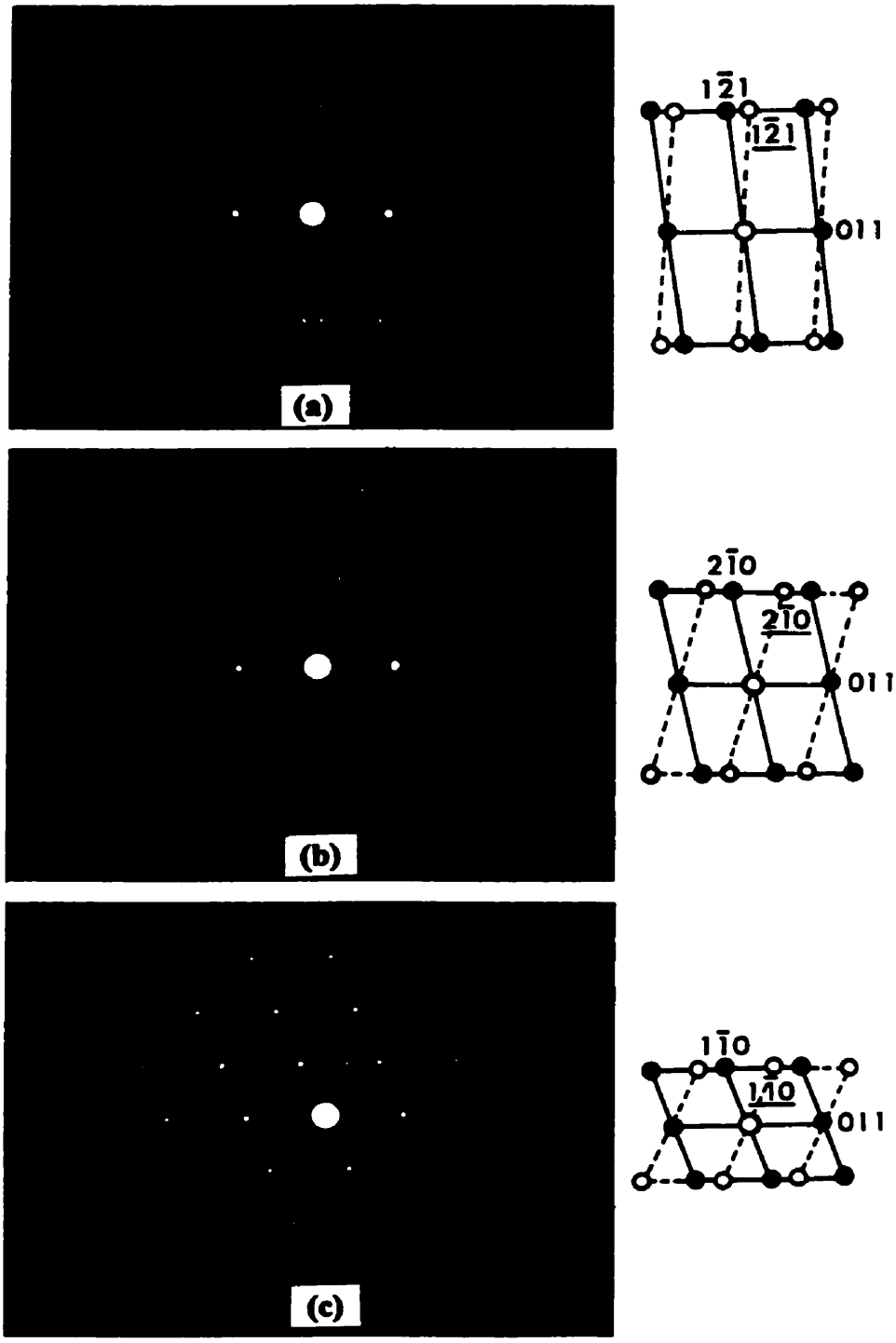

Fig. 6.12 *(continued)*

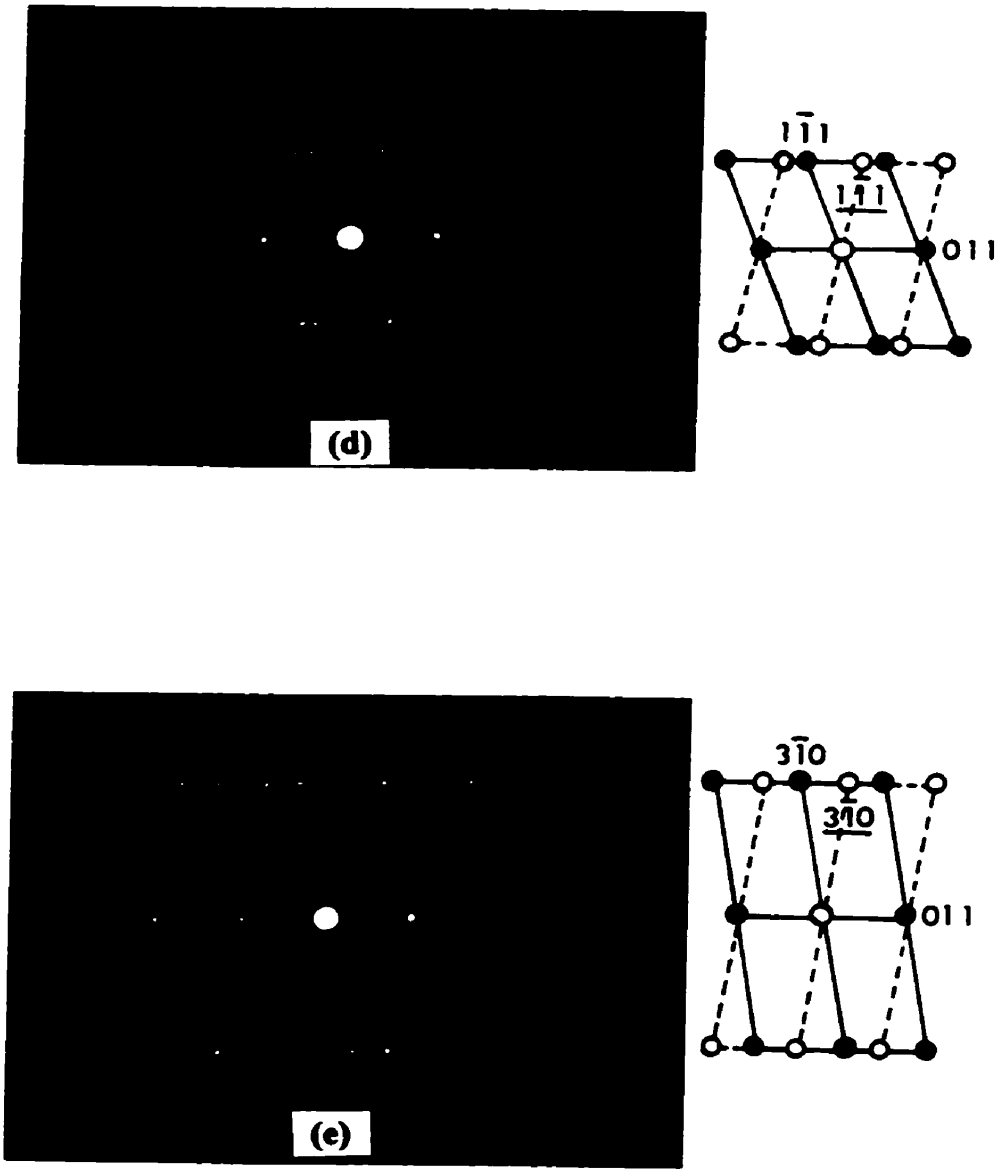

Fig. 6.12 Selected area diffraction patterns of the twin particles. (a) Zone $[\bar{1}\,\bar{3}\,3]$, (b) Zone $[\bar{1}\,\bar{2}\,2]$, (c) Zone $[\bar{1}\,\bar{1}\,1]$, (d) Zone $[\bar{2}\,\bar{1}\,1]$ and (e) Zone $[\bar{3}\,\bar{1}\,1]$.

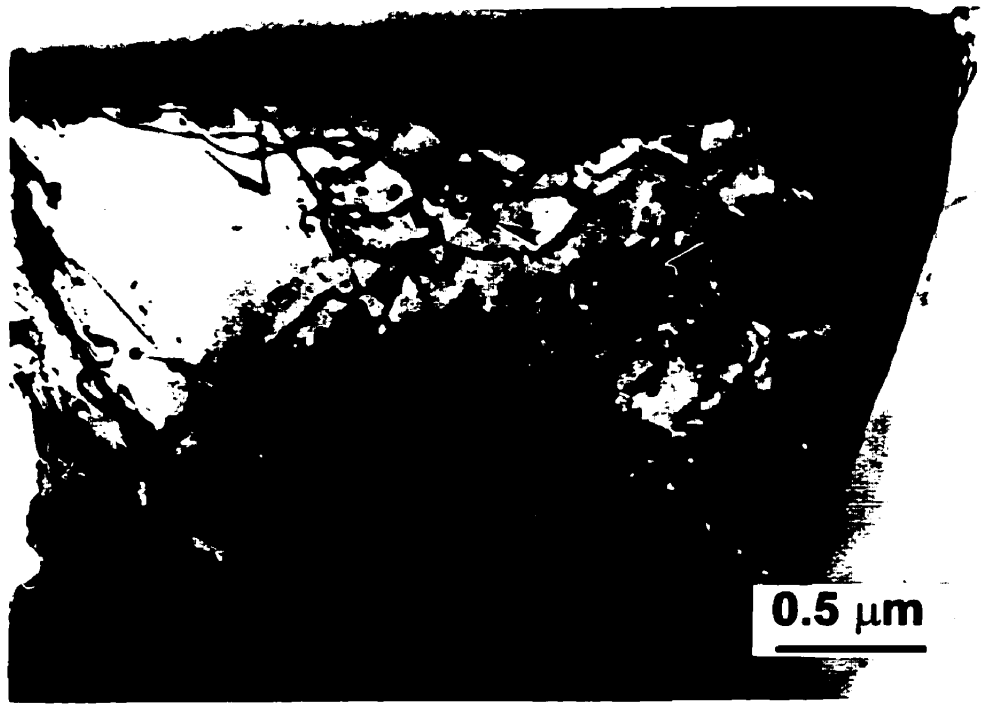

(a)

(b)

Fig. 6.13 *(continued)*

(c)

(d)

Fig. 6.13 Dislocation structures in the subsurface below the worn surface of the composite. Note that dislocation loops were formed as a result of dislocation interactions and movement, such as climbs, in the subsurface. Some dislocation loops were about to form as indicated. (a) B=[101], $\vec{g}$=[111], (b) B=[101], $\vec{g}$=[111], (c) B=[101], $\vec{g}$=[111], and (d) Weak beam dark field, $B = [101], \vec{g} = [111]$.

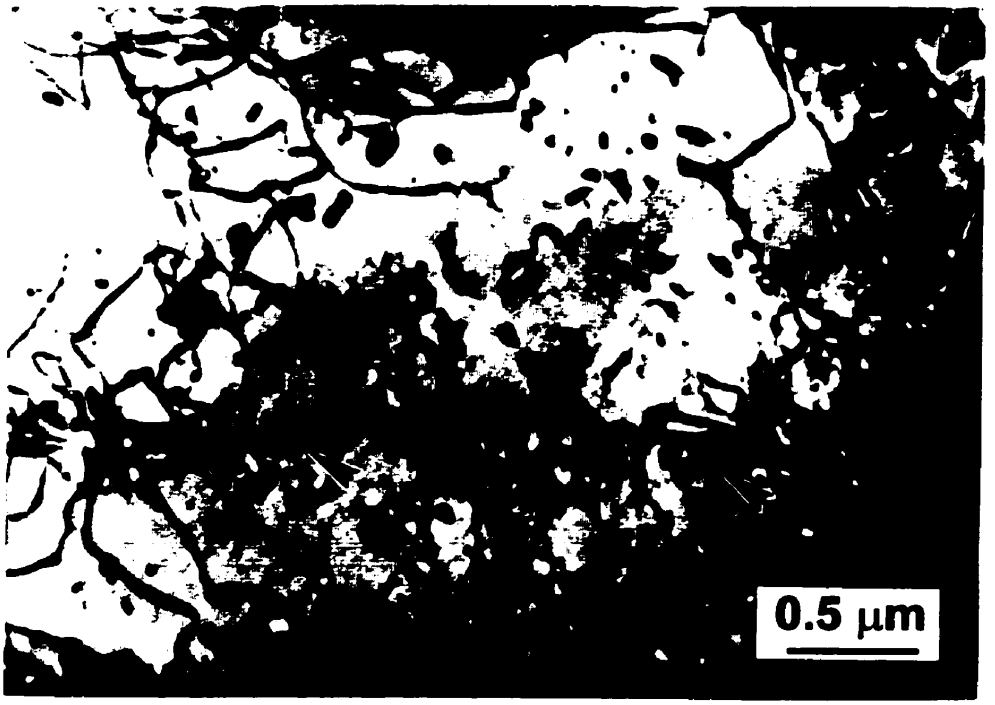

(a)

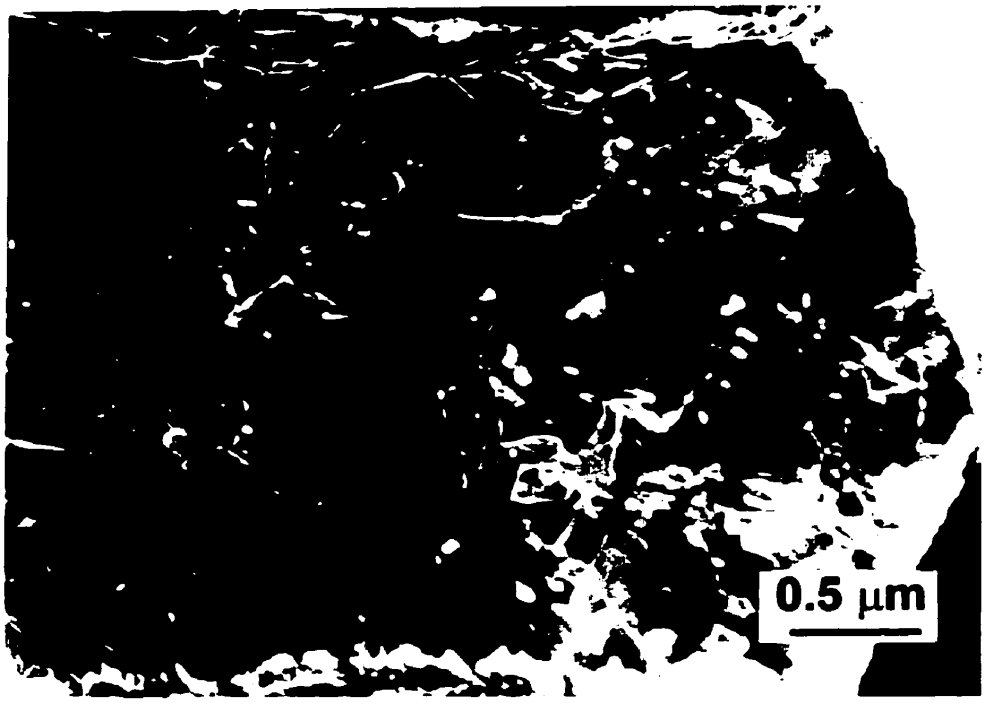

(b)

Fig. 6.14 Dislocation structures in the subsurface below the worn surface of the composite at a high magnification. Note that some dislocation loops, as indicated, were formed probably on the same slip plane. (a) Bright field, B=[101], $\vec{g}$=[111], and (b) Weak beam dark field, $B = [101], \vec{g} = [111]$.

fact that α-Al solid solution was refined mechanically in the mixed surface layer during wear[156]. Therefore, the wear process could be treated similar to mechanical alloying which has been shown to produce amorphous transformations in powder metallic materials[73, 157, 158], especially with the occurrence of the hard reinforcing particle SiC. As is well known, during a sliding motion high compression plus shear stresses result in a large number of cells and dislocations in the worn surface. In terms of D. Kuhlmann-Wilsdorf 's work hardening theory in which cell structure is pronounced and dislocations are quite mobile in the deformed metals, some of dislocations generated and located in grain boundaries can be driven into motions which are kinetically preferable compared with thermodynamic factor under these conditions[158]. Figs. 6.13 (a) to (c) show dislocation arrangement in a subgrain in the subsurface of the worn surface in the longitudinal cross section sample. The images were obtained by tilting the thin foil using different reflection operation $\vec{g}$. It can be seen that a number of dislocation loops were formed, and some of loops were about to form most probably as a result of dislocation climb, for example, the dislocations as indicated in the figures. Fig. 6.14 shows the dislocations at a higher magnification at a different $\vec{g}$ as compared to Fig. 6.13(a). A group of dislocation loops were noted lying on the same direction as indicated by arrows. It can be determined that these loops are very likely on the same slip plan, but it is beyond the present study. It is evident, however, that the dislocations were quite mobile and dislocation movements were active in the subsurface of the worn surface. The motion of the dislocations can result in the grain boundary migration and proliferation as schematically shown in Fig. 6.15. The grain boundary spacing D could decrease as a

result of the proliferation in a certain volume. According to [159], critical spacing D of the boundaries is logarithmically inversely proportional to the critical shear strain under which the dislocations are driven into motion. On the other hand, break-down of grain boundaries can also act as a source of dislocations, thus resulting in the cascade proliferation of dislocations during the severe deformation. Consequently, behind the moving of the dislocations a disordered region occurs which corresponds to local amorphous region. In summary, the movement of the dislocations produces disordered regions which may contribute to the formation of local amorphous zones and induce the microsegregation[160] of Ti element which is primarily added as a grain refiner[161] during the casting of the composite. Some immobile dislocations accompanying the above dislocation motion and multiplication responsible for the amorphization can provide sites for the nucleation of the crystalline precipitates as a result of strain induced microsegregation.

Regarding the existence of the reinforcing particle SiC, its possible influence on the formation of the amorphous layer may be attributed to the fact that the addition of hard particles enhances the dislocation density of the Al matrix due to the different coefficient of thermal expansion(CTE) of the SiC particles and the Al matrix[85-88], and the hard particles act as an obstruction during the plastic deformation caused by sliding wear. It was observed in the previous SEM work and the work conducted by Feng and Tandon[68] that the depth of the surface mixed layer, in which the fragmented SiC particles and the amorphous layer were found, increased with the sliding cycles under a certain load and with the loads at a given sliding cycles. The observations suggest that the existence of the mixed layer was dominantly dependent on the contact stress and the

sliding cycles (or the sliding distance). No mixed layer existed at all when the contact stress dropped. Therefore, it is reasonable that local shear behavior could be altered by the hard particles, and the presence of the fragmented SiC particles, due to the incorporation of the contact stress and the sliding cycles, further enhances the mechanical mixing during the sliding wear.

It is well known that the defect concentration caused by mechanical attrition will raise the Gibbs free energy of crystalline phases. As proposed by Schwarz[145, 157], the amorphization by mechanical alloying could be explained by Gibbs free energy differences between the crystalline phases and the amorphous phases. Fig. 6.16 schematically shows the thermodynamic consideration of the two phases. Curves 1 and 2 are free energies of the amorphous and the crystalline phases in a binary system, respectively. The free energy of the solid solution (curve in dotted line) is raised by creation of a large number of defects induced by the wear deformation, thus resulting in a large discrepancy of the Gibbs free energy required for the amorphization. According to the common tangent line rule, the composition of the amorphous phases should be corresponding to the line of the common tangent line, i.e., at x_1. It can be noted that the composition of the amorphous phase could be extended to x_2 owing to the rising Gibbs free energy. It implies that the amorphization composition range of the alloys in a deformation mechanism under mechanical alloying is broader as compared to amorphization under a thermal mechanism (rapidly quenching). Similarly, the rising free energy caused by the defects could also contribute to the segregation of Ti as described in Maxwell-Boltzmann relationship:

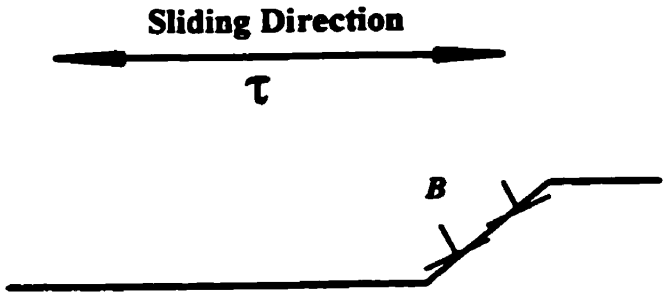

(a)

(b)

Fig. 6.15 Schematic illustration of dislocation model. Dislocation B suffers severe stress. Some of the dislocations are driven into motion, and some are immobile. A local amorphous region occurs behind the moving of the dislocations and the grain boundary migration.

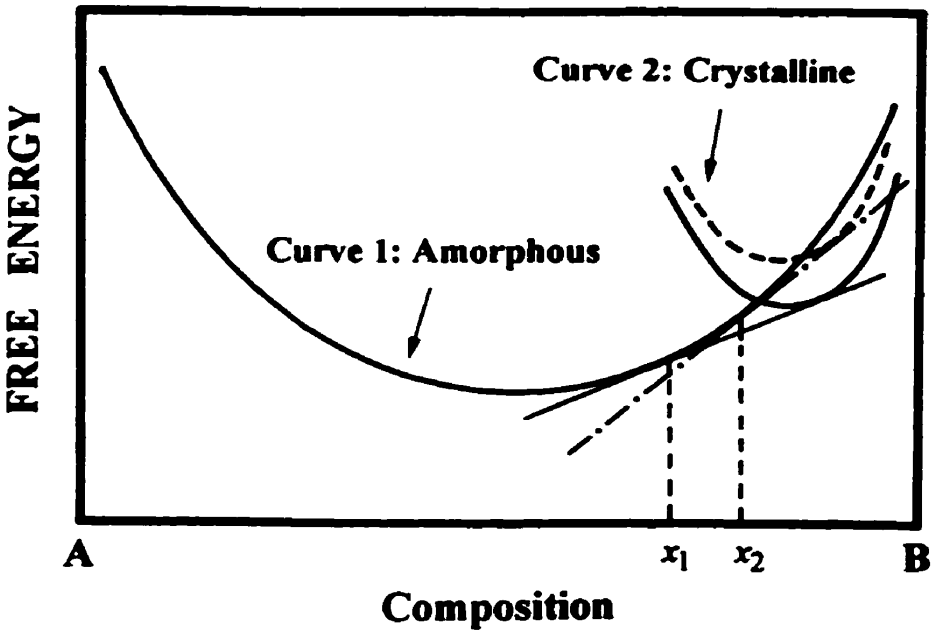

Fig. 6.16 Schematic Gibbs free energy diagram for a binary system AB regarding formation of an amorphous phase.

$$\frac{x_p(\mathrm{B})}{x_s(\mathrm{B})} = \exp(-\frac{\Delta G}{RT})$$

where $\Delta G = G_p - G_s < 0, x_p(\mathrm{B}), x_s(\mathrm{B})$ are fraction covered with segrant and bulk solute fraction, and G_p, G_s are free energies of the precipitate and the solid solution, respectively. The segregation will increase as the free energy difference, $|\Delta G|$, increases due to the increase of G_s.

It is noted that the EDS analysis of the precipitate shows a peak of oxygen occurring in the particles shown in Fig. 6.4. This is an expected phenomenon since Al matrix in the very near surface was exposed to the fresh air during the wear process. Preferential depletion of Ti caused by oxidation in a local zone may also explain the fast diffusion of Ti owing to the stronger affinity of Ti to oxygen. Actually, in Al-rich alloys with 0.12-0.15 %Ti, Ti-Al intermetallic phases have been observed to precipitate in a peritectic reaction[161].

As the precipitates were observed to have internal twinning, the twins did not produce a shape change in the single crystal of the precipitate. It seems that the twins were formed in the embryonic nuclei and not in their mature grains by the subsequent shear process during wear deformation. They grew coherently at parallel sides mirrored by the twin plane, and the nucleation of the growth twins may originate from defects such as stacking faults for which the energy required for the coherent twin growth would be smaller compared to untwinned precipitates. Such a stacking fault may exist in the migrating grain boundaries associated with the amorphous formation as a result of dislocation motions, and the stacking energy of local areas could be reduced because of the segregation of Ti. It is well known that in some cases of plastic deformation, fracture could propagate preferentially along the coherent twin boundaries. Actually, as mentioned above, microcracks were observed in some particles shown in Fig. 6.5, which most probably occurred at the twin boundaries due to severe shear deformation during the sliding wear. These characteristics may, on the other hand, substantiate the fact that the formations of the precipitates and the amorphous layer are due to the severe deformation caused by the dry sliding wear.

6.6. SUMMARY

The present work has provided a new evidence of the formation of amorphous phase induced by sliding wear on the Al matrix composites under reciprocal dry wear. Coexisting with the amorphous phases, precipitate Ti-Al-O was identified as a tetragonal structure which is different from the well-known Ti-Al intermetallic or oxide compounds. The lattice parameters of the tetragonal structure are: $a = b = 4.423$ Å, $c = 2.844$ Å. Internal twinning with the element (011)[011] was also found in the precipitates. The formation mechanisms of the amorphous phase and the precipitates are explained as follows:

1) In terms of dislocation and grain boundary migration: mechanical grinding and mixing caused by the sliding wear result in dislocation movements and grain boundary migration thus promoting the proliferation or multiplication of the dislocations and the grain boundaries. When they have broken down, a local amorphous region occurs. Accompanying this amorphization, a unique crystalline precipitate is also formed due to the defect-induced microsegregation.

2) In terms of Gibbs free energy: thermodynamically, the Gibbs free energy of a phase is increased with increasing level of defects caused by plastic deformation during the dry sliding wear, thus the free energy of the crystalline solid solution is greater than that of the amorphous phase, i.e., a large negative heat exists, which is required for the amorphization.

CHAPTER SEVEN MICROSTRUCTURAL CHARACTERIZATION OF WEAR DEBRIS

7.1. INTRODUCTION

As discussed earlier, a reliable approach to understand the wear mechanism in sliding wear is to experimentally investigate nature of the resultants of the wear system[57], namely, worn surface and wear debris. From previous chapters, it has been shown that not only do large subsurface strains and extensive plastic deformation are generated near the worn surface during the wear process, but also a considerable amount of transfer of materials and mechanical mixing take place between the contacting surfaces, thus resulting in the formation of a mechanically mixed layer in the worn surface. On the other hand, wear debris, that fall off the wearing system as schematically shown in Fig. 7.1, can provide information about single and instant events during the sliding wear, some of which might not be available from the worn surface due to possible influences of subsequent events. Therefore, an understanding of the nature of the wear debris, especially their microstructures and composition, could provide important insight into the wear mechanisms of these alloys and substantiate the findings that were obtained from the observations on the worn surfaces.

This Chapter deals with the characterization of the wear debris from the Al-Si alloy and the Al based composite sliding against the M2 steel using Scanning Electron Microscopy with EDS attachment and X-ray mapping, X-ray diffraction, and Mössbauer

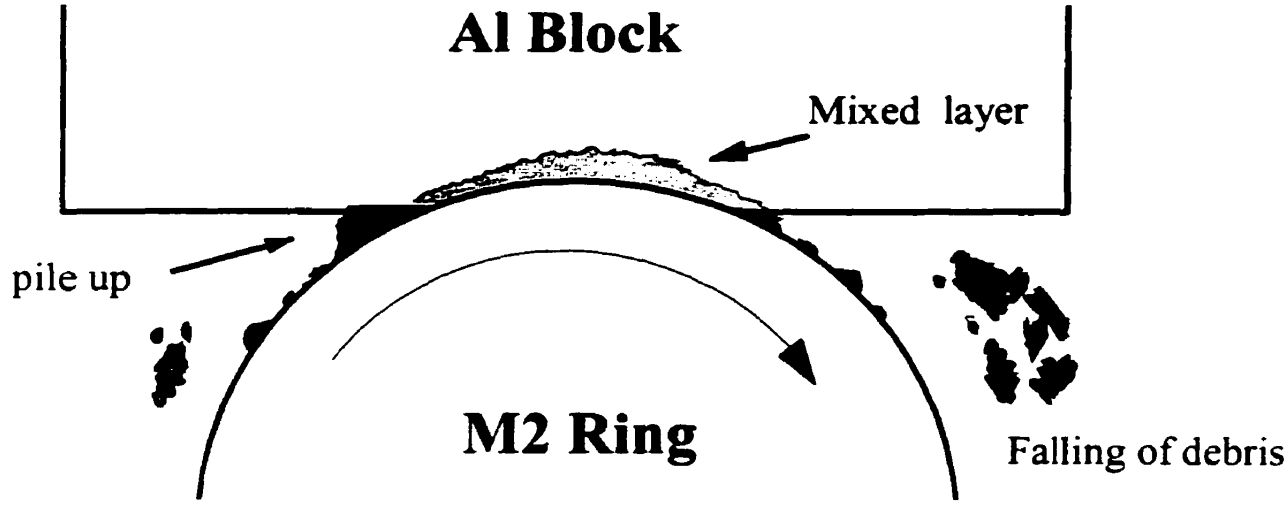

Fig. 7.1 Schematic illustration of the formations of wear debris and mechanically mixed layer in the block on ring sliding wear test.

spectroscopy. Wear debris from the HP Al against the same steel was also analyzed and compared to those of the base alloy and the composite. In particular, the microstructural features and crystallographic structure of the debris were extensively studied using transmission electron microscopy with EDS attachment. The formation mechanism of the debris and its relation to the formation of surface layers are also discussed.

7.2. SCANNING ELECTRON MICROSCOPY

Two types of morphology were observed in the wear debris of the Al alloys (HP Al, Al-Si alloy and the Al composite) under a microscope, depending on the applied loads at the sliding speed used. Visually, the first type of wear debris appeared dark in color, and was in the form of aggregates containing very fine equiaxed particles, as shown in Fig. 7.2. The aggregates were found to fall from the wearing system

individually or as clusters in a wide range of sizes (less than 1 μm to a few hundred microns). Another type of wear debris was comprised of relatively large particles with plate-like morphology, and they were often observed at high loads. To naked eyes, one side of the plate-like debris was dark in color, while another side had a metallic shine. Fig. 7.3 shows a typical morphology of the plate-like debris particles under SEM.

At low loads, most of wear debris were present as aggregates consisting of very fine particles. The equiaxed particles within the aggregates were in size of about 0.2-5.0 μm. Morphology features of the fine particles in the aggregates were similar in the wear debris of the three Al base materials in the present work. Figs. 7.4 (a) to (c) show typical SEM micrographs of wear debris of the HP Al, Al-Si alloy and the Al-Si/SiC composite, respectively. The morphologies of the ultrafine particles in the debris were very similar to those found in the crater area at the worn surfaces as discussed in Chapter 5.

EDS analyses of the wear debris revealed that a significant amount of iron was present in the wear debris, which was obviously transferred from the steel counterpart, as shown in Fig. 7.5 (a). It was noted that the amount of elemental iron in the debris increased with an increase in the sliding load as demonstrated in Fig. 7.5(b). It seems that the transfer behavior of the elemental iron was different for the Al-Si alloy and the Al composite at different sliding loads, especially at the low load level. As is seen from Fig. 7.5, the increase rate of the amount of Fe with the sliding load can be divided into two stages for the base alloy, i.e., a rapid linear increase from a low load up to 7 kg, beyond which it seemed to get saturated. In the case of the Al-Si/SiC composite, a considerably high amount of Fe was built up in the debris at very low loads, and it increased slowly in

(a)

(b)

Fig. 7.2 Wear debris in a form of aggregates containing fine equiaxed particles generated from of the Al-Si/SiC sliding against the steel at a load of 1 kg. (a) at a low magnification and (b) at a high magnification.

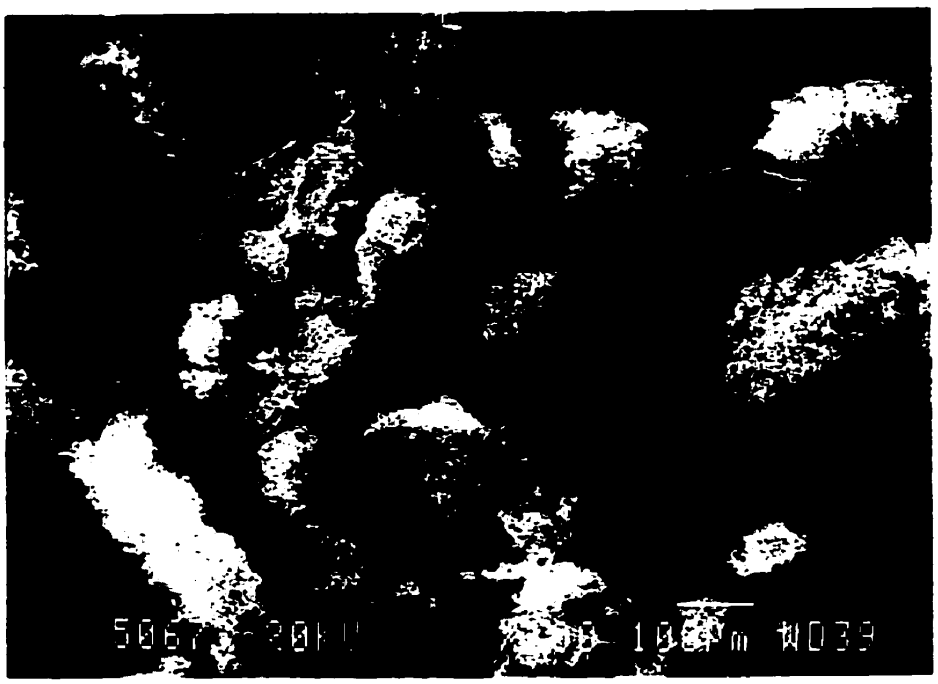

Fig. 7.3 A typical morphology of the plate like wear debris of the Al-Si/SiC sliding against the steel at a load of 10 kg.

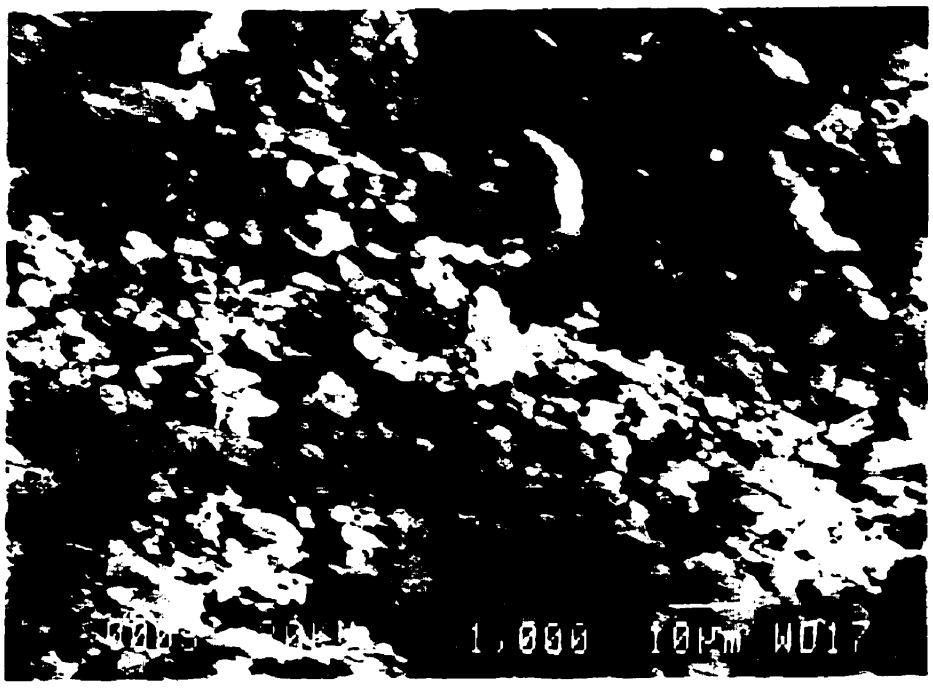

(a)

(b)

Fig. 7.4 *(continued)*

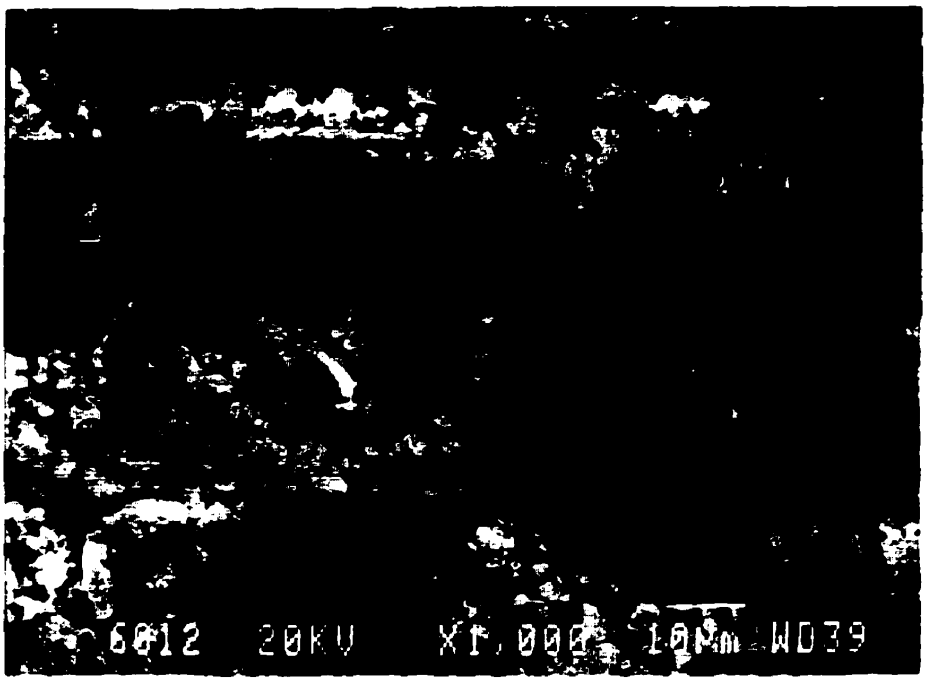

(c)

Fig. 7.4 Typical morphologies of the fine equiaxed particles in the wear debris generated from of the HP Al (a), Al-Si alloy (b) and the Al-Si/SiC composite (c) sliding against the steel at a load of 3 kg.

an approximately linear relationship with an increase in the sliding load. The element iron was present exclusively in the aggregates with ultrafine particles, and the amount of Fe was relatively less on the surface of the majority of the plate-like debris. It is interesting that a correlation of the iron transfer behavior to the wear behavior shown in Fig. 5. 6, shows similarities in the transfer and wear behavior of the Al-Si alloy and the Al-Si/SiC composite at the high load level, suggesting that the transfer iron and mechanical mixing might play an important role in the sliding wear of these materials.

It was also noted that some small flakes were mixed with fine equiaxed particles. As shown in Fig. 7. 6 and Fig. 7.7, the flake debris were usually 10 to 20 μm in size, and

EDS showed that they were mainly composed of Al. With a further increase in the sliding load, large flake-like debris were present either as a mixture with the ultrafine particles (Fig. 7.8) or as individually (Fig. 7.9). It was interesting to note that microstructural features of the plate-like debris were different for different materials at different sliding loads. In the debris of the HP Al and the Al-Si alloy, it was found that at a low load (3 -7 kg), lamella structures were found predominantly on the surface of the flakes, in addition to the presence of sliding grooves on the surface of the plate-like debris. The lamella patterns were noted to be perpendicular to the directions of the sliding grooves that were apparently along the sliding direction. Figs. 7.10 (a) to (c) show the lamella patterns on a plate-like debris of the HP Al, which is obviously an indicative of severe plastic deformation caused by the sliding wear. A careful examination showed that the lamella features were prominent in between the sliding deformed "lips", as shown in Fig. 7.10 (a). One example area, as marked by a square in Fig. 7.10(a), shows that the lamella patterns were closely spaced and the spacings between the lamellae were quite uniform. Fig. 7.10(b) shows a close-up image of the lamellae corresponding to the area marked in Fig. 7.10(a). Some lamellae were extended into micro-lips extruding out of the debris surface as a result of shear deformation, as indicated by arrows in Fig. 7.10(b). It was estimated that the spacings were approximately 1.0 μm when they were measured from top view. The thickness of the extruding micro-lips would be much thinner, if they were viewed and measured in a direction parallel to the surface. Though in most cases the spacings of the lamellae were noted to be uniform, it was observed that the spacings of lamellae changed progressively along the sliding direction in some areas on the plate debris, as seen in Fig. 7.10 (c). The average spacing changed gradually from

approximately 2.5 μm to 0.5 μm. This implies that the shear stresses at these locations might be altered during the course of the sliding.

Similar features were also found in the plate-like debris of the Al-Si alloy, as shown in Fig. 7.11. It is observed that the deformed layers or lips were inhomogeneous with a variety of spacings, whereas the detailed striation patterns within the deformed layers were surprisingly uniform with an average spacing of 1.2 μm, as shown in Fig. 7.11 (b). These deformed lips or striation like patterns are very similar to "chatter marks" due to a "stick-slip" motion suggested by Bowden [162]. In "stick-slip" motion, the worn surface is actually subjected to a cyclic force, as fluctuation of coefficients of friction (or friction force) can be measured during the sliding[136, 163]. In the present work, careful observation on the striation patterns within the shear deformed lips suggests that the striation patterns with extremely uniform spacings were very similar to fatigue striations that are unique characteristics of fatigue of materials under a cyclic stress [164]. The fatigue striations can be clearly or poorly delineated taking different shapes, from almost straight to very curved. Since the extruding deformed lips contained a number of the closely spaced lamellae, i.e., the striation-like patterns found in the present work, there might be a correlation between the deformed lips and the striation patterns. Kou and Rigney [4] reported a lamella structure in the extruded material of the worn surface of HP Al. Their lamella patterns were similar to the extruding deformed lips observed in the present work, but no structures similar to the present striation patterns were reported in their work. From the present work, the microstructural characteristic of the striation patterns in the flake debris suggests that there were a cyclic stress in the sliding surfaces.

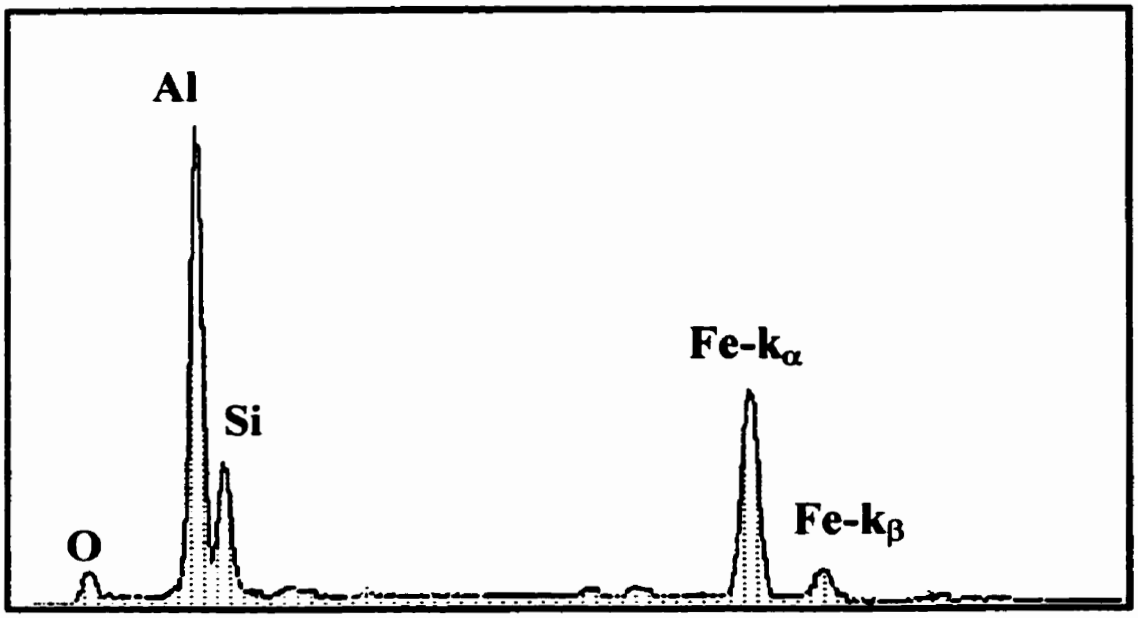

(a)

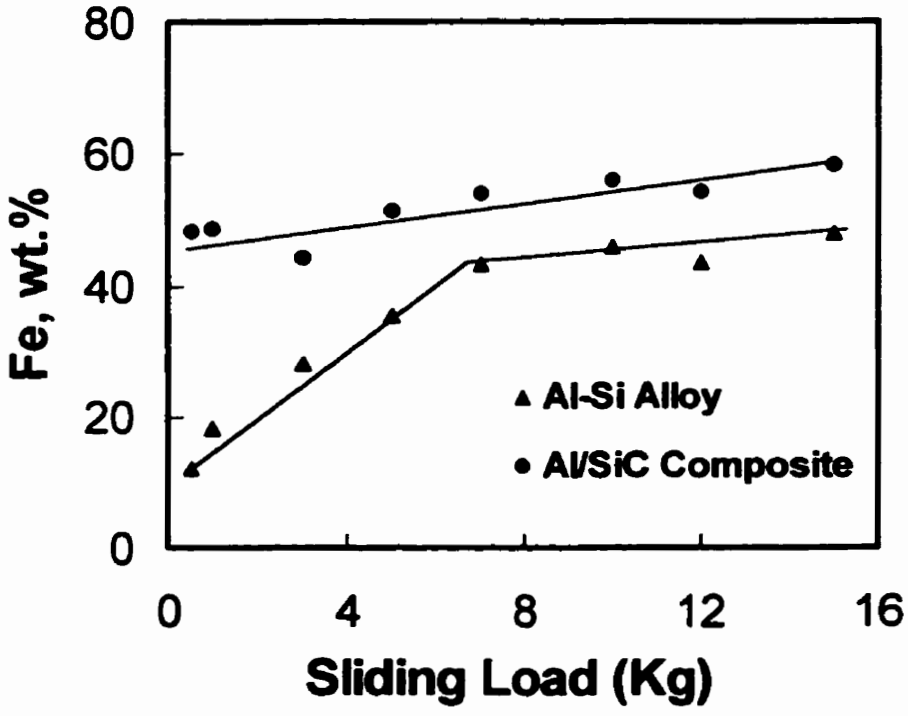

(b)

Fig. 7.5 Energy dispersive X-ray analysis of wear debris using SEM-EDS mode.
(a) EDS spectrum of the debris, showing presence of Fe in the debris;
(b) Mass percentage of Fe in the debris as a function of the sliding load.

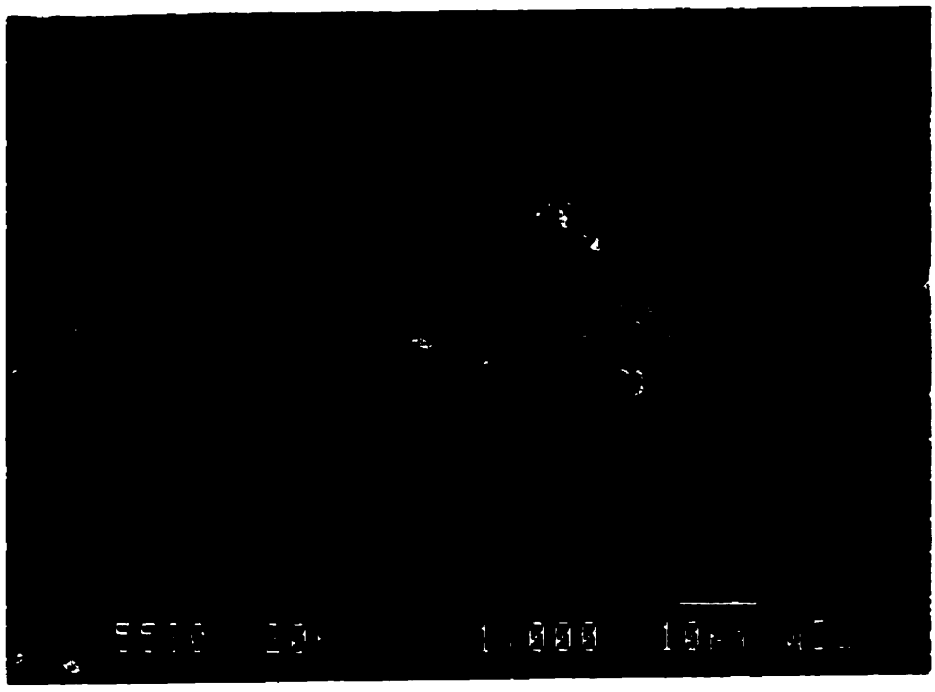

(a)

(b)

Fig. 7.6 Small flakes in the mixture of fine equiaxed particle debris of the Al-Si/SiC composite at a load of 5 kg. EDS analysis showed that the flake debris were mainly comprised of Al. (a) At a low magnification, and (b) At a high magnification.

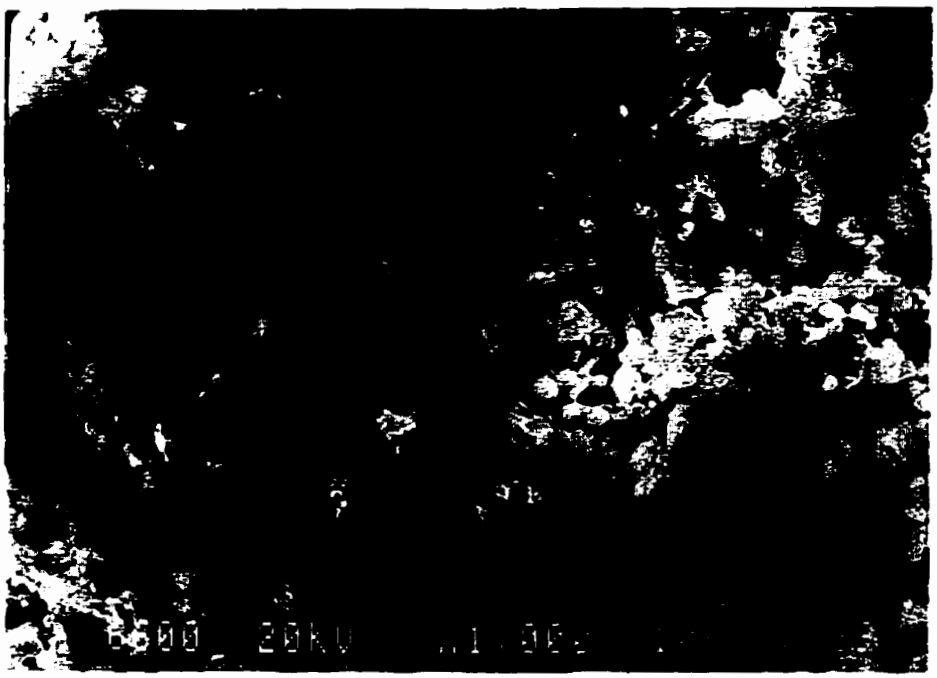

Fig. 7.7 A mixture of ultrafine particles and small flakes in the wear debris of the Al-Si alloy at a load of 5 kg. Note sliding groovings on the flake surface.

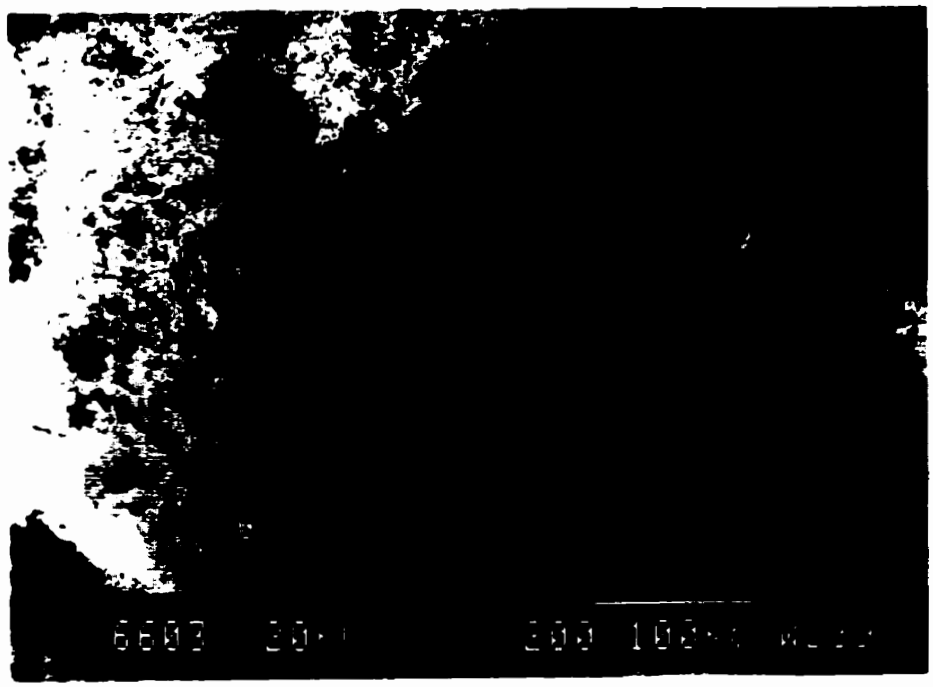

Fig. 7.8 Plate debris was present and mixed with the ultrafine particles of the Al alloy at a load of 7 kg. Note the size of the plate debris was larger than that of the wear flakes at low loads.

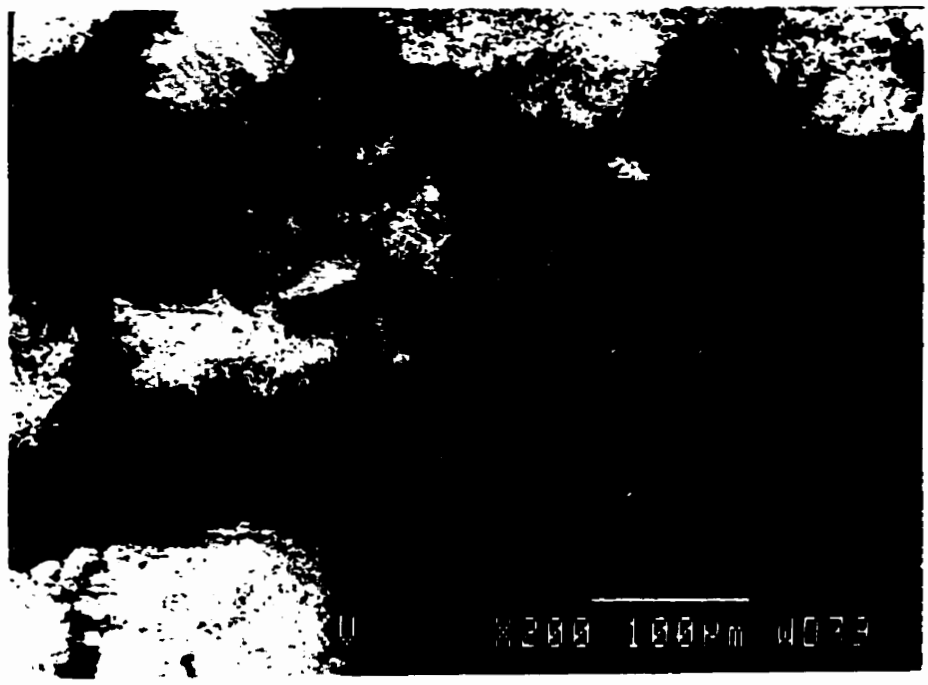

Fig. 7.9 Debris Plates was present in the wear debris of the Al-Si/SiC composite at a load of 7 kg.

(a)

(b)

Fig. 7.10 *(continued)*

(c)

Fig. 7.10 Lamella or striation patterns on the surface of the plate like debris of the HP Al at a load of 3 kg. (a) At a low magnification. (b) Striations corresponding to the marked area in (a) at a high magnification. The spacings are estimated about 1 μm. The arrows indicate some lamellae extruding out of the debris surface. (c) Striations with progressively changed spacings.

(a)

(b)

Fig. 7.11 Lamella and striation patterns on the surface of the plate like debris of the Al-Si alloy at a load of 5 kg. Note that two kinds of lamella structures are present, i.e., deformed lips or layers with a relative larger and non-uniform spacings, and striations with extremely uniform spacings as shown in (b) in detail. (a) At a low magnification. (b) At a higher magnification.

The plate-like debris of the Al-Si/SiC composite at a higher sliding load (>5 kg) show similar features to those found in the worn surface. Fig. 7.12 shows a typical morphology of the plate debris of the composite at a load of 7 kg. The surface of the plate debris exhibited severe ploughing along the sliding direction and contained an evidence of extensive cracks that were perpendicular to the sliding grooves. It should be noted that fragments and very fine particles were present in the plate debris, as shown in Fig. 7.12. With a further increase in the sliding load, the fine particles and fragments occurred extensively in the plate-like debris, characteristic of which was very similar to that found in the aggregated debris of ultrafine particles mentioned above. As shown in Fig. 7.13, the fine particles were predominant in the plate debris. In the smooth area as shown in Fig. 7.13 (b), it can be identified that fine particles were embedded in the plate surface, and their shape and size were the same as those of the particles on the surface. EDS analysis showed that a considerable amount of Fe was present in the plate debris with the fine particles, and also oxygen content was relatively higher than those at lower loads. It was observed that the amount of Fe was also higher in the fine particles than in the smooth area. Actually, some particles were embedded underneath and covered by a smooth layer that was mainly composed of Al element, as shown in Fig. 7.14. It seems that the particles were formed and compacted before a fresh layer of Al matrix alloy was smeared on them. It should be mentioned that no lamellae or striation patterns, similar to those found in the plate debris of the HP Al and the Al base alloy, were observed in the plate-like debris of the Al-Si/SiC composite. It implies that the presence of the reinforcements might possibly alter crack propagation behavior of the composite and change the local shear stress condition in the worn surface.

As mentioned previously, the plate-like debris of the HP Al and the Al base alloy showed lamella or striation pattern as a result of local shear stress and a repeated motion at a low load (< 7 kg). However, it was not a case for the debris of the HP Al and the Al base alloy at a high load. Similar to the debris of the Al composite, the plate-like debris of the HP Al and the base alloy also contained a significant number of very fine particles at higher loads. Fig. 7.15 shows a typical morphology of the plate debris of the HP Al. It can be seen that two distinct areas were present showing different features, namely, an area containing very fine particles, and a smooth area. In some smooth areas, it was noted that ultrafine particles seemed to be covered by a thin smeared layer, as shown in Fig. 7.16. The X-ray mapping showed that the presence of Fe significantly associated with the fine particles. Fig 7.17 shows a compositional contrast between the very fine particles and smeared base alloy in a plate debris of the Al-Si alloy, by using a comparison between secondary electron (SE) images and backscattering electron (BE) images in SEM. In SE mode, a few small particles were noted on the surface of the plate debris due to the topographic contrast. However, the BE image highlighted the fact that a number of fine particles did exist under a thin film of the Al matrix material, since the fine particles had different compositions from the Al matrix material.

It was also note that the fractured section of the plate-like debris contained a considerable amount of Fe. Fig. 7.18 shows a group of wear debris particles containing a large plate debris. Features of the fractured section of the plate were obviously different from those of a typical fracture surface in bulk Al alloys [165]. As shown in Fig. 7.18 (b), the fractured section exhibited two regions: 1) Region 1, near the top surface, showing

the occurrence of ultrafine equiaxed particles; 2) Region 2, below region 1, showing a layered structure without equiaxed particles. Interestingly, X-ray mapping indicates that there was more iron in the fractured section than on the surface, as shown in Fig. 7.18(c). Equiaxed particles were also noted in the subsurface, corresponding to the Fe-rich area on the surface as shown in the X-ray mapping. In Si mapping, a large white spot might be from a SiC particle because the size was much larger than that of the eutectic Si, and the SiC particle appears embedded underneath the Al matrix as compared with Fig. 7.18(b). The SiC (about 5 μm) was smaller than the average size (10 μm) of SiC in the original composite, implying that it might be a fragment of a fractured SiC particle. The above results strongly suggested that at a high load extensive mechanical mixing, such as fracture, fragmentation and repeated transfer and compaction, occurred between the contact surfaces during the sliding wear.

In summary, SEM observations showed that the wear debris of the HP Al, Al-Si alloy and the Al composite exhibited a morphology of aggregates in which ultrafine particles clustered together at low loads. With an increase in the sliding load, both the plate-like debris and the ultrafine grained aggregates were generated from the sliding surfaces. For the HP Al and the Al-Si alloy at relative low loads(<7 kg), the characteristic of the plate debris suggested that the severe shear deformation was probably the predominant factor governing the wear mechanism based on the findings of lamella or striation structures. At high loads, the transfer of materials and mechanical mixing between the sliding contacts were extensively found in the three materials, since a considerable amount of Fe was found in the wear debris.

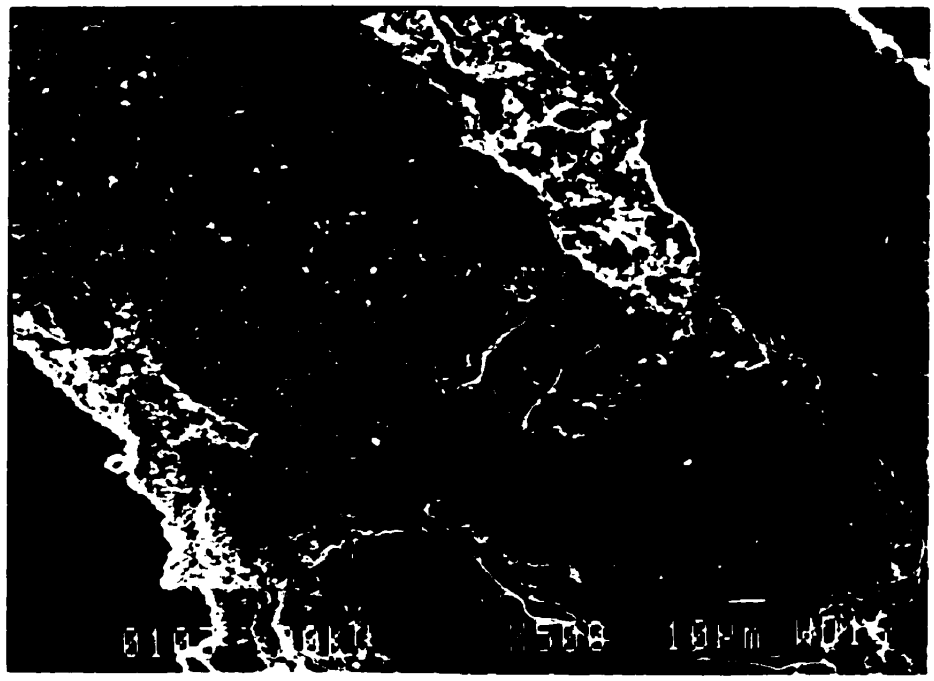

(a)

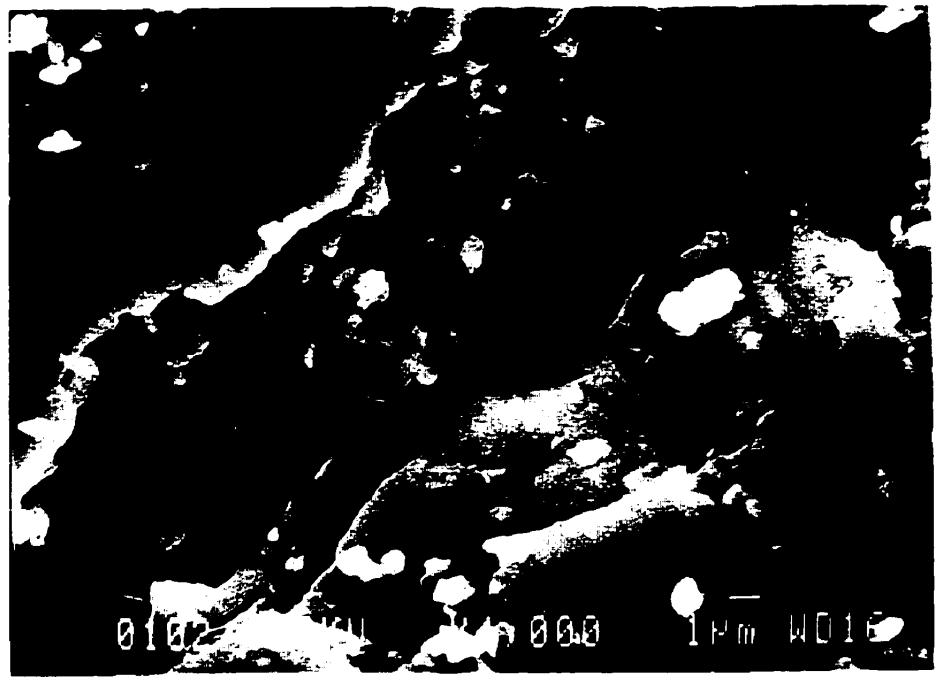

(b)

Fig. 7.12 A typical morphology of the plate like debris of the Al composite at a load of 7 kg. Note extensive cracks were present on the surface of the wear debris plate. (b) At a high magnification.

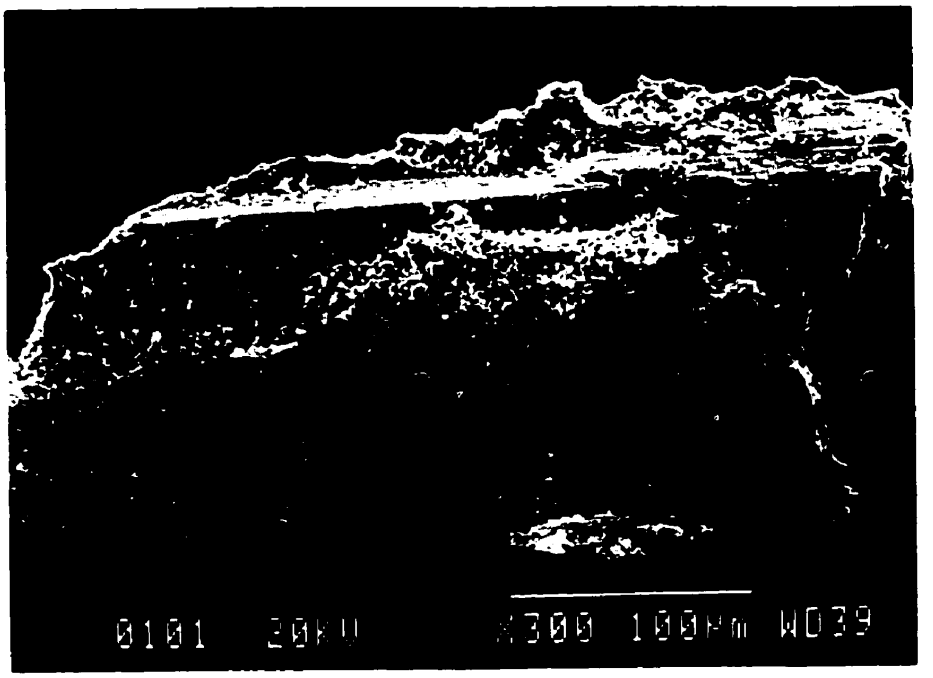

(a)

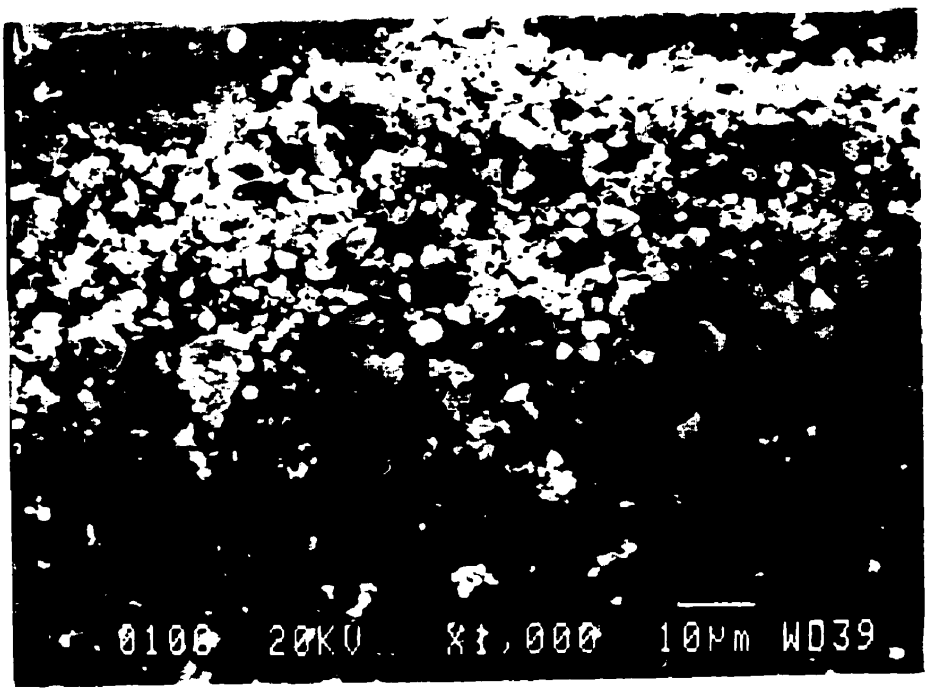

(b)

Fig. 7.13 A plate like debris of the Al composite at a load of 10 kg. Note fine equiaxed particles were present on the surface and the fracture cross section of the plate as indicated. (b) At a high magnification. Some particles were embedded in the surface as marked.

(a)

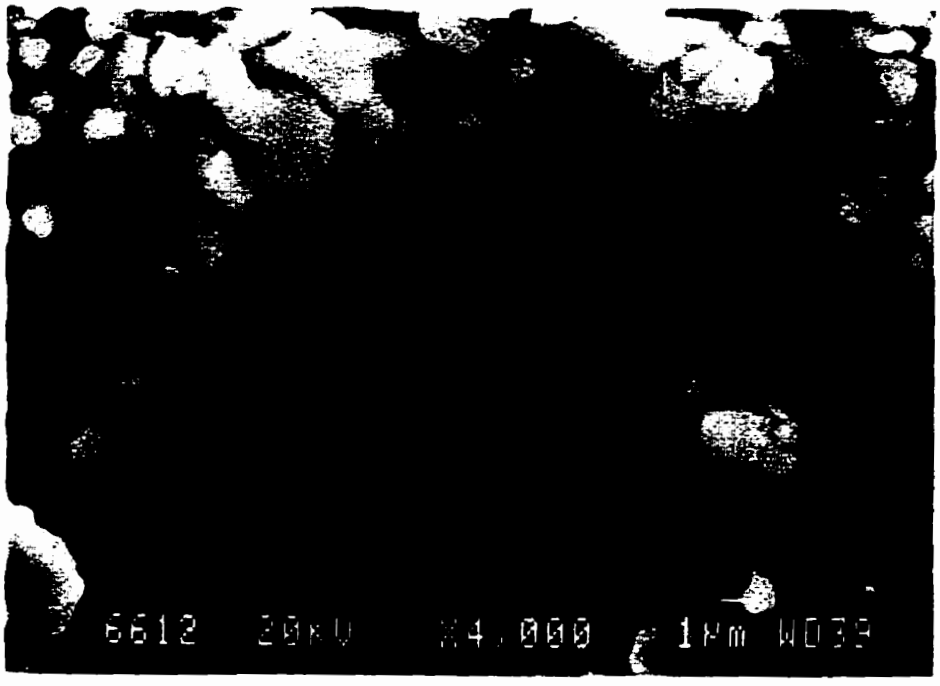

(b)

Fig. 7.14 Ultrafine particles were embedded underneath and covered by a smooth layer of the Al matrix. The arrow indicates the area that was viewed at a high magnification as in (b).

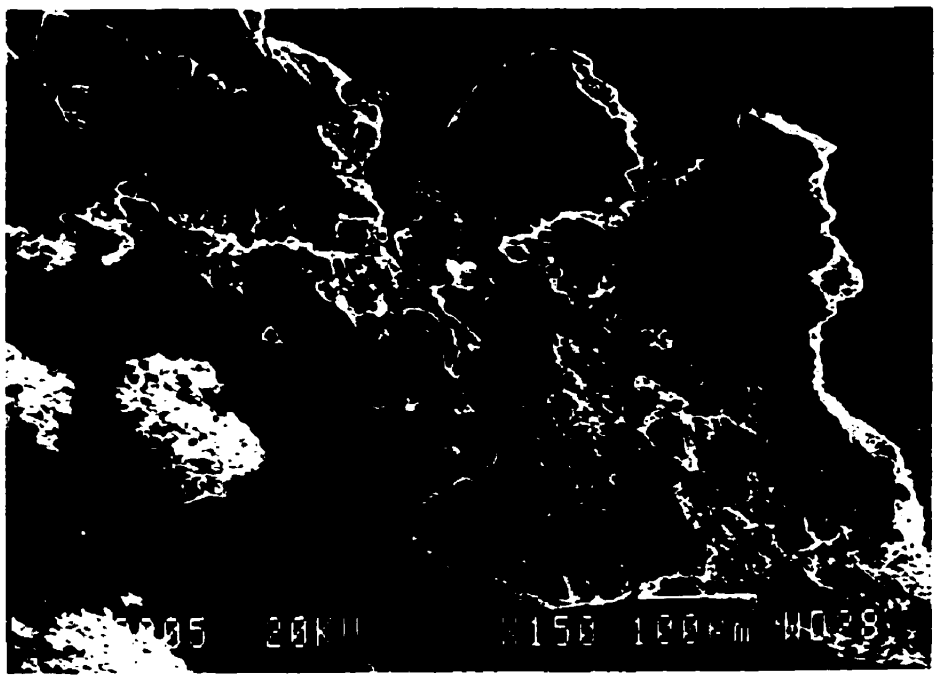

(a)

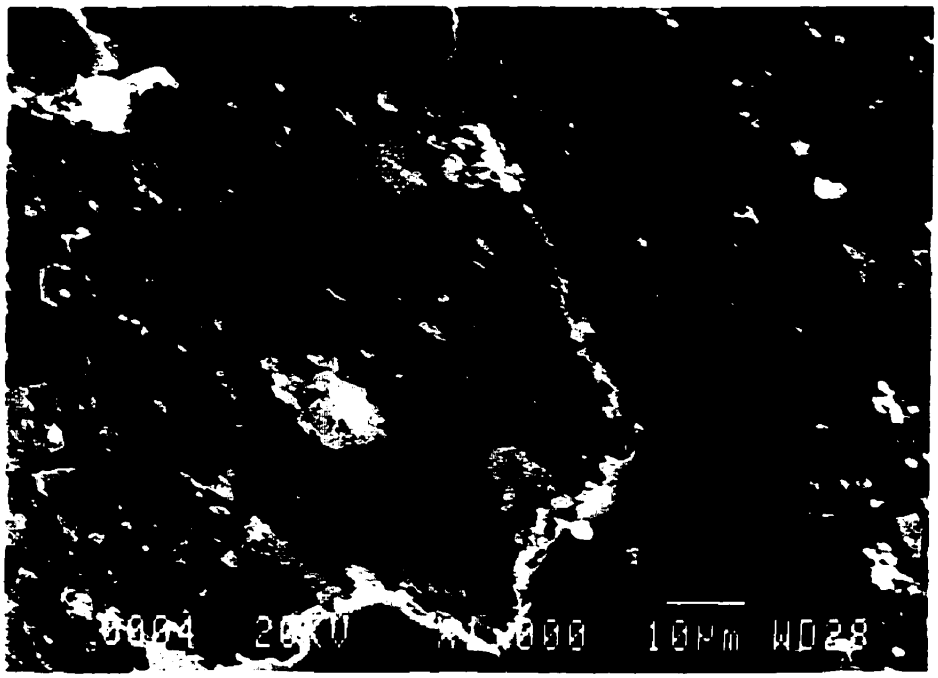

(b)

Fig. 7.15 A typical morphology of the plate like debris of the HP Al at a load of 5 kg, showing the presence of ultrafine particles in the debris. (b) At a high magnification.

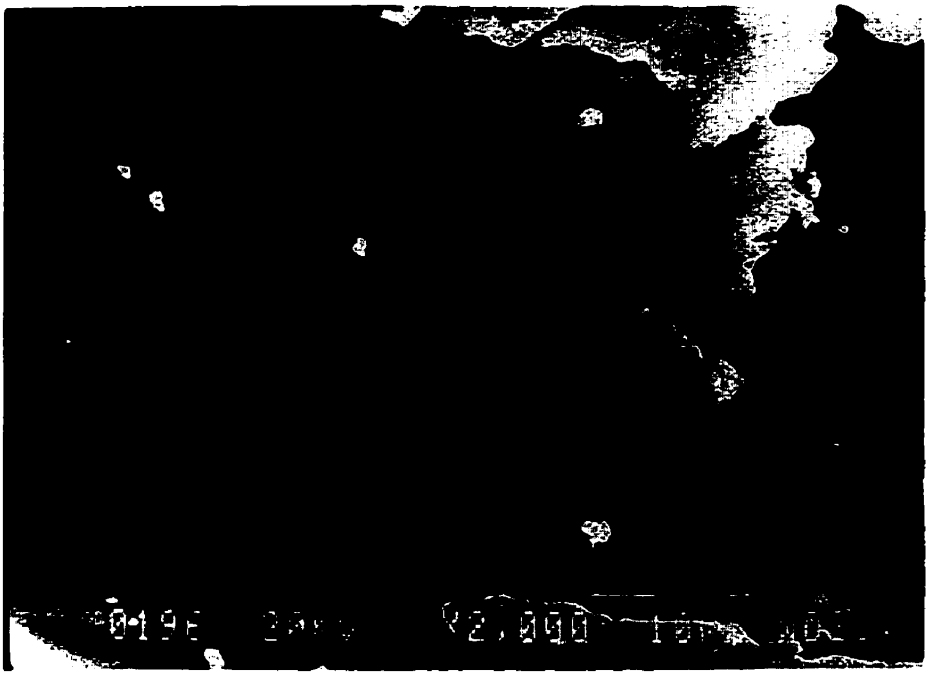

(a)

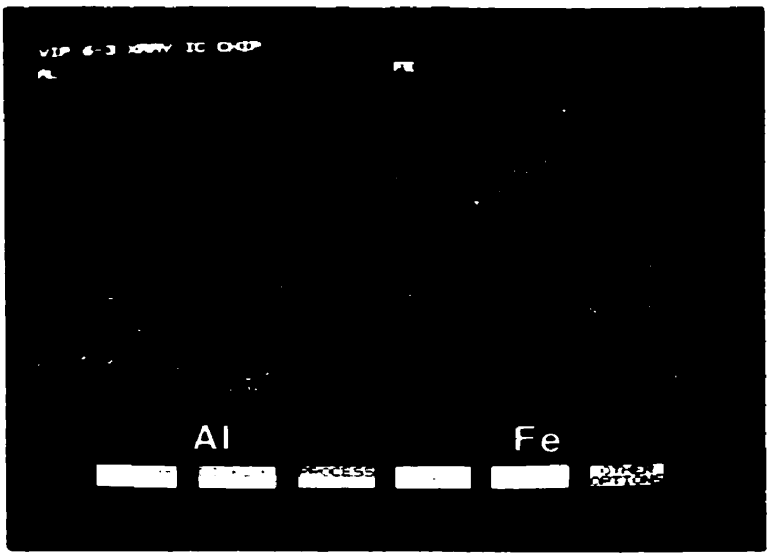

(b)

Fig. 7.16 A plate like debris of the HP Al at a load of 5 kg. Note that ultrafine particles were embedded underneath a film of Al on the surface of the debris plate. (b) X-ray mapping conducted on (a), showing presence of Fe element.

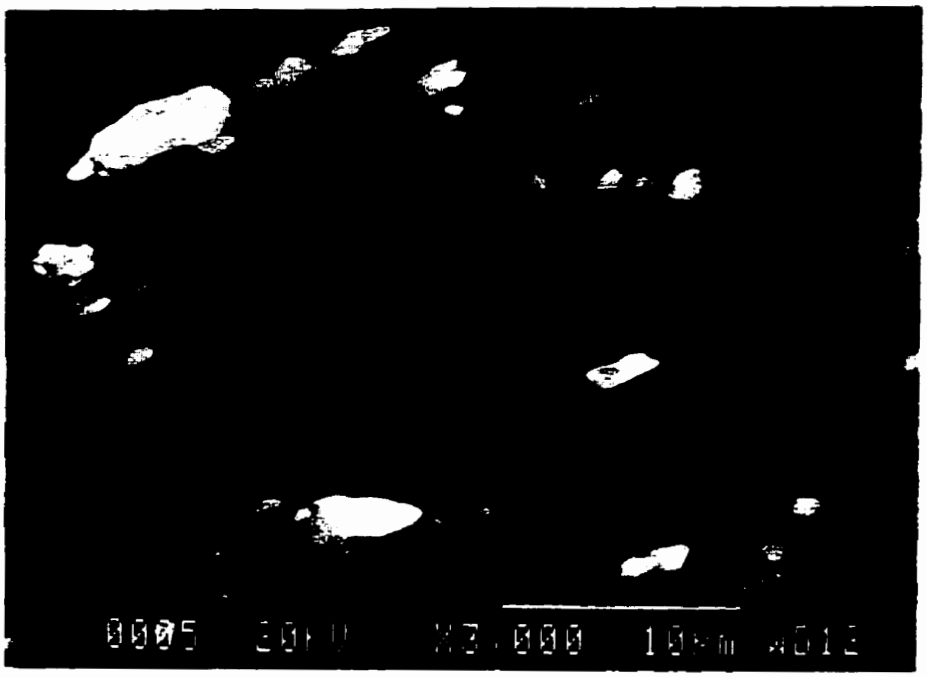

(a)

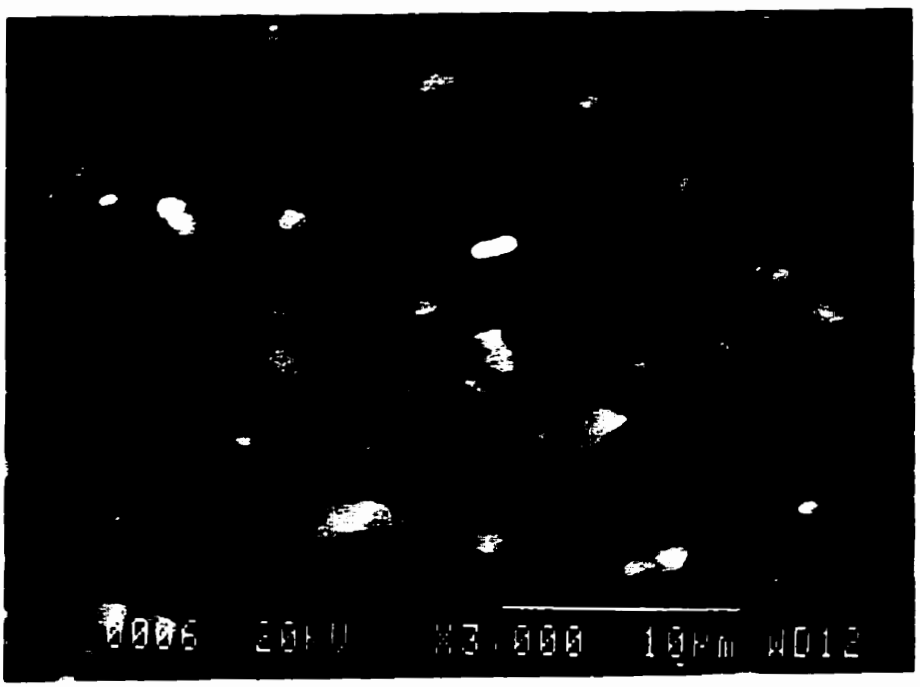

(b)

Fig. 7.17 Topographic and compositional contrasts of the ultrafine particles in the plate debris of the Al-Si alloy at a load of 10 kg, by using SE mode (a) and BE mode (b) in the SEM. The compositional contrast resulted from the existence of Fe in the ultrafine particles.

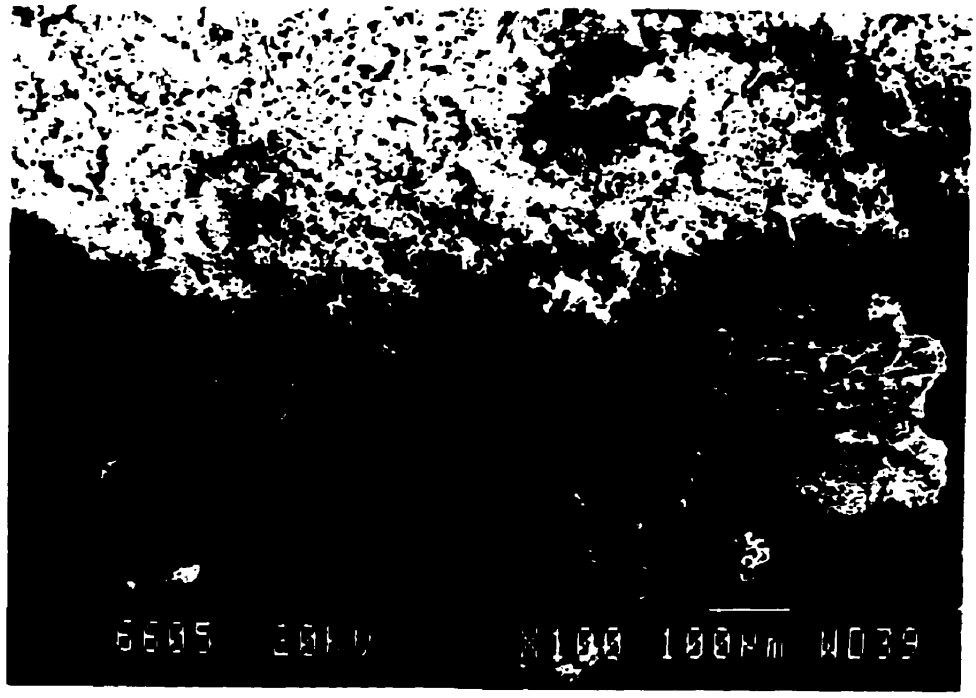

(a)

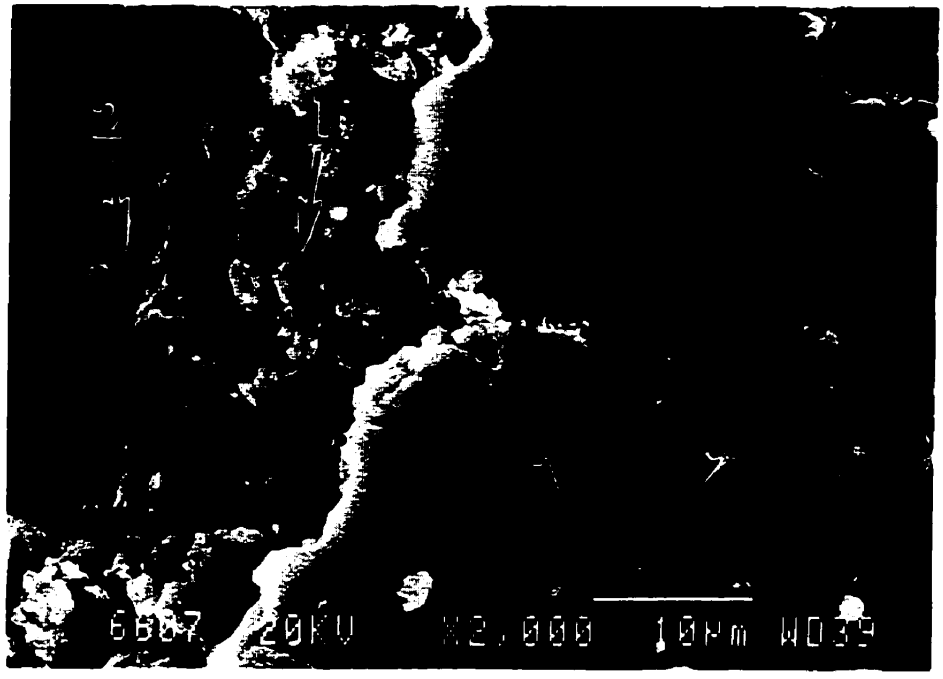

(b)

Fig. 7.18 *(continued)*

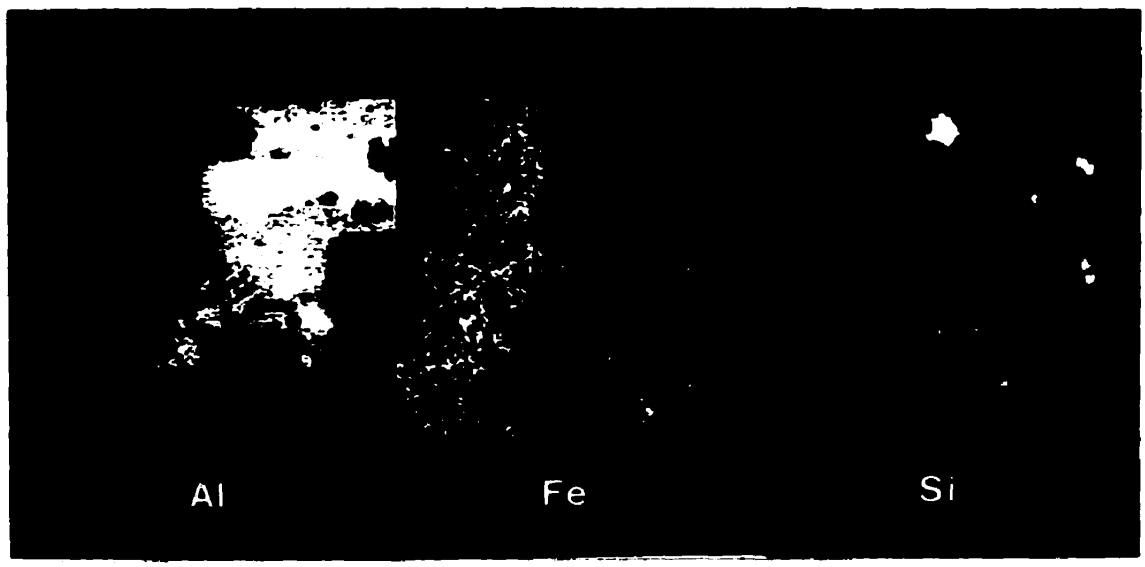

(c)

Fig. 7.18 Comparison of plate like debris and ultrafine particles regarding the presence of Fe and mechanical mixing caused by the sliding wear.
(a) A group of wear debris with a presence of a large plate;
(b) Cross section and surface morphology of the plate debris, showing two regions, i.e., Region 1, compacted layer with similar ultrafine particles; and Region 2, with a layered structure due to plastic deformation. The arrows indicate some particles containing Fe embedded in the subsurface;
(c) X-ray mapping analysis performed on the plate debris corresponding to (b), showing elemental distribution of Al and Fe and Si.

7.3. X-RAY DIFFRACTION

7. 3. 1 The HP Al and the Al base alloy

Fig. 7.19 shows XRD patterns of the wear debris of the Al base alloy generated under several sliding loads and that of the original alloy before wear. It can be seen that the Al (α-solid solution) and the eutectic Si are easily identified as narrow peaks in the XRD pattern of the original binary alloy. The intensities of the Al (α-solid solution) peaks were in agreement with those of Al in the x-ray powder diffraction standards (JCPDS) according to structure factor calculations. In the XRD patterns of the wear debris, it is evident that changes in the XRD spectrum of the wear debris occurred in comparison with that of the original alloy. The XRD patterns of the wear debris consisted of extensively broadened diffraction peaks, and the relative intensities of the peaks were not expected for the α-Al according to the structure factor calculations. It is noted that the Al(200), Al(220) and Al(222) peaks of the wear debris were drastically broadened and the intensities of the peaks were increased, compared with the Al(111) peak which had the highest intensity in the original alloy. The broadening and increase in intensity became greater with an increase in the sliding load. For instance, at a load of 15 kg, the intensity of the Al(200) was significantly greater than that of the Al(111). This strongly suggests that the iron coming from the counterpart was present in the wear debris, as in agreement with the findings using EDS in the SEM observations. All α-iron peaks were superimposed on the Al peaks with the even number indices (hkl), as indicated in the spectra.

It is generally known that an ultrafine particle size and possibly high strain levels or a high dislocation density in the debris could be partially responsible for diffraction peak broadening according to Scherrer relationship [166] and Williamson and Hall method [167]. It is, however, noted that in the present work only the peaks, which overlapped with those of the α-iron, were broadened, while the Al(111) and Al(311) did not show obvious broadening over the entire sliding load range. According to Scherrer relationship, the breadth β resulting from fine particles is inversely proportional to the particle size D and a cosine function of the Bragg angles θ, that is,

$$\beta=0.9\lambda/D\ \cos\theta$$

where λ is the X-ray wavelength. If the broadening had occurred mainly due to the particle size, the Al(311) would have also been broadened and this effect would be even larger than those at low angles, but this was not the case in the present work. It is also noted that the broadening of the peaks seems to extend to a low Bragg angle direction rather than a symmetric broadening, as can be obviously seen in Fig. 7.19, with reference to the Al(200) and Al(222) peaks. Moreover, XRD analyses of the wear debris that was annealed in an encapsulated vacuum tube at 480^0 C for 2 h showed no significant changes with respect to the broadening, suggesting that strain levels were not primarily responsible for the broadening in this work. It appears therefore that the broadening mainly resulted from the presence of the element iron. Phases other than the α-Al and α-Fe can also contribute to the broadening at 2θ ranges close to those of the overlapping peaks of the α-Al and α-Fe, as a result of interdiffusion of the Fe and Al elements involved in the sliding system during the sliding wear.

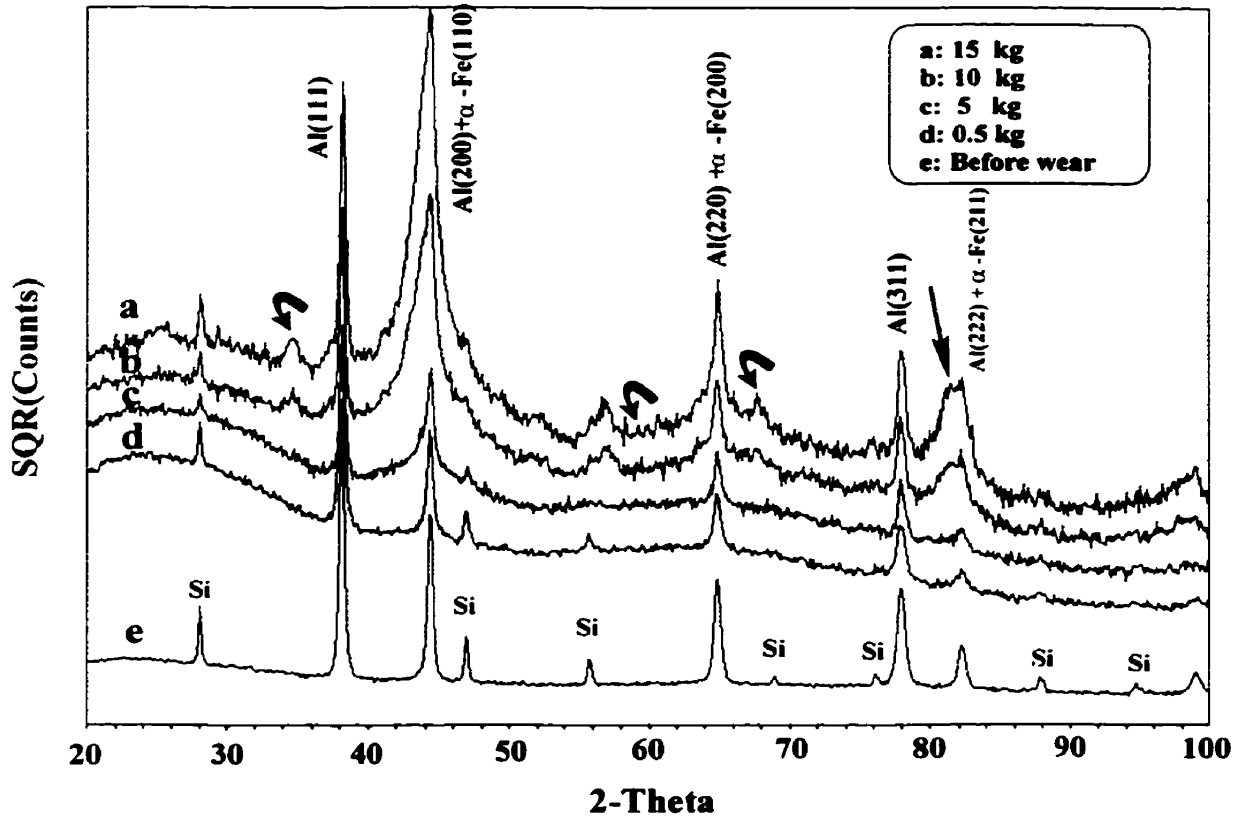

Fig. 7. 19 XRD analyses of wear debris at a variety of sliding loads and of the original Al alloy before wear. The straight arrow indicates a peak shifting away from that of the α-Al and corresponding to the FeAl phases. The curved arrows point to an aluminum oxide phase formed at high loads. Note that these oxide peaks are away from those of Si phases.

The asymmetric broadening, that is, a shift of the broadened peaks to low angles, can be fit to an intermetallic compound of FeAl, as shown in Fig. 7.20, which is based on the analyses of the lattice parameter range and the diffraction intensities, using the whole diffraction pattern fitting analysis provided by the database of Rigaku. The intensities for the individual peaks of the FeAl were very similar to those of the α-Fe, but the Bragg

angles of the FeAl phase were smaller than those of the α-Fe, since the lattice parameters of the phase increased due to the fact that the Al atoms diffused into the heavily deformed iron particles. In order to confirm the formation of the intermetallic phase, parallel sliding wear tests were conducted using the high purity Al (HP Al) as a sliding block in an Ar gas environment with the same steel ring. In the sliding tests of the HP Al, the sliding loads were relatively low since the HP Al was soft. The XRD results of the debris collected with the sliding of the HP Al in the Ar atmosphere revealed that similar broadening and diffraction peaks other than those of Al and Fe were present, as shown in Fig. 7.20. In the case of the HP Al, no silicon peaks were present, and new peaks corresponding to the intermetallic phase of FeAl were observed. The new peak shifted significantly away from the overlapping peaks of the Al(222) and Fe(211).

It should also be noted that other new peaks appeared with an increase in the sliding load, as indicated with curved arrows in Fig. 7.19. It appears that the intensities of the peaks become higher with an increase in the sliding load, and no such peaks were found at low loads. Careful examinations show that these peaks were away from those of Si, and matched those of aluminum oxide rather than iron oxide using the Rigaku database. As well, the strongest aluminum oxide peak is very close to and overlaps the Al(111) and Fe(200) peaks as well as the strongest FeAl peak. This superimposition can also contribute significantly to the drastic broadening in the 2θ range of 40° to 48° in the XRD patterns. This suggests that with an increase in the sliding load, oxidation of the Al matrix occurred as a result of frictional heating. At low Bragg angles, a relatively high background diffusive diffraction peak was present. This is similar to that reported by

Zhang and Alpas [52] who suggested that it corresponded to the formation of an aluminum oxide phase with an amorphous structure. However, this does not seem to be the case in the present work, since the glass slide, on which the debris was placed for the XRD analysis, did show the same diffusive pattern when it was run as a blank in the XRD analysis. It appeared as a noise background in the XRD spectra from the amorphous glass slide. This has also been confirmed by Bishop et al [161].

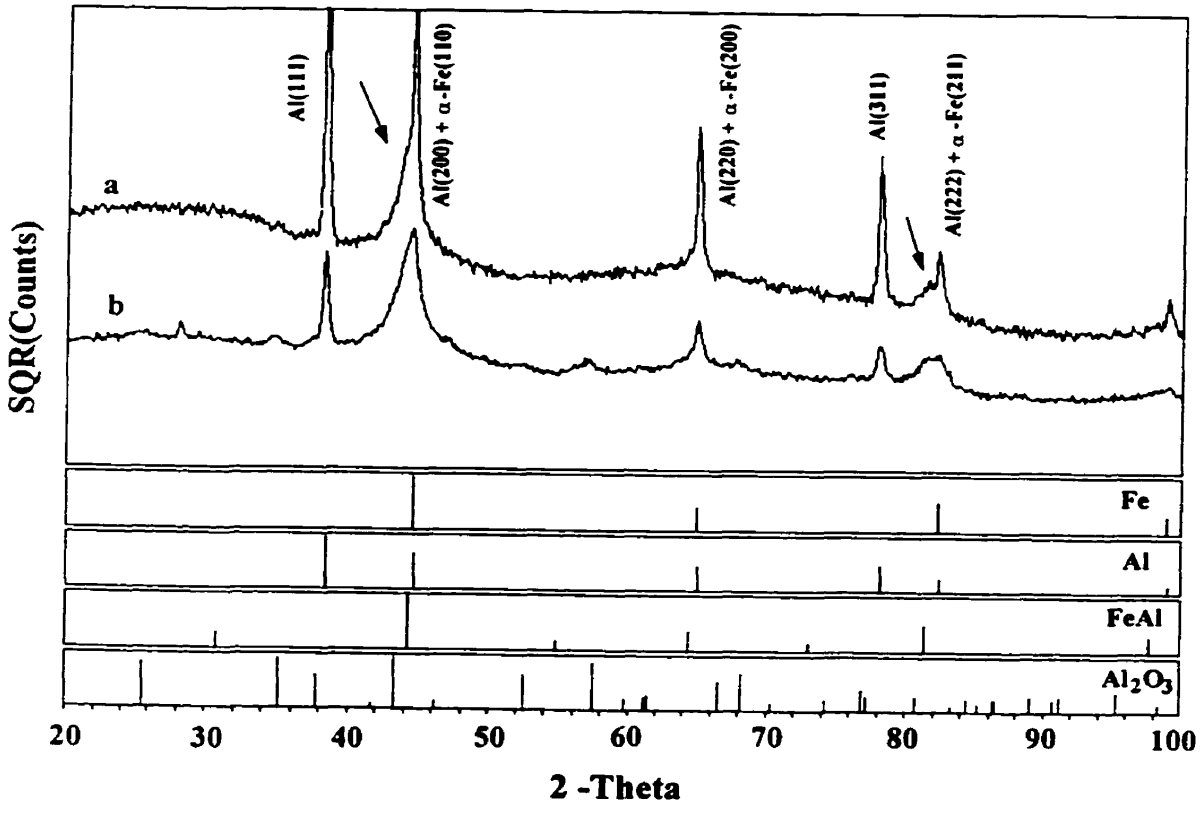

Fig. 7.20 Comparison of XRD analyses of the wear debris of the HP Al in an Ar atmosphere and the Al-Si alloy in the ambient condition. The bottom shows the standard XRD spectra (JCPDS) for different phases.

It was also observed that the peaks of the α-Al shifted to higher angles progressively with an increase in the sliding load. Since the Al(111) did not show a broadening, it was used to calculate the lattice parameter of the α-Al, as corrected and calibrated using pure silicon and the Si phase in the samples tested. Fig. 7.21 shows the lattice parameter contraction as a function of the sliding load. The lattice parameter contraction suggests that during the sliding wear, Fe and/or Si dissolved into the α-Al since the atomic radii of Fe and Si were smaller than that of Al.

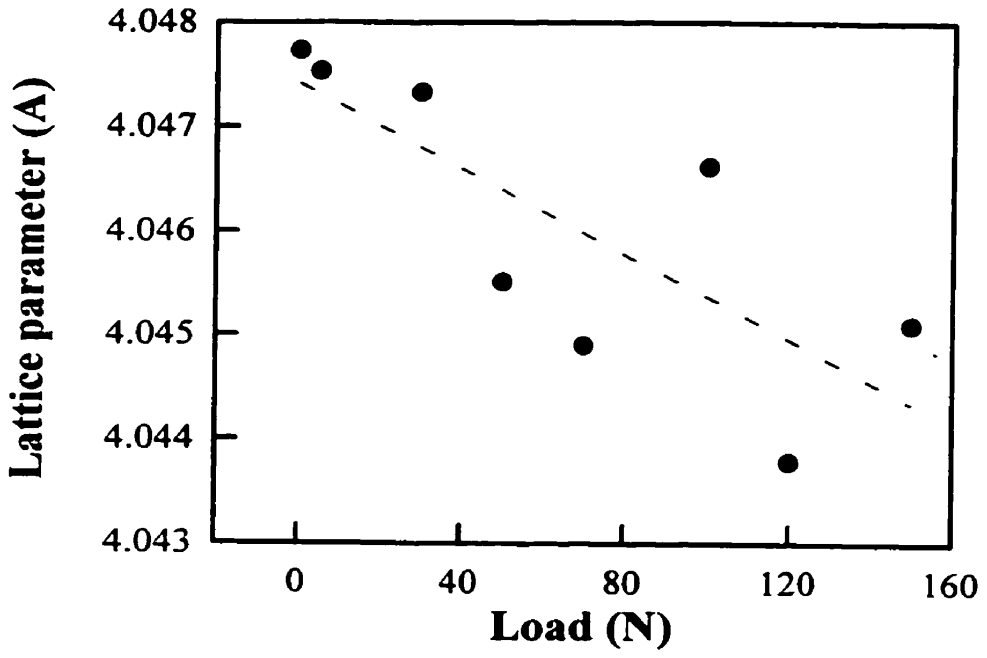

Fig. 7.21 Influence of dissolution of Fe and Si into the α-Al solid solution in the debris on the lattice parameter of the solid solution as a function of sliding load.

7. 3. 2 The Al-Si/SiCp Composite

Fig. 7.22 shows the XRD results of the wear debris of the Al composite sliding against the steel ring at a variety of sliding loads. It can be seen that the structural features of the wear debris of the Al composite were similar to those of the wear debris of the Al base alloy. From the XRD, the eutectic Si and SiC reinforcing particles were found to be present in the debris over the entire sliding load range. The Al(200) and Al(222) diffraction peaks were broadened and the intensities of these peaks were increased as compared to that of Al(111), due to the presence of Fe transferred from the counterpart as discussed in the case of the Al base alloy. It should be noted that the broadening of the Al peaks occurred even at very low loads, as shown in Fig. 7.22. At a sliding load of 0.5 kg, the overlapping peaks of the Al(200) and Fe(110) were significantly higher than the Al(111) peak and largely broadened. This suggests that Fe transferring from the steel counterpart started to occur at very low loads, mostly because of the presence of the SiC reinforcements that could act as microcutters during the sliding process. This is in agreement with the compositional observations using EDS that showed a considerably high amount of Fe in the debris of the Al/SiC composite even at a low load, as compared to those in the debris of the Al base alloy, as shown in Fig. 7.5.

With respect to the formation of the FeAl phases and oxidation at higher loads, there might be similar phenomena to those in the Al base alloy, since the broadening and shifts of diffraction peaks near the Al peaks were observed. It was also noted that at high sliding loads, a peak corresponding to the aluminum oxides occurred, as indicated in Fig.

7.22. However, the situation was more complicated than in the Al base alloy, due to the fact that some peaks of the SiC particles were very close to those of the Al, Fe and FeAl phases.

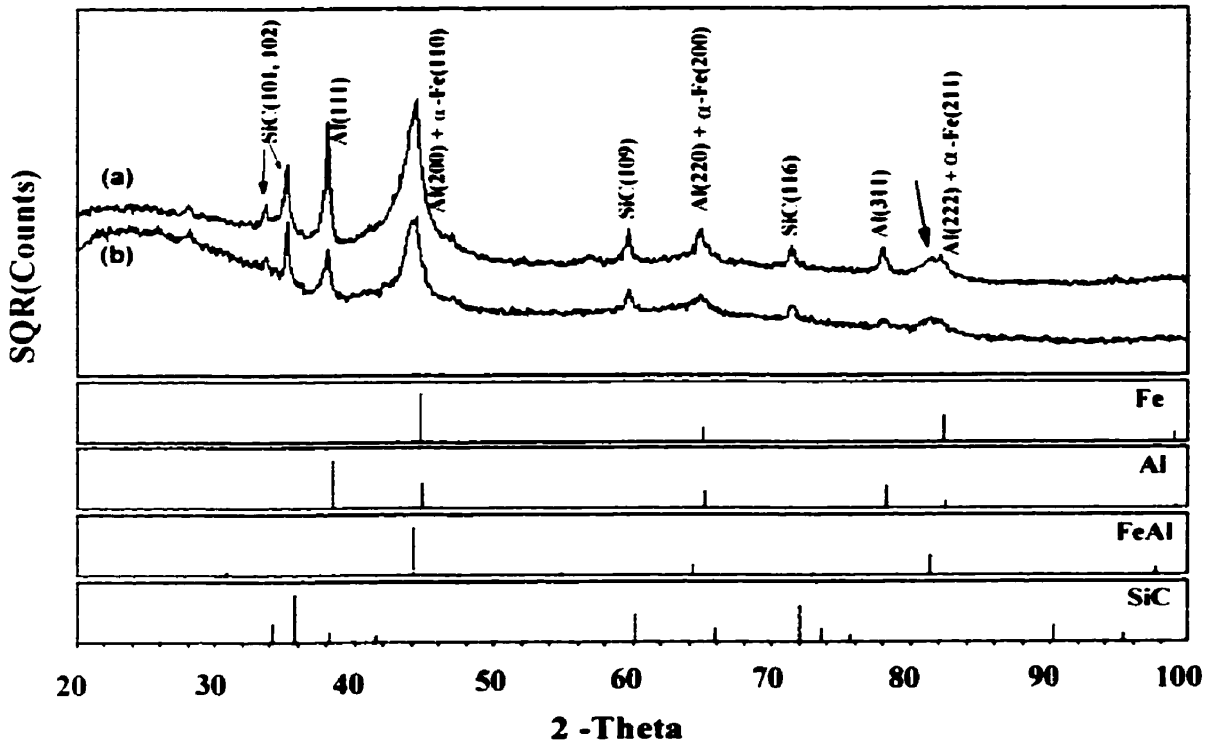

Fig. 7. 22 XRD analyses of the wear debris of the Al-Si/SiC at loads of 10 kg (a) and 0.5 kg (b) in the ambient condition. The bottom shows the standard XRD spectra (JCPDS) for different phases.

7.4. TRANSMISSION ELECTRON MICROSCOPY

7. 4. 1 The Al alloy and the Al composite

In order to reveal more detailed microstructure of the wear debris and verify the formation of the FeAl intermetallic phases and aluminum oxides mentioned above, TEM was utilized for the debris samples. The results show that the microstructural features were similar for the HP Al, Al-Si alloy and the Al composite. For simplicity, therefore, the microstructural characteristic of the wear debris of the HP Al and Al alloy is mainly discussed in the sliding wear against the tool steel under dry condition using the block-on-ring wear tester at loads of 5 kg, 10 kg and 15 kg. Fig. 7.23 shows a typical morphology of the wear debris at a load of 5 kg. It can be seen that the debris formed as aggregates with a very fine-grained structure. The ultrafine substructure within the aggregates was about 2-20 nm in size, while the average size of the aggregates was about 0.25 to 1.0 μm. The selected area electron diffraction showed that most of the aggregates exhibited FCC structure-like patterns, which were mainly from the α-Al solid solutions, as shown in the insert in Fig. 7.23(a). EDS analyses indicated that a significant amount of iron was present in the aggregates, and the amount of iron was in a range of 30 at. % to 40 at. % in the debris that was in excess of the solubility of iron in the α-Al solution (0.025 at. % at an equilibrium state), as shown in Fig. 7.23(c). Since the size of the nanocrystallites was much smaller than that of the focused electron beam used in the EDS mode, it was not possible to differentiate whether the particles contained some iron or they were "pure" iron particles. Based on the compositional and structural information above, it is believed that the FCC structure-like patterns shown in Fig. 7.23(a) result from

combined electron diffraction of the α-Al (FCC) and α-Fe (BCC), in which all the diffracted rings of the BCC iron were overlapped by those of the α-Al with the even *hkl* indices. At this low sliding load, it appeared that the formation of oxides and intermetallic compounds was minimal.

At a high load (10 kg), the nanocrystalline structure within the aggregates of debris was found to be more complex as shown in Fig. 7. 24. The majority of the nanocrystallites were still equiaxed particles and the size of the crystallites was obviously smaller than those at the lower load level. It is of interest to note that some particles exhibited evidently a strong material flow in a direction that resulted from severe plastic flow during the sliding wear. With further increase in the sliding load, the microstructure of the debris gave rise to a further evidence of refinement of particles within the aggregates. In addition to the equiaxed particles, lamella structures with extremely fine spacings were found, as shown in Fig. 7. 25. It can be observed that the lamella structure was about 20 to 30 nm in length with spacings less than 5 nm. Sub-regions with different orientations of the lamella structures can also be identified in the ultrafine-grained structures of the debris. No obvious boundaries between the sub-regions were noted when tilting the debris sample in TEM. EDS analyses indicated that a considerable amount of iron and oxygen was present in the debris aggregates at the high sliding load, as shown in Fig. 7 26.

Electron diffraction of these particles showed distinct patterns as compared to those obtained at the low load of 5 kg. Diffraction was found to be different from one

region to another, although morphologic features were hardly distinguishable in the TEM study due to the extremely small sizes of the particles. Figs. 7.27 (a) and (b) shows typical diffraction patterns obtained from the ultrafine particles. It can be seen in Fig. 7. 27(a) that a new set of diffraction rings was present with extra peaks as compared to the overlapping patterns shown in Fig. 7. 23(a). Based on the calculations of atomic plane spacings obtained from the diffraction patterns in reference to those of the α-Al solid solution, it was found that the new set of patterns could be interpreted as the intermetallic compound FeAl. Other phases such as, aluminum oxides, iron oxides, and silicide were easily ruled out by the calculations of the atomic plane spacings. Thus, the extra peaks were indexed according to the FeAl (CsCl-type) superlattice compound with some peaks being overlapped by those of the α-Al and α-Fe. Fig. 7.27(b) shows diffraction patterns found in the debris at a higher load. It was noted that a strong diffraction ring with the smallest spacing occurred, and the rings corresponding to the Al (111) and Al (200) were broadened. According to the calculations of reciprocal lattice vectors in reference to those of Al, the smallest ring can be associated with α-Al_2O_3, while other diffraction rings were most likely overlapped by those of the α-Al and α-Fe since their atomic spacings were very close to each other. It should also be noted that a diffraction ring with a weak intensity corresponding to FeAl(100) also existed in concurrence with those of the aluminum oxide. This ring was present between the Al_2O_3 (012) and Al (111). Therefore, the patterns were indexed as a combination of different phases, as shown in Fig. 7. 27(c). Table 7. 1 summarizes the analysis of the electron diffraction patterns based on calculations of *d*-spacings of the phases. The results suggest that at a high sliding load the aggregates were comprised of α-Al_2O_3, FeAl, α-Al, α-Fe, in agreement with the

results using X-ray diffraction discussed in the previous section.

It should also be mentioned that partial amorphization was observed in some aggregates in the debris samples. Much less change in contrast of the image of the debris was noted as the samples were tilted in a large range of angles in the double goniometer in TEM. The diffraction patterns showed a mixture of polycrystalline diffraction pattern and a halo pattern, confirming the amorphization in the debris, as shown in Fig. 7. 28.

No detailed microstructural characterization of the SiC reinforcing particles was available in the TEM study of the wear debris of the Al composite, since differentiation of the sputtering rate between the SiC and other particles was quite large during the ion milling process of the TEM samples. However, the eutectic Si particles were observed in the debris of the Al alloy and the composite, as shown in Fig. 7.29. It is seen that the Si particle had the same morphology as in the original material, and their size (about 0.1 μm) was relatively smaller than that in the original material. This is in agreement with the observations of SEM cross sections of the worn surfaces where the Si particles were found to be fragmented. A large number of stacking faults were also noted in the Si particles, the same as those in the original material. It appears that the Si particle shown in Fig. 7.29 was detached as an individual particle from the Al matrix and mixed in the wear debris. Some of particles were found to be embedded and intermixed within the ultrafine grained structures, for example as shown in Fig. 7.30. The electron diffraction pattern of the particles confirmed that the particles were Si, as shown in Fig.7.30 (c). It is evident that some of Si were fragmented into very small particles and intermixed in the

wear debris. It seems that the fragmented Si particle in a very fine size was forced to orient along the plastic flow of the ultrafine grained structure, as shown in Fig. 7. 31.

7. 4. 2 The HP Al

The wear debris from the high purity of Al block sliding against the steel was also analyzed in comparison with the results of the Al alloy and the composite. Wear debris samples at a load of 5 kg in Ar atmosphere were chosen only because X-ray diffraction results showed a formation of iron aluminum compound in the debris of the HP Al at this load. Fig. 7.32 demonstrates a TEM micrograph of the wear debris, showing a mixture of Al flake-like debris and nanocrystalline structures. The electron diffraction showed that the area marked as Al exhibited a typical FCC structure and the area marked FeAl gave rise to a combined microstructure as shown in Fig. 7.32 (b). It can be seen that the diffraction was similar to that indicated in Fig. 7.27(a), i.e. a mixture of the Al-Fe intermetallic compounds, α-Al and α-Fe. No oxides were noted, or the amount of oxide, if any, was much less to be detected. The EDS analyses also showed that the ultrafine grained structures contained a considerable amount of iron and aluminum, while the flake like debris was mainly comprised of aluminum with a small amount of iron being dissolved, as shown in Fig. 7.32 (b) and (c), respectively. From the micrograph, it can also be observed that a heavy plastic flow existed within the ultrafine grained structures. It seemed that some particles were elongated or heavily deformed due to the plastic flow.

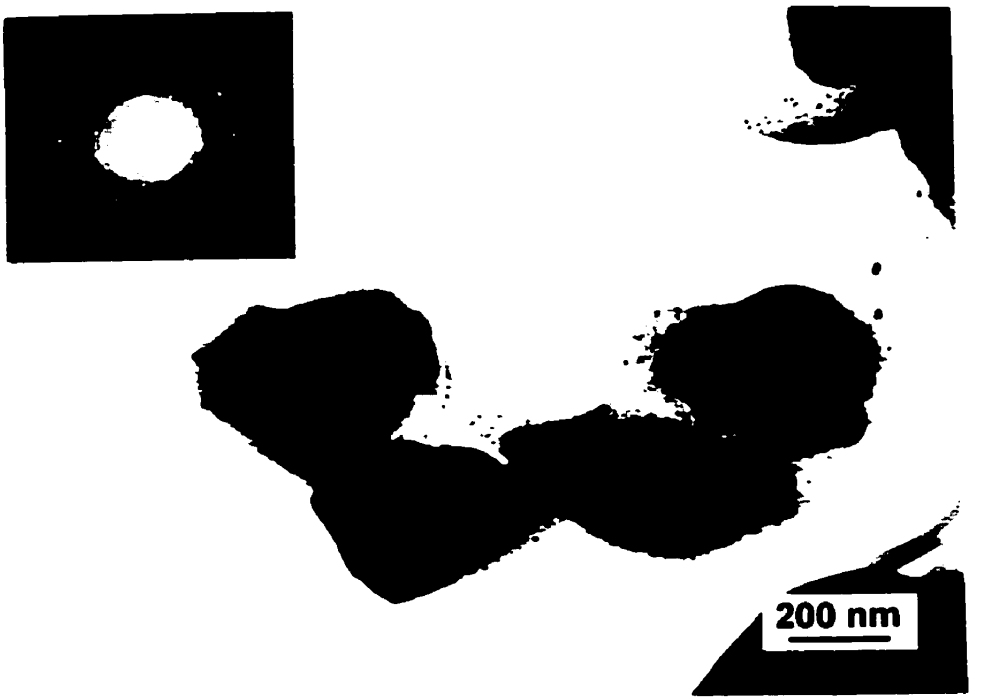

(a)

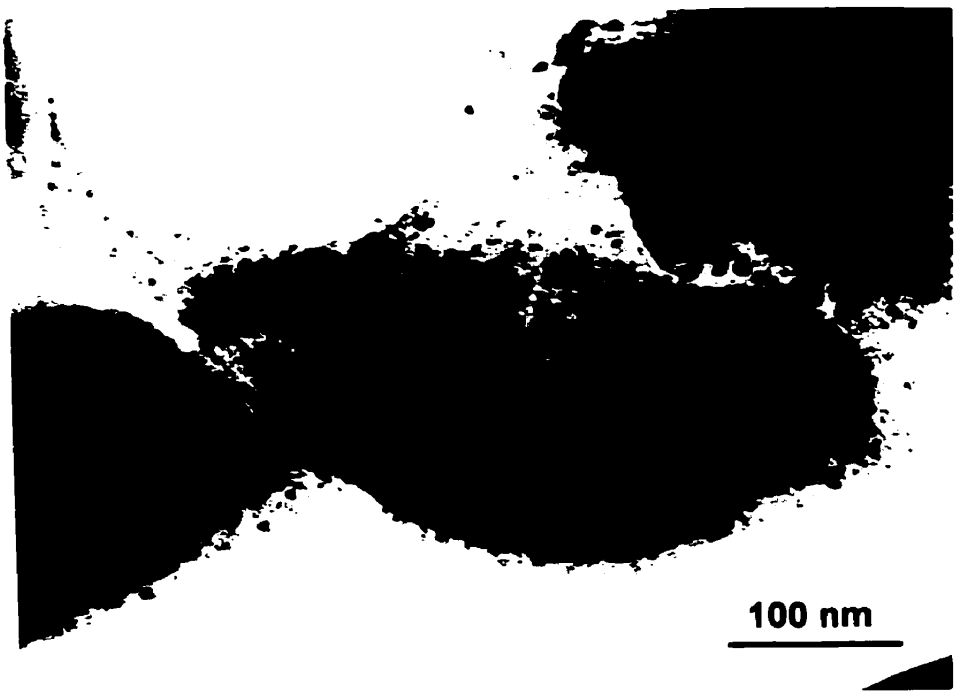

(b)

Fig. 7. 23 *(continued)*

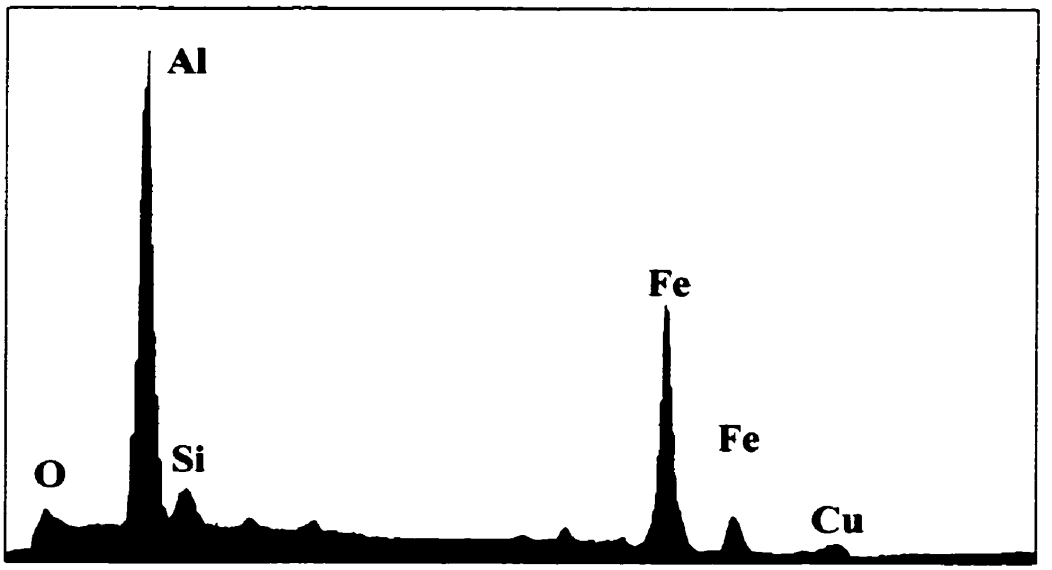

(c)

Fig. 7. 23 TEM morphology of wear debris of the Al-Si alloy at a load of 5 kg, showing the aggregates with ultrafine grained structures, (a) and (b). The insert is an electron diffraction pattern of the aggregates. (c) EDS analysis of the wear debris corresponding to (a) and (b), showing the presence of Fe.

(a)

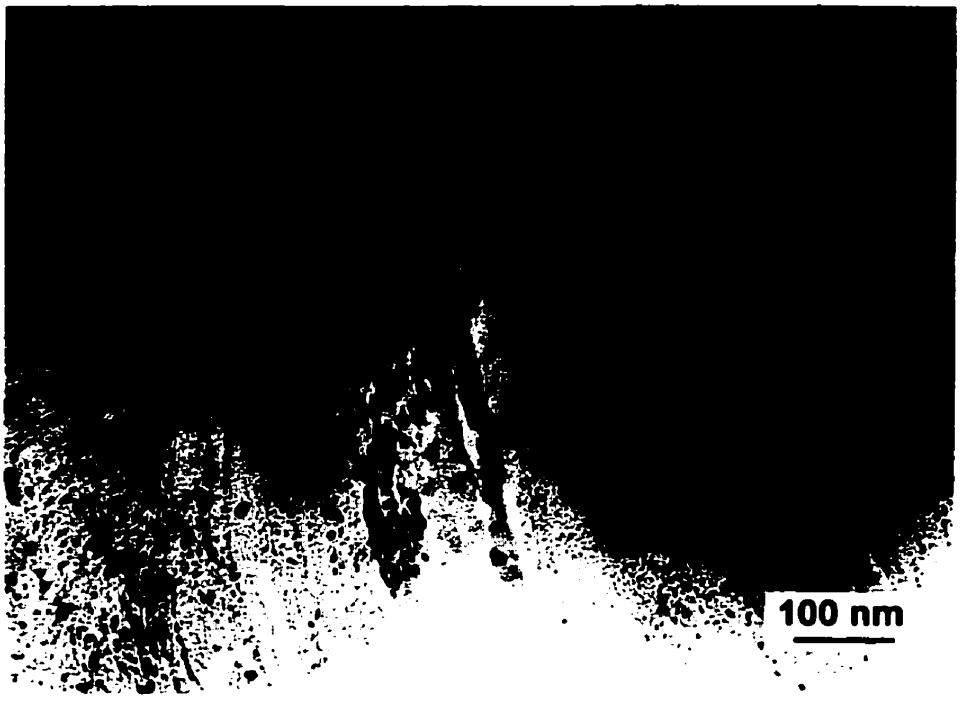

(b)

Fig. 7. 24 TEM micrographs of wear debris of the Al-Si alloy at a load of 10 kg.
(a) An aggregate at a low magnification.
(b) Nanocrystalline structures within the aggregate at a high magnification.

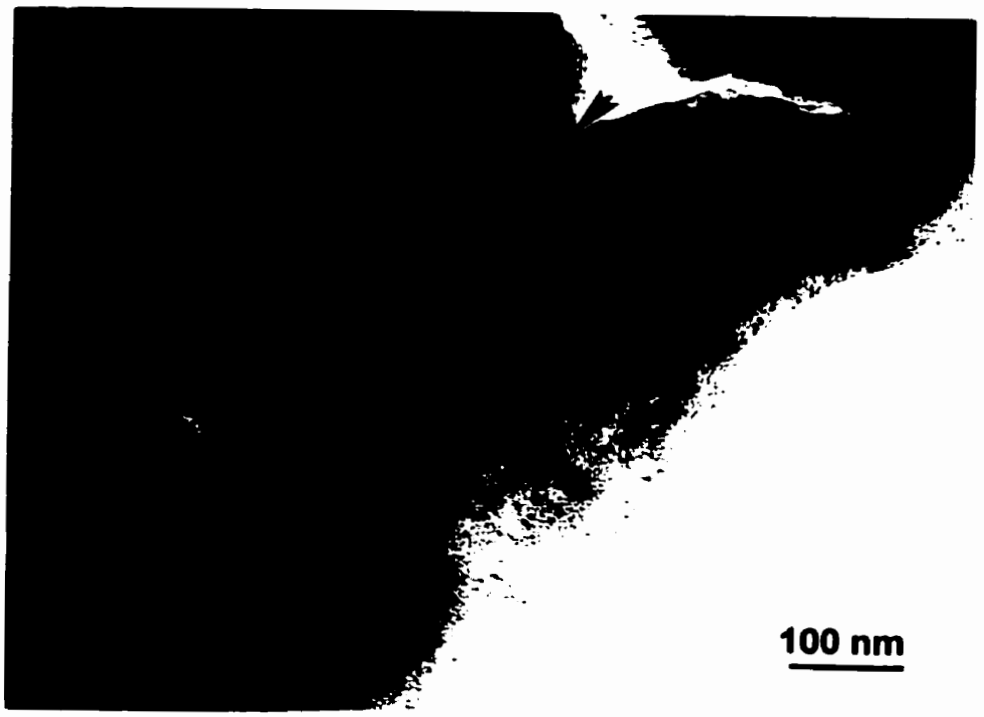

(a)

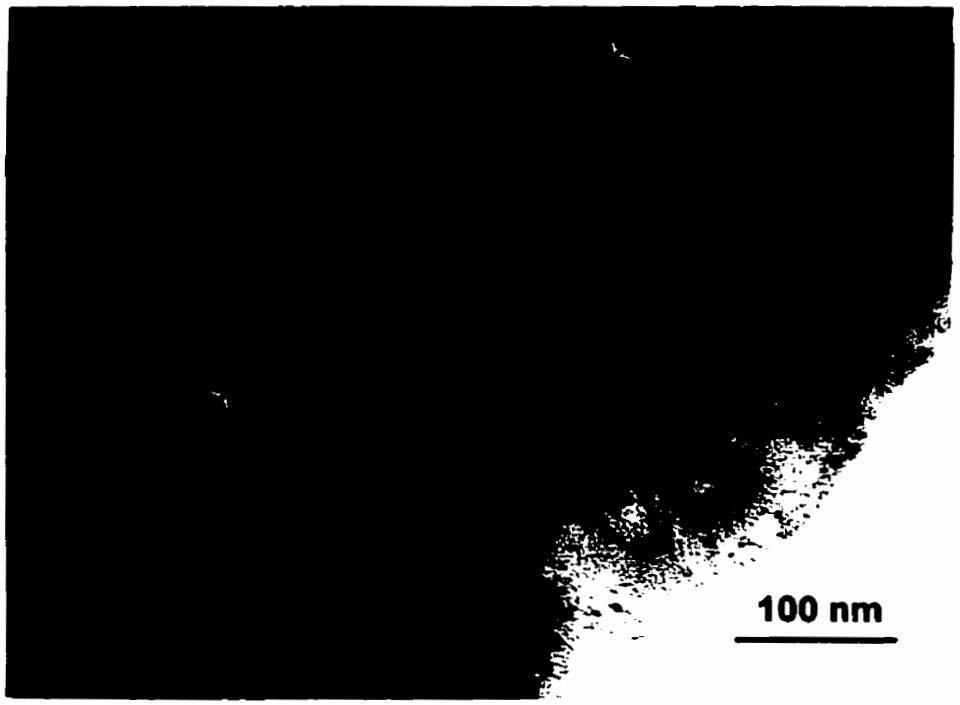

(b)

Fig. 7. 25 TEM micrographs of wear debris of Al-Si alloy at a load of 15 kg, showing nanocrystalline structures of a mixture of FeAl and Al_2O_3. (a) At a low magnification. (b) At a high magnification. The arrows show sub-boundary between regions with different orientations of the lamella structures.

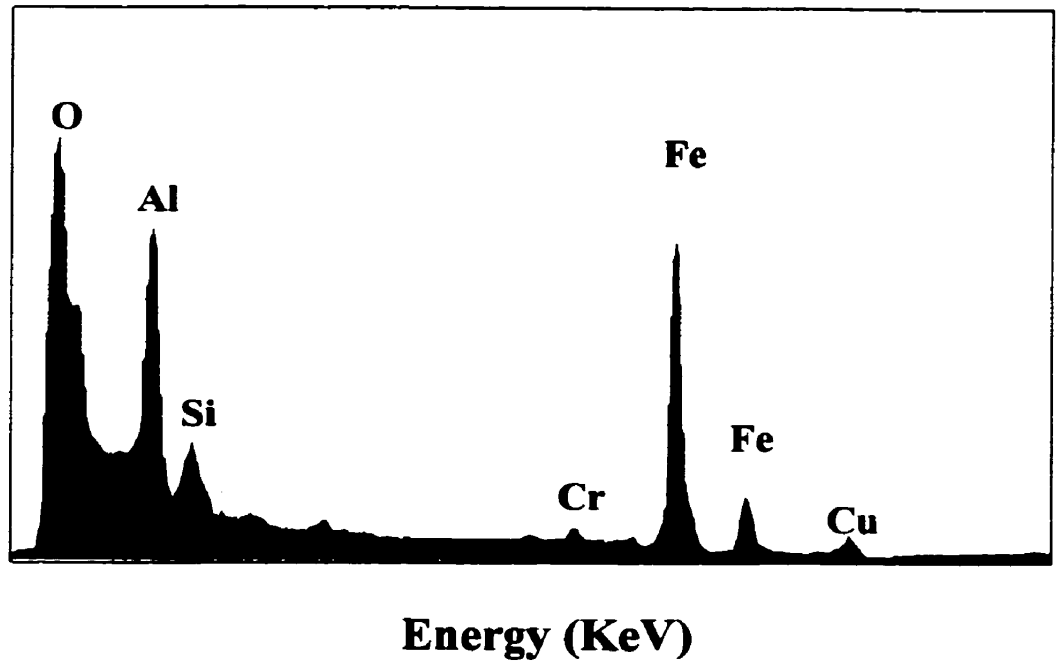

Fig. 7. 26 EDS analysis of the wear debris in Fig. 7.25, showing a considerable amount of Al, Fe and oxygen in the aggregate debris.

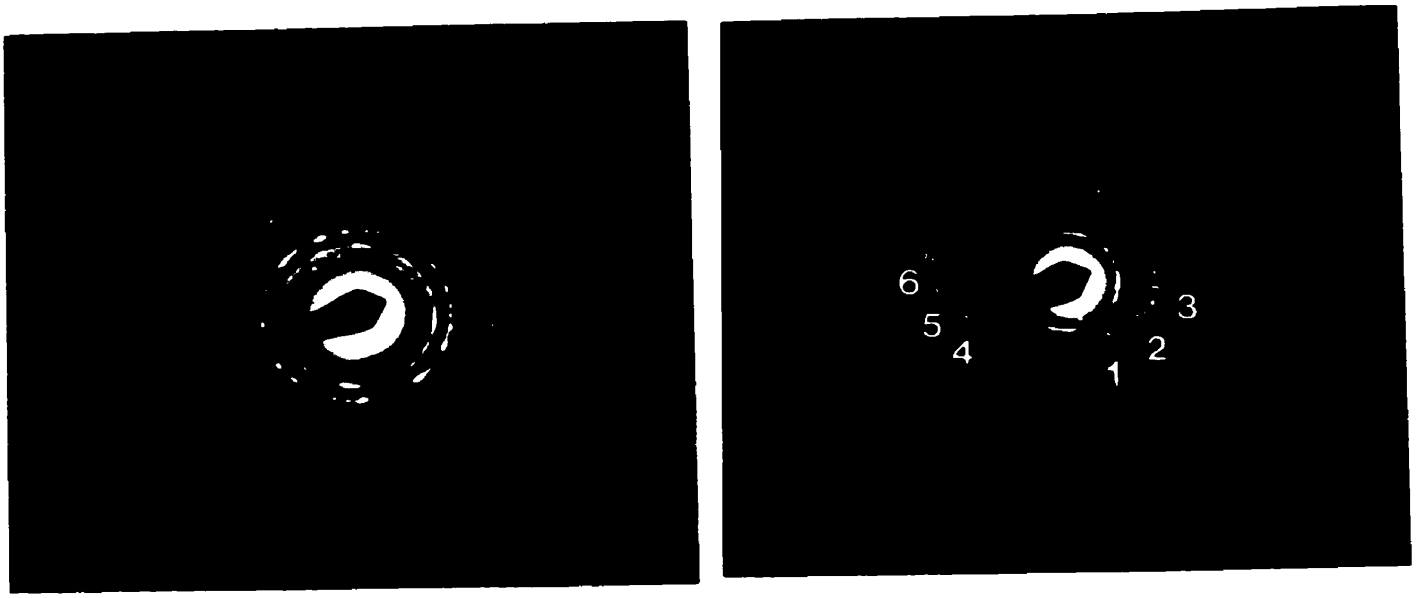

(a) (b)

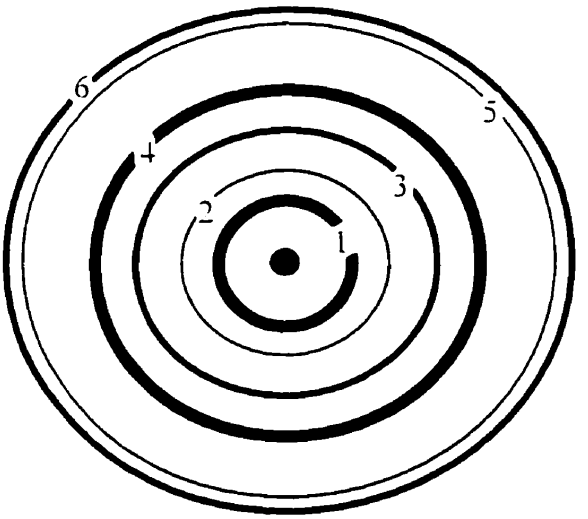

2. FeAl(100)

4. Al(200), Fe(110), FeAl(110), Al_2O_3 (113)

6. Al(220), Fe(200) FeAl(200)

1. Al_2O_3 (012)

3. Al(111), Al_2O_3 (110)

5. Al_2O_3 (211)

(c)

Fig. 7. 27 Electron Diffraction patterns of wear debris at high loads, corresponding to Figs 7.24 and 7.25. (c) Schematic illustration and indices of the diffraction patterns.

Fig. 7. 28 Partial amorphization of wear debris in the aggregates. The insert shows the electron diffraction of the partial amorphization in the debris.

Fig. 7. 29 Eutectic Si particle in the wear debris of the Al alloys. Note that the particle size was smaller as compared to that in the original materials.

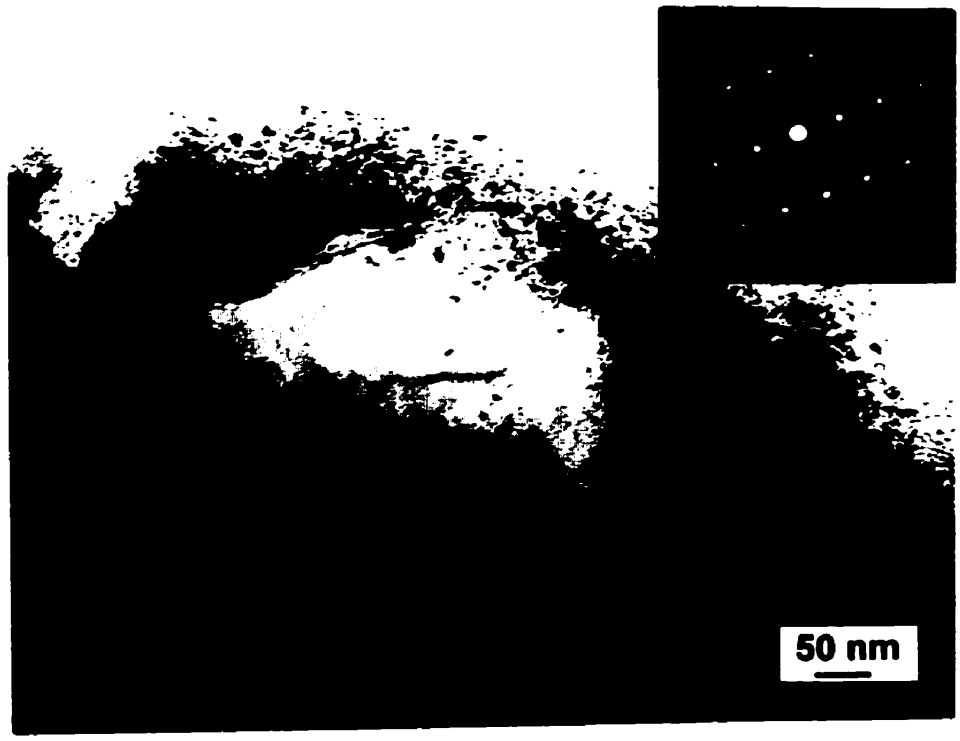

(a)

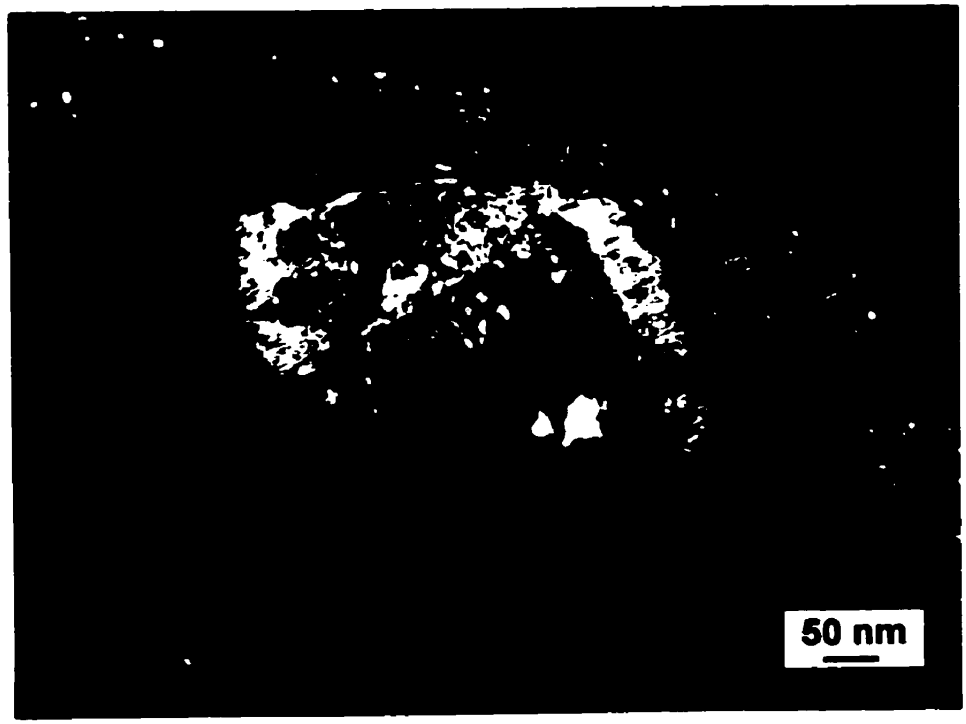

(b)

Fig. 7. 30 A Si particle was intermixed in the ultrafine grained aggregates in the wear debris of the Al alloys. (a) Bright field image, (b) Dark field image. The insert shows the electron diffraction patterns of the Si.

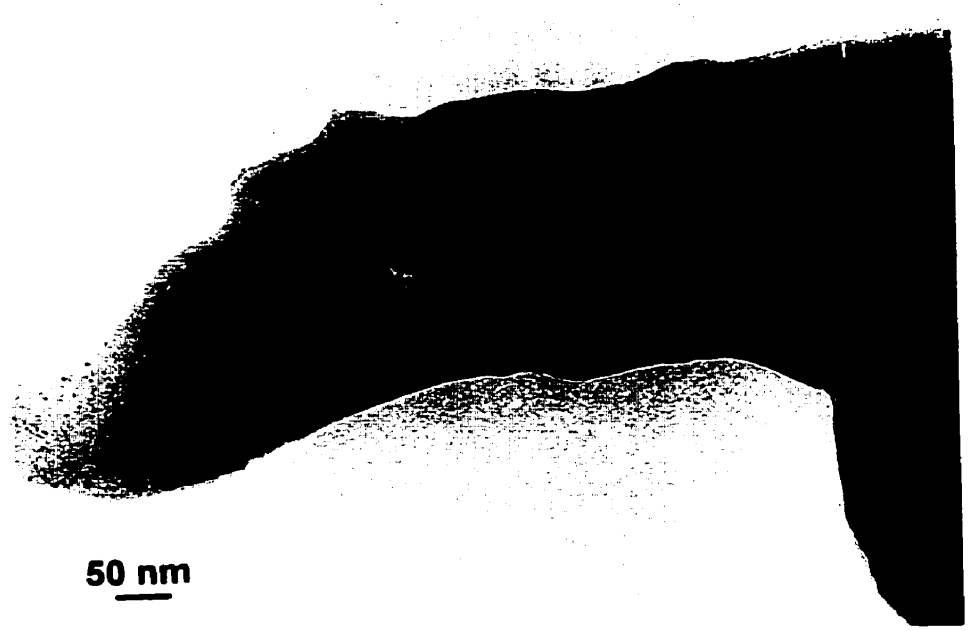

Fig. 7. 31 Fragmented Si particles in a very small size were intermixed in the ultrafine grained aggregates in the wear debris of the Al alloys. Note that the Si particles were forced to orient the plastic flow in the ultrafine grained structure.

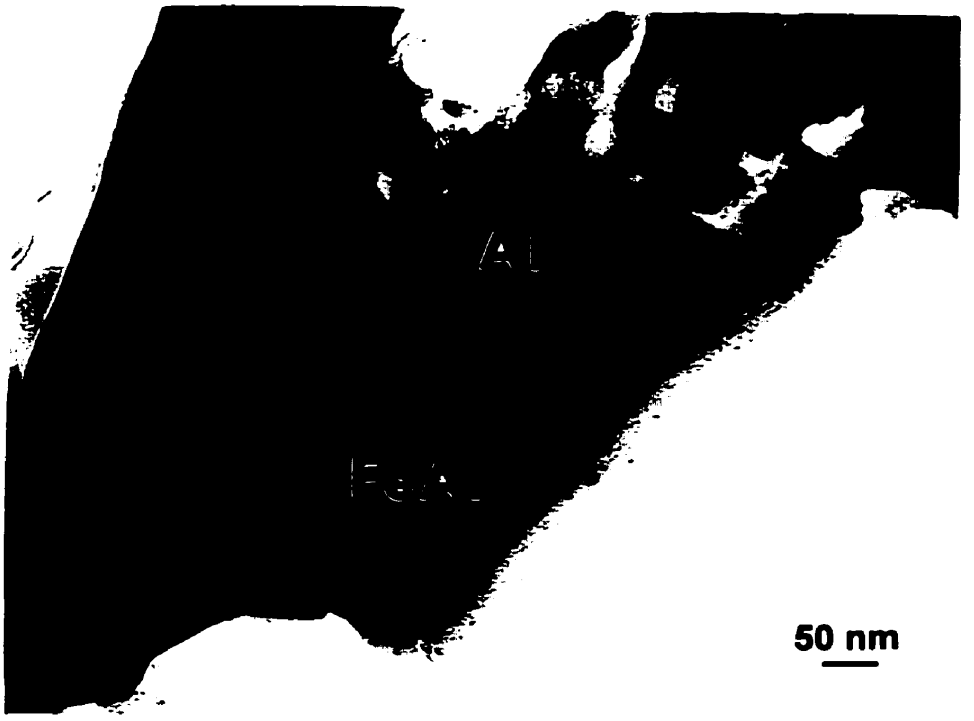

(a)

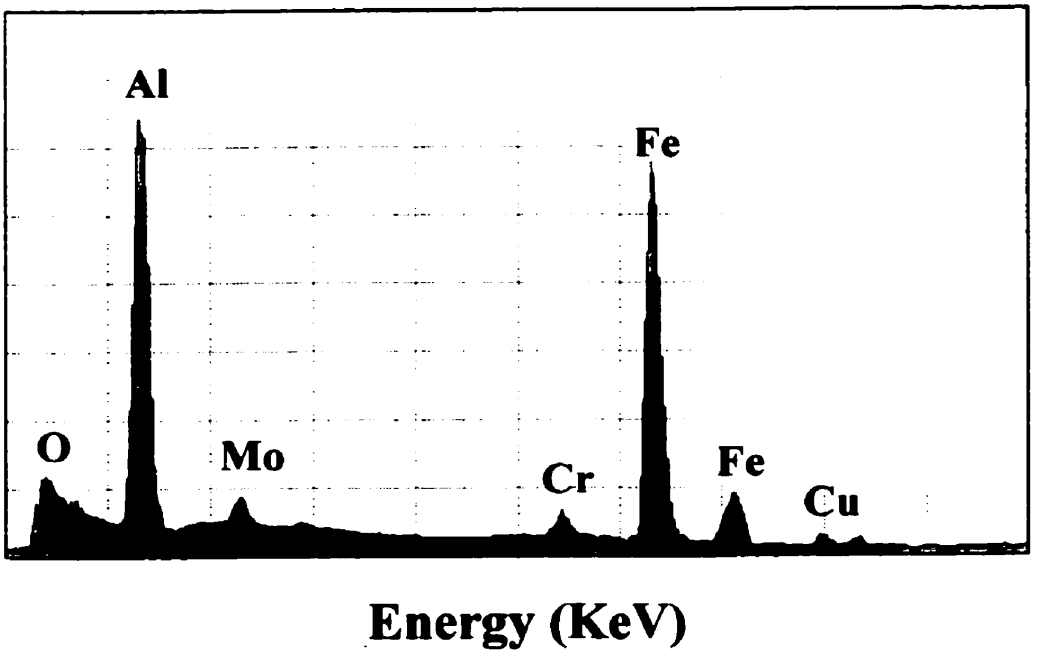

(b)

Fig. 7. 32 *(continued)*

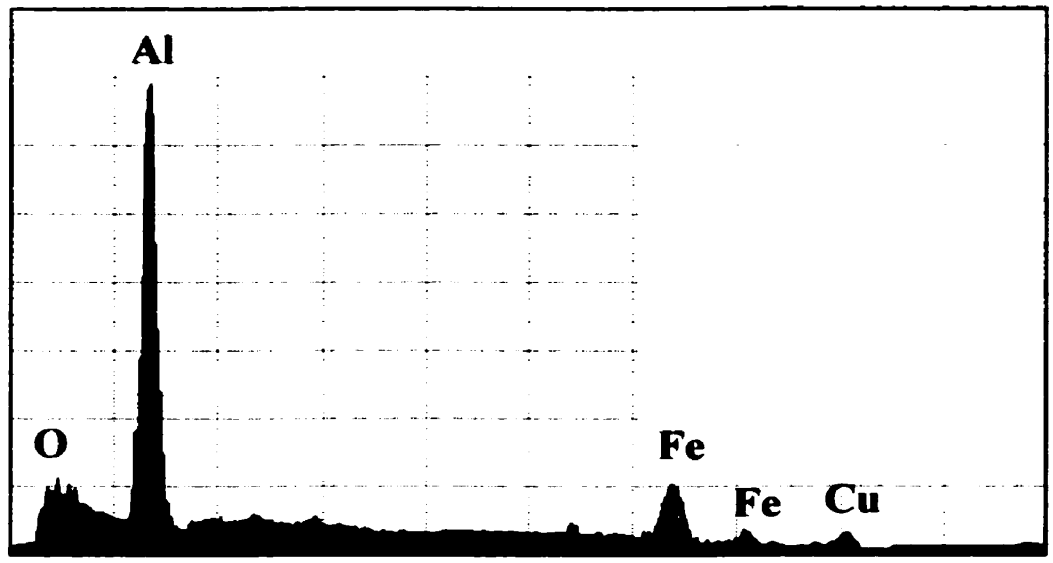

(c)

Fig. 7. 32 A mixture of ultrafine grained aggregates and plate like wear debris of the HP Al. (a) Bright field image; (b) EDS conducted on the ultrafine grained aggregates; (c) EDS conducted on the plate debris.

Table 7.1 Analysis of electron diffraction patterns of wear debris corresponding to Fig. 7. 27.

No. of Ring	Measured d-spacing (Å)	Al		Fe		FeAl		Al_2O_3	
		d_s(Å)	*hkl*	d_s(Å)	*hkl*	d_s(Å)	*hkl*	d_s(Å)	*hkl*
1	3.478							3.479	012
2	2.871					2.899	100		
3	2.359/2.414	2.338	111					2.379	110
4	2.032/2.0733	2.024	200	2.0268	110	2.048	110	2.085	113
5	1.544							1.546	211
6	1.435/1.446	1.431	220	1.4332	200	1.4472	200		

d_s is the plane spacing of lattice from the X-ray powder diffraction standards (JCPDS).

7.5. MÖSSBAUER SPECTROSCOPY

Fig. 7. 33 shows Mössbauer spectra of the HP Al debris and the Al alloy debris. The hyperfine parameters obtained from experiments and calculations after the least-square fitting are shown in Table 7.2. The lines with dotted symbols were from the experimentally acquired data and the solid lines from fitting to the data.

Table 7.2 Mössbauer parameters of the wear debris of the HP Al and Al-Si alloy, relative to α-Fe. I.S.= Isomer Shift; Q.S., Quadrupole Splitting; Hhf, Hyperfine Field.

Phases	Pure Al/Steel			Al-Si/Steel		
	I.S. (mm/s)	Q.S (mm/s)	Hhf (kOe)	I.S. (mm/s)	Q.S (mm/s)	Hhf (kOe)
Fe-Al(Si)	-0.0404	0	0	0.1172	0.6765	0
	-0.2849	0	0	-0.0637	0	0
Fe^{2+}	1.1761	1.5277	0	1.173	1.5244	0
Steel	0.0127	0.0278	327.0.39	0.0127	0.0278	327.0.39
	-0.0051	0.0247	289.310	-0.0051	0.0247	289.310
	-0.0409	0.0249	251.024	-0.0409	0.0249	251.024

As can be seen, the spectra consist mainly of a large portion of central singlet and a small portion of sextets. According to the hyperfine parameters obtained, the singlet is indicative of paramagnetic components and the sextets result from ferromagnetic components in the debris. In the case of the HP Al, as shown in Fig. 7.33, the central singlet strongly suggests that the debris was composed of paramagnetic substances containing the element iron. Fig. 7.33(a) shows the Mössbauer Spectrum of α-Fe as a reference.

It is well known that the characteristic hyperfine parameters (isomer shift, quadrupole splitting and hyperfine field) observed in a Mössbauer spectrum can be used

to identify phases in a way similar to X-ray diffraction patterns. Although the applicability of the Mössbauer effect is not nearly as general as XRD for this purpose, the Mössbauer effect, in some cases, may play an important role in identification of phases. In the Fe-Al system studied, the well-known phases (Al_6Fe, $Al_{13}Fe_4$, Al_5Fe_2, AlFe and Al(Fe) solid solution) could have a paramagnetic component in Mössbauer spectroscopy. Fig. 7.34 shows typical Mössbauer spectra of the above phases obtained as general references, which are indicatives of characteristics of these phases regarding hyperfine interactions[169]. If the phases in the debris in the present work were attributed to the phases Al_6Fe, $Al_{13}Fe_4$, Al_5Fe_2, the spectrum would have strong quadrupole split components, due to the formation of complicated nearest neighbor configurations of Fe atoms [170]. This does not appear to be the case in the present spectrum in terms of the shape and hyperfine parameters, as compared to those in Fig. 7.34. Therefore, possible configurations that can contribute to the presence of the singlet in the obtained spectrum are α-Al(Fe) solid solutions and an Fe-Al intermetallic compound with iron content approaching 50 at.%. Taking the line widths of the spectra into consideration, Al(Fe) solid solution could not be responsible for the singlet only, since the width (Γ=0.579 mm/sec) in the spectrum was much wider as compared to that (Γ=0.26 mm/sec) of the α-Al(Fe) solid solution reported in the literature [171,172]. The singlet can therefore be understood as a superposition of single lines due to the formation of the FeAl intermetallic compounds and α-Al solid solution with iron dissolved. This is consistent with the XRD and TEM results as discussed in the previous sections.

The sextet structures in the spectra resulted clearly from various configurations of

Fe atoms in the original steel slider. It is believed that the sextet must be overlapped by structures with different nearest neighbor configurations, since the sextet was greatly broadened [173]. The steel slider of BCC structure contained an number of alloying elements (W, Mo, Cr and V) symbolized as *M*. For a given Fe atom, there exist 15 nearest neighboring configurations, i. e., (14Fe, 0M), (13Fe, 1M), ..., (1Fe, 13M), (0Fe, 14M). The observed Mössbauer spectrum with a broadened line, in fact, was an overlap of subspectra with various neighboring configurations. The probability for each configuration approximately obeys Binomial distribution. Among the 15 configurations, only (14Fe, 0M), (13Fe, 1M), and (12Fe, 2M) are important, while the others can be neglected because of their trivial probabilities. Therefore, the sextet was fitted using three subspectra based on above mechanisms and probability calculation of the atomic configurations. A divalent doublet was also noted as a small contribution in the spectrum, and it was attributed to a phase with Fe^{2+} according to its isomer shift and quadrupole split, being very likely an iron oxide formed during sliding in the ambient environment. This result is in agreement with that obtained by Antoniou et al[133].

Similarly, the Mössbauer spectrum of the debris of the Al-Si alloy also indicates the formation of paramagnetic substances, in addition to the sextet resulting from the original steel slider, as shown in Fig. 7.35. It was observed that the paramagnetic component in the spectrum exhibited a central doublet structure. This implies that the surroundings of Fe atoms in a cubic structure corresponding to the paramagnetic substances were altered as a result of addition of Si in the Al alloy, in comparison with that in the HP Al system. Since the quadrupole splitting of the doublet was much greater

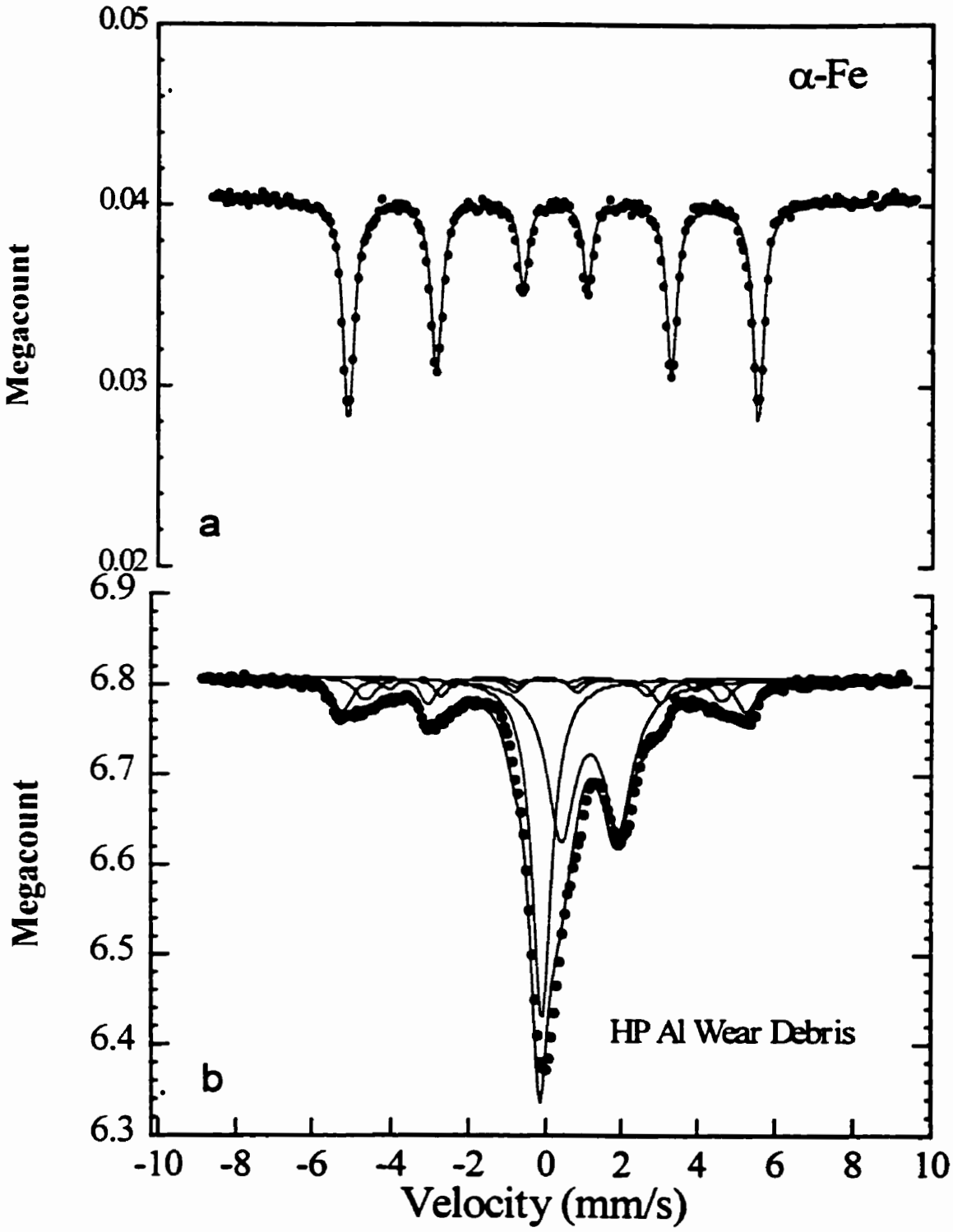

Fig. 7. 33 (a) Mössbauer spectrum of α-Fe as a reference; (b) Mössbauer spectrum of the wear debris of the HP Al sliding against the steel ring at a load of 5 kg. The experimental data (dotted patterns) are fit in solid lines using least square method. The velocities are relative to α-iron.

(Q. S. = 0.68 mm/s), the doublet was less likely to be the binary phases of the Al_6Fe (Q.S.=0.26 mm/s) and Al_5Fe_2 (Q.S.= 0.46 mm/s), although these phases show similar doublet spectra [170,173]. It is reasonably assumed that the doublet could be due to the formation of an FeAl(Si) compound in which some of Al atoms are substituted by Si. Based on this consideration, the doublet can be satisfactorily fitted as shown in Fig. 7.35, and the Mössbauer parameters are shown in Table 7.2. From the spectrum, it can also be noted that the doublet corresponding to Fe^{++} was small since the debris was generated in the Ar atmosphere.

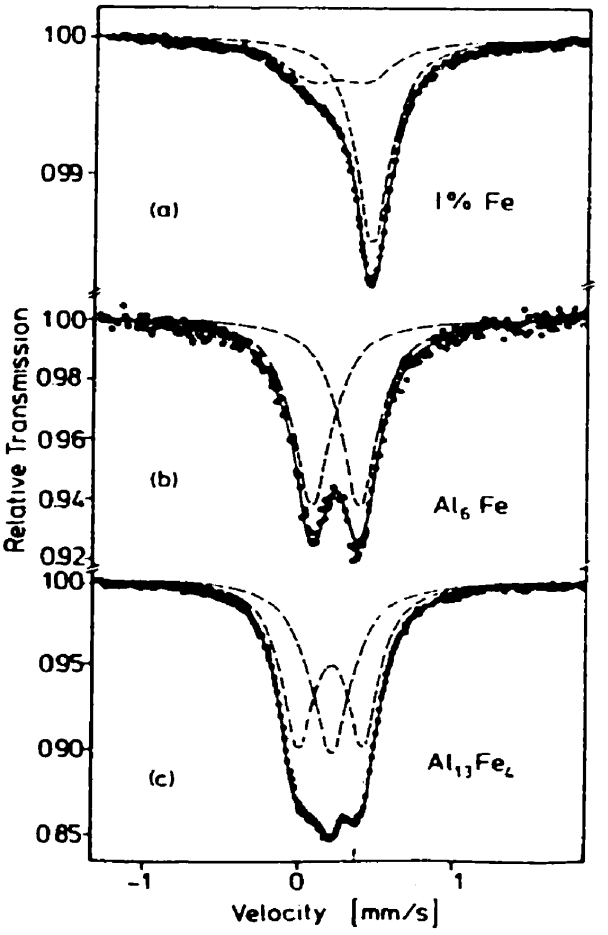

Fig. 7. 34 Typical Mössbauer spectra of the phases in the binary alloy of Al-Fe. (After [169].)

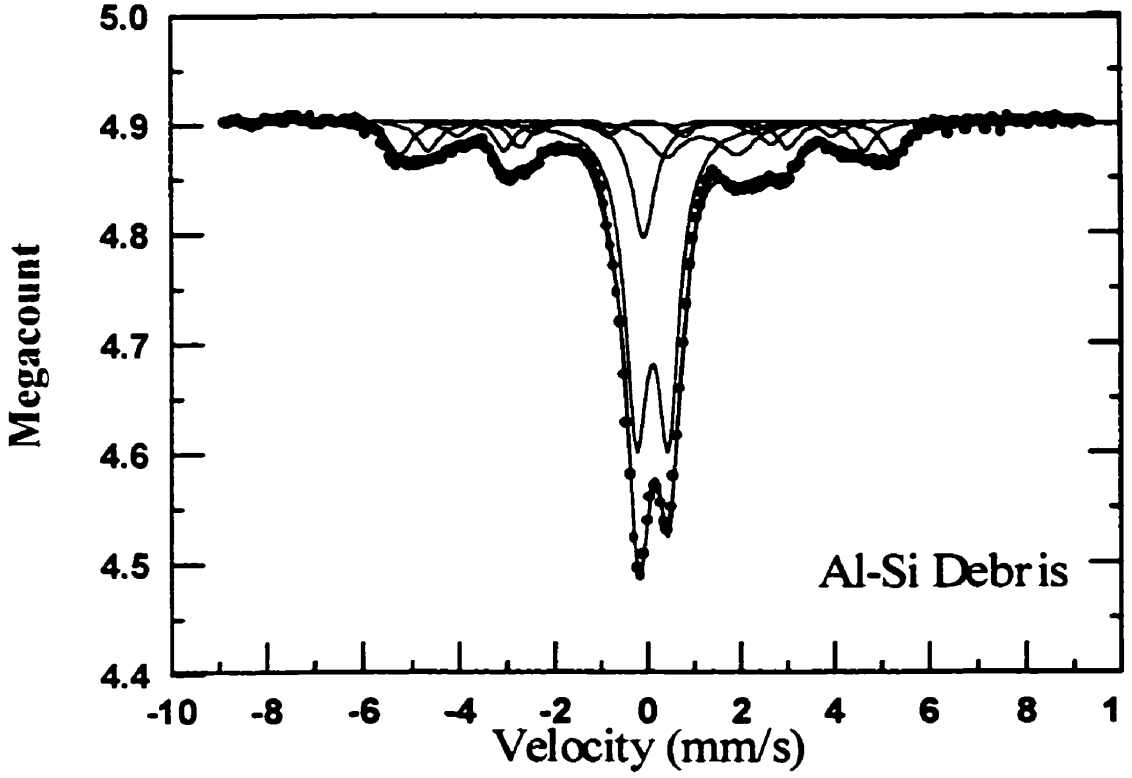

Fig. 7. 35 Mössbauer spectrum of the wear debris of the Al-Si alloy sliding against the steel ring at a load of 12 kg. The experimental data (dotted patterns) are fit in solid lines using least square method. The velocities are relative to α-iron.

7.6. DISCUSSION

7. 6. 1 Formation of wear debris and wear mechanism

In the literature of wear studies of Al alloys and Al composite[22,34,52,74,78,79, 101,174], it is generally acknowledged that there are two kinds of wear debris generated by the sliding wear of the Al based alloys, 1) aggregates with very fine particles at low loads and 2) plate-like debris with a relatively large size at median or high loads. This consideration was made in terms of geometric features of the wear debris. According to a detailed characterization of the microstructures of the wear debris in this work, each kind of debris mentioned above can be further classified. The aggregates generated at a low load were mainly comprised of a mechanical mixture of α-Al and α-Fe, while the ultrafine grained aggregates were products of solid state reaction and oxidation caused by the severe deformation and frictional heating. The formation mechanisms of the two kinds of ultrafine grained aggregates will be discussed in detail in the following section. With respect to the plate-like debris with a relatively large size, the plate debris generated at a relatively low load were not composed of fine particles but instead were monolithic Al alloys with extensive shear deformation structures. At a high load, however, the plate-like debris were actually compacted layers that consisted mainly of the ultrafine grained particles similar to those found in the mechanically mixed layers (MML) in the wear surface of the materials. This kind of wear debris plate contained a considerable amount of Fe that was transferred from the sliding counterpart. It is apparent that different plate debris were indicatives of different sliding wear stages or different the wear mechanisms that governed wear behavior during the sliding wear.

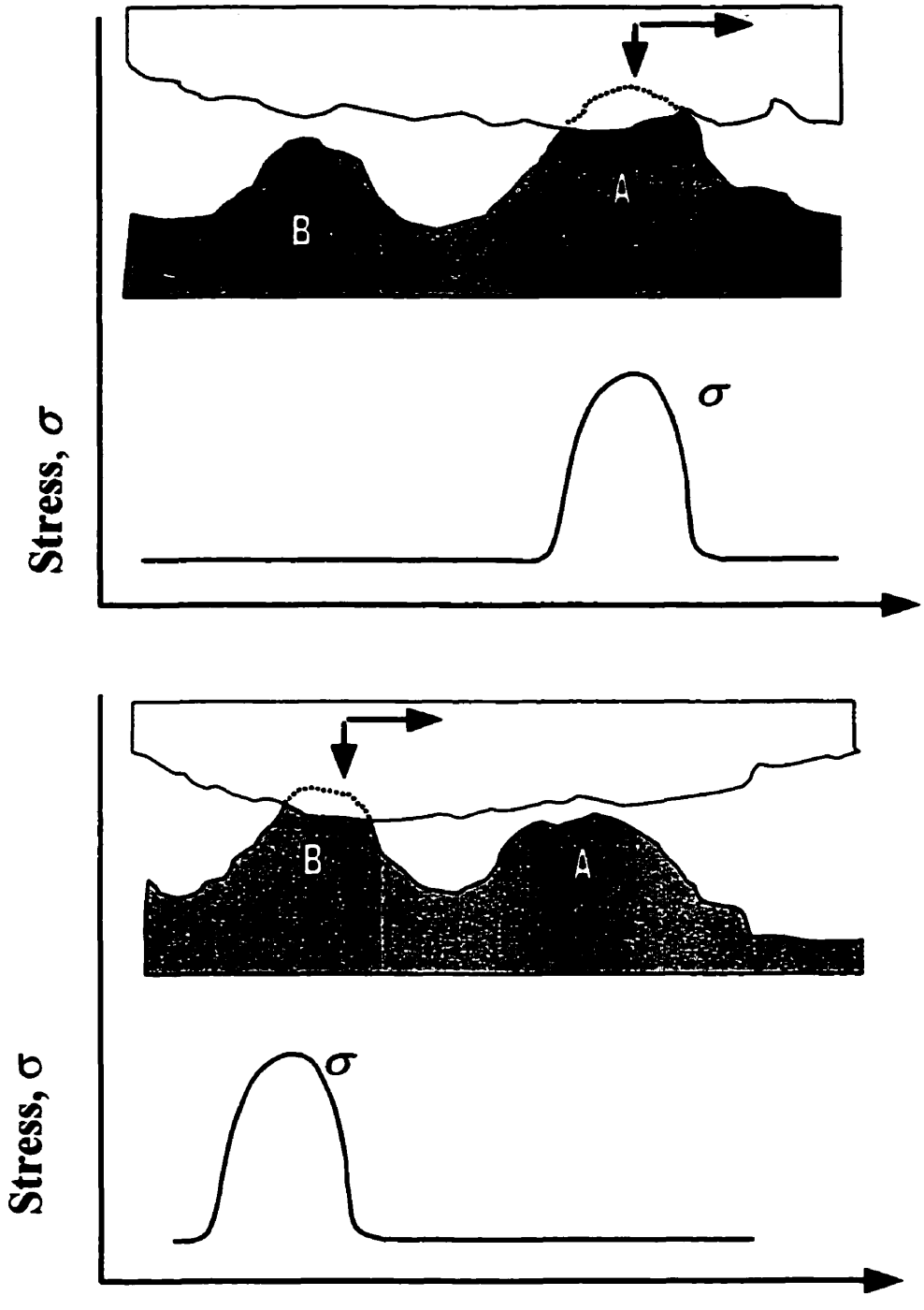

Fig. 7. 36 Schematic illustration of the repeated contact and cyclic loading condition of the asperities. (a) Asperity A is loaded; (b) Asperity B is loaded while asperity A plastically deformed.

The wear debris plates having monolithic Al alloys were generated in conjunction with ultrafine grained aggregates in which aluminum and iron were mechanically mixed at low loads. The debris plates were less dominant in proportion in the wear debris as compared to the ultrafine grained particles at this load range. Based on the microstructure observations, it is very likely that this kind of debris plates was generated at the exit end of the wear tracks as a result of shear deformation when they were extruded from the worn surface. The lamella or striation patterns that were observed on the debris plates might be formed as a result of "stick-slip" motion [162] in which a cyclic stress was involved. A cyclic stress state could be also associated with local asperity contact. Given the fact that the real contacts between the sliding surfaces would be asperities, each asperity could be brought into contact in a cyclic manner, that is, asperities could be loaded and unloaded alternatively due to plastic deformation. One asperity would be brought into contact, once another asperity lost contact with the asperities on the counterpart surface due to plastic deformation at a relatively low load. Therefore, this would result in cyclic loading and unloading of the asperities during the sliding course of practical contact surfaces. Fig. 7. 36 schematically shows the repeated contact and cyclic loading condition of the asperities. It should be mentioned that the cyclic loading condition and alternative plastic deformation at the asperities could occur in both sliding contacts. This may result in a fatigue-like failure in the worn surfaces.

It is seen that the surface and subsurface are subjected to a combined compression-shear stress, under which the fatigue crack growth is very complex, and no clear and sufficient data are available yet to address the complicated situation[120, 175,

176]. In Rosenfield 's shear instability model of sliding wear, a shear crack in Mode II as defined in fatigue of materials[176] could form as a result of competition between the flow strength of the material and the stress intensity. This model, to some extent, could be used to interpret the results observed in the present work, and moreover, the TEM microstructural observations of the shear bands in the worn surface as discussed in Chapter 5, also support the model and is in agreement with striation findings. It should be mentioned that the actual situation of the crack growth in the subsurface of the worn surface is far more complicated than those described in Rosenfield's model. The actual cracks might be deviated from the shear direction due to defects in the material and most probably due to the presence of particulate wear debris from mechanically mixed layer although the MML was just a simple mixture of aluminum and iron at the relatively low load. Therefore, the cyclic shear-induced-fatigue (Mode II) might extend and develop into tension fatigue (Mode I), as shown in Fig. 7. 37.

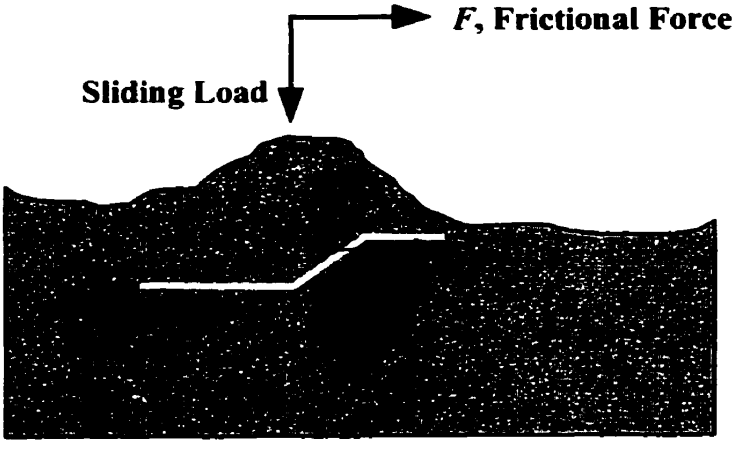

Fig. 7. 37 Extension and development of shear induced fatigue (Mode II) into tension fatigue (Mode I) as a result of disturbance of secondary particles in the subsurface of the worn surface.

The role of fatigue in the sliding wear has been reviewed in several papers [177-179]. The fatigue concept in the wear of materials has been initially developed to re-examine the Adhesive theory [39]. Although some interesting discussions have been reported in the literature, a clear evidence of fatigue-like striations in the worn surface or wear debris is still insufficient to support the fatigue concept of wear. As reviewed in [178], striation like patterns were found in a sliding system of a Ni-Cu alloy slid against a stainless steel, but the spacings of the striation were found to be as large as 4 to 5 μm. According to fatigue theory of materials [162, 176], this could give rise to an extremely fast crack growth rate, thus it might not be fatigue striations. In the present work, it was shown that the observed striation spacings were about 1.2 μm, which are more reasonable if the striation patterns are referred to as fatigue striation features. These findings may suggest that at a relatively low load, cyclic deformation induced shear cracks were responsible for the formation of plate-like debris of the Al alloys. The formation mechanisms of the striation patterns observed in the wear debris, however, need to be further studied.

It should be mentioned that the absence of such a monolithic plate debris in the Al composite could be due to the presence of the SiC particles that increase the surface strength of the composite. Instead, the plate debris of the Al composite, either at relatively low loads or high loads, were comprised of mixtures that were similar to those observed in the mechanically mixed layers (MMLs) as discussed in Chapter 5. This is also true for the plate-like debris of the HP Al and Al alloys at high loads. It suggests that these plate debris were most probably generated from the MMLs in a manner of

delamination as proposed by Suh [41, 42] and reported by Zhang and Alpas[127].

7. 6. 2 Ultrafine grained structures in the wear debris

As described and analyzed above, the results obtained from different techniques are in agreement and show that the ultrafine grained structure was formed in the wear debris of the HP Al, Al alloy and the Al composite sliding against the tool steel under the unlubricated conditions. The ultrafine grained structure varied depending on the sliding loads at the constant sliding speed. At high loads, the wear debris contained a nanocrystalline mixture of oxides and Fe-Al intermetallic phases, in which iron came from the counterpart steel as a result of transfer of materials and mechanical mixing during the sliding motion. At low loads, the wear debris was mainly composed of a mechanical mixture of original materials from both the contacting surfaces, i.e., α-Al and α-Fe, and no intermetallic phases or oxides were found. As discussed in Chapter 5, the mechanically mixed layers (MMLs) in the worn surface were also comprised of the ultrafine grained structures which microstructural features were similar to those of the wear debris. This suggests that the formation of the MMLs was directly in conjunction with that of the wear debris.

In the present work, it is evident that the transfer of materials between the Al alloys and the steel slider was a common feature in the sliding system. Although the present work focused on the studies of the Al alloy and the Al composite, it was observed that the aluminum was also transferred to the steel slider, i.e., a mutual transfer was

literally occurring in the sliding system. As discussed previously, the actual contact points between the sliding surfaces were individual asperities on the microscopic scale as shown in Fig. 7.38(a). Plastic deformation would be first occurring on the local asperity contacts. The local fragmentation and fracture could take place at some of the asperities as the shear stress was sufficiently higher than strength of the materials. The local fragments could be generated on both surfaces in the sliding contact, especially in the present wear systems where hard secondary particles of Si and SiC in the Al matrix could act as microcutters, as shown in Fig. 7.38(b).

More importantly, adhesion would be favored due to the plastic deformation in the sliding contact, i.e., adhesive junctions were formed on one or both of the sliding materials. These adhesive junctions are believed to contain microstructures in which cell and subgrains of the deformed materials were pronounced. As the sliding motion continued, the adhesive junctions could be fractured and thus transfer of materials occurred in the sliding contact. Some of the loose fragments and the fractured adhesive junctions might stay in the sliding contact as they were compacted into the worn surface, whereas others might be detached from the sliding surfaces and fell as loose debris. The compacted materials, that were mostly not the same either structurally or chemically as the base materials [67], would continue to participate in the sliding process. Therefore, a complicated process of further compacting, smearing and mechanically mixing would occur under the sliding load and frictional force between the sliding contacts during a further sliding. Fig. 7.38 schematically shows major events of fragmentation and mechanical mixing during the sliding wear.

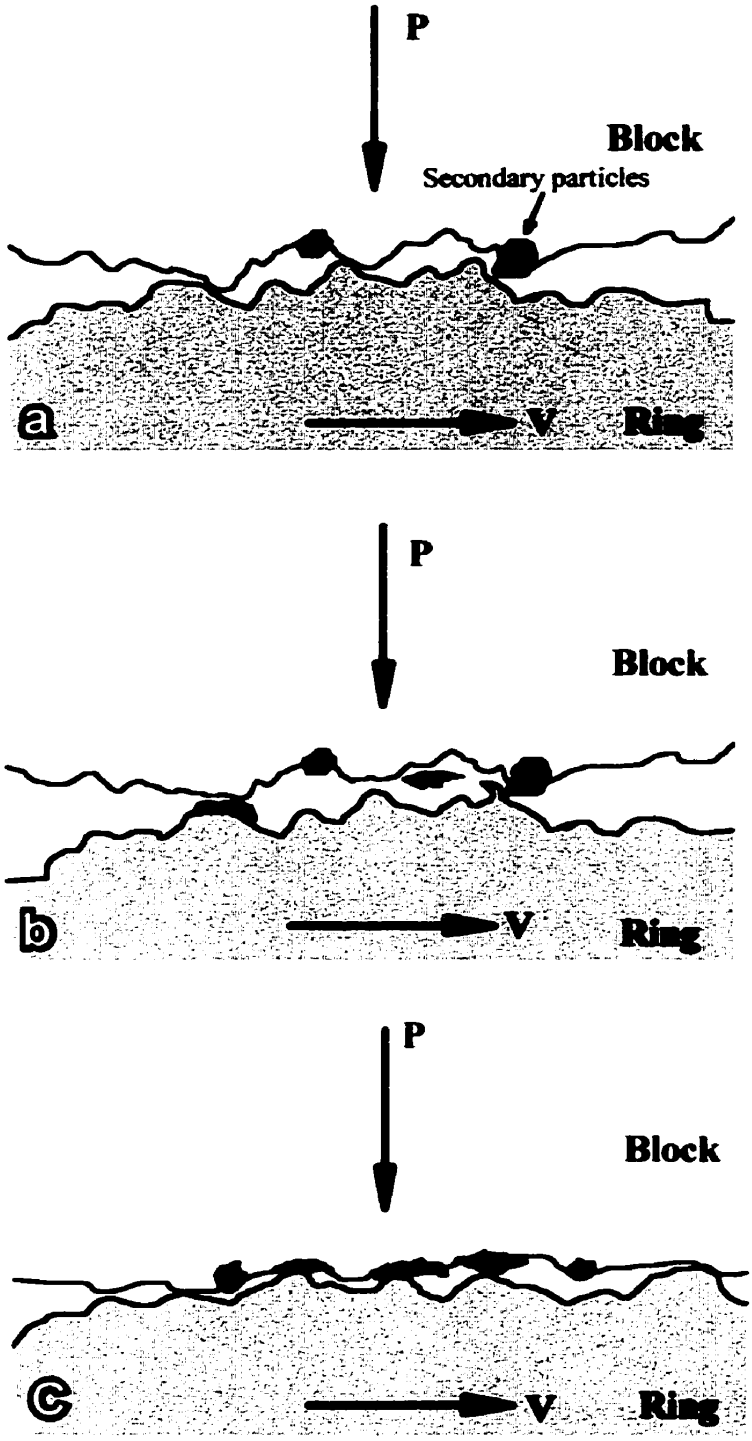

Fig. 7. 38 Interaction of asperities between the sliding surfaces in a dry wear of materials containing secondary or reinforcing particles.

(a) The actual contacts are individual asperities including protuberance of the secondary or reinforcing particles;

(b) Adhesive detachment, fragmentation and microchipping occur due to the further sliding under the normal load;

(c) Further fragmentation and mechanical mixing under a heavy stress in association with frictional heating. See text for details.

Although the fine grained structures containing aluminum and iron were observed at low and high sliding loads, the microstructural features were different, as indicated in the present work. The microstructural changes of the ultrafine grained structures were mainly dependent upon the sliding loads under the dry sliding conditions. With an increase in the sliding load, the shear strain was also increased in the worn surface, especially, the tendency of shear localization could be enhanced. This was favorable for further transfer of materials as a result of local fracture and fragmentation, thus resulting in an increasing tendency of Fe content in the debris with an increase in the sliding load, as shown in Fig. 7. 5 (b). On the other hand, as discussed earlier in the formation of the MMLs in Chapter Five, the local flash temperature was substantially as higher as in a range of 180 °C to 450 °C depending on the loads at the sliding speed used, as estimated using Ashby model [51]. The elevated local temperature was thermodynamically favorable for interdiffusion of materials during the mechanical mixing caused by the sliding. Under the heavy plastic deformation in association with an increasing frictional heating, the mechanical mixing process resulted in mutual diffusion of atoms from both the contacting asperities on an atomic scale. The present finding of dissolution of Fe into the α-Al and formation of the intermetallic phase FeAl confirms an atomic model of mechanical mixing generated by the sliding wear, as shown in Fig. 7. 39. Under a high load during sliding wear, the two contacting surfaces might be brought into atomic contact, in particular between the local contacting asperities of the sliding surfaces. This might give rise to an increased attractive force between the atomic contact. However, some atoms in the interface might be forced to rearrange their positions in order to minimize surface free energy of the interface, as shown in Fig. 7.39 (a). Consequently,

the interface got well accommodated resulting in an adhesive bonding. With an increase in the frictional heating under the high pressure, frictional welding, i.e., interdiffusion of the atoms occurred between the sliding surfaces. At the same time, these adhesively bonded asperities were further refined as a result of fracture and fragmentation and were mixed with other fragments. Therefore, frictional welding of multi-particles could be generated with extensive interdiffusion between the interfaces, as shown in Fig. 7.39(b). The repeated frictional welding and fracture of the powder particles resulted in a very intimate mixing of the debris powder particles that were trapped between the sliding contacts. With continued sliding the grain size of the particles was further refined, and the strain and defect concentration in the mixed particles were also concomitantly increased. The diffusion rates of the atoms in the sliding contact might be enhanced due to the increased defects. This was favorable for the alloying that resulted in the formation of supersaturated solid solution and intermetallic compound. The mechanical mixing and interdiffusion process during the sliding wear at a high load is virtually similar to the commercial mechanical alloying (MA) of metallic powders in a high energy ball mill [73, 180, 181], which involves repeated welding, fracturing and rewelding of powder particles in a dry and high energy ball mill. In an MA process, the solid solubility of Fe in Al was reported to increase from the value as low as 0.025 at. % at an equilibrium state to a value up to 4.5 at. % [181]. The microstructure and morphology of the nanocrystalline aggregates in the wear debris in the present work also showed features similar to those of the nanocrystalline Fe-Al prepared by mechanical alloying [136, 137, 181, 182]. In particular, as discussed previously in the experimental results, the Mössbauer spectra of the wear debris significantly substantiated the findings of the formation of the

intermetallic compound and supersaturated α-Al solid solution containing Fe, in agreement with the observations using X-ray diffraction and TEM. The Mössbauer spectra showed very similar features of the mechanically alloyed materials in the Al-Fe system [136, 182, 183].

It is not surprising that the oxides were noted to coexist with the intermetallic compound in the debris at a high load, since the wear system was exposed to air, with a concomitant increase in the strain level and frictional heat as a result of the increased load. As mentioned above, the bulk surface temperature was considerably lower during the sliding than that would be required for the oxidation observed. It is unlikely that a film of oxide covering most of the sliding surface, would be formed as a result of frictional heat in the present sliding system, as proposed by Quinn[40] in which oxidation wear was dominant. Considering the model presented in Fig. 7.38, oxidation is likely to take place locally at some asperities which were not in contact with the counterpart but could be hot sinks, since a large amount of frictional heat could be transferred into these spots from nearest asperities that were in contact and plastically deformed. As sliding proceeded, the oxidized spots were also brought into contact and underwent a mechanical mixing process, and finally got mixed with others including the intermetallic particles in the mixing process generated by sliding. This interpretation is in agreement with that proposed by Razavizadeh and Eyre [79] and consistent with the results observed in the present work which indicated the presence of oxides mixed with metallic debris. It is very likely that there was a competition between the formation of oxides and intermetallic phases depending mainly on the sliding loads under the sliding conditions.

The oxides, on the other hand, provided microstructural stability as a second phase in the ultrafine grained structure in the debris. It is generally known that a structure with very fine grain size may be unstable because of a large number of grain boundaries that could induce grain growth to minimize the Gibbs free energy of the system. The oxides formed in the manner mentioned above were fractured and comminuted as sliding continued. Participating in the mechanical mixing process, the crushed oxides dispersed into the mixed surface layer, and acted as a pinning points for grain boundaries in the ultrafine mixture in the wear debris.

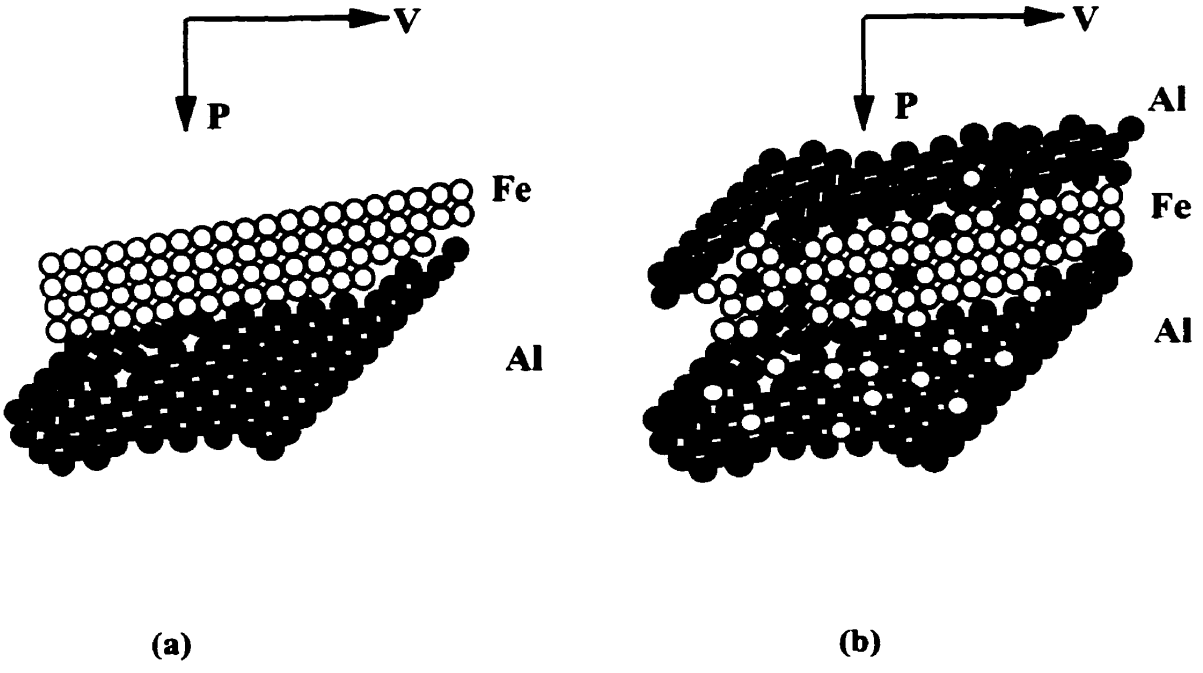

Fig. 7. 39 Atomic Model of the mechanical mixing during the sliding wear. (a) At a high load, rearrangement of surface atoms because of intimate contact; (b) Mutual diffusion in the interface as result of increased defects and frictional heating.

From the microstructural characterization and formation mechanisms of the wear debris, it is clear that the formation of wear debris was virtually related to that of the mechanically mixed layer as discussed in Chapter Five. The material transfer and the mechanical mixing were dominant events in the dry sliding wear at the range of loads used in the present work. The debris particles generated at an early stage during the sliding would be entrapped in the sliding contact and could act as abrasives in the subsequent process of transfer and mixing. With further refining and fragmentation in the above mentioned manner, intimate mixing and alloying of the very fine grained particles occurred and the particles were compacted and incorporated into the worn surface thus forming the MML. Once the MML formed, it provided a protection and could be treated as a layer of solid lubricant before some critical conditions were reached and then loose debris was detached or delaminated from the mixed layer. As observed in the present work, microcracks occurred in the MML and could propagated into large cracks parallel to the sliding direction. As a result, these cracks gave rise to delamination wear in a manner as proposed by Suh[41,42]. Therefore, wear debris, either as aggregates with ultrafine grained structures or plate-like, were mainly detached from the MMLs. The wear debris and the MML were basically comprised of the mixtures that possessed the same chemical and microstructures.

CHAPTER EIGHT SUMMARY

(1) The sliding wear tests showed that the wear resistance of the Al/Si-SiCp composites either at as-cast or T6 conditions was superior to that of the Al-Si base alloy (T6). The increase in the wear resistance, however, was significant only at the low load range. With increasing sliding loads, the wear resistance was almost the same for the composite and the base alloy, and the reinforcing SiC particles did not seem to offer a significant improvement to the wear resistance of the Al-Si alloy during the dry sliding wear. As discussed in the present work, the improvement in the wear resistance at low loads was mainly due to the incorporation of the reinforcing SiC particles that acted as load bearing components during the sliding wear. At high loads, wear mechanisms were mainly governed by the formation, fragmentation and delamination of the mechanically mixed layers in which the majority of the SiC particles became fragmented and were no longer exerted as major load-bearing components.

(2) The wear resistance of the Al-Si/SiC composite can slightly be increased by a T6 heat treatment (solid solution plus artificial aging). The increase in the wear resistance was not significant when compared to the increase in the hardness of the matrix due to the heat treatment, while the hardness of the matrix was increased by almost twice by the age hardening. This wear behavior can be attributed to the findings that an *in-situ* precipitation occurred in the subsurface during the sliding wear of the as-cast Al composites. The precipitates were found to be the same as those in the matrix in the T6 state. It was also found that the coarsening of the precipitates occurred during the sliding wear of the composite.

Based on the microstructural characterization of the precipitates and the dislocation structures in the subsurface of the worn surface by using cross section TEM technique, it was proposed that the in-situ precipitates were induced mainly due to the high shear stress in association with the frictional heating during the sliding wear. The in-situ precipitation was not a stable structure in the worn surface, and as discussed in the present work, some precipitates were very small in size, thus giving a precipitation strengthening of the matrix in the worn surface. Some precipitates were coarsened due to the frictional heating, thus giving an overaged matrix.

(3) Microstructural observations of the subsurface in the worn surface showed that the deformed structures produced by the sliding wear contained a large number of cells and elongated subgrains. The deformed structures varied along the depth, i.e., with an increase in the depth below the worn surface, the size of the cells increased and the elongated subgrains became less developed from the well-developed structures in the near surface. The microstructural evolution along the depth was consistent with the strain distribution in the subsurface that could be best described by an exponential law. It was also found that the elongated deformation structures were less developed in the worn surface of the Al based composite than those in the Al base alloy at the same sliding load. A considerable quantity of dislocations was also observed in the interior of the subgrains.

(4) Small equiaxed subgrains were observed in the near surface of the worn surface. It was identified that the small equiaxed subgrains were formed as a result of recovery and recrystallization process. Based on the microstructural observations, the present work has provided an evidence that the recovery was a dynamic process during the sliding wear, and on the other hand, this initiated a dynamic recrystallization.

(5) Extensive fracture and fragmentation of the secondary particles and reinforcing particles were found in the worn surface. The fracture of the reinforcing particles was one of major reasons why the composite did not show a superior wear resistance as compared to the Al base alloy at a high load.

(6) Mechanically mixed layers were formed in the sliding wear of the Al-Si/SiC composite and Al-Si alloy as well as the HP Al against the M2 steel under the dry sliding conditions. The MMLs were found to consist of elements from both the sliding surfaces, and the detailed microstructures and chemical conditions of the transferred elements were mainly determined by the sliding load at the sliding speed selected in the present investigation. At a low load, the MMLs consisted mainly of simple mechanical mixtures of α-Al and α-iron, whereas intermetallic phases and oxides coexisted in the MMLs at a high sliding load. The microstructural features of the MMLs were noticed to be similar to those of the wear debris which were mostly detached from the MMLs.

(7) It was also observed that a layered structure or sandwich structure, i.e, sublayers, either Fe-riched or Al-riched, existed alternately in the MMLs and was one of major features of the MMLs. Subjected to a further sliding motion, the sandwich structure could be brought into further compaction, fragmentation and extensive mixing. The formation of the sandwich structures provided an evidence of material replenishment in terms of material transfer and mixing during the sliding wear.

(8) Microstructural evolution of the wear debris of the Al based materials was extensively carried out by using XRD, SEM, TEM, and Mössbauer spectroscopy. From the geometric features of the wear debris observed in SEM, two types of

debris can be identified: 1) aggregates with very fine particles; and 2) plate-like debris with a relatively large size. However, the two types can be further classified in terms of the microstructural characterization of the aggregate debris and the plate-like debris. The debris aggregates generated at a low load were mainly composed of a mechanical mixture of α-Al and α-iron. With an increase in the sliding load, the agglomerated debris of nanocrystalline structure were incorporated with Fe-Al(Si) intermetallic compounds, and aluminum- and iron oxides as a result of mechanical alloying and oxidation caused by a large amount of plastic deformation during the sliding process in association with frictional heating. With respect to the plate-like debris in a relatively large size, they were not composed of ultrafine particles but instead were monolithic Al matrix material with extensive shear deformation structures at a low load. However, the plate debris at a high load were formed as a compacted layer that consisted mainly of the ultrafine particles containing iron element similar to those found in the MMLs.

Based on the microstructural characterization, the present work has provided a strong evidence of the formation of the intermetallic compound FeAl, as confirmed using XRD, TEM, and Mössbauer spectroscopy.

(9) A new evidence of the formation of amorphous phases was found in the worn surface of the Al-Si/SiC composite sliding against a bearing steel under the reciprocating dry wear. The amorphous layer was formed in the very near surface of the worn surface, and it was mainly composed of Al element with an occurrence of oxygen. No significant amount of Fe from the steel slider was observed. Coexisting with the amorphous phases, the precipitates containing Ti, Al and O were also observed in the near worn surface. By means of SAD and CBED in TEM, the precipitates were identified as a tetragonal structure phase that was different from

the known Ti-Al intermetallic or oxide compounds. The lattice parameters of the tetragonal structure are: $a = b = 4.423\dot{A}, c = 2.844\dot{A}$. The formation of the precipitates was associated with that of the amorphous phases during the sliding wear.

(10) Amorphization was also observed in the wear debris of the Al-Si alloy and the Al-Si/SiC composite sliding against M2 tool steels under a unidirectional dry wear. It was found that the amorphous phases coexisted with the ultrafine grained aggregates in the wear debris. The mixture of the amorphous phase and the ultrafine grained particles was mainly comprised of Al, Fe and oxygen, suggesting that an extensive mechanical mixing of elements from both the sliding contacts occurred during the sliding wear.

CHAPTER NINE GENERAL SUMMARY AND FUTURE WORK

Friction and wear of materials is a surface phenomenon of interacting materials in relative motion under different conditions such as applied load, velocity, ambient enviroment and with or without lubrication. These different conditions plus different materials give rise to many variables which are involved in a wearing system. Therefore, wear of materials is a complicated process and a thoroughly understanding of wear problems is still a big challenge to engineers and scientists. The present dissertation was undertaken with a primary target of microstructural characterization of worn surfaces and wear debris of Al based materials. In particular, elaborate characterization of mechanically mixed layers (MMLs), that was generated during sliding wear, was conducted by using the modern analytical methods.

From the present work, it was concluded that the structural and chemical features of the mechanically mixed layers, which were found to be common feature of the worn surface of these materials, were dependent on sliding conditions, for example sliding loads in the present sliding systems. The influences of the MMLs on wear mechanisms or wear regimes would be different even for the same sliding materials but different sliding conditions. Correlation of the structural and chemical features of the MMLs and wear debris has suggested that the MMLs played an important role in the intermediate and relatively high load range in the present work. Since the similarities of the MMLs and plate-like debris, the detachment of the plate-like debris from the MML may provide

some new thoughts about the delamination theory of wear proposed by Suh[41,42], i.e., the delamination occurs due to crack initiation in the subsurface or it happens in the MMLs. Obviously, there is difference between the MMLs and subsurface of matrix in terms of plastic deformation and fracture mechanisms. The incorporation of the MMLs in the worn surfaces may largely alter the sliding contacts in the sliding system, and thus any mechanisms or formula (such as wear equation, estimation of frictional temperature rise etc.) without consideration of the mixed layer are inadequate for real situations of the sliding systems.

In the present work, longitudinal and transverse cross-sections were extensively used. A fractured cross section method was also proposed in order to provide clear and direct information of the worn surfaces. This simple method has its unique advantages as compared to conventional cross section preparation since no contamination or artifacts are involved in the sample preparation. This method may be of benefits to other wear systems where mechanically mixed layers and subsurface are of interest. gyghgjgy

As mentioned above, many variables can affect wear mechanism and worn surface of materials. Although the present work has addressed some fundamental aspects of the microstructural characterization of the worn surface and wear debris in the Al based materials, it has not conducted investigations on the effects of sliding speed, ambient temperature and different counterface materials on wear behavior and microstructures of these alloys. In particular, the microstructural features and formation mechanism of the mechanically mixed layer could be altered by different sliding speed

since it may give rise to different strain rate and flash surface temperatures in the worn surface. As well, mechanical features (or properties) of the MMLs also need to be studied in a greater detail, such as hardness, coefficient of friction, residual stress and fracture phenomena which could provide further information how the MMLs play an role in governing or influencing the wear behavior of these materials.

REFERENCES

[1] D. A. Rigney, *Scripta Metall.*, 24(1990)799-803.

[2] D. Kuhlmann-Wilsdorf, Dislocation Concept in Friction and Wear, in *Fundamentals of Friction and Wear of Materials*, ed by D. A. Rigney, ASM, Metals Park, Ohio, 1980, pp.119-186.

[3] J. H. Dautzenberg, *Wear*, 60(1980)401-411.

[4] S. M. Kuo and D. A. Rigney, *Materi. Sci. Eng.* A157(1992)131-143.

[5] S. R. Nutt and A. W. Ruff, Proc. Int. Conf. on *Wear of materials*, 1983, ASME, p4261.

[6] W. M. Rainforth, R. Stevens and J. Nutting, *Phil. Mag.* A, 66(1992)621-641.

[7] Z. Y. Yang, M. G. S. Naylor and D. A. Rigney, *Wear, 105*(1985)73-86.

[8] M. Kerridge, Proc. Roy. Soc. London, Ser. A, 238(1955)515-528.

[9] A. P. Sannino, H. J. Rack, *Wear, 189* (1995)1-19.

[10] P. K. Rohatgi, S. Ray, and Y. Liu, *Int. Materi. Rev.*, 37(1992)129-149.

[11] S. V. Prasad and K. R. Mecklenburg, *Wear*, 162/164 (1993)47-56.

[12] O. P. Modi, B. K. Prasad, A. H. Yegneswaran and M. L. Viadya, *Mater. Sci. Eng., A151*(1992)235-245.

[13] B. Venkataraman and G. Sundararajan, *Acta Mater., 44*(1996)451-473.

[14] S. Wilson and A. Ball, in *Tribology of Composite Materials*, P. K. Rohatgi, P. J. Blau and C. S. Yust eds., ASM International, Metals Park, OH, 1990, pp.103-112.

[15] W. Wu, K. C. Goretta, and J. L. Routbort, *Materi. Sci. Eng.*, A151(1992)85-95.

[16] F. M. Hosking, F. Folgarportillo, R. Wunderlin, and R. Mehrabian, *J. Materi. Sci.*, 17(1982)477-498.

[17] A. T. Alpas and J. Zhang, *Wear*, 155(1992)83-104.

[18] B. N. Pramila Bai, B. S. Ramasesh, and M. K. Surappa, *Wear*, 157(1992)295-304.

[19] A. Jokinen and P. Anderson, Annu. Powder Metallurgy Conf. Proc., American Powder Metallurgy Institute, Princeton, NJ, 1990, pp. 517-530.

[20] A. T. Alpas and J. D. Embury, in *Wear of Materials*, ed. by K. C. Ludema, ASME, New York, 1991, pp.159-166.

[21] A. Wang and H. J. Rack, *Mater. Sci. and Eng., A147* (1991)211-224.

[22] J. Zhang and A. T. Alpas, *Materi. Sci. and Eng.*, A161 (1993)273-284.

[23] A. T. Alpas and J. Zhang, *Metall. Trans., 25*A, (1994)969-983.

[24] M. A. Martinez, A. Matin, J. Llorca, *Metall. Trans.*, 28(1993)207-212.

[25] A. Matin, M. A. Martinez, J. Llorca, *Wear*, 193(1996)169-179.

[26] S. Wilson, and A. T. Alpas, *Wear*, 196(1996)270-278.

[27] A. T. Alpas and J. D. Embury, *Wear*, 146(1991)285-300.

[28] Y. M. Pan, M. E. Fine, and H. S. Cheng, *Scripta Metall.*, 24(1990)1341-1345.

[29] W. Q. Song, P. Krauklis, A. P. Mouritz, S. Bandyopadhyay, *Wear, 185* (1995)125-130.

[30] S. Skolianos and T. Z. Kattamis, *Mater. Sci. Eng.*, A163(1993)107-113.

[31] M. Hunt, Aerospace composites, *Mater. Eng., 108*(6)(1991)27-30.

[32] J. E. Allison and G. S. Cole, *JOM, 45* (1) (1993)19-24.

[33] D. A. Rigney, in *Fundamentals of Friction and Wear of Materials*, ed by D. A. Rigeny, ASM, Metals Park, Ohio, 1980, pp.1-12.

[34] R. Antoniou and D. W. Borland, *Materi. Sci. and Eng.*, A93(1987)57-72.

[35] J. F. Archard and W. Hirst, *Proc. Roy. Soc. London*, 236A(1956)397-410.

[36] J. Halling, *Introduction of Tribology*, Wykeham publication Ltd., London and Winchester, 1976, p33.

[37] L. E. Samuels, E. D. Doyle and D. M. Tueley, in *Fundamentals of Friction and Wear of Materials*, ed by D. A. Rigeny, ASM, Metals Park, Ohio, 1980, pp.13-42.

[38] J. F. Archard, *J. Appl. Phy.*, 24(1953)981-988.

[39] J. F. Archard, , *Wear*, 2(1959)438.

[40] T. J. F. Quinn, *British J. Appl. Phys.*, 133(1962)33-37.

[41] N. P. Suh, *Wear*, 25(1973)111-124.

[42] N. P. Suh, and co-workers, *Wear*, 44(1977)1-162.

[43] T. Kayaba and K. Kato, in *Wear of Materials* 1979, New York(ASME), p.45.

[44] S. C. Lim and M. F. Ashby, *Acta Metall.*, 35(1987)1-24.

[45] T. J. F. Quinn, *ASCE Trans.* 21(1978), p.78.

[46] D. Kuhlmann-Wilsdorf, *Mater. Sci. Eng.*, 93(1987)107-117.

[47] D. Kuhlmann-Wilsdorf, *Mater. Sci. Eng.*, 93(1987)119-133

[48] D. M. Rowson and T. F. J. Quinn, *J. Phys. D*, 13(1980)209-219.

[49] W. Hirst and J. K. Lancaster, *Proc. Roy. Soc. London*, A259(1961)228-259.

[50] T. J. F. Quinn, J. C. Sullivan and D. M. Rowson, *Wear of Materials*, Dearborn, Michgen, (1979), p.1.

[51] M. F. Ashby, J. Abulaw and H. S. Kong, *Tribology Trans.*, 34(1991)577-587.

[52] J. Zhang, A. T. Alpas, *Acta Materi.*, 45(1997)513-528.

[53] M. A. Moore and R. M. Douthwaite, *Metall. Trans. A*, 7(1976)1833-1839.

[54] D. A. Rigeny, and W. A. Glaeser, *Wear*, 46(1978)241-250.

[55] D. A. Rigeny and J. P. Hirth, *Wear*, 53(1979)345-370.

[56] D. A. Rigney, M. G. S. Naylor and R. Divakar, and L. K. Ives, *Mater. Sci. Eng.*, 81(1986)409-425.

[57] J. J. Bikerman, *Wear*, 39(1976)1-13.

[58] A. T. Alpas, H. Hu and J. Zhang, *Wear*, 162/164(1993)188-195.

[59] R. A. Antoniou, L. J. Brown, J. D. Cashion, *Acta Metall.*, 42(1994)3545-3553.

[60] N. Ohmae, T. Tsukizoe and F. Akiyama, *Phil. Mag.* 40(1979)803-810.

[61] P. Heilmann, W. A. T. Clark and D. A. Rigney, *Acta Metall.* Vol.31, No.8, (1983)1293-1305.

[62] A. S. Malin and M. Hatherly, *Met. Sci.*, 13(1979)463-472.

[63] D. Kuhlmann-Wilsdorf, *Metall. Trans.*, 1(1970)3173-3179.

[64] D. M. Turley, *Metall. Trans.*, 2(1971)3233-3235.

[65] J. Singh and A. T. Alpas, *Metall. Trans. A*, 27(1996)3135-3148.

[66] T. Sasada, *Wear*, 100(1984)561-577.

[67] D. A. Rigney, L. H. Chen, M. G. S. Naylor and A. R. Rosenfield, *Wear*, 100(1984)195-219.

[68] Z. C. Feng and K. N. Tandon, *Scripta Metall.*, 32, (1995)523-526.

[69] M. Kerridge and J. K. Lancaster, *Proc. R. Soc. London, Ser. A*, 236(1956)250-264.

[70] P. Heilmann, J. Don, T. C. Sun, D. A. Rigney and W. A. Glaeser, *Wear*, 91(1983)171-190.

[71] L. H. Chen, *Scripta Metallurgica*, 24(1986)827-832.

[72] D. A. Rigney, *Ann. Rev. Mater. Sci.*, 18(1988)141-163.

[73] J. S. Benjamin and T. E. Volin, *Metall. Trans*, 5(1974)1929-1934.

[74] C. Subramanian, *Wear*, 161(1993)53-60.

[75] Y. Wang, C. Q. Gao, T. C. Lei and H. X. Lu, *Scripta Metall.* Vol. 22, (1988)1251-1254.

[76] S. K. Ganapathi and D. A. Rigney, *Scripta Metall.* 24, (1990)1675-1678.

[77] M. S. Bednar and D. Kuhlmann-Wilsdorf, *Wear*, 181/183 (1995)922-937.

[78] K. Razavizadeh and T. S. Eyre, *Wear*, 79(1982)325-333.

[79] K. Razavizadeh and T. S. Eyre, *Wear*, 87(1983)261-271.

[80] B. N. Pramila Bai and S. K. Biswas, *Acta Metall.*, 39(1991)833-840.

[81] D. L. Lloyd, *Int. Mater. Rev.*, 39(1994)1-24.

[82] D. L. McDanels, *Metall. Trans.*, 16A, (1985)1105-1117.

[83] T. Christman, A. Needleman, and S. Suresh, *Acta Metall.*, 37(1989)3029-3050.

[84] R. J. Lederich and S. M. L. Sastry, *Mater. Sci. Eng.*, 55(1982)143-146.

[85] R. J. Arsenault and R. M. Fisher, *Scripta Met.*, 17(1983)67-71.

[86] R. J. Arsenault, L. Wang and C. R. Feng, *Acta Metall.*, 39(1991)47-57.

[87] M. Taya and K. E. Lulay, *Acta Metall.*, 39(1991)73-87.

[88] R. J. Arsenault, *Mater. Sci. Eng.*, 64(1984)171-181.

[89] V. C. Nardone and K. M. Prewo, *Scripta Met.*, 20(1986)43-48.

[90] C. G. Levi, G. J. Abbaschian, and R. Mehrabian, *Metall. Trans.* A, 9A(1978)697-711.

[91] N. Wang, Z. R. Wang and G. C. Weatherly, *Metall. Trans.*, 23A(1992)1423-1430.

[92] S. R. Nutt and R. W. Carpenter, *Materi. Sci. Eng.*, 75(1985)169-177.

[93] D. L. lloyd, H. Lagace, A. Mcleod, and P. L. Morris, *Materi. Sci. Eng.*, 107(1989)73-80.

[94] D. L. Lloyd, *Acta Metall.*, 39(1991)59-71.

[95] J. J. Lewandowski, C. Liu, and W. H. Hunt, Jr., *Mater. Sci. Eng.*, 107(1989)241-255.

[96] D. L. Davidson, Fracture toughness of particulate Metal Matrix Composites, in *Metal Matrix Composites: Mechanisms and Properties,* eds, R. K. Everett and R. J. Arsenault, Academic Press, Boston, 1991, pp.217-234.

[97] Z. R. Wang and R. J. Zhang, *Metall. Trans.*, 22A(1991)1585-1593.

[98] M. Manoharan and J. J. Lewandowski, *Acta Metall.*, 38(1990)489-496.

[99] C. Perrin and W. M. Rainforth, *Wear, 181/183* (1995)312-324.

[100] T. Christman and S. Surech, *Acta Metall., 36*(1988)1691-1704.

[101] A. S. Reddy, B. N. Pramila Bai, K. S. S. Murthy and S. K. Biswas, *Wear*, 171(1994)115-127.

[102] R. Shivanath, P. K. Sengupta and T. S. Eyre, *The British. Foundryman*, 70(1977)349-356.

[103] S. Usmani and K. N. Tandon, *J. Therm Spray Tech.*. 1(1992)249-253.

[104] Vander Voort, *Metallography Principles and Practice*, McGraw-Will Book Company, New York, 1984.

[105] X. Y. Li, F. J. Wang, T. C. Ma, (1988), Composite Modification On The Surface Of High Speed Steel By Ion Beam Assisted Deposition, Proc. Sino-Germany joint symp. On Vacuum And Surface Analysis (VASA-88), World Scientific Press, Singapore, 1988, pp.180-192.

[106] U. Gonser and M. Ron, Analysis of Phases and States in Metallic Systems, in *Applications of Mössbauer Spectroscopy*, ed. By R. L. Cohen, Academic Press, New York, 1980, p.285.

[107] T. Suzuki, K. Arai, M. Shiga and Y. Nakamura, *Metall. Trans. A*, 16A(1985)1937-1942.

[108] G. P. Huffman and R. M. Fisher, *J. of Applied Physics*, 38(1967)735-742.

[109] P. K. Rohatgi, R. Asthana, and S. Das, *Int. Met. Rev.*, 31(1986)115-139.

[110] M. H. Jacobs, *Phil. Mag., 26* (1972)1-13.

[111] K. Matsuda, S. Tada and S. Ikeno, *J. Electron Microsc., 42*(1993)1-6.

[112] G. C. Weatherly and R. B. Nicholson, *Phil. Mag., 17*(1968)801-831.

[113] A. Korbel and P. Martin, *Acta Metall.*, 34(1986)1905-1909.

[114] M. A. Meyers and K. K. Chawla, *Mechanical Metallurgy*, Prentice- Hall International Inc., 1984.

[115] H. Gudmundsson, D. Brooks and J. A. Wert, *Acta Metall.*, 39(1991)19-35.

[116] W. Pfeiler, M. Zehetbauer and J. Schrank, *Scripta Metall.*, 19(1985)505-510.

[117] C. M. Rao and T. H. Kosel, *Wear of Materials*, 1985, pp.364-372.

[118] Y. Song and T. N. Baker, *Materi. Sci. and Techno.*, 10(1994)406-413.

[119] H. J. Rack, *Materi. Sci. and Techno.*, 29(1977)179-188.

[120] A. R. Rosenfield, *Wear*, 61(1980)125-132.

[121] A. R. Rosenfield, *Wear*, 72(1981)97-103.

[122] A. R. Rosenfield, *Wear*, 116(1987)311-328.

[123] J. H. Dautzenburg and J. Zaat, *Wear*, 23(1973)9-19.

[124] C. Perrin, W. M. Rainforth, *Wear*, 203/204(1997)171-179.

[125] TableCurve 2D, V. 4.0, AISN Software Inc., 1996.

[126] E. Voce, *J. Inst. Metals*, 74(1948)537-562.

[127] J. Zhang and A. T. Alpas, *Mater. Sci. Eng.*, A160(1993)25-35.

[128] H. J. McQueen, O. Knustad, N. Ryum and J. K. Solberg, *Scripta Metall.*, 19(1985)73-78.

[129] F. J. Humphreys and M. Hatherly, *Recrystallization and related annealing phenomena*, Pergamon, 1995, p370.

[130] M. E. Kassner, M. M. Myshlyaev and H. J. McQueen, *Materi. Sci. Eng.* A, 108(1989)45-61.

[131] G. Gottstein, T. Lee and U. Schemidt, *Mater. Sci. Eng. A*, 114(1989)21-28.

[132] A. J. Leonard, C. Perrin, and W. M. Rainforth, *Materi. Sci. Tech.*, 13(1997)41-48.

[133] R. A.Antoniou, L. J. Brown and J. D. Cashion, *Acta Metall.*, 42(1994) 3545-3553.

[134] K. N. Tandon and X. Y. Li, *Scripta Materialia*, 38(1998) 7-13.

[135] X. Y. Li and K. N. Tandon, *Wear*, 225/229(1999)640-648.

[136] S. M. Kou, Surface and Subsurface deformation of aluminum and aluminum alloys in dry sliding wear, Ph.D. Thesis, The Ohio state University, 1987.

[137] S. Enzo, R. Frattini, R. Gupta et al, *Acta Metall.*, 4(1996)3105-3113.

[138] B. Huang, K. N. Ishihara, P. H. Shingu, *Mater. Sci. Eng.*, A231(1997)72-79.

[139] D. Zhao, F. R. Tuler and D. J. Lloyd, *Acta Metall. Mater.*, 42(1994)2525-2533.

[140] R. J. Arsenault and N. Shi, *Materi. Sci. Eng.*, 81(1986)175-187.

[141] X. I. Wang and D. A. Rigney, *Wear*, 181/183(1995)290-301.

[142] J. P. Cottu, J. J. Couderc, B. Viguier and L. Bernard, *J. Mater. Sci., 27*(1992)3068-3074.

[143] X. Y. Li and K. N. Tandon, *Wear*, 203/204(1997)703-708.

[144] A. T. Alpas and J. Zhang, *Scripta Metall.* , 26(1992)505-509.

[145] R. B. Schwarz and W. L. Johnson, *Physical Review Letters*, 51, No. 5, (1983)415-418.

[146] A. Skopp, M. Woydt and K. H. Habig, *Tribol. Int.*, 23(1990)189-199.

[147] H. Furuichi, K. Matsuura, K. Yamazaki and S. Watanabe, *Wear*, 189(1995)86-90.

[148] H. Torabian, J. P. Pathak and S. N. Tiwari, *Wear*, 172 (1994)49-58.

[149] J. I. Goldstein, D. B. Williams and G. Cliff, Quantitative X-ray Analysis, in *Principles of Analytical Electron Microscopy*, D. C. Joy, A. D. Romig Jr., and J. I. Goldstein, eds.Plenum Press, NY, 1986, p155.

[150] K. W. Andrews, D. J. Dyson, S. R. Keown, *Interpretation of Electron Diffraction Patterns*, Adam Hilger Ltd, 2nd edition, London, 1971.

[151] Y. Jin, C. Li, J. Mi, and M. Yan, *J. of Materi. Sci.*, 28(1993)6000-6006.

[152] G. Hug, A. Loiseau and P. Veyssiere, *Phil. Mag. A*, 57(1988)499-523.

[153] A. Loiseau and A. Lasalmonie, *Mater. Sci. and Eng.*, 67(1984)163-168.

[154] V. Jayaram, *Philo. Mag. A*, 57 No. 3 (1988) 525-542.

[155] B. F. Buxton, J. A. Eades, J. W. Steeds and G. M. Rackham, *Phil. Trans.*, A281, (1976)171.

[156] X. Y. Li and K. N. Tandon, *Scripta Met.*, 33(1995)485-490.

[157] R. B. Schwarz and C. C. Koch, *Appl. Phys. Lett.*, 49(1986)146-148.

[158] I. A. Ovid'ko, *J. Phys D, Appl. Phys.*, 24, (1991)2190-2195.

[159] D. Kulhmann-Wilsdorf and M. S. Bednar, *Scripta Metall.*, 28 (1993)371-376.

[160] E. D. Hondros and M. P. Seah, in *Physical Metallurgy*, ed. by R. W. Cahn and P. Haasen, North-Holland Physics Publishing, Amsterdam, 1983, p.875

[161] J. E. Hatch, *Aluminum, Properties and Physical Metallurgy*, American Society for Metals, Metal Park, Ohio, 1984.

[162] F. P. Bowden and L. Leben, *Proc. Roy. Soc.*, A169(1939)371.

[163] C. Gao, D. Kuhlman-Wilsdorf and M. S. Bednar, *Wear*, 149(1991)297-312.

[164] M. Klesnil and P. Lukas, *Fatigue of Metal Materials*, Elsevier, Amsterdam, 1992, 2nd edition, p92.

[165] A. M. Gokhale, N. U. Deshpande, D. K. Denzer, *Proc. 4th Int. Conf. On Aluminum Alloys*, Atlanta, 1994, **1**, p.685.

[166] B. D. Cullity, *Elements of X-ray Diffraction*, Addison-Wesley MA, 1978, p. 102.

[167] G. K. Williamson and W. H. Hall, *Acta Metall.*, 1(1953)22.

[168] P. Bishop, X. Y. Li and W. K. Caley, and K. N. Tandon, *Wear*, 222(1998)84-92.

[169] S. Nasu, U. Gonser, P. H. Shingu and Y. Murakami, *J. Phys.*, F4(1974)L24.

[170] S. Nasu, U. Gonser and R. S. Preston, *Journal de Physique*, 41(1980) C1-385.

[171] R. S. Preston, *Metall. Trans.*, 3(1972)1831-1835.

[172] L. Murgas, S. Nagy, Z. Homonnay, A. Vertes, J. Lakner, *Hyperfine Interactions*, 28(1986)967-970.

[173] C. A. Stickels and R. H. Bush, *Metall. Trans.*, 2(1971)2031-2042.

[174] S. Wilson and A. T. Alpas, *Wear*, 225/229(1999)440-449.

[175] W. T. Shieh, *Eng. Fract. Mech.*, 9(1977)37-54.

[176] S. Suresh, *Fatigue of Materials*, Cambridge University Press 1991, Chapter 11.

[177] J. Halling, A contribution to the theory of mechanical wear, *Wear*, 34(1975)239-249.

[178] Y. Kimura, The role of fatigue in sliding wear, in *Fundamentals of Friction and Wear of Materials*, ed by D. A. Rigney, ASM, Metals Park, Ohio, 1980, pp.187-219.

[179] K. H. Zum Gahr, Microstructure and wear of materials, Elsevier, Amsterdam, 1987, Chapter 6, pp.367-377.

[180] R. B. Schwarz, *Mater. Sci. Eng.*, 97(1988)71-78.

[181] D. Mukhopadhyay, Structural Evolution in Mechanically Alloyed Al-Fe Powder Mixtures, TMS website, *http://www.tms.org/students*.

[182] D. K. Mukhopadhyay, C. Suryanarayana, and F. H. Froes, *Scripta Metall.*, 31(1994)333-338.

[183] Y. D. Dong, W. H. Wang, L. Liu et al, *Materi. Sci. Eng.*, A134(1991)867-871.

Appendix Mössbauer Effect and Application in Physical Metallurgy

The Mössbauer spectroscopy is referred to as a phenomenon of the emission or absorption of a γ-ray photon without loss of energy due to recoils of the nucleus and without thermal broadening. It was discovered by R. Mössbauer in 1957 and has had an important impact in many branches of physics and chemistry as well as physical metallurgy [A1]. Its unique feature is in the production of monochromatic electromagnetic radiation with a very narrowly defined energy spectrum, so that it can be used to resolve minute energy differences. Because it can be applied to almost every field of science and technology and provides an important insight of nature of substances, R. Mössbauer was awarded with a Nobel Prize in 1961, just a few years later after the young scientist discovered the phenomenon in his PhD graduate research.

Since the Mössbauer effect was established on the basis of nuclear physics and solid state physics, an understanding of the physical insight of the effect could not be completely addressed in a short frame of work such as the present appendix. Only basic concepts are given in terms of explanation of a Mössbauer spectrum related to the present research. The comprehensive theory and principle of the Mössbauer effect is available in the literature[A1, A2]

1. A Mössbauer Spectrum

The resonance absorption of radiation is a phenomenon well known in many areas of physics. The excitation of a tuning fork by sound at its resonance frequency, is a familiar example. It might be thought that the same phenomenon should occur for the γ-radiation emitted when nuclei in excited states loss their energy by radiation. However,

the effect of the recoil momentum, which can be neglected for sound, becomes dominant for γ-radiation, because of its much higher energy. In order to compensate the energy loss resulting from the recoil and observe the nuclear resonance absorption, two methods were used before the discovery of the Mössbauer effect, 1) Increase the velocity of the emitting nuclei, or 2) Increase the thermal broadening by heating the source and absorber. In 1957, R. Mössbauer carried out experiments of this kind and found that lowering the temperature increases the absorption rather than decreasing it. This can be simply explained by the fact that emitting atoms, bound in a crystal (through lowering the temperature), are no longer able to recoil individually. This is known as the Mössbauer Effect.

Experimentally, a Mössbauer spectrum can be obtained through the following method. If γ-rays from a source which has a substantial recoil-free fraction are passed through an absorber of the same material, the transmission of the γ-rays in the direction of the beam will be less than expected because of their resonant reabsorption and subsequent re-emission. This source is mounted on the "velocity modulator". A stationary absorber is placed between the source and the detector. If the nuclear levels in the absorber are split by hyperfine interaction, there will be a number of different energies at which absorption takes place. The accounting rate at the detector will drop whenever the Doppler velocity applied to the source brings the emitted γ -ray into coincidence with an absorption energy in the absorber. A typical Mössbauer spectrum obtained in the above manner is shown in Fig. A1.

2. Basic parameters in the Mössbauer spectrum

It is well known that the Mössbauer effect can produce monochromatic radiation with a definition of the order of 1 part in 10^{12}. This high precision makes it possible that

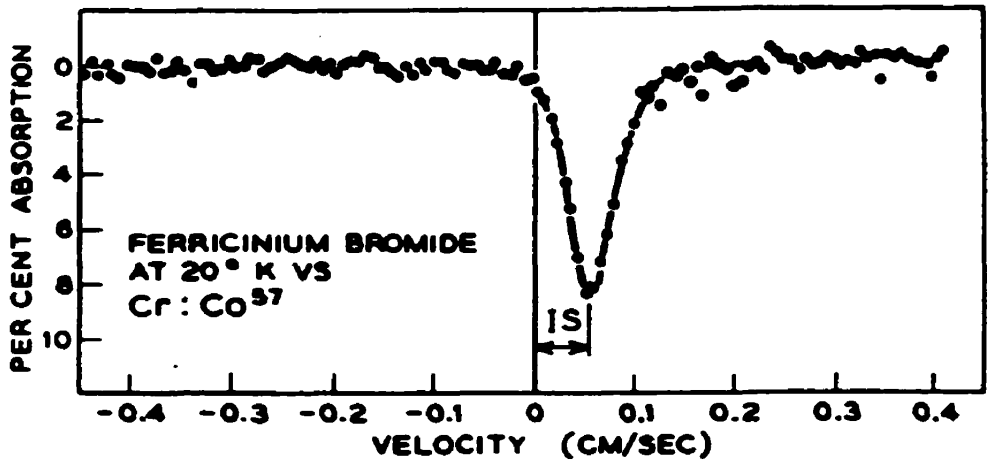

Fig. A1 A typical Mössbauer spectrum of a paramagnetic substance, showing an isomer shift.

chemical information of atoms and their surroundings can be analyzed. The key to the problem lies in the total interaction Hamiltonian [A1] for an atom, which contains terms relating to interactions between the nucleus on the one hand and the electrons (and hence chemical environment) on the other. The Hamiltonian can be written as

$$H = H_0 + E_0 + M_1 + E_2 + \ldots.$$

where H_0 represents all the terms in the Hamiltonian for the atom except the hyperfine interactions being considered; E_0 refers to electric monopole interactions

between the nucleus an the electrons; M_1 refers to magnetic dipole hyperfine interactions; E_2 refers to electric quadrupole interactions. Higher terms are usually negligible.

The E_0 Coulombic interaction alters the energy separation between the ground state and the excited state of the nucleus, thereby causing a slight shift in the position of the observed resonance line. The shift will be different in various chemical compounds, and is generally known as isomer shift, I.S., as shown in Fig. A1. The isomer shift measures the charge density of the atomic electrons and is therefore directly related to chemical bonding and covalency.

The E_2 electric quadrupole splitting is one of the most useful features of Mössbauer spectroscopy. This is the result of the interaction of the nuclear quadrupole moment, Q, with the gradient of the electric field due to other charges in the crystal. The nuclear quadrupole moment reflects the deviation of the nucleus from spherical symmetry. Therefore, the quadruple splitting can provide information of the nucleus with its surrounding electronic charge, thus being helpful for further identification of the chemical structure of the substance. For example, the absence of quadrupole splitting is indicative of cubic or near-cubic site symmetry; its presence, of significant distortion of the crystal structure.

The third important hyperfine interaction is the nuclear Zeeman effect[A2]. This will occur if there is a magnetic field at the nucleus. It is acknowledged that all compounds containing unpaired valence electrons would show a hyperfine magnetic splitting effect in the Mössbauer spectrum. As a result, an alloy or compound is of ferromagnetism or antiferromagnetism, a splitting will be recorded and a sextet line will be shown in the Mössbauer spectrum. On the other hand, a singlet Mössbauer spectrum will be observed in a paramagnetic compound.

3. Application of the Mössbauer spectroscopy in the Al-Fe system

One of the more active areas of Mössbauer spectroscopy has been in the study of metallic systems. Here are examples of the applications of the Mössbauer spectroscopy in the Al-Fe system related to the present graduate research.

It is known that there are a number of phases: $FeAl_3$ (Fe_4Al_{13}), Fe_2Al_5, $FeAl_2$, FeAl and Fe_3Al and ordered structures in the binary Al-Fe system. In a dilute Al alloy, Fe atoms are located on substitutional sites, and from the absence of any quadrupole interaction one can deduce that the distortion by an Fe impurity is cubicly symmetric. As a result, the Mössbauer spectrum of the dilute Al alloy containing a small amount of Fe shows a characteristic line of singlet as shown in Fig. A2. The spectrum is actually comprised of a single line, corresponding to monomers, and a quadrupole line, mainly due to dimers. The frequency of occurrence of dimers is rather larger, which indicates a deviation from randomness in the solid solution [A3].

The agglomeration of iron and the development of phases can be enhanced and advanced by aging, thermal annealing, radiation, cold work, etc. Chill casting of an Al-0.5 at.% Fe has been shown to form the phase Al_6Fe, which appears to exist only as a metastable precipitates in an Al matrix with an orthorhombic structure. The Mössbauer spectrum of the structure is shown in Fig. A3 (b).

The annealing of Al-rich Fe alloys lead to $Al_{13}Fe_4$ or Al_3Fe precipitates with a monoclinic structure. This intermetallic compound shows a Mössbauer spectrum of a single line in the center superimposed on quadrupole components as shown in Fig. A3 (c). With increasing iron in the Al alloys, ordered or disordered FeAl and Fe_3Al are

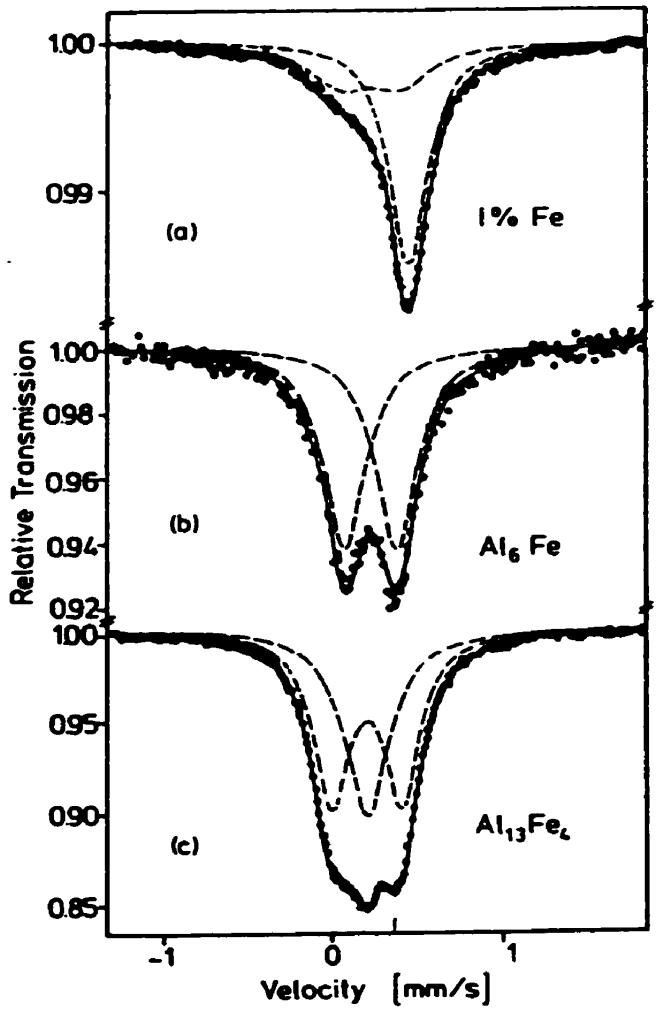

Fig. A2 Mössbauer spectra at room temperature obtained with a Co^{57}-Cu source. (a) Al-1at.%Fe specimen. The single line represents Fe in solution, and the doublet represents the dimers. (b) Al_6Fe precipitates. (c) $Al_{13}Fe_4$ precipitates. (after [A3]).

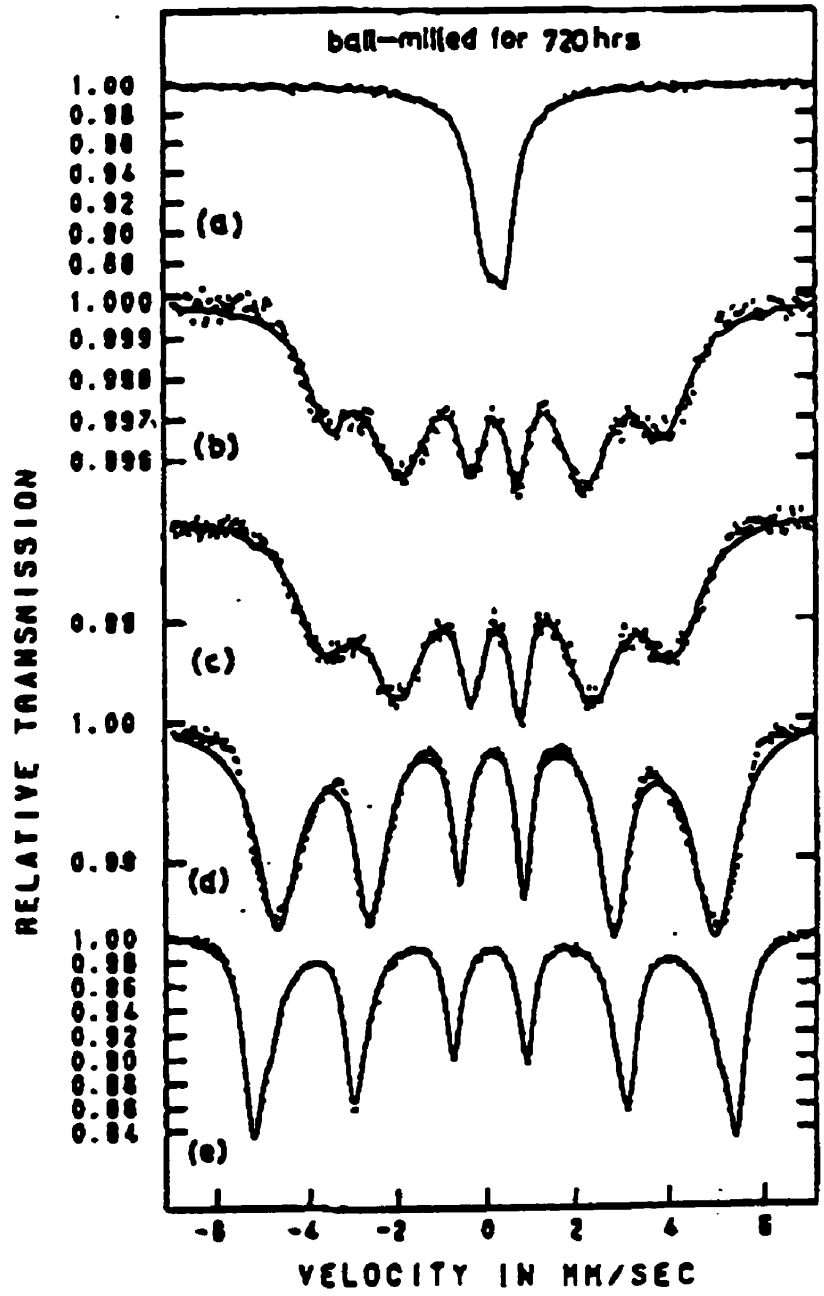

Fig. A3 Mössbauer spectra at room temperature of mechanical alloying samples. (a) 50 at.% Al; (b) 40 at.% Al; (c) 33 at.% Al; (d) 20 at.% Al; and (d) 10 at.% Al. (after [A4]).

formed. In ordered FeAl no magnetic moment is associated with the Fe atoms, and therefore a single-line spectrum is observed. After severe cold working by crushing, the spectrum exhibits coexisting paramagnetic and magnetic hyperfine lines, due to the fact that partially disordered alloys are formed with a deviation of near neighbor configuration of the Fe atoms. In the ordered Fe_3Al intermetallic compound the Fe atoms possess magnetic moments. The Mössbauer spectrum of the Fe_3Al phase exhibits two superimposed six-line patterns. The phase changes with different composition of Al in the Al-Fe alloys obtained by a commercial mechanical alloying process provide good examples of the different characteristics of the Mössbauer spectra of the alloys, as shown in Fig. A4. It can be seen that the Mössbauer spectra gradually change from the six lines at a lower Al content into a singlet when the Al content approaches to 50 at.% [A4].

Reference:

[A1] N. N. Greenwood and T. C. Gibb, Mössbauer Spectroscopy, Chapman and Hall Ltd., London, 1971.

[A2] T. E. Cranshaw, B. W. Dale, G. O. Longworth and C. E. Johnson, Mössbauer Spectroscopy and Its Applications, cambridge University Press, Cambridge, London, 1985.

[A3] U. Gonser and M. Ron, Applications of Mössbauer Spectroscopy, Vol. II, ed. By Richard L. Cohen, Academic Press, Now York, 1980.

[A4] B. Huang, K. N. Ishihara, P. H. Shingu, Materi. Sci. Eng., A231(1997)72-79.

Refereed Publications from the Present Research

[1] Microstructural Characterization of Mechanically Mixed Layer and Wear Debris in Sliding Wear of Al Alloys and Al based Composite,
Li, X. Y. and Tandon K. N., accepted as an invited paper in Int. Symp. On Genesis and role of transfer layer/mechanically mixing layer in wear of materials, India, December 1998, accepted for publication in *Journal of Wear*, 1999.

[2] Mechanical Mixing Induced by Sliding Wear of An Al-Si Alloy Against M2 Steel,
Li, X. Y. and Tandon, K. N., Journal of *Wear*, 225(1999)640-648.

[3] Wear Behavior of SiC Particulate Reinforced Aluminum Composites Sliding Against Steel Balls Under Dry and Lubricated Conditions,
Tandon, K. N., Feng Z. C. and Li, X. Y., *Tribology Letters*, 6(1999)113-122.

[4] Dry Sliding Wear Behaviour of Aluminum alloy 2014 Microalloyed With Sn and Ag, Bishop D. P., X. Y. Li, K. N. Tandon and W. F. Caley, Journal of *Wear*, 222(1998)84-92.

[5] Wear Debris Characterization Of Al-Si Alloys Sliding Against Steel Under Dry Wear Conditions,
Tandon, K. N. and Li, X. Y., *Scripta Metallurgica*, Vol.38 (1998)7-13.

[6] Subsurface Microstructures Generated by Sliding Wear on as-cast and Heat Treated Al Metal Matrix Composites,
Li, X. Y. and Tandon, K. N., Journal of *Wear*, 203/204(1997)703-708.

[7] Effect Of Ion Implantation On The Dry Sliding Wear Behavior Of SiC Reinforced Al-Si Composite,
Li, X. Y. and Tandon, K. N, *Surface & Coatings Technology*, 90(1997)136-142.

[8] Sliding Wear Properties Of TiAl Alloys With/Without TiN Coatings.
Wang Y., Qian Z., Li, X. Y and Tandon, K. N., *Surface & Coatings Technology*, 91(1997)37-42.

[9] Amorphization And Precipitation Within The Amorphous Layer Induced By Dry Wear Of An Al-Si/SiCp Composite Material

Li, X. Y and Tandon, K. N., Acta Metallurgica, 44(1996)3611-3624.

[10] Formation of an Amorphous Phases of Al-Si During Dry Wear of An Al-Si/SiCp Composite.

Li, X. Y and Tandon, K. N., *Scripta Metallurgica*, 33(1995)485-490.